

*Journal of*  
***Mechanics of***  
***Materials and Structures***

*Volume 4, N° 3*

*March 2009*

 mathematical sciences publishers

# JOURNAL OF MECHANICS OF MATERIALS AND STRUCTURES

<http://www.jomms.org>

EDITOR-IN-CHIEF Charles R. Steele

ASSOCIATE EDITOR Marie-Louise Steele  
Division of Mechanics and Computation  
Stanford University  
Stanford, CA 94305  
USA

## BOARD OF EDITORS

D. BIGONI University of Trento, Italy  
H. D. BUI École Polytechnique, France  
J. P. CARTER University of Sydney, Australia  
R. M. CHRISTENSEN Stanford University, U.S.A.  
G. M. L. GLADWELL University of Waterloo, Canada  
D. H. HODGES Georgia Institute of Technology, U.S.A.  
J. HUTCHINSON Harvard University, U.S.A.  
C. HWU National Cheng Kung University, R.O. China  
IWONA JASIUK University of Illinois at Urbana-Champaign  
B. L. KARIHALOO University of Wales, U.K.  
Y. Y. KIM Seoul National University, Republic of Korea  
Z. MROZ Academy of Science, Poland  
D. PAMPLONA Universidade Católica do Rio de Janeiro, Brazil  
M. B. RUBIN Technion, Haifa, Israel  
Y. SHINDO Tohoku University, Japan  
A. N. SHUPIKOV Ukrainian Academy of Sciences, Ukraine  
T. TARNAI University Budapest, Hungary  
F. Y. M. WAN University of California, Irvine, U.S.A.  
P. WRIGGERS Universität Hannover, Germany  
W. YANG Tsinghua University, P.R. China  
F. ZIEGLER Technische Universität Wien, Austria

## PRODUCTION

PAULO NEY DE SOUZA Production Manager  
SHEILA NEWBERY Senior Production Editor  
SILVIO LEVY Scientific Editor

---

See inside back cover or <http://www.jomms.org> for submission guidelines.


---

Regular subscription rate: \$600 a year (print and electronic); \$460 a year (electronic only).

Subscriptions, requests for back issues, and changes of address should be sent to [contact@mathscipub.org](mailto:contact@mathscipub.org) or to Mathematical Sciences Publishers, 798 Evans Hall, Department of Mathematics, University of California, Berkeley, CA 94720-3840.

---

©Copyright 2009. Journal of Mechanics of Materials and Structures. All rights reserved.

 mathematical sciences publishers

## DESIGN OF CRACK-RESISTANT TWO-DIMENSIONAL PERIODIC CELLULAR MATERIALS

FABIAN LIPPERMAN, MICHAEL RYVKIN AND MOSHE B. FUCHS

The resistance to macrocrack propagation in two-dimensional periodic cellular materials subjected to uniaxial remote stresses is improved by redistributing the material of the solid phase. The materials are represented by beam lattices with regular triangular or hexagonal patterns. The purpose of the design is to minimize the maximum tensile stress for all possible crack locations allowed by the material microstructure. Two design cases are considered. In the cell design case material is redistributed between the otherwise uniform elements of the repetitive cell. In the element design case the shape of identical elements is optimized. The analysis of such infinite trellis with an arbitrary macroscopic crack is enabled by an efficient exact structural analysis approach. It is shown that the fracture toughness of the triangular layout can be significantly increased by redistribution of the material between the elements with uniform cross sections while for the case of hexagonal lattice the effect is achieved mainly by using identical elements with variable thickness distribution.

### 1. Introduction

The present paper is concerned with the improvement of the resistance of periodic cellular materials to the propagation of mature cracks by redesigning the repetitive cell. The two-dimensional cellular materials, or honeycombs, considered here are modeled as lattices with rigidly connected beam elements exhibiting both axial and flexural stiffness. Borrowing from the continuous case the resistance to crack propagation of a cellular material is given by the fracture toughness  $K_C$ . In contrast to a continuous material where the fracture toughness is determined experimentally, in cellular materials, where the tip of a macroscopic crack can be always associated with a void, thus precluding singularities in the stress field, the fracture toughness can, in principle, be determined numerically in terms of the rupture stress of the parent brittle material. The aim of the present paper is to improve the fracture toughness of cellular material by redesigning the repetitive cell using a formal mathematical programming approach.

A numerical structural optimization process is basically a conjunction of an analysis module embedded within an optimization algorithm. The availability of an efficient and robust analysis tool is thus a central concern since the optimizer will usually navigate through a plethora of candidate designs, each requiring a separate analysis, before reaching the best configuration. We need therefore an adequate capability for a detailed analysis of a cellular material in a given stress field in the presence of a crack. The basic problem in the presence of a crack is that the periodicity of the structure is lost, which causes difficulties for the analysis. Some authors have obtained the fracture toughness of cellular material numerically, most of them in some restrictive cases. The published methods of determining the fracture toughness either

---

*Keywords:* fracture toughness, honeycombs, design, discrete Fourier transform.

The second author gratefully acknowledges the support of the ISF (Israel Science Foundation) under grant No. 838/06.

involve some sort of representation of the honeycomb as an equivalent continuum (homogenization)—an indirect approach—as in [Maiti et al. 1984; Gibson and Ashby 1997; Chen et al. 1998], or tackle the problem directly with a finite element method by reducing the infinite honeycomb to a finite-size model [Huang and Gibson 1991; Schmidt and Fleck 2001; Choi and Sankar 2005; Fleck and Qiu 2007; Quintana Alonso and Fleck 2007].

In all these examples, and to the best of our knowledge, also among other publications which deal with the fracture toughness estimation of cellular materials no numerical work was published on the fracture toughness of honeycombs with asymmetric or irregular topologies. Recently, a general approach which uses exact structural analysis for a crack in an infinite lattice was presented in [Lipperman et al. 2007a] to determine the fracture toughness of honeycombs with prismatic-like elements. The method can accommodate any topology of the unit repetitive cell, with or without symmetry, and any type of remote loading.

The above references deal with the determination of the fracture toughness of cellular material. The present paper intends to redesign the unit cell in order to improve the fracture toughness, that is, to improve the resistance of all mature cracks which may exist in the cellular material, to propagate when subjected to a uniaxial stress field in a given direction. Since cracks are assumed *ab initio*, all possible crack types and orientations compatible with the internal arrangement of the microstructure of the particular material are made allowance for in each case. To this respect, this is probably a first attempt for a systematic design of crack-resistant honeycombs (we use the term *crack-resistant* to indicate the resistance of mature cracks to propagate).

Two design formulations are presented starting with the *cell* design case where material is moved between the otherwise uniform elements of the unit cell. In the *element* design formulation all the elements of the unit cell are identical and the shape of a typical prismatic element of variable cross-section is optimized. Note, elements with variable thickness were considered in [Warren and Kraynik 1987], where the linear elastic response of an *undamaged* hexagonal honeycomb was studied for three different element shapes, and in [Warren and Kraynik 1988] for a tetrahedral unit cell, but the shape of the elements were not optimized. The present paper deals with two basic topologies: regular triangular and regular hexagonal lattices. As indicated the honeycombs considered here will be redesigned to resist crack propagation of any possible mature crack under a given unidirectional remote tensile loading.

For the analysis, the method in [Lipperman et al. 2007a] is used. The analysis is direct, in the sense that it remains in the discrete realm without first associating the honeycomb with a continuous material using homogenization. A conjunction of the structural variation method of Majid et al. [1978], the representative cell method of Nuller and Ryvkin [1980] and stress localization [Michel et al. 1999; Lipperman et al. 2008a] allows for an exact analysis of fractured honeycombs with repeating unit cells of any shape and subjected to any type of remote loading. With this versatile analysis module at hand the honeycombs are optimized for maximum resistance to crack propagation.

In Section 2 the design problem is formulated. Section 3 gives a succinct description of the analysis process. In Sections 4 and 5 we present the redesign of the honeycombs for best crack-resistance. The paper closes with a summary of the main results and some conclusions (Section 6).

## 2. The design formulations

The purpose of the design is to produce honeycombs which have improved resistance to crack propagation under remote stresses. This property is characterized by the honeycomb fracture toughness. Huang and Gibson [1991], who evaluated the stress field in the vicinity of a Mode I crack of length  $2a$  in a square-celled honeycomb, calculated this quantity by means of the formula

$$K_C = \sigma_r \sqrt{\pi a}, \quad (1)$$

where  $\sigma_r$  is the remote tensile loading corresponding to the onset of fracture, that is, when the most stressed element in the crack-tip vicinity fails. We will follow this approach completed by the assumption that noninteracting cracks of same length, of all possible types and orientations, dictated by the material microstructure, are present simultaneously. Consequently, the magnitude of  $\sigma_r$  in (1) is defined by the stress field in the vicinity of the most dangerous crack. Clearly, the crack length used in the simulations must be large enough such as to produce self-similar  $K$ -fields close to the crack tips. The issue of possible crack types was investigated by Lipperman et al. [2007b], who found numerically that they are parallel to the microstructure symmetry planes. It should be noted that the optimization of the fracture properties was carried out for a specific loading direction.

The redesign is performed on honeycombs with two popular patterns: equilateral triangles and regular hexagons (Figure 1). The unit cells of the planar repetitive structures have walls of length  $L$ , rectangular cross sections of thickness  $t$  and a unity inward depth. For the analysis model, the cell walls are represented by rigidly connected Euler–Bernoulli beam elements, including their axial rigidity. A displacement-based analysis is used with 3 degrees of freedom defined at each node. The bulk material is assumed isotropic, homogeneous, linear-elastic and brittle with a rupture modulus  $\sigma_{fs}$ . The honeycombs are subjected to a uniaxial remote stress  $\sigma_r$  as shown in Figure 1.

We will take into account all the possible straight paths which can be formed by the sequential fracture of elements along the lattice axes of symmetry. As shown in Figure 2, top, the triangular pattern has a single crack type, denoted by T1, whereas the hexagonal grid exhibits 3 crack types: H1, H2 and H3 (see Figure 2, bottom). It will be seen that the macroscopic cracks in Figure 2 can for both patterns be rotated three times by an angle of  $\pi/3$  radians, yielding three possible propagation orientations in each case. Consequently, the triangular layout has in total 3 possible cracks whereas the hexagonal lattice has 9 possible cracks.

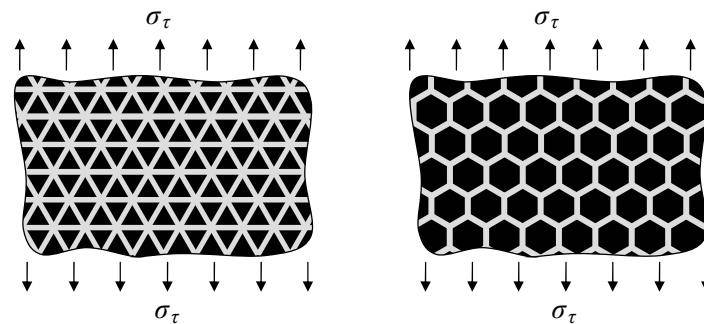


**Figure 1.** Honeycombs with equilateral triangles (left) and regular hexagons (right), subjected to a uniaxial remote loading.

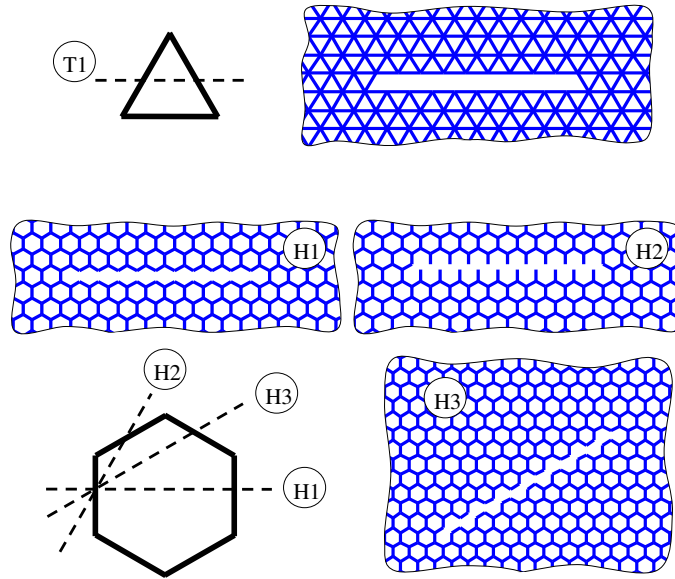


**Figure 2.** The possible macrocrack paths types of the triangular and hexagonal, honeycombs.

We consider two design cases. In the *cell design* case the beam-elements of the unit cell are uniform and the design variables are the thicknesses of the elements (Figure 3, left). During the optimization process material is moved between the elements until the optimal layout is reached. Moving material between elements creates nonsymmetric unit cells and as stated earlier, there are no published results for the analysis of such materials, with or without cracks. In the *element design* case the unit cells are composed of an identical typical element of variable thickness (Figure 3, right). The optimization searches for the optimal shape of the typical element and the design variables are parameters which govern the contour of the element.

A crack propagates by the failure of an element in the crack tip vicinity. It is assumed that an element will fail when the tensile stress, anywhere along the element, reaches the rupture modulus or when the axial load in a compressed element reaches the Euler buckling load. Note that the maximal tensile stress in a uniform element (cell design case, shown on the left in Figure 3) will occur at one of the ends of

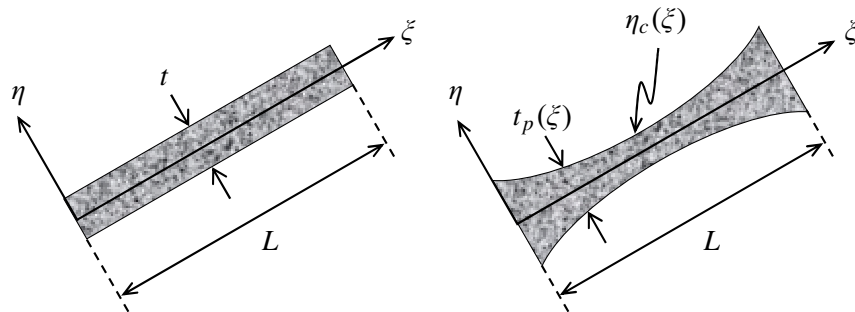


**Figure 3.** Beam elements with uniform and variable cross-sections.

the element. On the other hand, with variable cross-sections (element design case, shown on the right in Figure 3), the maximum stress can also occur at intermediate locations. As indicated, we can have several possible crack types and crack orientations. Consequently, we are in the presence of a minimax problem in the sense that we want to minimize the maximum stress anywhere along elements in the front of any possible crack and thus improving the resistance of the structure to the propagation of existing cracks. Minimizing the maximum stress in the elements is commensurate with maximizing the allowable remote stress, that is, maximizing  $K_C$ .

### 3. Analysis considerations

A central ingredient in a structural optimization scheme is the analysis module which provides the internal forces in the structure for any given candidate design. In the present case we need to analyze a fractured cellular material under remote uniaxial tension. The crack is formed by a series of fractured elements in contiguous cells along a linear path. It must be sufficiently long, so that the  $K$ -field in its vicinity emerges, allowing one to determine the fracture toughness. Since the fractured elements do not contribute to the stiffness of the assembly they can be removed from the analysis model which results in an infinite structure which is no longer periodic subjected to uniaxial tension at infinity. The central idea in analyzing the cracked honeycomb is to consider the failed elements as a finite set of components whose stiffness was modified (in our case, reduced to zero) in an otherwise repetitive infinite structure. We will refer to the undamaged honeycomb as the *nominal* structure, the cracked honeycomb as the *modified* structure and the stresses at infinity will be the *nominal loads*. The analysis will be based on the structural variations method of Majid et al. [1978], which is an efficient reanalysis method when only part of the stiffnesses of a structure are modified. In particular, for the broken elements considered here, the modification is to set the stiffnesses to zero. This method determines the internal forces in the modified structure on the basis of analyses performed on the nominal structure under the nominal loads and under self-equilibrating loads. The latter are unit and opposite forces applied in turn to the extremities of the elements that will eventually be removed to form the crack (Figure 4). This method suits the present needs perfectly since we need to analyze only intact infinite repetitive structures.

For the analysis of the nominal structure under the nominal loads, that is, the uniaxial stress field, we follow the methodology for stress localization for honeycombs in a macroscopic stress field [Michel et al. 1999]. Stress localization gives the detailed stresses in the repetitive cell of a cellular material subjected

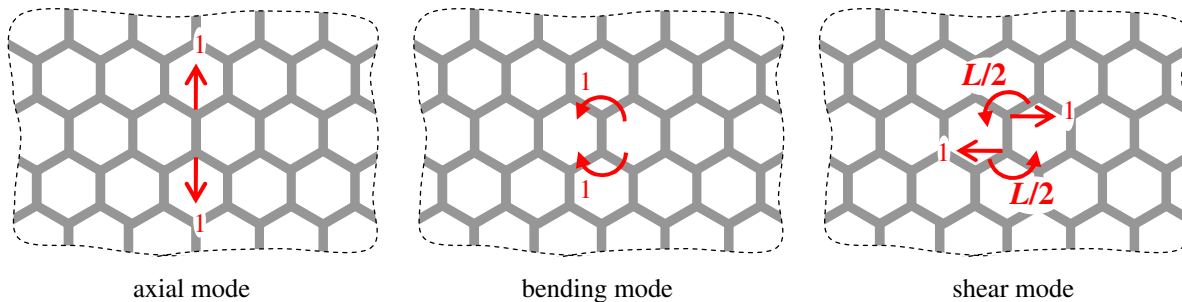


**Figure 4.** The unit loads applied at the nodes of an arbitrary rigid-jointed element of the hexagons honeycomb.

to a periodic stress field, without the need for prior homogenization. We will be using a slightly modified version of stress localization developed in [Lipperman et al. 2008a].

The unit loads solutions are obtained by the representative cell method [Nuller and Ryvkin 1980; Ryvkin and Nuller 1997], which enables to solve infinite and repetitive structures subjected to arbitrary loads, as opposed to periodic loads (see, for instance, [Ryvkin et al. 1999; Fuchs and Ryvkin 2002; Fuchs et al. 2004]). A discrete Fourier transform replaces the problem formulated for an infinite structure by an equivalent problem defined over the repetitive cell, albeit in transformed variables. After solving the analysis equations in the transformed space, inverse transforms can produce the requested analysis information in any cell of the infinite structure. It is instructive to emphasize that both stress localization and the representative cell method perform the analysis on a single repetitive module.

#### 4. Optimal design of the unit cell

In the cell design example we maximize the fracture toughness  $K_C$  of the cellular material by redistributing the material between the uniform elements of the unit cell while maintaining a constant material density. This is akin to minimizing the maximum skin stress in elements in the vicinity of the crack tips for all possible crack types and orientations. The mathematical programming formulation of this min-max optimization problem is

$$\min_{\mathbf{t}} \max \{ \boldsymbol{\sigma}(\mathbf{t}) \text{ such that } \rho(\mathbf{t}) = \rho_r \}, \quad (2)$$

where  $\mathbf{t}$  is the design vector composed of the unit cell elements thicknesses,  $\boldsymbol{\sigma}(\mathbf{t})$  is the vector containing the set of largest stresses in elements that are to be considered for all possible cracks,  $\rho(\mathbf{t})$  is the relative density of the cellular material defined as the ratio of the density of the honeycomb over the density of the bulk material and  $\rho_r$  is a given relative density, taken here as  $\rho_r = 0.15$ . The cracks length  $2a$  is chosen sufficiently long to ensure continuum fracture mechanics behavior characterized by the proportionality of the near tip stress field to the square root of the crack length.

Failure of an element is assumed to occur when the normal stress anywhere along the element reaches the critical tension stress or the critical compression stress. The critical tension stress  $\sigma_{\text{cr}}^T$  is simply the bulk material rupture modulus  $\sigma_{fs}$

$$\sigma_{\text{cr}}^T \equiv \sigma_{fs} \quad (3)$$

and the critical compression stress is adopted as the Euler buckling stress for the uniform hinge supported element

$$\sigma_{\text{cr}}^B \equiv \frac{E}{12} \pi^2 (t/L)^2, \quad (4)$$

where  $E$  is the Young's modulus of the solid material and  $t$  is the thickness of the element. Hinge supports are assumed for conservative reasons. In order to set the tensional and buckling modes on a common footing we have assumed  $E/\sigma_{fs} = 10^3$ , which is a common ratio for ceramics and many metal materials [Bolton 1998]. Consequently

$$\frac{\sigma_{\text{cr}}^T}{\sigma_{\text{cr}}^B} = \frac{12}{10^3 \pi^2 (t/L)^2}. \quad (5)$$



The value  $\sigma_j$  of the stress vector  $\boldsymbol{\sigma}$  is defined by the most critical axial stress failure mode

$$\sigma_j = \max(\sigma_j^T; \sigma_j^B), \quad (6)$$

where  $\sigma_j^T$  and  $\sigma_j^B$  are the skin stresses related to the tensional and buckling failure modes for element  $j$ , respectively given by

$$\sigma_j^T = \frac{N_j}{t_j} + \max\left(\frac{6|M_{1j}|}{t_j^2}; \frac{6|M_{2j}|}{t_j^2}\right) \quad \text{and} \quad \sigma_j^B = \frac{-N_j}{t_j} \left(\frac{\sigma_{cr}^T}{\sigma_{cr}^B}\right)_j. \quad (7)$$

$N_j$  is the internal axial force in element  $j$ , and  $M_{1j}$ ,  $M_{2j}$  are the internal bending moments at its extremities.

We consider two cell layouts, the triangular pattern and the hexagonal one. With each pattern we first take the basic repeating cell as the redesign unit. Next we consider a larger redesign unit consisting of four basic cells thus quadrupling the number of design variables and consequently enriching the optimization space. All computations were performed on a Matlab platform and for the actual minimization we have used the `fminimax` subroutine of Matlab which implements a sequential quadratic programming method.

**4.1. Triangles: one basic unit.** As a first design scenario we consider the triangular honeycomb for which the smallest repeating pattern possesses three elements, as shown in Figure 5(a). They will typically be referred to as 1-elements, 2-elements and 3-elements. The constraint on the relative density of the material is

$$\rho(\mathbf{t}) \equiv \frac{2}{\sqrt{3}L} \sum_{i=1}^3 t_i = 0.15. \quad (8)$$

As mentioned, the triangle has only one crack type, T1, with 3 possible orientations yielding the macroscopic cracks  $T1_0$ ,  $T1_{\pi/3}$ ,  $T1_{2\pi/3}$ , where the orientation angles  $\theta_p$  are given in the subscript. In parts (b) and (c) of Figure 5 one can see a depiction of cracks  $T1_0$  and  $T1_{\pi/3}$ .

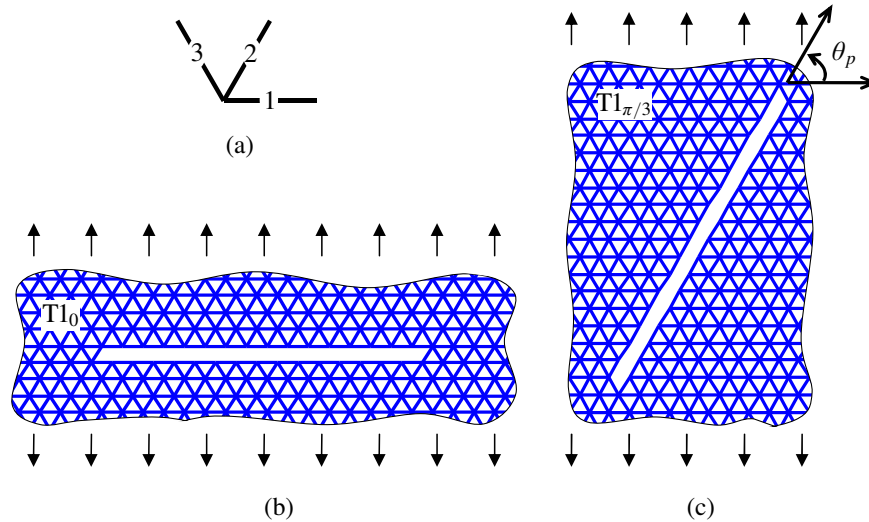


**Figure 5.** (a) The unit cell of the triangles honeycomb with (b)  $\theta_p = 0$  and (c)  $\theta_p = \pi/3$  paths orientations.

Each of the three cracks can end in front of two different unit cell elements. For instance, crack  $T1_0$  in Figure 5(b) ends in front of a 2-element but it could also stop in front of a 3-element. For the triangular case (one basic unit) we need to ensure that none of the  $3 \times 2 = 6$  possible cracks propagates while maximizing the fracture toughness. This triangular pattern with three design variables is a relatively simple case. We will see in the sequel that in more intricate designs with more elements in the repeating unit we may have several possible cracks in the material. It is therefore worthwhile to try to reduce the number of candidate cracks prior to solving (2). We need to determine not only which cracks should be considered for the optimization but also in front of which element they end.

The structure was analyzed in the initial configuration (identical elements) for every possible crack, and cracks with relatively low near-tip stresses were discarded. In the case of triangular cells this left only crack  $T1_0$ . Since we omit cracks on the basis of the initial design the optimal solution was again checked against all the cracks to ensure that in the final layout no crack propagates.

An arguably intrinsic feature of designing for crack-resistance is that including two cracks of a same type and orientation but with different end-elements may impede the process from reaching the optimal solution. To illustrate the concept consider again the  $T1_0$  of the triangular pattern. It propagates by sequential breaking of 2- and 3-elements — with the labeling as in Figure 5(a) — along the crack line illustrated in Figure 5(b). Including both cracks in the optimization will yield a symmetric design with equal thicknesses for elements 2 and 3 (and half the thickness for element 1). Consequently, a  $T1_0$  crack, whether facing a 2-element or a 3-element will not propagate. However, this may not be the best solution. In contrast to classical structural design where no failure is tolerated, with crack propagation we do not really care if a crack facing a 2-element breaks that element as long as it stops in front of the subsequent 3-element (or vice-versa.) We could thus weaken the 2-elements and reinforcing the 3-elements by moving material from 2 to 3. By setting the *trap* at 3 (or at 2) we should produce better resistant materials albeit with nonsymmetric repetitive cells. This can be achieved by including only one  $T1_0$  crack, facing either a 2- or a 3-element, in the optimization formulation.

For the triangular case with 3 design variables we need to include only one crack. With unit cells of complex geometries and more design variables, the selection of cracks and corresponding traps is not always obvious and in such cases (2) must be solved separately for several alternatives.

In this example we selected 2 as the trap element and the optimization in (2) gave elements of thicknesses

$$t_1^{\text{opt}} = 0.026L, \quad t_2^{\text{opt}} = 0.053L, \quad t_3^{\text{opt}} = 0.051L \quad (9)$$

with a normalized fracture toughness

$$K_C^{T_3}/(\sigma_{fs}\sqrt{L}) = 0.091, \quad (10)$$

where the superscript indicates that we deal with a triangular layout with 3 design variables. The improvement of this design with respect to a design with equal thicknesses [Lipperman et al. 2007a] is

$$\frac{K_C^{T_3}}{K_C^T} = 1.20. \quad (11)$$

Thus, the thicknesses distribution obtained in (9), increases the  $K_C$  of the triangular honeycomb, loaded in the direction given in parts (b) and (c) of Figure 5, by 20%.

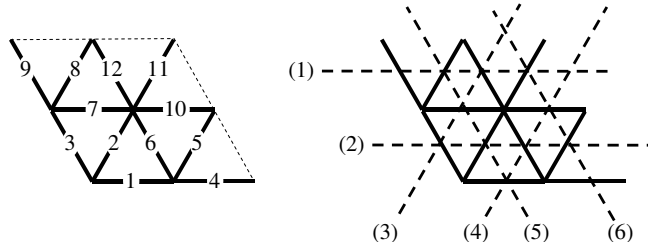


**Figure 6.** Left: The enlarged unit cell of the triangles honeycomb. Right: the six T1 propagation possibilities.

**4.2. Triangles: four basic units.** Improved results can be expected if we increase the size of the repeating cell and therefore the number of design variables. In this example we consider a repeating cell composed of 4 basic units. We have thus 12 design variables and 6 different T1 possibilities (Figure 6). However, as noted in Section 4.1, it suffices to consider the two horizontal paths. The relative density constraint is now

$$\rho(\mathbf{t}) \equiv \frac{1}{2\sqrt{3}L} \sum_{i=1}^{12} t_i = 0.15. \quad (12)$$

The selection of the trap elements is a little more intricate. Here one needs to make allowance for cracks to propagate in both directions. After due considerations the traps were set at elements 2, 6, 11 and 12 and from symmetry the number of independent design variables could be reduced to 4. The optimal layout given in Figure 7 has thicknesses

$$\begin{aligned} t_2^{\text{opt}} = t_6^{\text{opt}} = t_{11}^{\text{opt}} = t_{12}^{\text{opt}} &= 0.086L, & t_1^{\text{opt}} = t_4^{\text{opt}} &= 0.025L, \\ t_3^{\text{opt}} = t_5^{\text{opt}} = t_8^{\text{opt}} = t_9^{\text{opt}} &= 0.017L, & t_7^{\text{opt}} = t_{10}^{\text{opt}} &= 0.029L \end{aligned} \quad (13)$$

with an optimal fracture toughness  $K_C^{T_{12}}/(\sigma_{fs}\sqrt{L}) = 0.110$  which gives an improvement with respect to the original design of

$$\frac{K_C^{T_{12}}}{K_C^T} = 1.45. \quad (14)$$

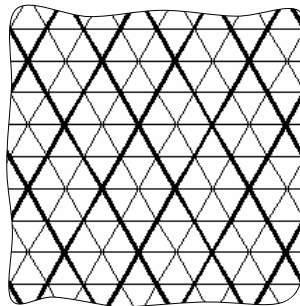


**Figure 7.** An option for an optimal triangles honeycomb where the maximal length and the minimal thickness of its elements have been previously set.

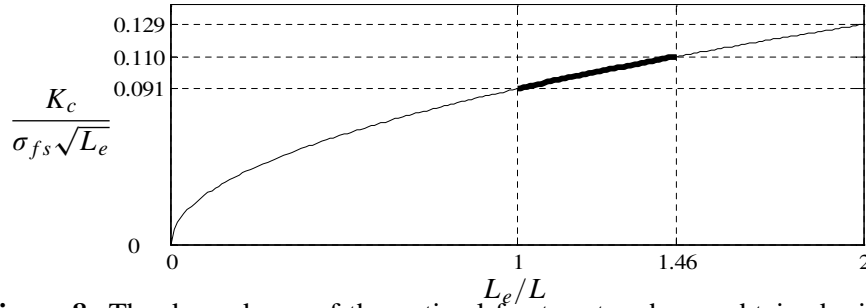


**Figure 8.** The dependence of the optimal fracture toughness obtained with 3 design variables on the scale length of the elements.

At this juncture it is instructive to address an issue related to the relative scale of the grid. In Figure 8 we show the dependence of the optimal fracture toughness on the element length  $L_e$  where the relative density was kept unchanged by maintaining a constant value of  $t/L_e$ . We assume that the basic value  $K_C^{T_3}/(\sigma_{fs}\sqrt{L}) = 0.091$  of (10) was obtained for a unit element length, that is, when  $L_e/L = 1$ . The fracture toughness is a square root function of the element length and doubling the latter ( $L_e = 2L$ ) should produce  $K_C^{T_3}/(\sigma_{fs}\sqrt{L}) = 0.091\sqrt{2} = 0.129$ , as indicated on the figure. This result could have been obtained by the optimization in the absence of Euler buckling constraints by removing elements 5, 6, 7, 8, 10 and 12. This is a classical case of a disjoint design space. The double-sized triangle lies in the shadow of the buckling constraints, however, once it is reached, the design is acceptable because the buckling constraints on the now vanished elements are no longer valid. The optimal design of the present problem should in fact be the trivial solution in the form of a triangle with double lengths and thicknesses.

We can however make a case for the design in Figure 7. Clearly, increasing  $L_e$  will improve the fracture toughness but it also increases the size of the *holes* or apertures in the material. The *holes* in the triangles with  $L_e = 2L$  have doubled and if we want to limit the size of the holes to the scale  $L_e = L$  (think of a net capturing fish) the design in Figure 7 is to be preferred. In fact, as shown on the graph, the design in Figure 7 of scale  $L_e = L$  is equivalent to an optimal solution with 3 design variables of scale  $L_e = 1.46L$ .

**4.3. Hexagons: one basic unit.** The basic hexagonal pattern has three design variables, with a relative density constraint

$$\rho(\mathbf{t}) \equiv \frac{2}{3\sqrt{3}L} \sum_{i=1}^3 t_i = 0.15. \quad (15)$$

As noted from Figure 2, right, there are a total of 9 propagation paths:  $H1_{0,\pi/3,2\pi/3}$ ,  $H2_{0,\pi/3,2\pi/3}$ ,  $H3_{\pi/6,\pi/2,5\pi/6}$ . A preliminary investigation of the initial design (equal thicknesses) has shown that the problem could be simplified. Because of symmetry, as noted for instance in Figure 9 for the  $H1_0$  crack, we have  $t_2 = t_3$  and the set of cracks can be reduced to  $H1_0$ ,  $H2_0$  and  $H3_{\pi/6}$  in view of the fact that the constraints produced by the remaining cracks can be shown to be nonactive.

The optimum result is

$$t_1^{\text{opt}} = 0.119L \quad \text{and} \quad t_2^{\text{opt}} = t_3^{\text{opt}} = 0.135L \quad (16)$$

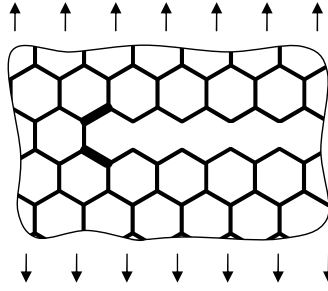


**Figure 9.** The  $H1_0$  macrocrack with its two most loaded elements (in bold).

for  $K_C^{H_3}/(\sigma_{fs}\sqrt{L}) = 0.016$ , an improvement of only 6% over the fracture toughness with equal cross-sections (0.015), given in [Lipperman et al. 2007a]. The resistance to macrocrack propagation in this case is only moderately improved.

The location of the most loaded elements (Figure 9) may be counterintuitive however an earlier work on crack nucleation and propagation has shown that this type of crack under same loads at some early stage of the crack formation changed direction from the path perpendicular to the loading to a direction inclined by  $60^\circ$  [Lipperman et al. 2007b]. The most loaded elements at the crack-tip are probably the harbingers of the kink in the crack path.

**4.4. Hexagons: four basic units.** We now consider an augmented design domain, composed of four basic unit cells with 12 design variables, as shown in Figure 10. The relative density constraint here is

$$\rho(\mathbf{t}) \equiv \frac{1}{6\sqrt{3}L} \sum_{i=1}^{12} t_i = 0.15. \quad (17)$$

The number of design variables could be reduced from 12 to 5 and from the 18 possible propagation paths only 5 were retained.

The thickness distribution for the optimal solution is

$$\begin{aligned} t_7^{\text{opt}} = 0.15L, \quad t_{10}^{\text{opt}} = 0.01L, \quad t_2^{\text{opt}} = t_6^{\text{opt}} = t_{11}^{\text{opt}} = t_{12}^{\text{opt}} = 0.09L, \\ t_1^{\text{opt}} = t_4^{\text{opt}} = 0.15L, \quad t_3^{\text{opt}} = t_5^{\text{opt}} = t_8^{\text{opt}} = t_9^{\text{opt}} = 0.18L. \end{aligned} \quad (18)$$

A typical unit cell and an overview of the hexagonal pattern are depicted in Figure 11. In the optimal layout we notice ellipse-like quasiholes in the form of cells with embedded slender elements oriented along the remote stress direction. The optimal fracture toughness is here  $K_C^{H_{12}}/(\sigma_{fs}\sqrt{L}) = 0.018$  which represents an increase of 18% over the initial design.

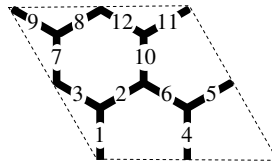


**Figure 10.** The enlarged hexagon unit cell with 12 elements.

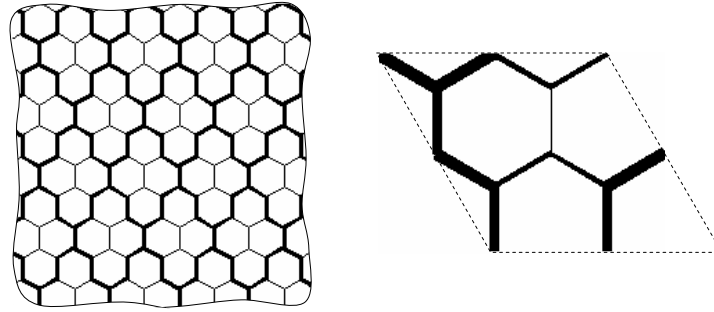


**Figure 11.** The optimal hexagonal honeycomb (left) with enlarged unit cell (right).

Unlike with the enlarged repetitive cell of the triangular honeycomb, the optimal hexagonal layout of scale  $L$  cannot be replicated on the present grid with elements of twice the length and thickness. The optimal design in Figure 11 is thus the only possible layout.

**4.5. Summary of results.** The main results for the optimal design of the cellular material with relative density  $\rho_r = 0.15$  are summarized in Table 1 for both layouts. The fundamental difference between the two patterns is already apparent in the initial design. The triangular patterns are markedly more resistant to crack propagation than the hexagonal ones. This is to be attributed to the axial mode being dominant in triangular lattices whereas hexagons deform primarily in bending [Deshpande et al. 2001]. In addition, the optimization is relatively more effective for triangles, where, for instance, a 45% improvement was obtained for repetitive cells with 12 design variables as compared to 18% in the hexagonal case. The counterexamples in the next section will show that using elements of varying thickness will prove much more effective for bending dominated patterns than for materials where the axial mode is predominant.

	Triangles	Hexagons
Initial (equal thicknesses)	0.076	0.015
Optimized (3 design variables)	0.091 (20%)	0.016 (6%)
Optimized (12 design variables)	0.110 (45%)	0.018 (18%)

**Table 1.** Optimal fracture toughness  $K_C/(\sigma_{fs}\sqrt{L})$  for triangular and hexagonal patterns with  $\rho_r = 0.15$  for two sizes of the repetitive module. The initial values correspond to equal thickness elements.  $\sigma_{fs}$  is the rupture stress of the bulk material and  $L$  is the beams length. Improvements with respect to the initial design are given in parentheses.

## 5. Optimal design of the element

In this section we improve the material's resistance to macroscopic crack propagation by using same beams but of variable thickness for the elements of the honeycomb. We assume the thickness of the elements  $t_p(\xi)$  along  $\xi = 0 \div L/2$  (see Section 2) to be

$$t_p(\xi) = 2\eta_c(\xi) = 2 \sum_{j=0}^p c_j \xi^j, \quad (19)$$

where  $p$  is the order of the polynomial and  $c_j$  are the parameters which define the shape of the elements and constitute the variables in this design problem. In addition we impose, for sound engineering design, a zero slope at the center of the symmetric element and positiveness of the thickness:

$$\frac{dt_p(\xi)}{d\xi} = 0 \quad \text{for } \xi = L/2, \quad t_p(\xi) \geq \varepsilon \quad \text{for } 0 \leq \xi \leq L/2, \quad (20)$$

with  $\varepsilon = 10^{-5}L$ . The mathematical programming formulation, solved with the same analysis and design subroutines as in Section 4, is here

$$\min_{\mathbf{c}} \max \{ \boldsymbol{\sigma}(\mathbf{c}) \text{ such that } \rho(\mathbf{c}) = \rho_r \}, \quad (21)$$

where the design vector  $\mathbf{c}$  holds the coefficients  $c_j$  ( $j = 0, 1, \dots, p$ ) of the polynomial. In line with (2),  $\boldsymbol{\sigma}(\mathbf{c})$  is the vector containing the set of stresses that are to be considered for all possible cracks. The relative density constraint is now

$$\rho(\mathbf{c}) \equiv \frac{n_{ce}A_e}{A_{uc}} = \rho_r, \quad (22)$$

where  $n_{ce}$  ( $= 3$  herein) is the number of elements of the unit cell,  $A_{uc}$  is the area of the unit cell and  $A_e$  is the area of the projection of the elements given by

$$A_e = 4 \int_0^{L/2} (c_0 + c_1\xi + \dots + c_p\xi^p) d\xi = 4 \sum_{j=0}^p \frac{c_j(L/2)^{j+1}}{j+1}. \quad (23)$$

For calculating the stiffness matrix of the beam element we have approximated the thickness by a piecewise linear function.

The material with the triangular pattern has a unit cell of area  $A_{uc} = \sqrt{3}L/2$  and making allowance for the symmetry of the problem we considered only macroscopic cracks  $T1_0$  and  $T1_{\pi/3}$  (Figure 5). The optimal solution  $t_p^{\text{opt}}(\xi)$  obtained with a second- and a third-order polynomial contour functions are presented in Table 2. The linear case is not addressed since it can not yield a zero slope at the middle of the element. Taking for baseline the material composed of elements with constant uniform cross-sections the improvement of the fracture toughness for honeycombs with optimized contours is given under the heading  $K_C^{T_{\text{opt}}}$  in Table 2. It will be seen that the improvements are not dramatic. Better results were obtained for the triangle when transferring material between the elements of the unit cell design.

We now turn our attention to the hexagonal pattern ( $A_{uc} = 3\sqrt{3}L/2$ ) where it was noticed that it suffices to include macroscopic cracks  $H1_0$ ,  $H2_0$  and  $H3_{\pi/6}$ , only. The results given in Table 3 clearly indicate a marked improvement in  $K_C^{H_{\text{opt}}}$ . In Figure 12 we have drawn the contours of the elements for different orders of the polynomial. It should be emphasized that the optimum was obtained for equal values of the skin stress at the root of an element and at mid-field. The latter could be calculated with

$p$	Contour function $t_p^{\text{opt}}(\xi)[10^{-2}L]$	$K_C^{T_{\text{opt}}}[\%]$
2	$4.6 - 1.4(\xi/L) + 1.4(\xi/L)^2$	4.2
3	$4.6 - 0.6(\xi/L) - 2.0(\xi/L)^2 + 3.4(\xi/L)^3$	4.8

**Table 2.** The optimal contour functions and fracture toughness increase of the triangles honeycomb.

$p$	Contour function $t_p^{\text{opt}}(\xi)[L]$	$K_C^{H_{\text{opt}}}[\%]$
2	$0.20 - 0.39(\xi/L) + 0.39(\xi/L)^2$	77.7
3	$0.17 - 0.05(\xi/L) - 0.82(\xi/L)^2 + 1.16(\xi/L)^3$	96.8
4	$0.18 - 0.15(\xi/L) + 0.13(\xi/L)^2 - 1.63(\xi/L)^3 + 2.50(\xi/L)^4$	103.7

**Table 3.** The optimal contour functions and fracture toughness increase of the hexagons honeycomb.

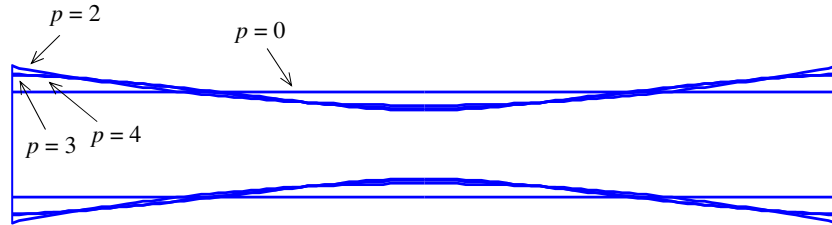


**Figure 12.** The optimal contours of the elements with  $\rho_r = 0.15$ .

relative confidence however at the root we have a concentration of material and consequently the model is locally less representative. As a consequence the stresses calculated at the ends may carry an error and should be utilized with care. The general trend is however clear and substantial improvements are to be gained by using variable thickness elements. In Figure 13 we give the shape of the hexagons obtained with optimal elements for densities  $\rho_r = 0.15, 0.25$ . The shape for the 0.25 density was added to show a tendency to form circular holes as the relative density of the cellular material increases. This

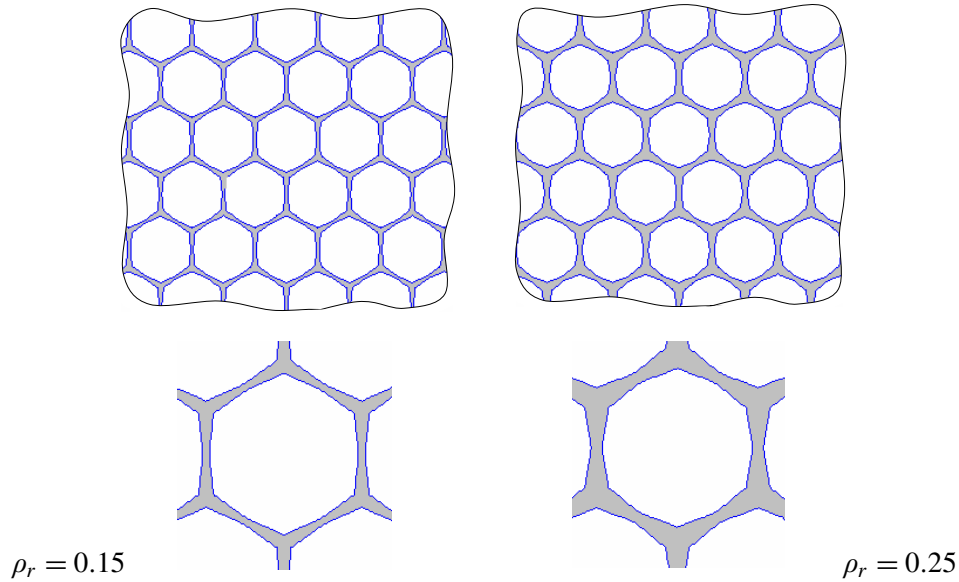


**Figure 13.** The topologies of the hexagons with the optimal elements obtained with the fourth-order contours, for  $\rho_r = 0.15$  and  $\rho_r = 0.25$ .



corroborates a result obtained in a separate work on the  $K_{IC}$  fracture toughness of perforated plates where a parametric study on the optimal shape of holes has shown that for holes stacked in a hexagonal pattern, circular holes produced optimal designs [Lipperman et al. 2008b].

It is interesting to notice that variable thickness elements have a rather marginal effect on the fracture of the triangular pattern but are of paramount importance in hexagonal honeycombs. This feature is to be related to the flexion versus stretch dominance of the two families of cellular materials which were studied in this work.

## 6. Conclusions

This paper has presented a methodology for designing two-dimensional cellular materials with improved resistance to crack propagation under macroscopic uniaxial tensile stresses. The material is modeled as repetitive patterns of bending resistant elements and crack propagation by the sequential breaking of the, assumed, brittle beam elements. With such grids the material can have cracks in a limited number of directions and we have defined the fracture toughness concept which is akin to the fracture toughness generalized by assuming the presence of all possible noninteracting cracks. The purpose is to maximize the fracture toughness by redistributing the material in the repetitive cell in an optimal fashion. Both the analysis and design are confined to the repetitive unit. For the analysis of the material with a crack we have used the representative cell method in conjunction with stress localization. These methods produce the results for the cracked medium by analyzing infinite pristine structures. The analysis is thus exact within the realm of Bernoulli–Euler beams. Two types of honeycombs were studied. A stretch dominated material with triangular patterns and a material with hexagonal unit cells which exhibits substantial flexion. It was shown that the material with triangles has only one type of crack which can appear in three directions. The hexagonal pattern presents three types of cracks each in three possible directions. In addition a given crack can end in front of different elements and each alternative should in principle be considered. Precluding an exhaustive optimization procedure where all the possibilities are tested it was suggested that the designer choose a *trap* element which is designed to arrest the crack and sacrifice other elements along the crack path. It was also shown that a prior study of the cracks can reduce the number of possibilities to a more tractable set. Since engineering judgment is involved the final design is always checked against all possible cracks. The actual computations were performed on a Matlab platform and for the optimization we have used a sequential quadratic optimization algorithm.

Two types of redesigns were considered. In the cell design case material was moved between the, otherwise uniform, elements. In the second design all elements were identical but had variable cross-sections. The parameters controlling the contour of the elements were here the design variables. The computations for the cell design were repeated for small repeating units (three design variables) and for larger ones (twelve design variables). As a rule results indicate that the stretch dominated triangular pattern is much more crack-resistant than the corresponding flexion dominated hexagonal layout. It is also much more sensitive to moving material between uniform elements than to the use of elements with variable thickness. An opposite conclusion can be drawn for the hexagonal honeycomb. A practical conclusion which could be drawn from the present work is that in order to increase the resistance to crack propagation of two dimensional cellular material one should redistribute the material between the elements of the repetitive model when the primary deformation mode of the structural elements is axial

deformation. In the case of models where bending is dominant the use of elements with variable thickness is the way to go. With the methodology presented herein one can quantify the expected improvements in a coherent manner. It is noteworthy that the computations, although confined to the repetitive unit, produce exact results for the infinite model.

The feasibility of manufacturing such optimal cellular materials may, at present, be questionable. It is however difficult to foresee what the future holds in store. MEMS technology, amongst others, could perhaps implement such optimal layouts.

### References

- [Bolton 1998] W. Bolton, *Engineering materials technology*, 3rd ed., Butterworth-Heinemann, Oxford, 1998.
- [Chen et al. 1998] J. Y. Chen, Y. Huang, and M. Ortiz, “Fracture analysis of cellular materials: a strain gradient model”, *J. Mech. Phys. Solids* **46**:5 (1998), 789–828.
- [Choi and Sankar 2005] S. Choi and B. V. Sankar, “A micromechanical method to predict the fracture toughness of cellular materials”, *Int. J. Solids Struct.* **42**:5–6 (2005), 1797–1817.
- [Deshpande et al. 2001] V. S. Deshpande, M. F. Ashby, and N. A. Fleck, “Foam topology: bending versus stretching dominated architectures”, *Acta Mater.* **49**:6 (2001), 1035–1040.
- [Fleck and Qiu 2007] N. A. Fleck and X. Qiu, “The damage tolerance of elastic-brittle, two-dimensional isotropic lattices”, *J. Mech. Phys. Solids* **55**:3 (2007), 562–588.
- [Fuchs and Ryvkin 2002] M. B. Fuchs and M. Ryvkin, “Explicit exact analysis of infinite periodic structures under general loading”, *Struct. Multidiscip. O.* **23**:4 (2002), 268–279.
- [Fuchs et al. 2004] M. B. Fuchs, M. Ryvkin, and E. Grosu, “Topological alternatives and structural modeling of infinite grillages on elastic foundations”, *Struct. Multidiscip. O.* **26**:5 (2004), 346–356.
- [Gibson and Ashby 1997] L. J. Gibson and M. F. Ashby, *Cellular solids: structure and properties*, 2nd ed., Cambridge University Press, Cambridge, 1997.
- [Huang and Gibson 1991] J. S. Huang and L. J. Gibson, “Fracture toughness of brittle honeycombs”, *Acta Metall. Mater.* **39**:7 (1991), 1617–1626.
- [Lipperman et al. 2007a] F. Lipperman, M. Ryvkin, and M. B. Fuchs, “Fracture toughness of two-dimensional cellular material with periodic microstructure”, *Int. J. Fract.* **146**:4 (2007), 179–190.
- [Lipperman et al. 2007b] F. Lipperman, M. Ryvkin, and M. B. Fuchs, “Nucleation of cracks in two-dimensional periodic cellular materials”, *Comput. Mech.* **39**:2 (2007), 127–139.
- [Lipperman et al. 2008a] F. Lipperman, M. B. Fuchs, and M. Ryvkin, “Stress localization and strength optimization of frame material with periodic microstructure”, *Comput. Methods Appl. Mech. Eng.* **197**:45–48 (2008), 4016–4026.
- [Lipperman et al. 2008b] F. Lipperman, M. Ryvkin, and M. B. Fuchs, “Crack arresting low-density porous materials with periodic microstructure”, *Int. J. Eng. Sci.* **46**:6 (2008), 572–584.
- [Maiti et al. 1984] S. K. Maiti, M. F. Ashby, and L. J. Gibson, “Fracture toughness of brittle cellular solids”, *Scr. Metall.* **18**:3 (1984), 213–217.
- [Majid et al. 1978] K. I. Majid, M. P. Saka, and T. Celik, “The theorems of structural variation generalized for rigidly jointed frames”, *Proc. Inst. Civ. Eng.* **65**:4 Part 2 (1978), 839–856.
- [Michel et al. 1999] J. C. Michel, H. Moulinec, and P. Suquet, “Effective properties of composite materials with periodic microstructure: a computational approach”, *Comput. Methods Appl. Mech. Eng.* **172**:1–4 (1999), 109–143.
- [Nuller and Ryvkin 1980] B. Nuller and M. Ryvkin, “On boundary value problems for elastic domains of a periodic structure deformed by arbitrary loads”, *Proc. State Hydraulic Inst.* **136** (1980), 49–55. In Russian.
- [Quintana Alonso and Fleck 2007] I. Quintana Alonso and N. A. Fleck, “Damage tolerance of an elastic-brittle diamond-celled honeycomb”, *Scr. Mater.* **56**:8 (2007), 693–696.

- [Ryvkin and Nuller 1997] M. Ryvkin and B. Nuller, "Solution of quasi-periodic fracture problems by the representative cell method", *Comput. Mech.* **20**:1–2 (1997), 145–149.
- [Ryvkin et al. 1999] M. Ryvkin, M. B. Fuchs, and B. Nuller, "Optimal design of infinite repetitive structures", *Struct. Multidiscip. O.* **18**:2–3 (1999), 202–209.
- [Schmidt and Fleck 2001] I. Schmidt and N. A. Fleck, "Ductile fracture of two-dimensional cellular structures", *Int. J. Fract.* **111**:4 (2001), 327–342.
- [Warren and Kraynik 1987] W. E. Warren and A. M. Kraynik, "Foam mechanics: the linear elastic response of two-dimensional spatially periodic cellular materials", *Mech. Mater.* **6**:1 (1987), 27–37.
- [Warren and Kraynik 1988] W. E. Warren and A. M. Kraynik, "The linear elastic properties of open-cell foams", *J. Appl. Mech. (ASME)* **55** (1988), 341–346.

Received 5 Mar 2008. Revised 7 Dec 2008. Accepted 14 Jan 2009.

FABIAN LIPPERMAN: [fabian@eng.tau.ac.il](mailto:fabian@eng.tau.ac.il)

*School of Mechanical Engineering, Tel Aviv University, Ramat Aviv 69978, Israel*

MICHAEL RYVKIN: [arikr@eng.tau.ac.il](mailto:arikr@eng.tau.ac.il)

*School of Mechanical Engineering, Tel Aviv University, Ramat Aviv 69978, Israel*

<http://www.eng.tau.ac.il/~arikr/>

MOSHE B. FUCHS: [fuchs@eng.tau.ac.il](mailto:fuchs@eng.tau.ac.il)

*School of Mechanical Engineering, Tel Aviv University, Ramat Aviv 69978, Israel*



# INFLUENCE OF THE NONLINEAR AERODYNAMIC FORCE COMPONENTS ON A VIBRATING BEAM, SIMPLY SUPPORTED OR CLAMPED AT BOTH ENDS, EXPOSED TO A HIGH SUPERSONIC AIRFLOW ALONG ITS AXIAL DIRECTION

SILVANO TIZZI

In this work we analyze the case of a vibrating beam, simply supported or clamped at both ends, under the effect of a high supersonic airflow along its axial direction. A complete aerodynamic model of the *piston theory*, which also takes into account the nonlinear components of the distributed aerodynamic transversal force, is used. The postcritical flutter behavior and its influence on the vibration state solutions of a fluttering beam without aerodynamic damping have been studied. This paper focuses particularly on the effects of these nonlinear aerodynamic forces on three frequencies, which are useful in characterizing the postcritical flutter solution set of the undamped beam in the whole frequency range: the minimum frequency, the frequency where the change of the modal shape with lower amplitude occurs, and the frequency corresponding to the solution with minimum amplitude of the vibration mode. Special attention has been given to the influence on the solution of the vibrating undamped beam with minimum modal amplitude, whose frequency is the most important among the three mentioned above; in fact, in the neighborhood of this particular solution, there exists the flutter state of the vibrating damped beam in limit cycle conditions.

Three different schemes, two of them semianalytical (based on the classical and well known Rayleigh–Ritz and Galerkin methods) and one of them numerical (based on the finite element method), have been herein exploited, as in the author’s previous papers, where beam flutter models with linear aerodynamic analysis were used. The good agreement between the results obtained by the three methods corroborates their effectiveness.

More sophisticated models have been herein set up, considering that a more accurate analysis is necessary than in previous cases, where the aerodynamic numerical model was limited to within the framework of the quasisteady linearized piston theory, both for the coupling component between odd and even order vibrating modes, and for the aerodynamic damping component.

The results obtained enable us to assess quantitatively the influence of these nonlinear aerodynamic forces on the postcritical beam flutter behavior, and particularly on the undamped beam solution with minimum amplitude of the vibration mode.

## 1. Introduction

For many years steady and unsteady aerodynamic theory for aeroelastic panels flutter computations has received a lot of interest, often in connection with high supersonic speeds. It is useful to recall the main authors who developed studies for flutter analysis of panels exposed to a high supersonic flow.

---

*Keywords:* vibrating beam, nonlinear, aerodynamic force, supersonic airflow, flutter.

Lighthill [1953] first proposed a *piston theory*, which was proved to be an efficient and powerful tool for panel flutter analysis. It can be used to calculate the pressure on an airfoil in steady or unsteady motion with remarkable accuracy, even under nonisentropic conditions, whenever the flight Mach Number  $M_\infty$  has such an order of magnitude that  $M_\infty^2 \gg 1$ . This piston theory is quite attractive for flutter studies due to its simplicity in comparison with other supersonic theories.

This theory has been discussed by Ashley and Zartarian [1956], who made suggestions for future research based on this new efficient aerodynamic tool, with particular regard to areas where computational labor can be reduced without losing the necessary accuracy.

Morgan et al. [1958] analyzed some of the theories for two dimensional oscillatory wing structures, which could be applied for flutter computations with high Mach Number. The results obtained by the various aerodynamic theories have been compared for their flutter prediction in various Mach Number ranges. Also some possible refinements of the piston theory have been proposed for high Mach Numbers.

The heritage of the studies of these authors enables us to know the complete expression of the aerodynamic transverse distributed force acting on a beam, which makes it possible to determine its flutter dynamic response after appropriate approximations.

The objective of this paper is to investigate the effects of the nonlinear components of the aerodynamic transverse force on the permanent postcritical solutions of a fluttering beam without air damping. Since the fluttering beam solution in limit cycle conditions, derived by the aerodynamic model with damping, is very near to the undamped vibrating beam state with minimum amplitude, these effects could also influence the damped beam aeroelastic vibration.

Three different schemes have been exploited for the flutter computational work, as in the case of the beam flutter analysis with linearized and idealized piston theory [Tizzi 1994; 2003]. First a numerical procedure [Tizzi 1994; 1996; 2003] which arises from the Rayleigh–Ritz method [Kantorovich and Krylov 1964, pp. 258–303; Mikhlin 1964, pp. 74–125 and 448–490; Reddy 1986, pp. 258–285] has been used, together with the finite element method (FEM) [Weaver and Johnston 1984, pp. 1–102; Reddy et al. 1988, pp. 41–89; Qin et al. 1993]. By knowing the structural and inertial forces potential functional and the aerodynamic generalized force, it has been possible to apply the Lagrange equations [Pars 1968, pp. 28–89] and derive the generalized governing equation in time, for which appropriate time-integration algorithms exist.

Then the Galerkin method [Kantorovich and Krylov 1964; Mikhlin 1964; Tizzi 1994; 2003] was employed in the case of a simply supported beam, as in Dowell’s model [1966; 1967], to validate the results of Ritz and FEM procedures.

The effectiveness of the three methods is apparent from the good accordance of the results obtained by the three different simulation approaches.

An analysis of the results achieved has been necessary to point out the influence of the nonlinear aerodynamic force components on particular frequency parameters characterizing the undamped beam solution set in the whole frequency range. It is fundamental to evaluate the effects of these nonlinear forces on the solution with minimum amplitude of the modal shape, considering that the flutter solution in limit cycle conditions of the damped vibrating beam lies in its neighborhood.

Studies on the influence of the nonlinear aerodynamic terms on the postcritical limit cycle of fluttering panels have also been developed by other authors [McIntosh 1973; Smith and Morino 1976]. However, investigations into the effects of these nonlinear aerodynamic components, in the presence of nonlinear

structural forces, on the postcritical flutter solutions of a beam in an airflow without damping, have been herein performed. Moreover, a fluttering beam with both simply supported and clamped ends has been considered; this is useful because the boundary conditions of panels actually employed in aerospace structures often lie between the two supposed ones in the analyzed cases.

### Index of notation

$A_s$	beam cross-section area	$P_a$	force per unit axial length acting on a side of the beam profile
$a_m$	nondimensional modal shape amplitude (maximum transverse displacement along the beam, divided by length of beam)	$Q_{i_p}^{(i_e)}$	generic degree of freedom in the $i_e$ -th element of FEM model
$a_\infty$	speed of sound	$q$	dynamic pressure
$b_w$	beam width	$t$	beam state evolution time
$a_{ij}, c_{ij}, b_{ijkl}, d_{ijkl}$	coefficients determined by integrals in Ritz and FEM models	$T_o$	reference time
$c_{i_p i_a}$	generic coefficient of the nondimensional flexural deflection series expansion in the generic $i_e$ -th element of FEM model	$U_\infty$	airflow speed
$E$	Young's modulus	$u, w$	beam points axial and flexural displacements, respectively
$F_a$	resultant of the aerodynamic forces acting on both sides of the beam per unit length	$W$	nondimensional flexural displacement
$F_i^{(a)}$	generalized aerodynamic force acting on the $i$ -th degree of freedom	$W_i$	generic coefficients of the nondimensional flexural displacement series expansion
$f_i(\zeta)$	generic trial describing function of the nondimensional flexural deflection through the beam length	$W_{i_e}$	nondimensional flexural displacement on a generic $(i_e + 1)$ -th section $S_{i_e}$ of FEM model
$h$	beam thickness	$x$	beam axial coordinate
$I$	flexural moment of inertia	<i>Greek symbols</i>	
$J_{sccc}, J_{sscc}$	particular integrals utilized in the Galerkin method	$\alpha$	nondimensional beam axial parameter
$k_{ij}$	stiffness matrix elements	$\beta, \gamma_m$	nondimensional Mach numbers parameters
$k_{ij}^*$	linear structural and aerodynamic forces resultant matrix elements	$\gamma$	ratio between the specific heat at constant pressure and volume, respectively
$L$	beam length	$\gamma', \gamma''$	nondimensional aerodynamic damping coefficients
$M_\infty$	Mach number	$\lambda$	nondimensional mass distribution parameter
$m_{ij}$	mass matrix elements	$\theta_{i_e}$	rotation parameter in the generic $(i_e + 1)$ -th section $S_{i_e}$ of FEM model
$N$	whole number of the degrees of freedom	$\mu$	mass per unit length
$N_E$	whole number of the elements in FEM model	$\zeta$	nondimensional axial coordinate of the beam
$p_\infty$	unperturbed air pressure	$\zeta_{i_e}$	nondimensional axial coordinate of the $(i_e + 1)$ -th section $S_{i_e}$ of the FEM model

$\zeta_n$	normalized axial coordinate of a beam element in the FEM model	$\circ u$	strain energy
$\rho_\infty$	unperturbed air density	$\mathbf{W}, \mathbf{Z}$	column vectors of the unknown variables and their time first derivatives
$\sigma$	dimensional dynamic pressure parameter	$\mathbf{W}^{(3)}$	column vector with elements the triple products between unknown variables
$\sigma_d$	dimensionless dynamic pressure parameter	$\mathbf{W}^{(3d)}$	column vector with elements the triple products between two unknown variables and a time first derivative of a third variable
$\tau$	nondimensional time	<i>Subscripts and superscripts</i>	
$\varphi_{ij}$	integral of the product between the first derivatives of the generic describing functions $f_i(\zeta)$ and $f_j(\zeta)$	$d$	subscript indicating dimensionless parameters
$\chi$	normal speed down- or up-wash	$i, j, k, l$	subscripts indicating functions and unknown variables coefficients of the flexural displacement series expansion
$\omega$	angular frequency	$i_e$	subscript indicating the $(i_e + 1)$ -th section $S_{i_e}$ of the FEM model
$\omega_d$	dimensionless angular frequency	$(i_e)$	superscript indicating the $i_e$ -th element of FEM model
<i>Special symbols</i>		$i_p, j_p, k_p, l_p$	subscripts characterizing the unknown variables and the coefficients of the flexural displacement series expansion in the $i_e$ -th element of FEM model
$\mathcal{H}_2(S)$	square summable functions space	$nd$	subscript indicating nondimensional variables
$S$	definition domain of the describing functions	$\infty$	subscript indicating the unperturbed airflow
$\mathbf{B}, \mathbf{D}$	utilized matrices in the generalized form equation		
$\mathbf{F}$	structural and linear aerodynamic forces matrix		
$\mathcal{L}$	extended Lagrangian functional		
$\mathbf{M}$	mass matrix		
$\mathcal{T}$	kinetic energy		

## 2. Mathematical formulation

A vibrating beam exposed to a high supersonic flow along the  $x$  axis, previously analyzed with the linear aerodynamic model [Tizzi 1994; 2003], is considered and drawn in Figure 1.

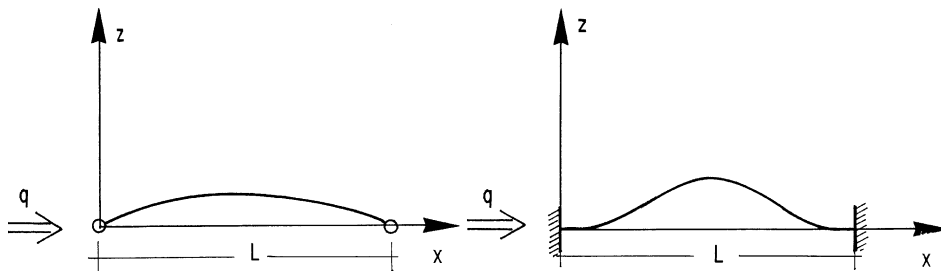


**Figure 1.** Beam, simply supported or clamped at both ends, exposed to a high supersonic flow.



The focus of the analysis developed here is limited to the nonlinear aerodynamic force components of piston theory, given that the terms of all structural and linear aerodynamic force components have been sufficiently illustrated. The exact expression of the pressure acting on a beam element (one-dimensional flow) is [Lighthill 1953; Ashley and Zartarian 1956; Morgan et al. 1958]:

$$\frac{p}{p_\infty} = \left( 1 + \frac{\gamma - 1}{2} \frac{\chi}{a_\infty} \right)^{2\gamma/(\gamma-1)}, \quad (1)$$

where  $\gamma = c_p/c_v$  is the ratio between the specific heats at constant pressure and volume ( $c_p$  and  $c_v$ );  $\chi$  is the normal down- or up-wash, that is, the component of the fluid velocity in the  $z$ -direction, normal to the beam profile;  $a_\infty = \sqrt{\gamma p_\infty/\rho_\infty}$  is the speed of sound; and  $p_\infty$  and  $\rho_\infty$  are the pressure and density of the unperturbed airflow. This pressure can be expressed in terms of series expansion function elements versus  $\chi$ , as follows:

$$\frac{p}{p_\infty} = 1 + \gamma \frac{\chi}{a_\infty} + \frac{1}{4} \gamma (\gamma + 1) \left( \frac{\chi}{a_\infty} \right)^2 + \frac{1}{12} \gamma (\gamma + 1) \left( \frac{\chi}{a_\infty} \right)^3 + \dots \quad (2)$$

The dimensional dynamic pressure parameter  $\sigma$  is also introduced:

$$\sigma = \frac{2q}{\beta} b_w, \quad (3)$$

where  $\beta = \sqrt{M_\infty^2 - 1}$ ,  $M_\infty = U_\infty/a_\infty$  is the Mach number,  $q = \frac{1}{2} \rho_\infty U_\infty^2$  is the dynamic pressure,  $U_\infty$  is the airflow speed, and  $b_w$  is the beam width. As in [Tizzi 2003], the aerodynamic expressions of an infinite plate along the third, not considered  $y$  axis are applied, together with the structural constitutive relations of a beam; this hypothesis can be accepted if the beam width  $b_w$  is much greater than  $L$ .

Since

$$\sqrt{M_\infty^2 - 1} \cong M_\infty, \quad (4)$$

if the Mach number is high enough, it is also true that

$$\sigma = \frac{2q}{\beta} b_w \cong \gamma p_\infty M_\infty b_w, \quad (5)$$

in view of the previously introduced expressions of  $q$ ,  $M_\infty$  and  $a_\infty$ .

Thus the force per unit axial length acting on each side of the beam profile can be evaluated from (2), and, by virtue of (5) and the expression for  $M_\infty$ , it can be written as

$$P_a = \Delta p b_w = \sigma \left[ \frac{\chi}{U_\infty} + \frac{\gamma + 1}{4} M_\infty \left( \frac{\chi}{U_\infty} \right)^2 + \frac{\gamma + 1}{12} M_\infty^2 \left( \frac{\chi}{U_\infty} \right)^3 + \dots \right], \quad (6)$$

where  $\Delta p = p - p_\infty$  is the pressure variation with respect to the unperturbed static conditions  $p = p_\infty$ .

The analysis has been developed only for symmetric cases, that is, both sides of the beam profile are exposed to the same airflow, and consequently only the odd powers give a contribution. In fact, taking into account that the normal speed component  $\chi$  has opposite values on the upper and lower side, their effects sum-up for the odd powers and vanish for the even ones. Thus the resultant of the aerodynamic

forces acting on both sides per unit length can be written as

$$F_a = 2\sigma \left[ \frac{\chi}{U_\infty} + \frac{\gamma + 1}{12} M_\infty^2 \left( \frac{\chi}{U_\infty} \right)^3 + \dots \right]. \quad (7)$$

The normal speed component due to the profile dynamics can be expressed as

$$\chi = U_\infty \frac{\partial w}{\partial x} + \frac{\partial w}{\partial t}, \quad (8)$$

where  $w$  is the beam point's flexural displacement.

Substituting (8) into (7) gives the new expression of the resultant aerodynamic distributed force:

$$F_a = 2\sigma \left[ \frac{\partial w}{\partial x} + \gamma_m \left( \frac{\partial w}{\partial x} \right)^3 + \dots \right] + 2\sigma \left\{ \frac{1}{U_\infty} \frac{\partial w}{\partial t} + \gamma_m \left[ 3 \left( \frac{\partial w}{\partial x} \right)^2 \frac{1}{U_\infty} \frac{\partial w}{\partial t} + \dots \right] + \dots \right\}, \quad (9)$$

where

$$\gamma_m = \frac{\gamma + 1}{12} M_\infty^2 \quad (10)$$

and the subsequent terms in the series expansion can be neglected. This is formed by two components:  $F_{a1}$ , containing only spatial derivatives, which is the coupling element between odd and even vibrating modes, and which exists also without damping; and  $F_{a2}$ , containing also time derivatives, which give rise to the aerodynamic dissipative force and damping. This second component is not considered for the undamped vibrating beam solution.

The linear component of the distributed aerodynamic force in (9) equals that obtained in [Bisplinghoff and Ashley 1975, pp. 416–437; Tizzi 2003], except for the presence of the ratio  $(M_\infty^2 - 2)/(M_\infty^2 - 1)$  before the time derivative  $\partial w/\partial t$ , which is approximately equal to unity for high Mach numbers.

It is necessary to recall the vibration-governing equation of the fluttering beam [Tizzi 2003]:

$$EI \frac{\partial^4 w}{\partial x^4} + \mu \frac{\partial^2 w}{\partial t^2} - EA_s \frac{1}{2} \overline{\left( \frac{\partial w}{\partial x} \right)^2} \frac{\partial^2 w}{\partial x^2} + F_a = 0, \quad (11)$$

where  $A_s = b_w h$  is the cross-sectional area,  $h$  is the beam thickness,  $E$  is the Young's modulus,  $\mu$  is the distributed mass per unit length, and  $I = Eb_w h^3/12$  is the flexural moment of inertia.

Furthermore,  $\overline{(\partial w/\partial x)^2}$  has been previously defined as the mean square value of the flexural displacement first axial derivative over the whole beam length; the third term of (11), containing this mean square value, corresponds to the nonlinear component of the transverse structural force, due to the beam axial stretching.

The axial inertia effects are being neglected, as in the previous analysis with a linearized aerodynamic model, considering that the axial vibration frequencies are higher than the corresponding ones of the flutter vibration, and so the axial vibration frequency range is different from the flutter frequency range.

Substitution of (9) into (11), with the approximation assumptions, leads to the following governing equation:

$$EI \frac{\partial^4 w}{\partial x^4} + \mu \frac{\partial^2 w}{\partial t^2} - EA_s \frac{1}{2} \overline{\left( \frac{\partial w}{\partial x} \right)^2} \frac{\partial^2 w}{\partial x^2} + 2\sigma \left[ \frac{\partial w}{\partial x} + \gamma_m \left( \frac{\partial w}{\partial x} \right)^3 \right] + 2\sigma \left\{ \frac{1}{U_\infty} \frac{\partial w}{\partial t} + \gamma_m \left[ 3 \left( \frac{\partial w}{\partial x} \right)^2 \frac{1}{U_\infty} \frac{\partial w}{\partial t} \right] \right\} = 0, \quad (12)$$

which can be reformulated in dimensionless form as

$$\frac{\partial^4 W}{\partial \xi^4} + \lambda \frac{\partial^2 W}{\partial \tau^2} + \sigma_d \left[ \frac{\partial W}{\partial \xi} + \gamma_m \left( \frac{\partial W}{\partial \xi} \right)^3 \right] - \frac{\alpha}{2} \left( \frac{\partial W}{\partial \xi} \right)^2 \frac{\partial^2 W}{\partial \xi^2} + \left[ \gamma' + \gamma'' \left( \frac{\partial W}{\partial \xi} \right)^2 \right] \frac{\partial W}{\partial \tau} = 0, \quad (13)$$

where the flexural displacement and the axial coordinate have been reformulated in nondimensional form, and other dimensionless parameters have been introduced:

$$W(\xi, \tau) = \frac{w(x, t)}{L}, \quad \xi = \frac{x}{L}, \quad \lambda = \frac{\mu L^4}{EIT_o^2}, \quad \tau = \frac{t}{T_o}, \quad (14)$$

$$\sigma_d = \frac{2\sigma L^3}{EI}, \quad \alpha = \frac{A_s L^2}{I}, \quad \gamma' = \frac{2\sigma}{U_\infty} \frac{L^4}{EIT_o}, \quad \gamma'' = 3\gamma' \gamma_m, \quad (15)$$

and  $T_o$  is a reference time.

The third and fifth terms in (13) refer to the nondimensional equivalent form of the distributed aerodynamic force expression in (9):

$$(F_a)_{nd} = \sigma_d \left[ \frac{\partial W}{\partial \xi} + \gamma_m \left( \frac{\partial W}{\partial \xi} \right)^3 \right] + \left[ \gamma' + \gamma'' \left( \frac{\partial W}{\partial \xi} \right)^2 \right] \frac{\partial W}{\partial \tau}. \quad (16)$$

Einstein's summation convention for repeated indices will be adopted in all the following expressions. A series expansion for  $W(\xi, \tau)$  in terms of function elements can be chosen:

$$W(\xi, \tau) = W_i(\tau) f_i(\xi), \quad i = 1, 2, \dots, N, \quad (17)$$

where each coefficient  $W_i(\tau)$  is a Lagrangian degree of freedom, and  $f_i(\xi)$  are polynomials describing functions, belonging to the space of the square summable functions  $H_2(S)$ , defined in the domain  $S$  (which in this case is the whole beam length). These satisfy only the geometric boundary conditions, as in the Ritz and FEM methods. The meaning of the coefficients  $W_i(\tau)$  and the describing functions  $f_i(\xi)$  are illustrated in the electronic supplement to this paper.

Equation (13) can be transformed into its generalized equivalent form by the variational principle [Pars 1968], if the Lagrangian functional is introduced:

$$\mathcal{L} = \mathcal{T} - \mathcal{U}, \quad (18)$$

where  $\mathcal{T}$  is the kinetic energy and  $\mathcal{U}$  is the strain energy. Thus the generic generalized  $i$ -th governing equation can be written in the classical Lagrangian form:

$$\frac{d(\partial \mathcal{L} / \partial \dot{W}_i)}{d\tau} - \frac{\partial \mathcal{L}}{\partial W_i} + F_i^{(a)} = 0, \quad i = 1, 2, \dots, N, \quad (19)$$

where  $F_i^{(a)}$  is the generalized aerodynamic force acting on the  $i$ -th degree of freedom. It is possible to set a correspondence between each term of this generalized equation with each one of (13).

The potential strain energy expression has been already determined [Tizzi 2003]:

$$\mathcal{U} = \frac{1}{2} k_{ij} W_i W_j + \frac{\alpha}{8} \varphi_{ijkl} W_k W_l W_i W_j, \quad i, j, k, l = 1, 2, \dots, N, \quad (20)$$

where

$$\varphi_{ij} = \int_0^1 \frac{\partial f_i(\xi)}{\partial \xi} \frac{\partial f_j(\xi)}{\partial \xi} d\xi. \quad (21)$$

The stiffness matrix elements  $k_{ij}$  have been previously evaluated [Tizzi 1994]; obviously  $k_{ij} \ddot{W}_j$  is the generalized linear structural force acting on the  $i$ -th degree of freedom, which corresponds to the first term in (13). The elements of the second term at the second member of (20), corresponding to the nonlinear contribution to the structural strain energy, are also known.

The expression for the generalized aerodynamic force  $F_i^{(a)}$  acting on the  $i$ -th degree of freedom, corresponding to the third and fifth terms in (13), can be obtained by the use of the series expansion (17) in (16), and projecting the whole equation (16) onto the generic function element  $f_i(\xi)$ . Thus

$$F_i^{(a)} = a_{ij} W_j + \gamma_m b_{ijkl} W_k W_l W_j + \gamma' c_{ij} \dot{W}_j + \gamma'' d_{ijkl} W_k W_l \dot{W}_j, \\ j, k, l = 1, 2, \dots, N, \quad i = 1, 2, \dots, N, \quad (22)$$

where the coefficients  $a_{ij}$  and  $c_{ij}$  are well known from the previous analysis [Tizzi 2003]:

$$a_{ij} = \sigma_d \int_0^1 f_i(\xi) \frac{\partial f_j(\xi)}{\partial \xi} d\xi, \quad c_{ij} = \int_0^1 f_i(\xi) f_j(\xi) d\xi, \quad (23)$$

and the newly introduced ones are defined as

$$b_{ijkl} = \sigma_d \int_0^1 f_i(\xi) \frac{\partial f_j(\xi)}{\partial \xi} \frac{\partial f_k(\xi)}{\partial \xi} \frac{\partial f_l(\xi)}{\partial \xi} d\xi, \quad d_{ijkl} = \sigma_d \int_0^1 f_i(\xi) f_j(\xi) \frac{\partial f_k(\xi)}{\partial \xi} \frac{\partial f_l(\xi)}{\partial \xi} d\xi. \quad (24)$$

The knowledge of the describing functions of the series in (17) allows us to determine the coefficients  $b_{ijkl}$  and  $d_{ijkl}$ ; see the electronic supplement.

The mass matrix elements  $m_{ij}$  in the kinetic energy expression,

$$\mathcal{T} = \frac{1}{2} m_{ij} \dot{W}_i \dot{W}_j, \quad \dot{W}_i = \partial W_i / \partial \tau, \quad i, j = 1, 2, \dots, N, \quad (25)$$

have also been previously evaluated [Tizzi 1994]. It is true that

$$m_{ij} = \lambda c_{ij}, \quad (26)$$

where the nondimensional coefficient  $\lambda$  has been defined in (14). It is well known that  $-m_{ij} \ddot{W}_j$  is the generalized inertial force acting on the  $i$ -th degree of freedom, corresponding to the second term of (13).

If the expressions of the strain and kinetic energy in (20) and (25), along with the expression of the generalized aerodynamic force in (22), are substituted into (19), in view of the Lagrangian functional expression in (18), it is possible to achieve the equivalent generalized form of (13), corresponding to the generic  $i$ -th degree of freedom, as follows:

$$\left[ k_{ij}^* + \frac{\alpha}{2} \varphi_{ij} (\varphi_{kl} W_k W_l) \right] W_j + \gamma_m b_{ijkl} W_k W_l W_j + m_{ij} \ddot{W}_j + \gamma' c_{ij} \dot{W}_j + \gamma'' d_{ijkl} W_k W_l \dot{W}_j = 0, \\ j, k, l = 1, 2, \dots, N, \quad i = 1, 2, \dots, N. \quad (27)$$

The matrix elements  $k_{ij}^*$ , referring to both structural and aerodynamic linear forces, can be written as

$$k_{ij}^* = k_{ij} + a_{ij}. \quad (28)$$

Thus  $k_{ij}^* W_j$  is the generalized linear structural-aerodynamic force acting on the same  $i$ -th degree of freedom, which corresponds to the first term and the first part of the third term of (13).

Furthermore, the term  $(\varphi_{kl} W_k W_l)$  between brackets in (27) is the mean square value  $\overline{(\partial W / \partial \xi)^2}$  of the first derivative  $\partial W / \partial \xi$  over the whole beam length, which has been already introduced in (11). This is the reason for which it has been written separately in round brackets. As mentioned above, it takes into account the beam axial stretching, which gives rise to the nonlinear component of the structural transverse force, as in the fourth term of (13).

The term containing the coefficient  $\gamma_m$  in (27) is equivalent to the second part of the third term of (13), and the terms containing  $\gamma'$  and  $\gamma''$  are equivalent to the ones with the same coefficients in (13).

The system of the generalized governing equations (27), in view of (26), can also be written in matrix form:

$$\mathbf{Z} = \dot{\mathbf{W}}, \quad \dot{\mathbf{Z}} = -\mathbf{M}^{-1} \mathbf{F} \mathbf{W} - \gamma_m \mathbf{M}^{-1} \mathbf{B} \mathbf{W}^{(3)} - \frac{\gamma'}{\lambda} \mathbf{Z} - \gamma'' \mathbf{M}^{-1} \mathbf{D} \mathbf{W}^{(3d)}, \quad (29)$$

where:  $\mathbf{W}$  and  $\mathbf{Z}$  are the column vectors of the coefficients  $W_j$  and their first derivatives  $\dot{W}_j$  versus time  $\tau$ , respectively;  $\mathbf{F}$  is the matrix whose elements are:

$$f_{ij} = k_{ij}^* + \frac{\alpha}{2} (\varphi_{kl} W_k W_l) \varphi_{ij}; \quad (30)$$

$\mathbf{M}$  is the mass matrix;  $\mathbf{B}$  is a matrix with dimensions  $N \times N^3$ , whose elements are  $b_{ij_{t3}} = b_{ijkl}$  ( $j_{t3}$  is the contraction of the three indices  $kl$  and obviously  $j_{t3} = 1, 2, \dots, N^3$ );  $\mathbf{W}^{(3)}$  is the column vector with dimensions  $N^3$ , whose elements are the triple products  $p_{j_{t3}} = W_k W_l W_j$  between the coefficients of the series expansion in (17);  $\mathbf{D}$  is a matrix whose elements are  $d_{ij_{t3}} = d_{ijkl}$  and with the same dimensions of  $\mathbf{B}$ ; and  $\mathbf{W}^{(3d)}$  is a column vector with the same dimensions of  $\mathbf{W}^{(3)}$ , whose elements are the triple products  $q_{j_{t3}} = W_k W_l \dot{W}_j$ .

Equations (27) and (29) are the same as in the previous analysis with linearized aerodynamic forces, except for the presence of the terms with  $b_{ijkl}$  and  $d_{ijkl}$  in (27), and the corresponding matrices  $\mathbf{B}$  and  $\mathbf{D}$  in (29), referring to the nonlinear contribution of the piston theory to the aerodynamic forces. The system (29) can be integrated in time by appropriate algorithms.

In the case of a simply supported beam it is easy to apply also the Galerkin method, as in Dowell's model [Dowell 1966; 1967]. The advantages of the Galerkin procedure arise from the diagonal form of the mass matrix  $\mathbf{M}$ , due to the orthogonality between different describing function elements; see the electronic supplement for details.

### 3. Applications and results

The analysis of the results is limited to the regular solutions with repetitive dynamic characteristics, obtained by giving particular starting conditions ( $\tau = 0$ ) to the vibrating system. There are also many more spurious solutions, which are quite irregular and without any particular meaning.

The first case considered is the simply supported beam. The ratio between the length  $L$  and the thickness  $h$  is assumed to be 100.

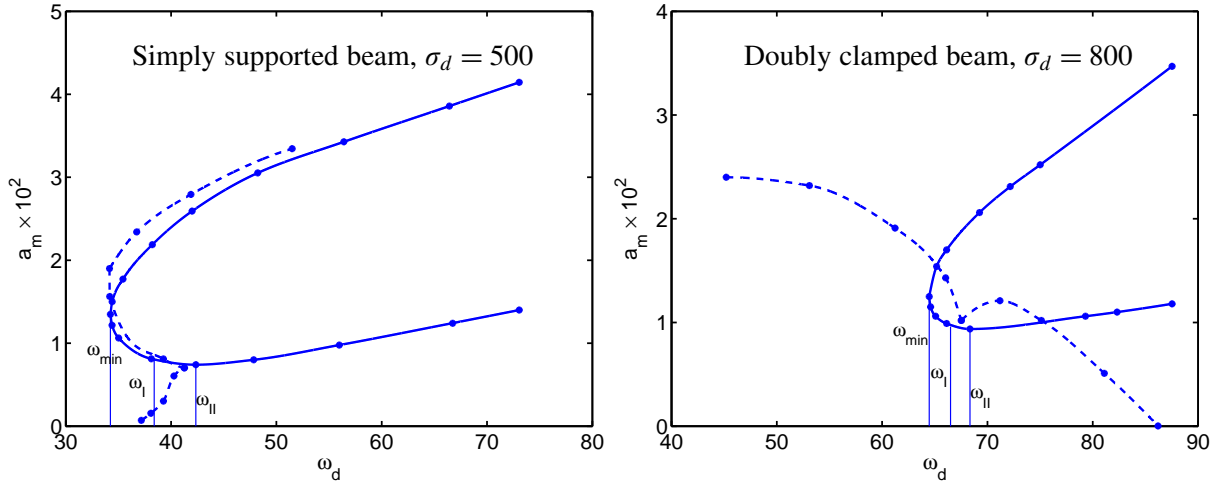


**Figure 2.** Solid curves: modal shape amplitude  $a_m$  versus dimensionless frequency  $\omega_d$  for two undamped beam systems (Table 1 lists the values). Dashed curves: evolution of the damped beam vibration state towards the limit cycle in each of the two systems (Table 2). All values take into account the nonlinear aerodynamic force components.

All the characteristic behavior features of the nondimensional modal shape amplitude  $a_m$  as a function of the dimensionless frequency

$$\omega_d = \omega \sqrt{\frac{\mu L^4}{EI}} \quad (31)$$

(where  $\omega$  is the angular frequency) are known from previous analyses [Tizzi 2003]. These features are illustrated by the solid curve in Figure 2, left, in the case of a simply supported undamped beam for  $\sigma_d = 500$ . (See also the top half of Table 1.) In fact this graph is similar to the one obtained without the nonlinear aerodynamic force components.

Three frequency values are particularly important and useful in characterizing this curve: the minimum frequency  $\omega_{min}$ ; the frequency  $\omega_I$ , which separates the frequency range where lower amplitude modal shapes have only one half-wave from the range where these shapes have two half-waves; and the frequency  $\omega_{II}$ , where the modal shape amplitude reaches its minimum.

The dashed lines in Figure 2 show the dynamic evolution of the fluttering beam towards the limit cycle conditions (still taking into account aerodynamic damping), for two different starting conditions. Clearly the dynamic solution of the fluttering beam in limit cycle conditions, also in the presence of nonlinear aerodynamic forces, lies in the neighborhood of the undamped beam solution with minimum amplitude. For this reason this particular solution is of paramount importance, and  $\omega_{II}$  plays a privileged role, along with its corresponding modal shape amplitude value.

To see the influence of the nonlinear aerodynamic components of the piston theory of a high supersonic idealized flow, it is necessary to show the functional dependence of these frequencies on the dynamic pressure, with and without nonlinear aerodynamic forces. Particular attention must be given to these nonlinear forces' effects on  $\omega_{II}$  and the corresponding modal amplitude behavior versus  $\sigma_d$ .

Simply supported, undamped beam, $\sigma_d = 500$							
$\omega_d$	$a_m$	$\omega_d$	$a_m$	$\omega_d$	$a_m$	$\omega_d$	$a_m$
73.06	0.04144	42.00	0.02592	34.24	0.01348	42.35	0.00741
66.43	0.03858	38.22	0.02188	34.40	0.01216	47.84	0.00800
56.40	0.03427	35.43	0.01772	35.02	0.01063	55.97	0.00978
48.23	0.03052	34.41	0.01501	38.13	0.00812	66.74	0.0124
						73.06	0.0140

Doubly clamped, undamped beam, $\sigma_d = 800$							
$\omega_d$	$a_m$	$\omega_d$	$a_m$	$\omega_d$	$a_m$	$\omega_d$	$a_m$
87.53	0.0347	66.12	0.0170	65.08	0.0106	82.31	0.0110
75.01	0.0252	65.17	0.0154	66.12	0.0099	87.53	0.0118
72.17	0.0231	64.47	0.0125	68.34	0.0094		
69.25	0.0206	64.60	0.0115	79.31	0.0106		

**Table 1.** Modal amplitude  $a_m$  versus dimensionless frequency  $\omega_d$ , taking into account nonlinear aerodynamic force components.

Simply supported beam						Doubly clamped beam					
$\tau$	$\omega_d$	$a_m$	$\tau$	$\omega_d$	$a_m$	$\tau$	$\omega_d$	$a_m$	$\tau$	$\omega_d$	$a_m$
Upper dashed curve			Lower dashed curve			Left dashed curve			Right dashed curve		
0.	51.5	0.0334	0.	37.18	0.00071	0.	45.20	0.0240	0.	86.20	0.00002
0.16	41.88	0.0279	0.16	38.08	0.0016	0.43	53.10	0.0232	0.47	81.10	0.0051
0.30	36.74	0.0234	0.24	39.27	0.0030	0.85	61.23	0.0191	2.63	75.12	0.0102
0.47	34.15	0.0190	1.33	40.27	0.0061	1.47	66.03	0.0143	5.33	71.19	0.0121
0.56	34.17	0.0156	1.81	41.28	0.0070	2.53	67.52	0.0102	9.81	67.52	0.0102
1.18	39.27	0.0081									
2.37	41.24	0.0070									

**Table 2.** Modal amplitude versus dimensionless frequency  $\omega_d$  at various times, taking into account aerodynamic damping and nonlinear aerodynamic force components.

In some of the following figures the frequency values, derived both by the idealized and linearized beam model and by the nonlinear approach, are drawn together. This is useful for having an overall picture of all the possible beam flutter solutions in pre- and postcritical conditions, obtained by the two different approaching models. It is important to emphasize the convergence of the nonlinear model solutions towards those of the linear approach, as the dynamic pressure, and consequently the flutter modal amplitude, diminishes. The solutions coincide when this amplitude vanishes, considering that the influence of the nonlinear components of the acting forces can be neglected as the vibrating modes tend to disappear.

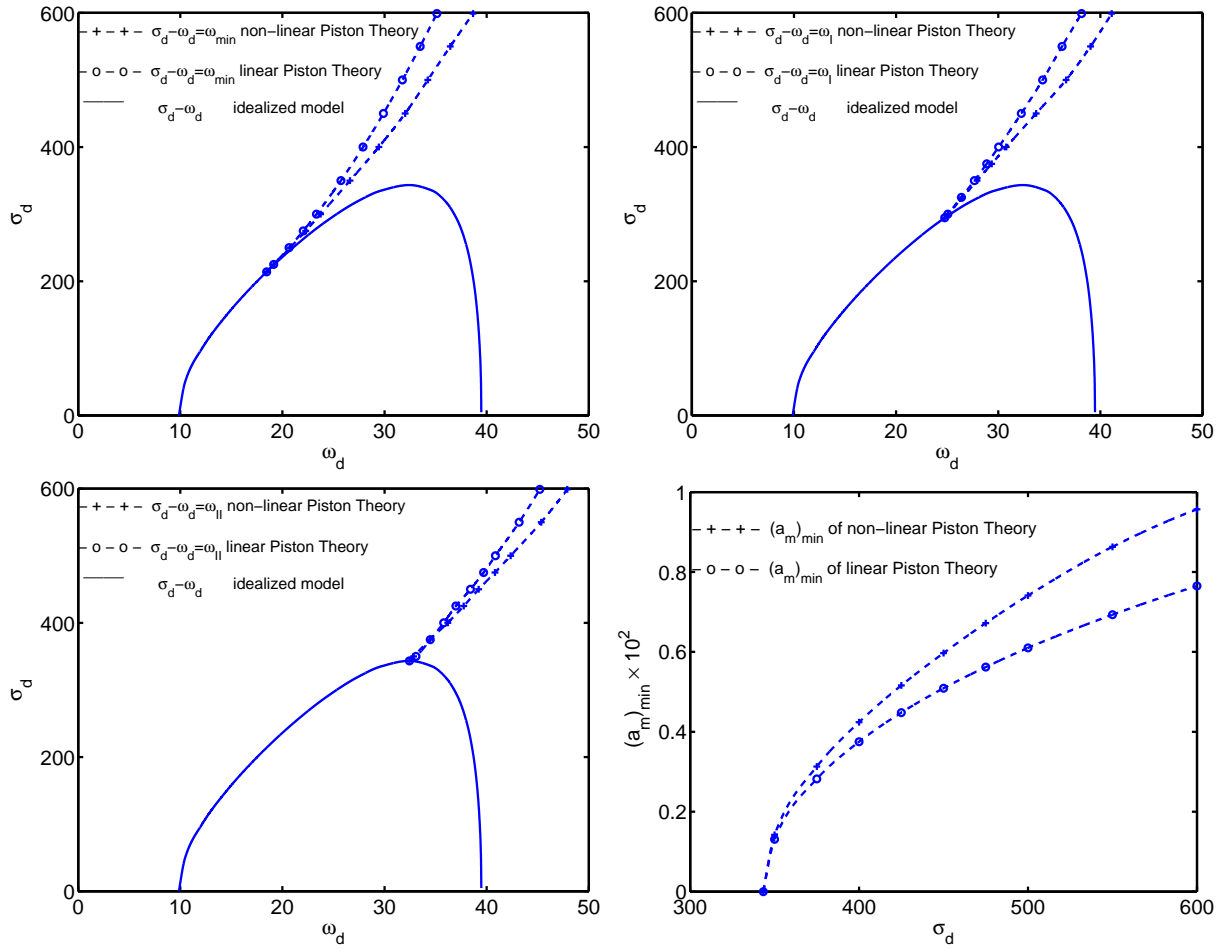


**Figure 3.** Frequencies  $\omega_{\min}$  (top left),  $\omega_I$  (top right) and  $\omega_{II}$  (bottom left) versus  $\sigma_d$  for the simply supported, undamped beam, with and without nonlinear aerodynamic force components (dashed lines). The horseshoe-shaped solid curve shows the dependence of  $\sigma_d$  on  $\omega_d$  for the linearized model (see text). Also shown is the minimum amplitude  $(a_m)_{\min}$  as a function of  $\sigma_d$  for the same beam system (bottom right).

Figure 3, top left, shows the behavior of the minimum frequency  $\omega_{\min}$  of the undamped solutions versus the dynamic pressure dimensionless parameter  $\sigma_d$ ; the two types of dashed lines indicate the presence or absence of nonlinear aerodynamic forces in the calculation. The solid line describes the classical and well known dependence of  $\sigma_d$  on  $\omega_d$  for the linearized beam flutter simulation model, where only the linear components of both structural and aerodynamic forces are considered.

The dependence of the frequencies  $\omega_I$  and  $\omega_{II}$  on  $\sigma_d$  is sketched in the next two parts of Figure 3, with the same conventions. Finally, the bottom right part of the figure is a graph of the minimum amplitude  $(a_m)_{\min}$  versus  $\sigma_d$ , with and without nonlinear aerodynamic forces. The bottom two graphs in Figure 3 are particularly important for the reasons mentioned above. See also the top half of Table 3.

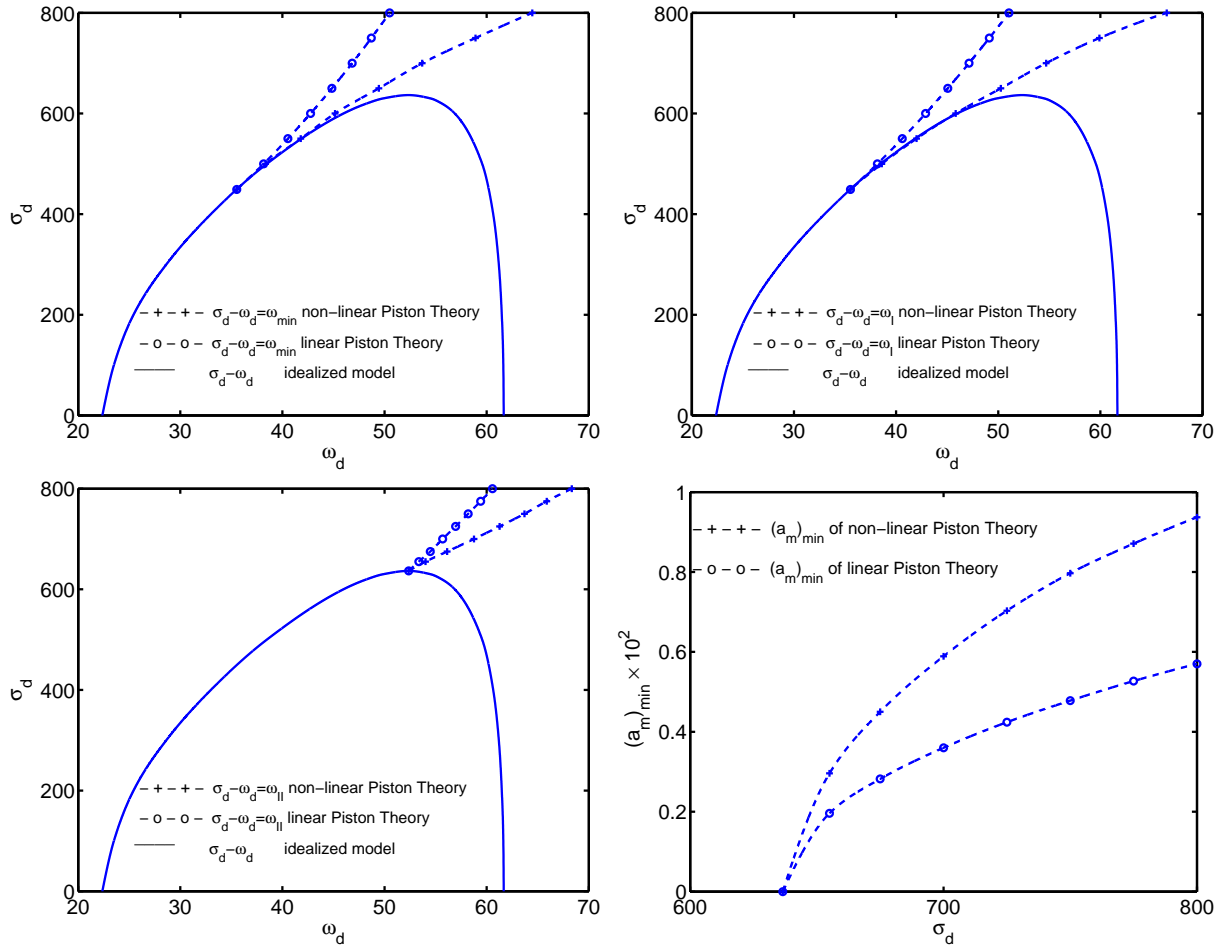


Simply supported, undamped beam								
$\sigma_d$	$\omega_{\min}$		$\omega_I$		$\omega_{II}$		$(a_m)_{\min} \times 10^2$	
	L	NL	L	NL	L	NL	L	NL
214	18.46	18.46						
225	19.15	19.18						
250	20.65	20.76						
275	22.04	22.28						
294.6			24.76	24.76				
300	23.34	23.75	25.06	25.08				
325			26.39	26.51				
343.356					32.43	32.43	0.	0.
350	25.73	26.62	27.66	27.93	32.95	33.02	0.13	0.14
375			28.87	29.36	34.40	34.48	0.28	0.31
400	27.90	29.44	30.04	30.79	35.79	36.19	0.37	0.42
425					36.99	37.75	0.45	0.52
450	29.89	32.02	32.26	33.71	38.41	39.22	0.51	0.60
475					39.70	40.81	0.56	0.67
500	31.75	34.24	34.35	36.64	40.86	42.35	0.61	0.74
550	33.49	36.44	36.25	39.04	43.18	45.34	0.69	0.86
600	35.12	38.67	38.16	41.11	45.20	47.89	0.76	0.96

Doubly clamped, undamped beam								
$\sigma_d$	$\omega_{\min}$		$\omega_I$		$\omega_{II}$		$(a_m)_{\min} \times 10^2$	
	L	NL	L	NL	L	NL	L	NL
449	35.53	35.53	35.53	35.53				
500	38.16	19.18	38.17	38.60				
550	40.54	41.80	40.60	42.00				
600	42.76	45.15	42.89	45.83				
636.569					52.36	52.36	0.	0.
650	44.85	49.44	45.06	50.25				
655					53.36	54.01	0.20	0.30
675					54.48	56.13	0.28	0.45
700	46.83	53.69	47.14	54.69	55.69	58.76	0.36	0.59
725					56.96	61.27	0.42	0.70
750	48.71	58.91	49.13	59.91	58.19	63.70	0.48	0.80
775					59.41	65.88	0.53	0.87
800	50.50	64.47	51.05	66.50	60.57	68.34	0.57	0.94

**Table 3.** Values of  $\omega_{\min}$ ,  $\omega_I$ ,  $\omega_{II}$  and  $(a_m)_{\min}$  versus the dimensionless dynamic pressure  $\sigma_d$ , without (L) and with (NL) nonlinear components of the aerodynamic forces for the undamped beam.



**Figure 4.** Frequencies  $\omega_{\min}$  (top left),  $\omega_I$  (top right) and  $\omega_{II}$  (bottom left) versus  $\sigma_d$  for the doubly clamped, undamped beam, with and without nonlinear aerodynamic force components (dashed lines). The horseshoe-shaped solid curve shows the dependence of  $\sigma_d$  on  $\omega_d$  for the linearized model (see text). Also shown is the minimum amplitude  $(a_m)_{\min}$  as a function of  $\sigma_d$  for the same beam system (bottom right).

We next display the results obtained in the case of a beam clamped at both ends. The ratio between the length  $L$  and the thickness  $h$  is taken to be 110. Figure 2, right, shows the modal amplitude  $a_m$  behavior of the fluttering undamped solution versus  $\omega_d$  for  $\sigma_d = 800$  (also described in the bottom half of Table 1), together with the vibrating damped beam state evolution towards the limit cycle point, which lies in the neighborhood of the representative point of the undamped solution with minimum amplitude. The two dashed lines correspond to two different starting values of the fluttering beam with damping. Figure 4, organized in the same way as Figure 3, shows the dependence of  $\omega_{\min}$ ,  $\omega_I$ ,  $\omega_{II}$  and  $(a_m)_{\min}$  on  $\sigma_d$  for the undamped beam clamped at both ends, again with and without taking into account the nonlinear components of the aerodynamic forces. See also the bottom half of Table 3.

#### 4. Conclusions

On the basis of the results achieved, some concluding remarks can be made.

(1) In both cases considered, the minimum frequency value  $\omega_{\min}$  is higher compared to the corresponding one derived by the linearized piston theory, which means that the frequency range of the undamped solutions decreases with respect to the case of the linearized aerodynamic model, although this reduction is very limited.

(2) Limited decrease of the resistance to the flutter phenomenon is introduced by the nonlinear aerodynamic force contributions, considering that the minimum value of the undamped vibration modal amplitude  $(a_m)_{\min}$ , which is very close to the limit cycle amplitude value, increases; but this relative growth is not considerable.

(3) Undoubtedly these nonlinear aerodynamic forces influence the whole postcritical flutter behavior of a beam under the effects of a high supersonic flow at both sides, but, unless the dynamic pressure grows very much over its critical value of the linear model, these effects are limited. Hence the linear aerodynamic analysis of the piston theory is sufficient to describe, within acceptable limits, this postcritical behavior.

(4) The results obtained don't predict a threat to the stability, because in the cases considered, the airflow speed doesn't exceed overmuch the limit critical value of the linearized model (limited Mach number), as in [McIntosh 1973; Smith and Morino 1976]. For very high values of  $M_\infty$  the destabilizing effect of aerodynamic nonlinearities is predominant and the limit cycle becomes unstable. However the presence of particular initial conditions (such as those induced by a gust) can lead to instability and chaos even before the dynamic pressure reaches its critical value [Dessi et al. 2002]. The presence of shock waves in transonic flight could also instigate instability in the flutter phenomenon.

(5) The dynamic analysis of the fluttering beam has been limited to the case of symmetrically distributed aerodynamic forces, which is worse, in terms of fluttering beam stability, than the case of a high supersonic flow acting only on one side of the vibrating beam. Therefore all considerations regarding the fluttering stability are very likely valid for asymmetric cases as well.

(6) This study of postcritical behavior has been limited to a one-dimensional panel, as in the linearized piston theory case, but similar conclusions are likely valid for two-dimensional panels.

(7) This dynamic analysis can also be extended to cases not considered here.

#### Acknowledgements

The author is grateful to Sandro Mileti for helping to improve his English.

#### References

- [Ashley and Zartarian 1956] H. Ashley and G. Zartarian, "Piston theory: a new aerodynamic tool for the aeroelastician", *J. Aeronaut. Sci.* **23**:12 (1956), 1109–1118.
- [Bisplinghoff and Ashley 1975] R. L. Bisplinghoff and H. Ashley, *Principles of aeroelasticity*, Dover, New York, 1975.
- [Dessi et al. 2002] D. Dessi, F. Mastroddi, and L. Morino, "Limit-cycle stability reversal near a Hopf bifurcation with aeroelastic applications", *J. Sound Vib.* **256**:2 (2002), 347–365.
- [Dowell 1966] E. H. Dowell, "Nonlinear oscillations of a fluttering plate", *AIAA J.* **4**:7 (1966), 1267–1275.

- [Dowell 1967] E. H. Dowell, "Nonlinear oscillations of a fluttering plate, II", *AIAA J.* **5**:10 (1967), 1856–1862.
- [Kantorovich and Krylov 1964] L. V. Kantorovich and V. I. Krylov, *Approximate methods of higher analysis*, Interscience, New York, 1964.
- [Lighthill 1953] M. J. Lighthill, "Oscillating airfoils at high Mach number", *J. Aeronaut. Sci.* **20**:6 (1953), 402–406.
- [McIntosh 1973] S. C. McIntosh, Jr., "Effect of hypersonic nonlinear aerodynamic loading on panel flutter", *AIAA J.* **11**:1 (1973), 29–32.
- [Mikhlin 1964] S. G. Mikhlin, *Variational methods in mathematical physics*, Pergamon, Oxford, 1964.
- [Morgan et al. 1958] H. G. Morgan, H. L. Runyan, and V. Huckel, "Theoretical considerations of flutter at high Mach numbers", *J. Aeronaut. Sci.* **25**:6 (1958), 371–381.
- [Pars 1968] L. A. Pars, *A treatise on analytical dynamics*, Heinemann Educational Books, London, 1968.
- [Qin et al. 1993] J. Qin, C. E. Gray, Jr., and C. Mei, "Vector unsymmetric eigenequation solver for nonlinear flutter analysis on high-performance computers", *J. Aircraft* **30**:5 (1993), 744–750.
- [Reddy 1986] J. N. Reddy, *Applied functional analysis and variational methods in engineering*, McGraw-Hill, New York, 1986.
- [Reddy et al. 1988] J. N. Reddy, C. S. Krishnamoorthy, and K. M. Seetharamu, *Finite elements analysis for engineering design*, Springer, Berlin, 1988.
- [Smith and Morino 1976] L. L. Smith and L. Morino, "Stability analysis of nonlinear differential autonomous systems with applications to flutter", *AIAA J.* **14**:3 (1976), 333–341.
- [Tizzi 1994] S. Tizzi, "A numerical procedure for the analysis of a vibrating panel in critical flutter conditions", *Comput. Struct.* **50**:3 (1994), 299–316.
- [Tizzi 1996] S. Tizzi, "Application of a numerical procedure for the dynamic analysis of plane aeronautical structures", *J. Sound Vib.* **193**:5 (1996), 957–983.
- [Tizzi 2003] S. Tizzi, "Influence of non-linear forces on beam behaviour in flutter conditions", *J. Sound Vib.* **267**:2 (2003), 279–299.
- [Weaver and Johnston 1984] V. Weaver, Jr. and P. R. Johnston, *Finite elements for structural analysis*, Prentice-Hall, Englewood Cliffs, NJ, 1984.

Received 16 Apr 2008. Revised 12 Sep 2008. Accepted 13 Nov 2008.

SILVANO TIZZI: [s.tizzi@caspur.it](mailto:s.tizzi@caspur.it)

University of Rome "La Sapienza", Aerospace and Astronautics Engineering Department, Via Eudossiana 16, Rome, 00184, Italy,

## FINITE ELEMENT FORMULATIONS VIA THE THEOREM OF EXPENDED POWER IN THE LAGRANGIAN, HAMILTONIAN AND TOTAL ENERGY FRAMEWORKS

JASON HAR AND KUMAR K. TAMMA

Traditionally, variational principles and variational methods have been employed in describing finite element formulations for elastodynamics applications. Here we present alternative avenues emanating from the theorem of expended power, using the differential calculus directly.

We focus on scalar representations under three distinct frameworks: Lagrangian mechanics, Hamiltonian mechanics, and a new framework involving a built-in measurable quantity, called the total energy in the configuration space. All three frameworks are derivable from each other, since they represent the same physics as Newton's second law; however, the total energy framework which we advocate inherits features that are comparable and competitive to the usual Newtonian based finite element formulations, with several added advantages ideally suited for conducting numerical discretization.

The present approach to numerical space-time discretization in continuum elastodynamics provides physical insight via the theorem of expended power and the differential calculus involving the distinct scalar functions: the Lagrangian  $\mathcal{L}(\mathbf{q}, \dot{\mathbf{q}}) : TQ \rightarrow \mathbb{R}$ , the Hamiltonian  $\mathcal{H}(\mathbf{p}, \mathbf{q}) : T^*Q \rightarrow \mathbb{R}$ , and the total energy  $\mathcal{E}(\mathbf{q}, \dot{\mathbf{q}}) : TQ \rightarrow \mathbb{R}$ . We show that in itself the theorem of expended power naturally embodies the weak form in space, and after integrating over a given time interval yields the weighted residual form in time. Hence, directly emanating from the theorem of expended power, this approach yields three differential operators: a discrete Lagrangian differential operator, a Hamiltonian differential operator, and a total energy differential operator.

The semidiscrete ordinary differential equations in time derived with our approach can be readily shown to preserve the same physical attributes as the corresponding continuous systems. This contrasts with traditional approaches, where such proofs are nontrivial or are not readily tractable.

The modeling of complicated structural dynamical systems such as a rotating bar and the Timoshenko beam are shown for illustration.

### 1. Introduction

Variational concepts have long played a significant role in the development of numerical discretization techniques. First, variational principles in physics and mechanics have been used to derive the governing differential equations from which numerical discretizations are routinely conducted. The principles—including Hamilton's principle in dynamics, in the electromagnetic and gravitational fields, and even in quantum mechanics; the principle of stationary potential energy and the Hu–Washizu's variational principle in continuum statics; Fermat's principle of least time leading to Snell's law in optics; Maupertuis'

---

*Keywords:* Lagrangian, Hamiltonian, total energy, finite elements, theorem of expended power,  $N$ -body problem, continuous bodies, elastodynamics.

principle of least action, Jacobi and Lagrange's principle of least action in dynamics again; and Gurtin's variational principles [1964a; 1964b] for initial value problems such as wave and transient heat transfer in lieu of Hamilton's principle — have been considered in engineering and science as an indispensable branch of mathematics to derive the differential equations, namely, the Euler–Lagrange equations. At the same time, variational methods such as the Rayleigh–Ritz method, the principle of virtual work, the Galerkin weighted residual method, the Kantorovitch method, and the Trefftz method have played a critical role in finding approximate solutions to the governing equations.

Thus, whether via the variation principle or the variational method, the notion of variation is ubiquitous. But the question arises: Can the differential formulation be used as an alternative to the variation formulation? This is the focus of this paper.

As mentioned, the calculus of variations, founded by Euler and Lagrange, has been used extensively to derive governing differential equations, especially for mechanical systems. It has been the focus of philosophical controversies and some misinterpretations due to the perception that it seems to bring a purpose to the flow of natural events. Both approaches are concerned with infinitesimal changes in physical quantities. However, in a sense the differential calculus uses the real quantity, while the variational calculus employs the imaginary quantity. The notion of variation is imaginary, but the notion of differential is real!

The biggest advantage of the variation over the differential seems to arise from problems described as *rheonomic systems*. Recall that holonomic systems where Lagrange's equations of motion and Hamilton's principle are true were classified by Boltzmann into scleronomic and rheonomic systems [Lanczos 1970]. In rheonomic systems, the direction of the differential differs from that of the variation, due to the presence of the partial derivative of any physical quantity with respect to time depending on time explicitly. The introduction of the variation enables one to eliminate the time partial derivative term. However, it is an imaginary and a mathematical abstract quantity.

Most engineering and science applications do not fall into the class of rheonomic systems [Castro 2000]. In scleronomic systems, the direction of the differential is identical to that of the variation. Therefore, for such applications, the variational approach is not indispensable in deriving governing equations or in finding approximate solutions. Fortunately, this is the case of most engineering and science problems.

In particular, the solid mechanics, elastodynamics and continuum mechanics problems to which the finite element formulations are usually applied are generally scleronomic. Variational formulations are not indispensable to such applications, and differential formulations also play an important role, as we now describe.

***Contributions of the present approach.*** Traditional practices for finite element discretization tend to employ the Newtonian framework. They mostly start from the Cauchy equations of motion and invoke the variational calculus, leading to the weak form or, equivalently, the principle of virtual work. In contrast, we have previously provided alternate developments via Hamilton's law of varying action as a starting point which is also based on the concept of variations [Har and Tamma 2009]. Unlike all these past developments, in this paper we employ the differential calculus and frameworks involving scalar representations, namely, the Lagrangian  $\mathcal{L}(\mathbf{q}, \dot{\mathbf{q}}) : TQ \rightarrow \mathbb{R}$ , the Hamiltonian  $\mathcal{H}(\mathbf{p}, \mathbf{q}) : T^*Q \rightarrow \mathbb{R}$ , and the total energy  $\mathcal{E}(\mathbf{q}, \dot{\mathbf{q}}) : TQ \rightarrow \mathbb{R}$ .

To our knowledge, this use of the differential calculus in describing finite element discretizations is novel. It provides alternate viewpoints and helps deepen physical insight.

For approximation procedures like the finite element formulation, the basic issue with the conventional approaches for continuum dynamics is that there is no notion of a *scalar function*, say energy, that is readily built-in or directly available. The procedure mostly relies upon numerical discretization of the governing equations with dependent variables in terms of vector quantities such as displacement, velocity, acceleration, etc. This gives rise to two issues:

- (a) To deal with a physical quantity such as total energy in a finite element computation, or to interpret the results from a Newtonian viewpoint, one often resorts to introducing the well known scalar functions typical of the Lagrangian or the Hamiltonian, even though one is not working in the Lagrangian or Hamiltonian framework.
- (b) To establish that the semidiscretized equations (which are of focus here) inherit the same physics as the continuous governing equations in space and time can be difficult in traditional frameworks, since no obvious scalar function is available for capitalizing on Noether's theorem and the like. In our framework involving scalar representations, by contrast, one can readily establish the symmetries for the continuous as well as the discrete scalar representations for the total energy, Lagrangian, and the Hamiltonian. (Proofs of the symmetries of  $\mathcal{E}$  are given in [Har and Tamma 2009], while those for  $\mathcal{L}(\mathbf{q}, \dot{\mathbf{q}})$  and  $\mathcal{H}(\mathbf{p}, \mathbf{q})$  appear in the standard literature.) In other words, we propose a new space-discrete finite element formulation that circumvents the weak-form Cauchy equations and the principle of virtual work. Although it must yield the same semidiscretized equations on physical grounds, the new formulation leads more easily to proofs that the discrete system preserves the physical attributes of the continuum system, via the scalar representations that are invariant. In summary, if the continuum system obeys the conservation laws, establishing the symmetries for the semidiscretized system also ensures the same physical attributes as in the continuum system.

***The role of symmetries.*** Noether's theorem relates the invariance properties of the Lagrangian to the conservation laws of physics [Noether 1918; Byers 1996; 1999]. Thus, the spatial translational invariance of the Lagrangian in configuration space gives rise to conservation of linear momentum, its rotational invariance to conservation of angular momentum, and the autonomous Lagrangian has invariance in time. The Hamiltonian in phase space shares the same invariance properties, by the Hamiltonian version of Noether's theorem; see [Simo et al. 1992], for example. It turns out that the autonomous total energy (which is not the Hamiltonian, nor it is in the same configuration space as that of the Hamiltonian) also possesses the three invariances. Hence it can be viewed as a total energy version of Noether's theorem [Har and Tamma 2009].

Conservation laws can be extended to the balance laws of mechanical systems, such as the linear momentum balance law, the angular momentum balance law, and the energy balance law in continuum mechanics [Marsden and Hughes 1983; Holzapfel 2000; Malvern 1969]. Newton's law for  $N$ -body dynamical systems or Cauchy's equations of motion for continuous-body dynamical systems can be obtained from the linear momentum balance law. We believe that, as the fundamental equation for  $N$ -body dynamical systems, d'Alembert's principle [Goldstein et al. 2002; Hand and Finch 1998] or the d'Alembert–Lagrange principle [Arnold 1989] or the generalized d'Alembert principle [Meirovitch 2003] or the Lagrangian form of d'Alembert's principle [Greenwood 1977] or the first form of the

fundamental equation [Pars 1965] result from the conceptual amalgamation of the linear momentum balance law and the principle of virtual work. Note that Lagrange's equations of motion can be derived from d'Alembert's principle; further, Hamilton's equations of motion can be deduced from Lagrange's equations of motion and the Legendre transformation. Thus the linear momentum balance law is at the origin of all these equations governing motion.

At the same time, it is known that Hamilton's principle has a logical inconsistency for handling transient initial value problems [Gurtin 1964a; 1964b; Tonti 1973; 1984; Bailey 1975; Simkins 1981; Carini and Genna 1998]. Hamilton's law of varying action, which is not a variational principle, circumvents this deficiency and is more appropriate to use. *However, both approaches use the notion of variation, and with respect to scalar representations of the governing equations of motion, they are, so to speak, secondary developments; Lagrange's equations of motion in configuration space are the first equations encountered in the logical derivation under these approaches.* It is from them that one obtains Hamilton's equations in phase space, by applying the Legendre transformation. Unlike the above, the theorem of expended power first yields naturally the so-called total energy representation of the equations of motion in the logical derivation in configuration space. Thereafter, employing a particular transformation that is not a Legendre transformation, one can then define the standard Lagrange equations of motion in configuration space. Through a Legendre transformation one is then led to Hamilton's equation in phase space.

As an alternative to the Lagrangian and the Hamiltonian frameworks, we proposed in [Har and Tamma 2009] a framework based on the directly measurable built-in scalar quantity called the total energy  $\mathcal{E}(\mathbf{q}, \dot{\mathbf{q}}) : TQ \rightarrow \mathbb{R}$ . The total energy has the same translation, rotation, and time invariance properties. The total energy we use here is the kinetic energy plus the potential energy for  $N$ -body systems and the kinetic energy plus the total potential energy for continuous-body systems.

Figure 1 summarizes the main quantities and equations in the total energy framework, as well as the traditional Lagrangian and Hamiltonian frameworks, for an  $N$ -body system. The figure also indicates the

Total energy framework	Lagrangian framework	Hamiltonian framework
$\frac{d}{dt} \left( \frac{\partial \mathcal{E}(\mathbf{q}, \dot{\mathbf{q}})}{\partial \dot{\mathbf{q}}} \right) + \frac{\partial \mathcal{E}(\mathbf{q}, \dot{\mathbf{q}})}{\partial \mathbf{q}} = \mathbf{0}$	$\frac{d}{dt} \left( \frac{\partial \mathcal{L}(\mathbf{q}, \dot{\mathbf{q}})}{\partial \dot{\mathbf{q}}} \right) - \frac{\partial \mathcal{L}(\mathbf{q}, \dot{\mathbf{q}})}{\partial \mathbf{q}} = \mathbf{0}$	$\dot{\mathbf{p}} = - \frac{\partial \mathcal{H}(\mathbf{p}, \mathbf{q})}{\partial \mathbf{q}}, \dot{\mathbf{q}} = \frac{\partial \mathcal{H}(\mathbf{p}, \mathbf{q})}{\partial \mathbf{p}}$
$\mathcal{E}(\mathbf{q}, \dot{\mathbf{q}}) = \frac{\partial \mathcal{L}(\mathbf{q}, \dot{\mathbf{q}})}{\partial \dot{\mathbf{q}}} \cdot \dot{\mathbf{q}} - \mathcal{L}(\mathbf{q}, \dot{\mathbf{q}})$ $\mathcal{L}(\mathbf{q}, \dot{\mathbf{q}}) = \frac{\partial \mathcal{E}(\mathbf{q}, \dot{\mathbf{q}})}{\partial \dot{\mathbf{q}}} \cdot \dot{\mathbf{q}} - \mathcal{E}(\mathbf{q}, \dot{\mathbf{q}})$	$\mathcal{L}(\mathbf{q}, \dot{\mathbf{q}}) = \mathbf{p} \cdot \dot{\mathbf{q}} - \mathcal{H}(\mathbf{p}, \mathbf{q})$ $\mathcal{H}(\mathbf{p}, \mathbf{q}) = \mathbf{p} \cdot \dot{\mathbf{q}} - \mathcal{L}(\mathbf{q}, \dot{\mathbf{q}})$	
$\mathbf{q} \in Q \subset \mathbb{R}^{3N-k}$ $\dot{\mathbf{q}} \in T_q Q \subset \mathbb{R}^{3N-k}$ $(\mathbf{q}, \dot{\mathbf{q}}) \in TQ \subset \mathbb{R}^{2(3N-k)}$ $TQ = \{(\mathbf{q}, \dot{\mathbf{q}})   \mathbf{q} \in Q, \dot{\mathbf{q}} \in T_q Q\}$	$\mathbf{q} \in Q \subset \mathbb{R}^{3N-k}$ $\dot{\mathbf{q}} \in T_q Q \subset \mathbb{R}^{3N-k}$ $(\mathbf{q}, \dot{\mathbf{q}}) \in TQ \subset \mathbb{R}^{2(3N-k)}$ $TQ = \{(\mathbf{q}, \dot{\mathbf{q}})   \mathbf{q} \in Q, \dot{\mathbf{q}} \in T_q Q\}$	$\mathbf{q} \in Q \subset \mathbb{R}^{3N-k}$ $\mathbf{p} \in T_q^* Q$ $(\mathbf{p}, \mathbf{q}) \equiv P \in T^* Q \subset \mathbb{R}^{2(3N-k)}$ $T^* Q = \{(\mathbf{p}, \mathbf{q})   \mathbf{q} \in Q, \mathbf{p} \in T_q^* Q\}$
$\mathcal{E}(\mathbf{q}, \dot{\mathbf{q}}) : TQ \rightarrow \mathbb{R}$	$\mathcal{L}(\mathbf{q}, \dot{\mathbf{q}}) : TQ \rightarrow \mathbb{R}$	$\mathcal{H}(\mathbf{p}, \mathbf{q}) : T^* Q \rightarrow \mathbb{R}$

**Figure 1.** Comparison of the autonomous Lagrangian, Hamiltonian, and Total Energy frameworks for the  $N$ -body problem.



equivalence between the three. As discussed, all three scalar functions (in configuration or phase space as appropriate) possess spatial invariance under translations and rotations, and also translational time invariance in the autonomous case. This holds equally for finite- and infinite-dimensional dynamical systems.

Via Hamilton's principle, the total energy framework can be viewed as a third perspective (the first and second being the Lagrangian and the Hamiltonian), providing meaningful insight. The total energy has a direct physical interpretation and practical utility, in contrast to the somewhat abstract scalar quantity that is the Lagrangian  $\mathcal{L}(\mathbf{q}, \dot{\mathbf{q}}) : TQ \rightarrow \mathbb{R}$  in configuration space. The second-order ordinary differential system arising from the total energy framework after space discretization offers the same features that apply to the Newtonian description for continuum mechanics, including considerations for designing time stepping algorithms. By contrast, the Hamiltonian  $\mathcal{H}(\mathbf{p}, \mathbf{q}) : T^*Q \rightarrow \mathbb{R}$  (which, as we recall, does not in general represent energy directly) is not as popular for numerical discretization in the computational mechanics community, because the resulting first-order system requires altogether a different form of time discretization.

**Remark.** A different alternative to traditional finite element practices, called the cell method and amounting to a direct discrete formulation of field laws, can be found in the literature [Tonti 2001a; 2001b]. Without resorting to differential governing equations, the discretization procedure is carried out directly from physical laws using physical variables such as configuration, source, and energy variables. For most simplex elements, the stiffness matrices obtained by the formulation coincide with the one obtained by traditional finite element practices. Likewise, our proposed formulation also yields the same stiffness matrices (as well as the mass and damping matrices, and load vectors) reached by traditional practices.

**Outline of paper.** In Section 2 we discuss the theorem of expended power — the starting point of our formulation — in the context of discrete  $N$ -body systems; the treatment is extended in Section 3 to continua. Section 4 is devoted to the consequences to the second law of thermodynamics. In Section 5 we use the theorem of expended power to provide scalar description formalisms of Lagrangian, Hamiltonian, and total energy representations equivalent to the Cauchy equations of motion. The application of the proposed formulation to nonholonomic or nonconservative systems is the subject of Section 6. We turn in Section 7 to the space-discrete finite element formulation, both in the traditional approaches and in the new total energy approaches. Section 8 contains numerical examples and illustrations. An Appendix discusses in detail the space discretization via density formalisms and the finite element formulation.

## 2. $N$ -body dynamical systems: theorem of expended power

For an illustration of the basic concepts, we focus first on a dynamical system of  $N$  particles moving in three-dimensional Euclidean space. Newton's equations of motion state that the rate of the total linear momentum of the constrained system is the total resultant acting on the system:

$$\mathbf{M}\ddot{\mathbf{x}} = \mathbf{F}_{\text{con}} + \mathbf{F}_{\text{nc}} + \mathbf{C}, \quad \ddot{\mathbf{x}} = (\ddot{\mathbf{x}}^1, \dots, \ddot{\mathbf{x}}^i, \dots, \ddot{\mathbf{x}}^N) : \mathbb{I} \rightarrow \mathbb{R}^{3N}, \quad t \in \mathbb{I} = [t_1, t_2], \quad (1)$$

where  $\ddot{\mathbf{x}}$  represents a set of  $\ddot{\mathbf{x}}^i$  acceleration vectors of the particles,  $\mathbf{M}$  the total diagonal mass matrix,  $\mathbf{F}_{\text{con}} \in \mathbb{R}^3$  the total conservative force,  $\mathbf{F}_{\text{nc}}(t) : \mathbb{I} \rightarrow \mathbb{R}^{3N}$ ,  $t \in \mathbb{I} = [t_1, t_2]$  the total nonconservative force, and  $\mathbf{C} \in \mathbb{R}^3$  the total constraint force. When the inertia term on the left-hand side of (1) is moved to the right, we have d'Alembert's principle, saying that the system is dynamically in equilibrium:

$$\mathbf{F}_{\text{con}} + \mathbf{F}_{\text{nc}}(t) + \mathbf{C} - \mathbf{M}\ddot{\mathbf{x}}(t) = 0. \quad (2)$$

We assume that the constraints are scleronomic (whether holonomic or not), confining the motion to a smooth surface. Then the constraint force is orthogonal to the velocity, which means it does not contribute to the virtual work. (Nonconservative forces are sometimes the result of nonholonomic constraints.)

Multiplying both sides of (2) by the velocity  $\dot{\mathbf{x}}(t) : \mathbb{I} \rightarrow \mathbb{R}^{3N}$ ,  $t \in \mathbb{I} = [t_1, t_2]$  we have

$$(\mathbf{F}_{\text{con}} + \mathbf{F}_{\text{nc}}(t) - \mathbf{M}\ddot{\mathbf{x}}(t)) \cdot \dot{\mathbf{x}}(t) = 0, \quad (3)$$

which can be recast as

$$\dot{\mathbf{x}}(t) \cdot \mathbf{M}\ddot{\mathbf{x}} = \mathbf{F}_{\text{con}} \cdot \dot{\mathbf{x}}(t) + \mathbf{F}_{\text{nc}}(t) \cdot \dot{\mathbf{x}}(t). \quad (4)$$

By invoking the kinetic energy  $\mathcal{K}(\dot{\mathbf{x}}) : \mathbb{R}^3 \rightarrow \mathbb{R}$ , the potential energy  $\mathcal{U}(\mathbf{x}) : \mathbb{R}^3 \rightarrow \mathbb{R}$ , and the power input  $\mathcal{P}_{\text{input}}$  for the  $N$ -body system, Equation (4) can be expressed in terms of the total energy  $\mathcal{E}(\dot{\mathbf{x}}, \mathbf{x})$  as

$$\frac{d\mathcal{E}(\dot{\mathbf{x}}, \mathbf{x})}{dt} = \mathcal{P}_{\text{input}}, \quad \mathcal{E}(\dot{\mathbf{x}}, \mathbf{x}) = \mathcal{K}(\dot{\mathbf{x}}) + \mathcal{U}(\mathbf{x}), \quad \mathcal{P}_{\text{input}} = \mathbf{F}_{\text{nc}}(t) \cdot \dot{\mathbf{x}}(t), \quad (5)$$

where the kinetic energy and the potential energy are defined as

$$\mathcal{K}(\dot{\mathbf{x}}) = \frac{1}{2} \dot{\mathbf{x}}(t) \cdot \mathbf{M}\dot{\mathbf{x}}(t), \quad \mathbf{F}_{\text{con}} = -\frac{\partial \mathcal{U}}{\partial \mathbf{x}} = -\nabla \mathcal{U}(\mathbf{x}). \quad (6)$$

Equation (5) corresponds to the principle of balance of energy for the  $N$ -body mechanical system.

Suppose the system is subject to  $k$  independent algebraic constraints. The constraints reduce the number of degrees of freedom to  $n_{\text{dof}} = 3N - k$ , and can be written in terms of the positions of  $N$  particles as

$$f_i(\mathbf{x}^1, \dots, \mathbf{x}^N) = 0, \quad i = 1, \dots, k. \quad (7)$$

Invoking generalized coordinates  $\mathbf{q} = (q^1, \dots, q^{n_{\text{dof}}})$  belonging to a local configuration space  $Q \subset \mathbb{R}^{n_{\text{dof}}}$ , the velocity in the Cartesian coordinate system can be expressed as

$$\dot{\mathbf{x}}(\mathbf{q}(\mathbf{x})) = \frac{\partial \mathbf{x}}{\partial \mathbf{q}} \cdot \dot{\mathbf{q}}, \quad \mathbf{q}(\mathbf{x}) = (q^1(\mathbf{x}), \dots, q^{n_{\text{dof}}}(\mathbf{x})). \quad (8)$$

Then, (4) can be rewritten in terms of generalized velocities, as

$$(\mathbf{M}\ddot{\mathbf{x}} - \mathbf{F}_{\text{con}}) \cdot \frac{\partial \mathbf{x}}{\partial \mathbf{q}} \cdot \dot{\mathbf{q}} = \mathcal{P}_{\text{input}}. \quad (9)$$

This equation can be regarded as an analogue of the first form of the fundamental equation or d'Alembert's principle. We have

$$\mathbf{M}\ddot{\mathbf{x}} \cdot \frac{\partial \mathbf{x}}{\partial \mathbf{q}} = \frac{d}{dt} \left( \mathbf{M}\dot{\mathbf{x}} \cdot \frac{\partial \mathbf{x}}{\partial \mathbf{q}} \right) - \mathbf{M}\dot{\mathbf{x}} \cdot \frac{\partial \dot{\mathbf{x}}}{\partial \mathbf{q}} = \frac{d}{dt} \left( \mathbf{M}\dot{\mathbf{x}} \cdot \frac{\partial \dot{\mathbf{x}}}{\partial \dot{\mathbf{q}}} \right) - \mathbf{M}\dot{\mathbf{x}} \cdot \frac{\partial \dot{\mathbf{x}}}{\partial \mathbf{q}}. \quad (10)$$

In view of (6), we have the generalized force given as

$$\mathbf{Q} = \mathbf{F}_{\text{con}} \cdot \frac{\partial \mathbf{x}}{\partial \mathbf{q}} = -\nabla \mathcal{U}(\mathbf{q}). \quad (11)$$

In terms of the kinetic energy  $\mathcal{K}(\mathbf{q}, \dot{\mathbf{q}})$  and potential energy  $\mathcal{U}(\mathbf{q})$ , Equation (9) can be rewritten as

$$\left( \frac{d}{dt} \frac{\partial \mathcal{K}(\mathbf{q}, \dot{\mathbf{q}})}{\partial \dot{\mathbf{q}}} - \frac{\partial \mathcal{K}(\mathbf{q}, \dot{\mathbf{q}})}{\partial \mathbf{q}} + \frac{\partial \mathcal{U}(\mathbf{q})}{\partial \mathbf{q}} \right) \cdot \dot{\mathbf{q}} = \mathcal{P}_{\text{input}}. \quad (12)$$

If the system is scleronomic, the kinetic energy must be quadratic in the generalized velocities [Greenwood 1977] and have no explicit time dependence. As a consequence, in terms of the autonomous total energy, (12) gives

$$\left( \frac{d}{dt} \frac{\partial \mathcal{E}(\mathbf{q}, \dot{\mathbf{q}})}{\partial \dot{\mathbf{q}}} + \frac{\partial \mathcal{E}(\mathbf{q}, \dot{\mathbf{q}})}{\partial \mathbf{q}} - 2 \frac{\partial \mathcal{H}(\mathbf{q}, \dot{\mathbf{q}})}{\partial \mathbf{q}} \right) \cdot \dot{\mathbf{q}} = \mathcal{P}_{\text{input}}, \quad (13)$$

and in terms of the autonomous Lagrangian  $\mathcal{L}(\mathbf{q}, \dot{\mathbf{q}}) : TQ \rightarrow \mathbb{R}$ , (12) also leads to

$$\left( \frac{d}{dt} \frac{\partial \mathcal{L}(\mathbf{q}, \dot{\mathbf{q}})}{\partial \dot{\mathbf{q}}} - \frac{\partial \mathcal{L}(\mathbf{q}, \dot{\mathbf{q}})}{\partial \mathbf{q}} \right) \cdot \dot{\mathbf{q}} = \mathcal{P}_{\text{input}}. \quad (14)$$

Suppose that there is no external power input. Since the generalized velocities are arbitrary, the governing equations of motion can be obtained as

$$\frac{d}{dt} \frac{\partial \mathcal{E}(\mathbf{q}, \dot{\mathbf{q}})}{\partial \dot{\mathbf{q}}} + \frac{\partial \mathcal{E}(\mathbf{q}, \dot{\mathbf{q}})}{\partial \mathbf{q}} - 2 \frac{\partial \mathcal{H}(\mathbf{q}, \dot{\mathbf{q}})}{\partial \mathbf{q}} = 0 \quad \text{or} \quad \frac{d}{dt} \frac{\partial \mathcal{L}(\mathbf{q}, \dot{\mathbf{q}})}{\partial \dot{\mathbf{q}}} - \frac{\partial \mathcal{L}(\mathbf{q}, \dot{\mathbf{q}})}{\partial \mathbf{q}} = 0. \quad (15)$$

In the special case that the kinetic energy does not depend on the generalized coordinates, we have

$$\frac{d}{dt} \frac{\partial \mathcal{E}(\mathbf{q}, \dot{\mathbf{q}})}{\partial \dot{\mathbf{q}}} + \frac{\partial \mathcal{E}(\mathbf{q}, \dot{\mathbf{q}})}{\partial \mathbf{q}} = 0. \quad (16)$$

Integrating both sides of (12) over the given time interval  $\mathbb{I} = [t_1, t_2]$ , we have

$$\int_{t_1}^{t_2} \left\{ \frac{d}{dt} \left( \frac{\partial \mathcal{H}}{\partial \dot{\mathbf{q}}} \cdot \dot{\mathbf{q}} - \mathcal{H} + \mathcal{U} \right) \right\} dt = \int_{t_1}^{t_2} \mathcal{P}_{\text{input}} dt. \quad (17)$$

For conservative systems, we have no external power input. Then, (17) implies that

$$\left( \frac{\partial \mathcal{H}(\mathbf{q}, \dot{\mathbf{q}})}{\partial \dot{\mathbf{q}}} \cdot \dot{\mathbf{q}} - \mathcal{H}(\mathbf{q}, \dot{\mathbf{q}}) + \mathcal{U}(\mathbf{q}) \right) \Big|_{t=t_1} = \left( \frac{\partial \mathcal{H}(\mathbf{q}, \dot{\mathbf{q}})}{\partial \dot{\mathbf{q}}} \cdot \dot{\mathbf{q}} - \mathcal{H}(\mathbf{q}, \dot{\mathbf{q}}) + \mathcal{U}(\mathbf{q}) \right) \Big|_{t=t_2} = \mathcal{E}(\mathbf{q}, \dot{\mathbf{q}}). \quad (18)$$

In terms of the Lagrangian, this equation can be rewritten as

$$\left( \frac{\partial \mathcal{L}(\mathbf{q}, \dot{\mathbf{q}})}{\partial \dot{\mathbf{q}}} \cdot \dot{\mathbf{q}} - \mathcal{L}(\mathbf{q}, \dot{\mathbf{q}}) \right) \Big|_{t=t_1} = \left( \frac{\partial \mathcal{L}(\mathbf{q}, \dot{\mathbf{q}})}{\partial \dot{\mathbf{q}}} \cdot \dot{\mathbf{q}} - \mathcal{L}(\mathbf{q}, \dot{\mathbf{q}}) \right) \Big|_{t=t_2} = \mathcal{E}(\mathbf{q}, \dot{\mathbf{q}}). \quad (19)$$

The term in big parentheses, called Jacobi's integral [Pars 1965, p. 82; Greenwood 1977], is identical to the autonomous total energy, which remains constant. Within the Hamiltonian framework, the preceding equation can be rewritten as

$$(\mathbf{p} \cdot \dot{\mathbf{q}} - \mathcal{L}(\mathbf{q}, \dot{\mathbf{q}})) \Big|_{t=t_1} = (\mathbf{p} \cdot \dot{\mathbf{q}} - \mathcal{L}(\mathbf{q}, \dot{\mathbf{q}})) \Big|_{t=t_2} = \mathcal{H}(\mathbf{q}, \mathbf{p}). \quad (20)$$

We thus arrive at the governing equations of motion in each of the three formalisms:

$$\begin{aligned} \frac{d\mathcal{E}(\mathbf{q}, \dot{\mathbf{q}})}{dt} &= \left( \frac{d}{dt} \frac{\partial \mathcal{E}(\mathbf{q}, \dot{\mathbf{q}})}{\partial \dot{\mathbf{q}}} + \frac{\partial \mathcal{E}(\mathbf{q}, \dot{\mathbf{q}})}{\partial \mathbf{q}} - 2 \frac{\partial \mathcal{H}(\mathbf{q}, \dot{\mathbf{q}})}{\partial \mathbf{q}} \right) \cdot \dot{\mathbf{q}} = 0, \\ \frac{d}{dt} \left[ \frac{\partial \mathcal{L}(\mathbf{q}, \dot{\mathbf{q}})}{\partial \dot{\mathbf{q}}} \cdot \dot{\mathbf{q}} - \mathcal{L}(\mathbf{q}, \dot{\mathbf{q}}) \right] &= \left( \frac{d}{dt} \frac{\partial \mathcal{L}(\mathbf{q}, \dot{\mathbf{q}})}{\partial \dot{\mathbf{q}}} - \frac{\partial \mathcal{L}(\mathbf{q}, \dot{\mathbf{q}})}{\partial \mathbf{q}} \right) \cdot \dot{\mathbf{q}} = 0, \\ \frac{d\mathcal{H}(\mathbf{p}, \mathbf{q})}{dt} &= \left( \dot{\mathbf{p}} + \frac{\partial \mathcal{H}(\mathbf{p}, \mathbf{q})}{\partial \mathbf{q}} \right) \cdot \dot{\mathbf{q}} - \left( \dot{\mathbf{q}} - \frac{\partial \mathcal{H}(\mathbf{p}, \mathbf{q})}{\partial \mathbf{p}} \right) \cdot \dot{\mathbf{p}} = 0. \end{aligned} \quad (21)$$

Integrating over time we reach the Galerkin time weighted-residual form for  $N$ -body dynamical systems under each formalism. For example, for the total energy formalism,

$$\int_{t_1}^{t_2} \left\{ \frac{d}{dt} \left( \frac{\partial \mathcal{E}(\mathbf{q}, \dot{\mathbf{q}})}{\partial \dot{\mathbf{q}}} + \frac{\partial \mathcal{E}(\mathbf{q}, \dot{\mathbf{q}})}{\partial \mathbf{q}} - 2 \frac{\partial \mathcal{K}(\mathbf{q}, \dot{\mathbf{q}})}{\partial \mathbf{q}} \right) \cdot \dot{\mathbf{q}} \right\} dt = 0. \quad (22)$$

### 3. Continuous-body dynamical systems: theorem of expended power

The focus next is on elastodynamics, where a continuous body is parametrized by a simply connected and bounded open set  $\mathcal{B}$ , called the reference configuration, assumed to have a piecewise smooth boundary  $\partial\mathcal{B}$ . The smooth motion of the body may be described by a mapping  $\boldsymbol{\varphi}(\mathbf{X}, t) : \mathcal{B} \times \mathbb{I} \rightarrow \mathbb{R}^3$  such that for each  $t \in \mathbb{I}$  the restriction to  $\mathcal{B} \times \{t\}$  is one-to-one and smooth; its image  $\mathcal{S}$  for a given  $t$  is called the current configuration. The set of all such maps is called the configuration space:

$$\mathcal{C} = \left\{ \boldsymbol{\varphi}(\mathbf{X}, t) : \mathcal{B} \times \mathbb{I} \rightarrow \mathbb{R}^3 \mid \boldsymbol{\varphi} \text{ is of class } C^{2m} \ (m \geq 1) \text{ in } \mathbf{X} \text{ and } t, |\nabla \boldsymbol{\varphi}| > 0, \text{ and } \boldsymbol{\varphi}|_{\Gamma_{\partial\mathcal{B}_\varphi}} = \bar{\boldsymbol{\varphi}} \right\}, \quad (23)$$

where  $\bar{\boldsymbol{\varphi}}$  denotes the prescribed quantity on the prescribed-displacement boundary. Hence, continuous-body dynamical systems are holonomic. The configuration space is a smooth infinite-dimensional manifold. In the nonpolar case, when distributed body or surface couples are not prescribed, the power input  $\mathcal{P}_{\text{input}}$  (the rate at which the external surface tractions and body forces are doing actual work) is defined as

$$\mathcal{P}_{\text{input}} = \int_{\mathcal{B}} \rho_0 \mathbf{B}(\mathbf{X}, t) \cdot \dot{\boldsymbol{\varphi}}(\mathbf{X}, t) dV + \int_{\partial\mathcal{B}_\sigma} \bar{\mathbf{T}}(\mathbf{X}, t) \cdot \dot{\boldsymbol{\varphi}}(\mathbf{X}, t) dA, \quad (24)$$

where  $\rho_0(\mathbf{X}) : \mathcal{B} \rightarrow \mathbb{R}$  denotes the referential density,  $\bar{\mathbf{T}}(\mathbf{X}, t) : \mathcal{B} \times \mathbb{I} \rightarrow \mathbb{R}^3$  the prescribed traction on the boundary  $\partial\mathcal{B}$ ,  $\mathbf{B}(\mathbf{X}, t) : \mathcal{B} \times \mathbb{I} \rightarrow \mathbb{R}^3$  the body force, and  $dA, dV$  the Lebesgue measures on the prescribed-traction boundary  $\partial\mathcal{B}_\sigma$  and in the body  $\mathcal{B}$ . Notice that the body forces are not prescribed, and the external forces are not dead loads.

Next, invoking Cauchy's law  $\bar{\mathbf{T}}(\mathbf{X}, t) = \mathbf{P}(\mathbf{X}, t) \cdot \hat{\mathbf{N}}(\mathbf{X}, t)$  and Gauss's theorem, we rewrite (24) as

$$\mathcal{P}_{\text{input}} = \int_{\mathcal{B}} \rho_0 \mathbf{B}(\mathbf{X}, t) \cdot \dot{\boldsymbol{\varphi}}(\mathbf{X}, t) dV + \int_{\mathcal{B}} \nabla \cdot (\mathbf{P} \cdot \dot{\boldsymbol{\varphi}}) dV, \quad (25)$$

where  $\mathbf{P}(\mathbf{X}, t)$  denotes the first Piola–Kirchhoff stress tensor (see [Marsden and Hughes 1983], for example) in the reference configuration. Recall the product rule

$$\nabla \cdot (\mathbf{P} \cdot \dot{\boldsymbol{\varphi}}) = (\nabla \cdot \mathbf{P}) \cdot \dot{\boldsymbol{\varphi}} + \mathbf{P} \cdot \cdot (\nabla \dot{\boldsymbol{\varphi}}) = (\nabla \cdot \mathbf{P}) \cdot \dot{\boldsymbol{\varphi}} + \mathbf{P} \cdot \cdot \dot{\mathbf{F}}, \quad (26)$$

where  $\dot{\mathbf{F}}$  denotes the total time derivative of the deformation gradient tensor,  $\mathbf{F}$ . Using (26), the power input can be expressed as

$$\mathcal{P}_{\text{input}} = \int_{\mathcal{B}} \{ \nabla \cdot \mathbf{P} + \rho_0 \mathbf{B}(\mathbf{X}, t) \} \cdot \dot{\boldsymbol{\varphi}}(\mathbf{X}, t) dV + \int_{\mathcal{B}} \mathbf{P} \cdot \cdot \dot{\mathbf{F}} dV. \quad (27)$$

By virtue of Cauchy's equations of motion, the power input can be expressed as

$$\mathcal{P}_{\text{input}} = \int_{\mathcal{B}} \rho_0 \ddot{\boldsymbol{\varphi}} \cdot \dot{\boldsymbol{\varphi}}(\mathbf{X}, t) dV + \int_{\mathcal{B}} \mathbf{P} \cdot \cdot \dot{\mathbf{F}} dV. \quad (28)$$

The first term on the right is the rate of the system's kinetic energy; the second is known as the stress power. As a consequence of (24) and (28), we have the theorem of expended power [Gurtin 1972, p. 110]:

$$\frac{d\mathcal{K}}{dt} + \int_{\mathfrak{B}} \mathbf{P} \cdot \dot{\mathbf{F}} dV = \int_{\mathfrak{B}} \rho_0 \mathbf{B}(\mathbf{X}, t) \cdot \dot{\boldsymbol{\varphi}}(\mathbf{X}, t) dV + \int_{\partial\mathfrak{B}_\sigma} \bar{\mathbf{T}}(\mathbf{X}, t) \cdot \dot{\boldsymbol{\varphi}}(\mathbf{X}, t) dA. \quad (29)$$

This holds whether the system is mechanical or thermomechanical. In addition, by use of Cauchy's law, the theorem of expended power can be readily rewritten as the modified Bubnov–Galerkin weighted residual form [Mikhlin 1964]

$$\int_{\mathfrak{B}} (\nabla \cdot \mathbf{P} + \rho_0 \mathbf{B} - \rho_0 \ddot{\boldsymbol{\varphi}}) \cdot \dot{\boldsymbol{\varphi}} dV + \int_{\partial\mathfrak{B}_\sigma} (\bar{\mathbf{T}} - \mathbf{P} \cdot \hat{\mathbf{N}}) \cdot \dot{\boldsymbol{\varphi}} dA = 0, \quad (30)$$

where  $\hat{\mathbf{N}}$  denotes the unit vector outward normal to the surface of the body. Thus, we observe that the theorem of expended power leads to the modified Bubnov–Galerkin weighted residual form, where the weighting function is the generalized velocity. Note that the traction boundary conditions (Cauchy's law) were applied to (24) and Cauchy's equations were imposed upon (27).

The first law of thermodynamics states that

$$\frac{d\mathcal{K}}{dt} + \frac{dU}{dt} = \int_{\mathfrak{B}} \rho_0 \mathbf{B}(\mathbf{X}, t) \cdot \dot{\boldsymbol{\varphi}}(\mathbf{X}, t) dV + \int_{\partial\mathfrak{B}_\sigma} \bar{\mathbf{T}}(\mathbf{X}, t) \cdot \dot{\boldsymbol{\varphi}}(\mathbf{X}, t) dA + \int_{\mathfrak{B}} \rho_0 R(\mathbf{X}, t) dV - \int_{\mathfrak{B}} \nabla \cdot \mathbf{Q}(\mathbf{X}, t) dV, \quad (31)$$

where  $U$  is the internal energy of the thermomechanical system,  $\mathbf{Q}(\mathbf{X}, t) : \mathfrak{B} \times \mathbb{I} \rightarrow \mathbb{R}^3$  the heat flux vector, and  $R(\mathbf{X}, t) : \mathfrak{B} \times \mathbb{I} \rightarrow \mathbb{R}$  the specific distributed internal heat supply. By Cauchy's law, (31) leads to

$$\int_{\mathfrak{B}} (\rho_0 \ddot{\boldsymbol{\varphi}} - \nabla \cdot \mathbf{P} - \rho_0 \mathbf{B}) \cdot \dot{\boldsymbol{\varphi}} dV + \int_{\mathfrak{B}} \left( \rho_0 \frac{\partial \bar{U}}{\partial t} - \mathbf{P} \cdot \dot{\mathbf{F}} - \rho_0 R + \nabla \cdot \mathbf{Q} \right) dV = 0, \quad (32)$$

which contains two governing equations: Cauchy's equations of motion and Kirchhoff's energy equations. Here  $\bar{U}$  denotes the specific internal energy density in the reference configuration. Thus, for thermomechanical systems, the two governing equations are coupled; but for mechanical systems Kirchhoff's equation of energy implies that the rate of the internal energy is identical to the stress power, namely,

$$\rho_0 \frac{\partial \bar{U}}{\partial t} = \mathbf{P} \cdot \dot{\mathbf{F}}. \quad (33)$$

Since the second integral in (32) vanishes owing to Kirchhoff's equation of energy, we obtain the Bubnov–Galerkin weighted residual form. Thus, we have the relation between the stress power and the specific internal energy density in mechanical systems as shown in (33).

#### 4. Continuous-body dynamical systems and the second law of thermodynamics

According to the second law of thermodynamics, the rate of the total entropy of the thermomechanical system is equal to or greater than the entropy input rate:

$$\frac{d}{dt} \int_{\mathfrak{B}} \rho_0(\mathbf{X}) S(\mathbf{X}, t) dV \geq \int_{\mathfrak{B}} \rho_0(\mathbf{X}) \frac{R(\mathbf{X}, t)}{\Theta(\mathbf{X}, t)} dV - \int_{\partial\mathfrak{B}} \frac{\hat{\mathbf{N}} \cdot \mathbf{Q}(\mathbf{X}, t)}{\Theta(\mathbf{X}, t)} dA, \quad (34)$$

where  $S(\mathbf{X}, t)$  is the specific entropy and  $\Theta(\mathbf{X}, t)$  is the absolute temperature. This relation is often called the Clausius–Duhem inequality. In an adiabatic process without heat sources, the total entropy should be nonnegative:

$$\frac{d}{dt} \int_{\mathfrak{B}} \rho_0(\mathbf{X}) S(\mathbf{X}, t) dV \geq 0. \quad (35)$$

An application of Gauss’s theorem yields the local form of the principle of entropy inequality:

$$\rho_0(\mathbf{X}) \frac{\partial S(\mathbf{X}, t)}{\partial t} - \rho_0(\mathbf{X}) \frac{R(\mathbf{X}, t)}{\Theta(\mathbf{X}, t)} + \nabla \cdot \frac{\mathbf{Q}(\mathbf{X}, t)}{\Theta(\mathbf{X}, t)} \geq 0. \quad (36)$$

The sum of terms on the left-hand side is the rate of entropy production. Use of Kirchhoff’s equation of energy yields

$$\mathbf{P} \cdot \dot{\mathbf{F}} - \rho_0 \frac{\partial \bar{U}}{\partial t} + \rho_0(\mathbf{X}) \Theta(\mathbf{X}, t) \frac{\partial S(\mathbf{X}, t)}{\partial t} - \frac{\mathbf{Q}(\mathbf{X}, t) \cdot \nabla \Theta(\mathbf{X}, t)}{\Theta(\mathbf{X}, t)} \geq 0. \quad (37)$$

Since the entropy production by heat flux should be positive [Coleman and Noll 1963], we have

$$-\frac{\mathbf{Q}(\mathbf{X}, t) \cdot \nabla \Theta(\mathbf{X}, t)}{\Theta(\mathbf{X}, t)} \geq 0. \quad (38)$$

Hence (37) can be rewritten as

$$\mathcal{D}_{\text{int}} = \mathbf{P} \cdot \dot{\mathbf{F}} - \rho_0 \frac{\partial \bar{U}}{\partial t} + \rho_0(\mathbf{X}) \Theta(\mathbf{X}, t) \frac{\partial S(\mathbf{X}, t)}{\partial t} \geq 0; \quad (39)$$

here  $\mathcal{D}_{\text{int}}$ , the internal dissipation, vanishes if and only if the process is reversible. In view of (39), for mechanical systems only, the internal dissipation can be rewritten as

$$\int_{\mathfrak{B}} \mathcal{D}_{\text{int}} dV = \mathcal{P}_{\text{input}} - \frac{dE}{dt}, \quad (40)$$

where  $E = \mathcal{K} + U$  is the sum of the kinetic energy and the internal energy. In the literature,  $E$  is called the total energy, but we reserve this term for a more comprehensive quantify; see (50).

In a thermomechanical system, the Helmholtz free energy  $\Psi$  satisfies

$$\frac{\partial \Psi}{\partial \Theta} = -S. \quad (41)$$

Via the Legendre transformation, this equation leads to the relation between the specific internal energy function and the Helmholtz free energy:

$$\bar{U}(\Phi, S) = \Psi(\Phi, \Theta) + \Theta S, \quad (42)$$

where  $\Phi$  denotes an internal state variable. Substituting (42) into (39) leads to

$$\mathcal{D}_{\text{int}} = \mathbf{P} \cdot \dot{\mathbf{F}} - \rho_0 \frac{\partial \Psi}{\partial t} - \rho_0 S(\mathbf{X}, t) \frac{\partial \Theta(\mathbf{X}, t)}{\partial t} \geq 0. \quad (43)$$

In the case of no entropy production or in an isothermal process, this reduces to

$$\mathcal{D}_{\text{int}} = \mathbf{P} \cdot \dot{\mathbf{F}} - \rho_0 \frac{\partial \Psi}{\partial t} \geq 0. \quad (44)$$

In a thermodynamic process, a material whose mechanical behavior shows no internal dissipation, is called perfect [Truesdell and Noll 2004, p. 303]. Then, we have the equality

$$\mathcal{D}_{\text{int}} = \mathbf{P} \cdot \dot{\mathbf{F}} - \rho_0 \frac{\partial \Psi}{\partial t} = 0. \quad (45)$$

The first Piola–Kirchhoff stress tensor is the thermodynamics force work-conjugate to the deformation gradient tensor:

$$\mathbf{P} = \rho_0 \frac{\partial \Psi(\mathbf{F})}{\partial \mathbf{F}}. \quad (46)$$

In a reversible process this equation also holds, so for mechanical systems we have

$$\mathbf{P} \cdot \dot{\mathbf{F}} = \rho_0 \frac{\partial \Psi}{\partial t} = \rho_0 \frac{\partial U}{\partial t} = \frac{\partial W}{\partial t}, \quad (47)$$

where  $W$  stands for the elastic potential energy. Regardless of whether the system is thermomechanical or mechanical, (29) can be written as

$$\frac{d\mathcal{H}}{dt} + \int_{\mathfrak{B}} \rho_0 \frac{\partial \Psi}{\partial t} dV = \int_{\mathfrak{B}} \rho_0 \mathbf{B}(\mathbf{X}, t) \cdot \dot{\boldsymbol{\varphi}}(\mathbf{X}, t) dV + \int_{\partial \mathfrak{B}_\sigma} \bar{\mathbf{T}}(\mathbf{X}, t) \cdot \dot{\boldsymbol{\varphi}}(\mathbf{X}, t) dA. \quad (48)$$

Thus the sum of the rate of the kinetic energy and the rate of the internal energy equals the power input.

### 5. The theorem of expended power and scalar description formalisms equivalent to the Cauchy equations of motion: continuous-body dynamical systems

Still under the assumption of scleronomic systems, the power input is

$$\mathcal{P}_{\text{input}} = \int_{\mathfrak{B}} \rho_0 \mathbf{B}(\mathbf{X}) \cdot \dot{\boldsymbol{\varphi}}(\mathbf{X}, t) dV + \int_{\partial \mathfrak{B}_\sigma} \bar{\mathbf{T}}(\mathbf{X}) \cdot \dot{\boldsymbol{\varphi}}(\mathbf{X}, t) dA = -\frac{d\Pi_{\text{ext}}}{dt}. \quad (49)$$

In such a system the external loads, including surface tractions and body forces, are dead loads. Therefore, the system is conservative in the sense that the total energy, which we defined as the sum of the kinetic energy  $\mathcal{H}(\dot{\boldsymbol{\varphi}}) : \mathbf{T}_\varphi \mathcal{C} \rightarrow \mathbb{R}$  and the total potential energy  $\mathcal{U}(\boldsymbol{\varphi}) : \mathcal{C} \rightarrow \mathbb{R}$ , is conserved. The body forces and tractions above are prescribed; as a result, external potential energies do exist. In view of (48) and (49), the theorem of expended power for perfect continuum materials has the following expression in terms of a naturally defined total energy:

$$\frac{d\mathcal{E}(\boldsymbol{\varphi}, \dot{\boldsymbol{\varphi}})}{dt} = 0, \quad \mathcal{E}(\boldsymbol{\varphi}, \dot{\boldsymbol{\varphi}}) = \mathcal{H}(\dot{\boldsymbol{\varphi}}) + \mathcal{U}(\boldsymbol{\varphi}), \quad \mathcal{U} = \Pi_{\text{int}} + \Pi_{\text{ext}}. \quad (50)$$

Here  $\mathcal{U}$  denotes the total potential energy and the internal and external potential energy are defined as

$$\Pi_{\text{int}} = \int_{\mathfrak{B}} \rho_0 \Psi(\mathbf{F}) dV, \quad \Pi_{\text{ext}} = -\int_{\mathfrak{B}} \rho_0 \mathbf{B}(\mathbf{X}) \cdot \boldsymbol{\varphi}(\mathbf{X}, t) dV - \int_{\partial \mathfrak{B}_\sigma} \bar{\mathbf{T}}(\mathbf{X}) \cdot \boldsymbol{\varphi}(\mathbf{X}, t) dA, \quad (51)$$

where  $\Psi(\mathbf{F})$  is the Helmholtz free energy per unit mass in homogeneous materials. The autonomous total energy is defined on the tangent bundle to the configuration space,  $\mathbf{T}\mathcal{C} := \{(\boldsymbol{\varphi}, \dot{\boldsymbol{\varphi}}) \mid \boldsymbol{\varphi} \in \mathcal{C}, \dot{\boldsymbol{\varphi}} \in \mathbf{T}_\varphi \mathcal{C}\}$ , and can be written as

$$\mathcal{E}(\boldsymbol{\varphi}, \dot{\boldsymbol{\varphi}}) = \int_{\mathfrak{B}} \bar{\mathcal{E}}(\boldsymbol{\varphi}, \dot{\boldsymbol{\varphi}}, \mathbf{F}) dV - \int_{\partial \mathfrak{B}_\sigma} \bar{\mathbf{T}}(\mathbf{X}) \cdot \boldsymbol{\varphi}(\mathbf{X}, t) dA, \quad (52)$$

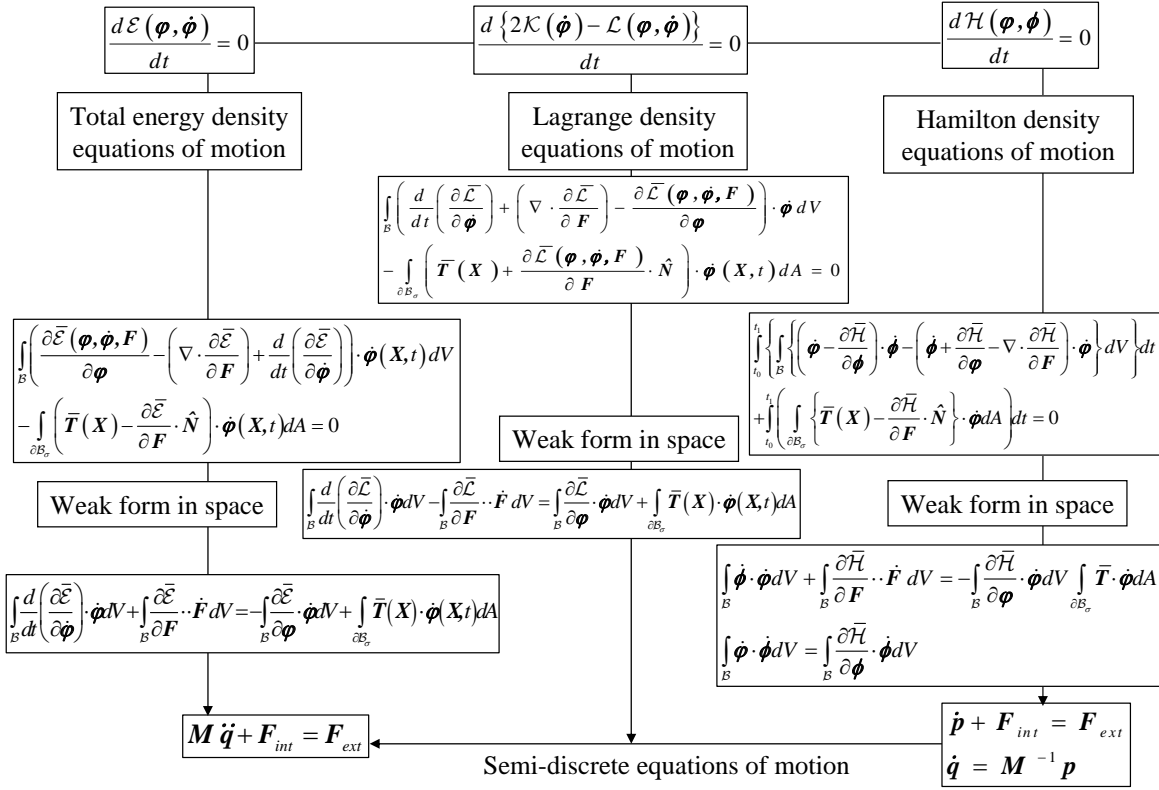


**Figure 2.** The theorem of expended power yields the strong and weak forms for elastodynamics; and their equivalence is shown within the Lagrangian, Hamiltonian, and Total Energy frameworks. (See also the Appendix.)

where the total energy density function  $\bar{\mathcal{E}}(\boldsymbol{\varphi}, \dot{\boldsymbol{\varphi}}, \mathbf{F})$  is defined as

$$\bar{\mathcal{E}}(\boldsymbol{\varphi}, \dot{\boldsymbol{\varphi}}, \mathbf{F}) = \frac{1}{2} \rho_0 \dot{\boldsymbol{\varphi}} \cdot \dot{\boldsymbol{\varphi}} + \rho_0 \Psi(\mathbf{F}) - \rho_0 \mathbf{B}(X) \cdot \boldsymbol{\varphi}. \quad (53)$$

Next, we derive the strong form representation from (50). We first give the scalar description formalism for deriving the total energy equation of motion from the theorem of expended power. By the chain rule, the rate of the total energy density function is

$$\frac{d\bar{\mathcal{E}}(\boldsymbol{\varphi}, \dot{\boldsymbol{\varphi}}, \mathbf{F})}{dt} = \frac{\partial \bar{\mathcal{E}}}{\partial \boldsymbol{\varphi}} \cdot \dot{\boldsymbol{\varphi}} + \frac{\partial \bar{\mathcal{E}}}{\partial \dot{\boldsymbol{\varphi}}} \cdot \ddot{\boldsymbol{\varphi}} + \frac{\partial \bar{\mathcal{E}}}{\partial \mathbf{F}} \cdot \dot{\mathbf{F}}. \quad (54)$$

The last term on the right can be represented as

$$\frac{\partial \bar{\mathcal{E}}}{\partial \mathbf{F}} \cdot \dot{\mathbf{F}} = \frac{\partial \bar{\mathcal{E}}}{\partial \mathbf{F}} \cdot \nabla \dot{\boldsymbol{\varphi}} = \nabla \cdot \left( \dot{\boldsymbol{\varphi}} \cdot \frac{\partial \bar{\mathcal{E}}}{\partial \mathbf{F}} \right) - \left( \nabla \cdot \frac{\partial \bar{\mathcal{E}}}{\partial \mathbf{F}} \right) \cdot \dot{\boldsymbol{\varphi}}. \quad (55)$$

Besides, we have

$$\frac{\partial \bar{\mathcal{E}}}{\partial \dot{\boldsymbol{\varphi}}} \cdot \ddot{\boldsymbol{\varphi}} = \frac{d}{dt} \left( \frac{\partial \bar{\mathcal{E}}}{\partial \dot{\boldsymbol{\varphi}}} \cdot \dot{\boldsymbol{\varphi}} \right) - \frac{d}{dt} \left( \frac{\partial \bar{\mathcal{E}}}{\partial \dot{\boldsymbol{\varphi}}} \right) \cdot \dot{\boldsymbol{\varphi}} = \frac{d}{dt} \left( \frac{\partial \bar{\mathcal{E}}}{\partial \dot{\boldsymbol{\varphi}}} \right) \cdot \dot{\boldsymbol{\varphi}} \quad (56)$$



because the total energy density function is quadratic in  $\dot{\boldsymbol{\varphi}}$ . Substituting (55) and (56) into (54), we find

$$\frac{d\bar{\mathcal{E}}(\boldsymbol{\varphi}, \dot{\boldsymbol{\varphi}}, \mathbf{F})}{dt} = \left( \frac{\partial \bar{\mathcal{E}}(\boldsymbol{\varphi}, \dot{\boldsymbol{\varphi}}, \mathbf{F})}{\partial \boldsymbol{\varphi}} - \left( \nabla \cdot \frac{\partial \bar{\mathcal{E}}}{\partial \mathbf{F}} \right) + \frac{d}{dt} \frac{\partial \bar{\mathcal{E}}}{\partial \dot{\boldsymbol{\varphi}}} \right) \cdot \dot{\boldsymbol{\varphi}} + \nabla \cdot \left( \dot{\boldsymbol{\varphi}} \cdot \frac{\partial \bar{\mathcal{E}}}{\partial \mathbf{F}} \right). \quad (57)$$

By Gauss's theorem, the last term on the right yields

$$\int_{\mathfrak{B}} \nabla \cdot \left( \dot{\boldsymbol{\varphi}} \cdot \frac{\partial \bar{\mathcal{E}}}{\partial \mathbf{F}} \right) dV = \int_{\partial \mathfrak{B}_\sigma} \dot{\boldsymbol{\varphi}} \cdot \frac{\partial \bar{\mathcal{E}}}{\partial \mathbf{F}} \cdot \hat{\mathbf{N}} dA. \quad (58)$$

In view of (57) and (58), we obtain from (50)

$$\int_{\mathfrak{B}} \left( \frac{\partial \bar{\mathcal{E}}(\boldsymbol{\varphi}, \dot{\boldsymbol{\varphi}}, \mathbf{F})}{\partial \boldsymbol{\varphi}} - \left( \nabla \cdot \frac{\partial \bar{\mathcal{E}}}{\partial \mathbf{F}} \right) + \frac{d}{dt} \frac{\partial \bar{\mathcal{E}}}{\partial \dot{\boldsymbol{\varphi}}} \right) \cdot \dot{\boldsymbol{\varphi}}(\mathbf{X}, t) dV - \int_{\partial \mathfrak{B}_\sigma} \left( \bar{\mathbf{T}}(\mathbf{X}) - \frac{\partial \bar{\mathcal{E}}}{\partial \mathbf{F}} \cdot \hat{\mathbf{N}} \right) \cdot \dot{\boldsymbol{\varphi}}(\mathbf{X}, t) dA = 0. \quad (59)$$

This equation takes the modified Bubnov–Galerkin weighted residual form [Mikhlin 1964] involving the strong form, namely, the governing equations and the natural boundary conditions are both included. Since the generalized velocities are arbitrary within the two open sets, we have the governing equations of motion in terms of the total energy density function as

$$\frac{d}{dt} \left( \frac{\partial \bar{\mathcal{E}}}{\partial \dot{\boldsymbol{\varphi}}} \right) = \left( \nabla \cdot \frac{\partial \bar{\mathcal{E}}}{\partial \mathbf{F}} \right) - \frac{\partial \bar{\mathcal{E}}(\boldsymbol{\varphi}, \dot{\boldsymbol{\varphi}}, \mathbf{F})}{\partial \boldsymbol{\varphi}} \quad \text{in } \mathbf{X} \in \mathfrak{B}, \quad (60)$$

subject to the traction boundary condition

$$\bar{\mathbf{T}}(\mathbf{X}) - \frac{\partial \bar{\mathcal{E}}}{\partial \mathbf{F}} \cdot \hat{\mathbf{N}} = 0 \quad \text{on } \mathbf{X} \in \partial \mathfrak{B}_\sigma. \quad (61)$$

Within the Lagrangian framework, the theorem of expended power for perfect continuum materials reduces to

$$\frac{d\{2\mathcal{H}(\dot{\boldsymbol{\varphi}}) - \mathcal{L}(\boldsymbol{\varphi}, \dot{\boldsymbol{\varphi}})\}}{dt} = 0, \quad \mathcal{L}(\boldsymbol{\varphi}, \dot{\boldsymbol{\varphi}}) = \mathcal{H}(\dot{\boldsymbol{\varphi}}) - \mathcal{U}(\boldsymbol{\varphi}), \quad (62)$$

the term in braces being again Jacobi's integral. On the tangent bundle  $T\mathcal{C} = \{(\boldsymbol{\varphi}, \dot{\boldsymbol{\varphi}}) \mid \boldsymbol{\varphi} \in \mathcal{C}, \dot{\boldsymbol{\varphi}} \in T_{\boldsymbol{\varphi}}\mathcal{C}\}$ , the autonomous Lagrangian  $\mathcal{L}(\boldsymbol{\varphi}, \dot{\boldsymbol{\varphi}}) : T\mathcal{C} \rightarrow \mathbb{R}$  is defined as the kinetic energy minus the total potential energy, and so can be written

$$\mathcal{L}(\boldsymbol{\varphi}, \dot{\boldsymbol{\varphi}}) = \int_{\mathfrak{B}} \bar{\mathcal{L}}(\boldsymbol{\varphi}, \dot{\boldsymbol{\varphi}}, \mathbf{F}) dV + \int_{\partial \mathfrak{B}_\sigma} \bar{\mathbf{T}}(\mathbf{X}) \cdot \boldsymbol{\varphi}(\mathbf{X}, t) dA, \quad (63)$$

where the Lagrangian density function  $\bar{\mathcal{L}}(\boldsymbol{\varphi}, \dot{\boldsymbol{\varphi}}, \mathbf{F})$  is defined as

$$\bar{\mathcal{L}}(\boldsymbol{\varphi}, \dot{\boldsymbol{\varphi}}, \mathbf{F}) = \frac{1}{2} \rho_0 \dot{\boldsymbol{\varphi}} \cdot \dot{\boldsymbol{\varphi}} - \rho_0 \Psi(\mathbf{F}) + \rho_0 \mathbf{B}(\mathbf{X}) \cdot \boldsymbol{\varphi}. \quad (64)$$

Likewise, in terms of the Lagrangian density function, (62) can be rewritten as

$$\int_{\mathfrak{B}} \left( \frac{d}{dt} \frac{\partial \bar{\mathcal{L}}}{\partial \dot{\boldsymbol{\varphi}}} + \nabla \cdot \frac{\partial \bar{\mathcal{L}}}{\partial \mathbf{F}} - \frac{\partial \bar{\mathcal{L}}(\boldsymbol{\varphi}, \dot{\boldsymbol{\varphi}}, \mathbf{F})}{\partial \boldsymbol{\varphi}} \right) \cdot \dot{\boldsymbol{\varphi}} dV - \int_{\partial \mathfrak{B}_\sigma} \left( \bar{\mathbf{T}}(\mathbf{X}) + \frac{\partial \bar{\mathcal{L}}(\boldsymbol{\varphi}, \dot{\boldsymbol{\varphi}}, \mathbf{F})}{\partial \mathbf{F}} \cdot \hat{\mathbf{N}} \right) \cdot \dot{\boldsymbol{\varphi}}(\mathbf{X}, t) dA = 0. \quad (65)$$

Since the generalized velocities are arbitrary in the body and on the traction boundary surface, we have the governing equations in terms of the Lagrangian density function as

$$\frac{d}{dt} \frac{\partial \bar{\mathcal{L}}}{\partial \dot{\boldsymbol{\phi}}} + \left( \nabla \cdot \frac{\partial \bar{\mathcal{L}}}{\partial \mathbf{F}} \right) - \frac{\partial \bar{\mathcal{L}}(\boldsymbol{\varphi}, \dot{\boldsymbol{\phi}}, \mathbf{F})}{\partial \boldsymbol{\varphi}} = 0 \quad \text{in } \mathbf{X} \in \mathcal{B}, \quad (66)$$

subject to the traction boundary condition

$$\bar{\mathbf{T}}(\mathbf{X}) + \frac{\partial \bar{\mathcal{L}}(\boldsymbol{\varphi}, \dot{\boldsymbol{\phi}}, \mathbf{F})}{\partial \mathbf{F}} \cdot \hat{\mathbf{N}} = 0 \quad \text{on } \mathbf{X} \in \partial \mathcal{B}_\sigma. \quad (67)$$

Equation (66) represents the Lagrangian density equations of motion, and is identical to Cauchy's equation of motion.

In addition, within the Hamiltonian framework involving the canonical momentum as a new dependent variable  $\boldsymbol{\phi} \in \mathbf{T}_\varphi^* \mathcal{C}$  belonging to the cotangent space, we have

$$\boldsymbol{\phi} = \frac{\partial \bar{\mathcal{L}}(\boldsymbol{\varphi}, \dot{\boldsymbol{\phi}}, \mathbf{F})}{\partial \dot{\boldsymbol{\phi}}} = \rho_0 \dot{\boldsymbol{\phi}}(\mathbf{X}, t). \quad (68)$$

In view of this, we may define the Hamiltonian density function via the Legendre transformation

$$\bar{\mathcal{H}}(\boldsymbol{\varphi}, \boldsymbol{\phi}, \mathbf{F}) = \boldsymbol{\phi} \cdot \dot{\boldsymbol{\phi}} - \bar{\mathcal{L}}(\boldsymbol{\varphi}, \dot{\boldsymbol{\phi}}, \mathbf{F}), \quad (69)$$

where the Hamiltonian density function in view of (64) is given by

$$\bar{\mathcal{H}}(\boldsymbol{\varphi}, \boldsymbol{\phi}, \mathbf{F}) = \frac{1}{2\rho_0} \boldsymbol{\phi} \cdot \boldsymbol{\phi} + \rho_0 \Psi(\mathbf{F}) - \rho_0 \mathbf{B}(\mathbf{X}) \cdot \boldsymbol{\varphi}. \quad (70)$$

On the cotangent bundle (phase space)  $\mathbf{T}^* \mathcal{C} = \{(\boldsymbol{\varphi}, \boldsymbol{\phi}) \mid \boldsymbol{\varphi} \in \mathcal{C} \text{ and } \boldsymbol{\phi} \in \mathbf{T}_\varphi^* \mathcal{C}\}$ , an infinite-dimensional space, the autonomous Hamiltonian  $\mathcal{H}(\boldsymbol{\varphi}, \boldsymbol{\phi}) : \mathbf{T}^* \mathcal{C} \rightarrow \mathbb{R}$  can be defined as

$$\mathcal{H}(\boldsymbol{\varphi}, \boldsymbol{\phi}) = \int_{\mathcal{B}} \bar{\mathcal{H}}(\boldsymbol{\varphi}, \boldsymbol{\phi}, \mathbf{F}) dV - \int_{\partial \mathcal{B}_\sigma} \bar{\mathbf{T}}(\mathbf{X}) \cdot \boldsymbol{\varphi}(\mathbf{X}, t) dA, \quad (71)$$

where the external forces are dead loads. Then, the theorem of expended power for perfect continuum materials yields

$$\frac{d\mathcal{H}(\boldsymbol{\varphi}, \boldsymbol{\phi})}{dt} = 0, \quad \mathcal{H}(\boldsymbol{\varphi}, \boldsymbol{\phi}) = \mathcal{K}(\boldsymbol{\phi}) + \mathcal{U}(\boldsymbol{\varphi}). \quad (72)$$

For conservative systems, the Hamiltonian is the kinetic energy plus the total potential energy, just like the total energy that we previously described. However, the preceding equation is true if and only if the continuous-body dynamical system is scleronomic (otherwise, the Hamiltonian is not the total energy). In terms of the Hamiltonian density function, (72) can be rewritten as

$$\begin{aligned} \frac{d\mathcal{H}}{dt} &= \int_{\mathcal{B}} \left( \left( \dot{\boldsymbol{\phi}} + \frac{\partial \bar{\mathcal{H}}}{\partial \boldsymbol{\varphi}} - \nabla \cdot \frac{\partial \bar{\mathcal{H}}}{\partial \mathbf{F}} \right) \cdot \frac{d\boldsymbol{\varphi}}{dt} + \left( \frac{\partial \bar{\mathcal{H}}}{\partial \boldsymbol{\phi}} - \dot{\boldsymbol{\phi}} \right) \cdot \frac{d\boldsymbol{\phi}}{dt} \right) dV - \int_{\partial \mathcal{B}_\sigma} \left( \bar{\mathbf{T}}(\mathbf{X}) - \frac{\partial \bar{\mathcal{H}}}{\partial \mathbf{F}} \cdot \hat{\mathbf{N}} \right) \cdot \dot{\boldsymbol{\phi}}(\mathbf{X}, t) dA \\ &= 0. \end{aligned} \quad (73)$$

In the Hamiltonian framework, generalized coordinates and generalized momentum are arbitrary. We readily observe that the rate of the autonomous Hamiltonian contains the strong form, namely, the Hamiltonian version of Cauchy's equations of motion and the traction boundary conditions:

$$\dot{\boldsymbol{\phi}} = -\frac{\partial \bar{\mathcal{H}}}{\partial \boldsymbol{\phi}} + \left( \nabla \cdot \frac{\partial \bar{\mathcal{H}}}{\partial \mathbf{F}} \right), \quad \dot{\boldsymbol{\phi}} = \frac{\partial \bar{\mathcal{H}}}{\partial \boldsymbol{\phi}} \quad \text{in } \mathbf{X} \in \mathfrak{B} \quad (74)$$

subject to the traction boundary condition

$$\bar{\mathbf{T}}(\mathbf{X}) - \frac{\partial \bar{\mathcal{H}}}{\partial \mathbf{F}} \cdot \hat{\mathbf{N}} = 0 \quad \text{on } \mathbf{X} \in \partial \mathfrak{B}_\sigma. \quad (75)$$

Equation (74) represents the Hamiltonian density equations of motion; they are differential equations of the first order in time.

## 6. Application of the proposed formulation to nonholonomic/nonconservative systems

The rate of the total energy, Jacobi integral, and Hamiltonian presented in (50), (62) and (72), respectively, reflects geometric nonlinearity. However, when the material undergoes contact or impact deformation, the system is no longer holonomic due to nonlinear contact boundary conditions. Furthermore, if the external tractions are not dead loads and the body forces are prescribed, an external potential energy for the tractions cannot be defined and the system is no longer conservative. (The external potential energy for the body forces can still be defined).

For nonconservative systems (using elastoplastic contact/impact problems as an illustration), with time-independent body forces, the theorem of expended power for perfect materials leads to

$$\frac{d\mathcal{E}(\boldsymbol{\varphi}, \dot{\boldsymbol{\varphi}})}{dt} = \int_{\partial \mathfrak{B}_\sigma} \bar{\mathbf{T}}(\mathbf{X}, t) \cdot \dot{\boldsymbol{\varphi}} dA, \quad \mathcal{E} = \mathcal{H}(\dot{\boldsymbol{\varphi}}) + \mathcal{U}(\boldsymbol{\varphi}), \quad \mathcal{U} = \Pi_{\text{int}} + \Pi_{\text{ext}} \quad (76)$$

with

$$\Pi_{\text{int}} = \int_{\mathfrak{B}} \rho_0 \frac{\partial \Psi}{\partial t} dV, \quad \Pi_{\text{ext}} = - \int_{\mathfrak{B}} \rho_0 \mathbf{B}(\mathbf{X}) \cdot \boldsymbol{\varphi}(\mathbf{X}, t) dV;$$

that is, the autonomous total energy  $\mathcal{E}(\boldsymbol{\varphi}, \dot{\boldsymbol{\varphi}}) : \mathcal{T}\mathcal{C} \rightarrow \mathbb{R}$  is given by

$$\mathcal{E}(\boldsymbol{\varphi}, \dot{\boldsymbol{\varphi}}) = \int_{\mathfrak{B}} \bar{\mathcal{E}}(\boldsymbol{\varphi}, \dot{\boldsymbol{\varphi}}, \mathbf{F}) dV, \quad \bar{\mathcal{E}}(\boldsymbol{\varphi}, \dot{\boldsymbol{\varphi}}, \mathbf{F}) = \frac{1}{2} \rho_0 \dot{\boldsymbol{\varphi}} \cdot \dot{\boldsymbol{\varphi}} + \rho_0 \Psi(\mathbf{F}) - \rho_0 \mathbf{B}(\mathbf{X}) \cdot \boldsymbol{\varphi}. \quad (77)$$

External potential energies do not exist in the case of nonconservative forces; accordingly, the total energy in (76) is not conserved. Note that the total energy in (77) differs from the one in (52) in that the traction depends on time.

In the Lagrangian framework, the theorem of expended power for perfect materials becomes

$$\frac{d}{dt} \left[ \int_{\mathfrak{B}} \left( \frac{\partial \bar{\mathcal{L}}}{\partial \dot{\boldsymbol{\varphi}}} \cdot \dot{\boldsymbol{\varphi}} - \bar{\mathcal{L}} \right) dV \right] = \int_{\partial \mathfrak{B}_\sigma} \bar{\mathbf{T}}(\mathbf{X}, t) \cdot \dot{\boldsymbol{\varphi}} dA, \quad \mathcal{L}(\boldsymbol{\varphi}, \dot{\boldsymbol{\varphi}}) = \mathcal{H}(\dot{\boldsymbol{\varphi}}) - \mathcal{U}(\boldsymbol{\varphi}), \quad \mathcal{U} = \Pi_{\text{int}} + \Pi_{\text{ext}} \quad (78)$$

with

$$\Pi_{\text{int}} = \int_{\mathfrak{B}} \rho_0 \frac{\partial \Psi}{\partial t} dV, \quad \Pi_{\text{ext}} = - \int_{\mathfrak{B}} \rho_0 \mathbf{B}(\mathbf{X}) \cdot \boldsymbol{\varphi} dV,$$

that is, the autonomous Lagrangian  $\mathcal{L}(\boldsymbol{\varphi}, \dot{\boldsymbol{\varphi}}) : \mathcal{T}^{\mathcal{C}} \rightarrow \mathbb{R}$  is given by

$$\mathcal{L}(\boldsymbol{\varphi}, \dot{\boldsymbol{\varphi}}) = \int_{\mathcal{B}} \overline{\mathcal{L}}(\boldsymbol{\varphi}, \dot{\boldsymbol{\varphi}}, \mathbf{F}) dV, \quad \overline{\mathcal{L}}(\boldsymbol{\varphi}, \dot{\boldsymbol{\varphi}}, \mathbf{F}) = \frac{1}{2} \rho_0 \dot{\boldsymbol{\varphi}} \cdot \dot{\boldsymbol{\varphi}} - \rho_0 \Psi(\mathbf{F}) + \rho_0 \mathbf{B}(\mathbf{X}) \cdot \boldsymbol{\varphi}. \quad (79)$$

Jacobi's integral of the system in (78) is not conserved. Note that the Lagrangian in (79) is different from the one in (63).

Finally, in the Hamiltonian framework, the theorem of expended power for perfect materials becomes

$$\frac{d\mathcal{H}(\boldsymbol{\varphi}, \boldsymbol{\phi})}{dt} = \int_{\partial\mathcal{B}_\sigma} \overline{\mathbf{T}}(\mathbf{X}, t) \cdot \dot{\boldsymbol{\varphi}} dA, \quad \mathcal{H}(\boldsymbol{\varphi}, \boldsymbol{\phi}) = \mathcal{H}(\boldsymbol{\phi}) + \mathcal{U}(\boldsymbol{\varphi}), \quad \mathcal{U} = \Pi_{\text{int}} + \Pi_{\text{ext}}, \quad (80)$$

with

$$\Pi_{\text{int}} = \int_{\mathcal{B}} \rho_0 \frac{\partial \Psi}{\partial t} dV, \quad \Pi_{\text{ext}} = - \int_{\mathcal{B}} \rho_0 \mathbf{B}(\mathbf{X}) \cdot \boldsymbol{\varphi}(\mathbf{X}, t) dV;$$

that is, the autonomous Hamiltonian  $\mathcal{H}(\boldsymbol{\varphi}, \boldsymbol{\phi}) : \mathcal{T}^*\mathcal{C} \rightarrow \mathbb{R}$  is given by

$$\mathcal{H}(\boldsymbol{\varphi}, \boldsymbol{\phi}) = \int_{\mathcal{B}} \overline{\mathcal{H}}(\boldsymbol{\varphi}, \boldsymbol{\phi}, \mathbf{F}) dV, \quad \overline{\mathcal{H}}(\boldsymbol{\varphi}, \boldsymbol{\phi}, \mathbf{F}) = \frac{1}{2\rho_0} \boldsymbol{\phi} \cdot \boldsymbol{\phi} + \rho_0 \Psi(\mathbf{F}) - \rho_0 \mathbf{B}(\mathbf{X}) \cdot \boldsymbol{\varphi}. \quad (81)$$

For continuum dynamical systems with nonholonomic scleronomic constraints, the rate of the total energy, Jacobi's integral, and Hamiltonian is given by

$$\int_{\partial\mathcal{B}_\sigma} \overline{\mathbf{T}}(\mathbf{X}, t) \cdot \dot{\boldsymbol{\varphi}} dA + \int_{\partial\mathcal{B}_{\sigma_c}} \boldsymbol{\lambda} \cdot \frac{d\mathbf{g}}{dt} dA, \quad (82)$$

rather than 0 as in (50), (62) and (72). Here  $\boldsymbol{\lambda}$  is the Lagrange multiplier,  $\mathbf{g}$  is the impenetrability condition, and  $\partial\mathcal{B}_{\sigma_c}$  is the contact boundary surface.

We briefly discuss next the elastoplastic contact/impact finite element formulation in the context of the total energy framework with the theorem of expended power. An illustrative example will demonstrate the applicability of the proposed formulation to a wide range of continuum-dynamic problems.

Suppose that we consider two bodies  $\mathcal{B}^A, \mathcal{B}^B$  that are in contact: that is, the reference configuration is the open set  $\mathcal{B} = \mathcal{B}^A \cup \mathcal{B}^B$ , with  $\partial\mathcal{B} = \partial\mathcal{B}^A \cup \partial\mathcal{B}^B$ . The external loads are assumed to be dead loads. Each body has its own contact boundary surface respectively, namely,  $\partial_{\sigma_c}\mathcal{B} = \partial_{\sigma_c}\mathcal{B}^A \cup \partial_{\sigma_c}\mathcal{B}^B$ . As a salient feature of contact/impact problems, an impenetrability condition is imposed on the contact boundary surface, characterizing the contact boundary conditions as unknown and not prescribed. The impenetrability condition on the contact surface  $\partial_{\sigma_c}\mathcal{B}^A$  can be written as

$$(\boldsymbol{\varphi}(\mathbf{X}_c^A, t) - \boldsymbol{\varphi}(\mathbf{X}_c^B, t)) \cdot \hat{\mathbf{N}}_c^A(\mathbf{X}_c^A, t) = 0, \quad (83)$$

where  $\boldsymbol{\varphi}(\mathbf{X}_c^A, t) = \mathbf{X}_c^A + \mathbf{U}(\mathbf{X}_c^A, t)$ ,  $\mathbf{U}(\mathbf{X}_c^A, t)$  being the displacement of the contact point on the body  $\mathcal{B}^A$ , and  $\hat{\mathbf{N}}_c^A(\mathbf{X}_c^A, t)$  is the unit outward vector normal to the contact surface of  $\mathcal{B}^A$ .

In order to have an unconstrained variational formulation, we briefly consider the Lagrange multiplier method and the penalty method. For further details, see [Laursen 2002; Wriggers 2006].

In view of (83), the Lagrange multiplier method [Papadopoulos et al. 1995] leads to the following value for the rate of the total energy, Jacobi's integral, and Hamiltonian:

$$\int_{\partial\mathcal{B}_\sigma} \overline{\mathbf{T}}(\mathbf{X}, t) \cdot \dot{\boldsymbol{\varphi}} dA + \int_{\partial\mathcal{B}_c} \boldsymbol{\lambda} \cdot \hat{\mathbf{N}}_c^B(\mathbf{X}_c^A, t) \cdot (\dot{\boldsymbol{\varphi}}(\mathbf{X}_c^A, t) - \dot{\boldsymbol{\varphi}}(\mathbf{X}_c^B, t)) dA, \quad (84)$$

where  $\lambda$  is the Lagrange multiplier corresponding to the contact force vector.

In the penalty method, fairly popular in commercial hydro codes [Hallquist 1998; ABAQUS 2002], the impenetrability condition on the contact surface can be rewritten in terms of the stress tensor as

$$(\mathbf{P}_c^A(\mathbf{X}_c^A, t) - \mathbf{P}_c^B(\mathbf{X}_c^B, t)) \cdot \hat{\mathbf{N}}_c^A(\mathbf{X}_c^A, t) = \mathbf{T}_c^A(\mathbf{X}_c^A, t) + \mathbf{T}_c^B(\mathbf{X}_c^B, t) = 0, \quad (85)$$

where  $\mathbf{P}_c^A(\mathbf{X}_c^A, t)$ ,  $\mathbf{P}_c^B(\mathbf{X}_c^B, t)$  are the first Piola–Kirchhoff stress tensors and  $\mathbf{T}_c^A(\mathbf{X}_c^A, t)$ ,  $\mathbf{T}_c^B(\mathbf{X}_c^B, t)$  are the contact tractions, which can be calculated by use of some appropriate penalty parameter [Hallquist et al. 1985]. Then, Equation (84) for contact-impact problems with nonholonomic constraints gives the following value for the rate of the total energy, Jacobi’s integral, and Hamiltonian:

$$\int_{\partial\mathcal{B}_\sigma} \bar{\mathbf{T}}(\mathbf{X}, t) \cdot \dot{\boldsymbol{\varphi}} dA + \int_{\partial\mathcal{B}_c} (\mathbf{P}_c^A - \mathbf{P}_c^B) \cdot \hat{\mathbf{N}}_c^A \cdot \dot{\boldsymbol{\varphi}} dA, \quad (86)$$

where  $\mathbf{P}^A = -\bar{\mathcal{L}}/\partial\mathbf{F} = \bar{\mathcal{E}}/\partial\mathbf{F} = \bar{\mathcal{H}}/\partial\mathbf{F}$  on  $\partial_{\sigma_c}\mathcal{B}^A$  and  $\mathbf{P}^B = -\bar{\mathcal{L}}/\partial\mathbf{F} = \bar{\mathcal{E}}/\partial\mathbf{F} = \bar{\mathcal{H}}/\partial\mathbf{F}$  on  $\partial_{\sigma_c}\mathcal{B}^B$ , and  $\hat{\mathbf{N}}_c^A = -\hat{\mathbf{N}}_c^B$ .

If frictional contact on the contact surface is considered, the frictional contact force should be included in the external force on the right hand side. The contact forces can be obtained by several methods; for example we can consider the master-slave sideline algorithm [Hallquist et al. 1985] in the penalty method or the Lagrange multiplier in the Lagrange multiplier method [Papadopoulos et al. 1995].

Next, we often encounter material nonlinearity in contact/impact problems or in finite deformation problems [Simo and Hughes 1998]. For convenience, we consider hyperelastic-plastic material behavior [Belytschko et al. 2000; Simo and Hughes 1998], because we have used the total Lagrangian description [Hibbitt et al. 1970] in this work. From a phenomenological viewpoint, the multiplicative decomposition of the deformation gradient tensor [Lee and Liu 1967; Lee 1969; Simo and Hughes 1998; Nemat-Nasser 1982; Asaro and Lubarda 2006] has been used in the context of not only phenomenological polycrystalline plasticity, but also single crystal metal plasticity as follows:

$$\mathbf{F}(\mathbf{X}, t) = \mathbf{F}^e(\mathbf{X}, t) \cdot \mathbf{F}^p(\mathbf{X}, t). \quad (87)$$

This motivates one to introduce the intermediate configuration  $\bar{\mathcal{B}}$  between the reference configuration  $\mathcal{B}$  and the current configuration  $\mathcal{S}$ . In (87) the plastic part of the total deformation gradient tensor  $\mathbf{F}^p(\mathbf{X}, t)$  characterizes the plastic flow in the body, while the elastic part  $\mathbf{F}^e(\mathbf{X}, t)$  is the portion caused by stretching and rotation of the crystal lattice. The first Piola–Kirchhoff stress tensor in the intermediate configuration is

$$\bar{\mathbf{P}} = -\frac{\partial\bar{\mathcal{L}}}{\partial\mathbf{F}^e} = \frac{\partial\bar{\mathcal{E}}}{\partial\mathbf{F}^e} = \frac{\partial\bar{\mathcal{H}}}{\partial\mathbf{F}^e} = \rho_0 \frac{\partial\bar{\Psi}(\mathbf{F}^e)}{\partial\mathbf{F}^e} = \mathbf{F}^e \bar{\mathbf{S}}, \quad (88)$$

where  $\bar{\mathbf{S}}$  stands for the second Piola–Kirchhoff stress tensor in the intermediate configuration. Then, the relation of the stress tensors between configurations can be obtained by the push-forward or pull-back operations. For instance, the second Piola–Kirchhoff stress tensor in the reference configuration is

$$\mathbf{S} = \mathbf{F}^{p-1} \bar{\mathbf{S}} \cdot \mathbf{F}^{p-T} = \mathbf{F}^{-1} \bar{\mathbf{P}}. \quad (89)$$

In general, the radial return mapping scheme, as a stress update algorithm [Simo and Hughes 1998], can be employed to find the stress on the yield surface at every time step. Therefore, the internal force can be calculated by use of the updated stress.

### 7. Space-discrete finite element formulation in the three formalisms

We now present a novel numerical discretization approach that is significantly different from traditional practices for transient/dynamic applications. We must start by saying that from a practical point of view, it is impossible to choose the admissible trial functions satisfying both the natural boundary conditions (traction boundary conditions) and the essential boundary conditions. The weighted residual forms without natural boundary conditions are difficult to apply in practice, because the trial functions must satisfy both the essential and natural boundary conditions. The trial functions must fulfill this requirement because in the use of the weighted residual form the errors should be minimized in the satisfaction of the differential equations (governing equations) and boundary conditions. If the weighted residual form is given by the governing equations only, there is no mechanism by which errors in the satisfaction of the boundary conditions would be minimized. However, as shown in (59), (65) and (73), the rate of the total energy, Jacobi integral, and Hamiltonian presented in (50), (62) and (72) contains the weighted residual forms in terms of the governing equation and natural boundary conditions. Hence, as in the Ritz solution, which operates on the functional corresponding to the problem, the natural boundary conditions are contained implicitly in the functional; the rate equation contains implicitly both the governing equations and natural boundary conditions. In that sense, therefore, there is a mechanism by which the errors in the satisfaction of the governing equations and natural boundary conditions are minimized, when substituting the trial functions into the rate of the total energy, Jacobi integral, or Hamiltonian to discretize the space [Bathe 1982, p. 108; Cook et al. 2002, p. 136; Zienkiewicz et al. 2005, p. 61; Reddy 2006, p. 74]. As a consequence, the errors in the satisfaction of (59), (65) and (73) could be minimized by making use of the admissible trial functions satisfying the essential boundary conditions. Firstly, focusing on the total energy framework and the Lagrangian framework, the admissible trial functions  $\tilde{\varphi}$  are required to be piecewise continuous, but they should be continuous along the interelement boundaries. They may be represented by a linear combination of coordinate functions  $N_i^h(\mathbf{X})$  and generalized coordinates  $\tilde{\varphi}_i^h(t)$ :

$$\begin{aligned}\tilde{\varphi}(\mathbf{X}, t) &\equiv \tilde{\varphi}^h(\mathbf{X}, t) = \sum_{i=1}^{n_{\text{node}}} N_i^h(\mathbf{X}) \tilde{\varphi}_i^h(t) = \mathbf{N} \mathbf{q}, \\ \mathbf{q}(t) &= \{\tilde{\varphi}_1^h(t) \dots \tilde{\varphi}_{n_{\text{node}}}^h(t)\}^T \in Q \subset \mathbb{R}^{n_{\text{dof}}=3n_{\text{node}}}, \quad \mathbf{M} = \int_{\mathfrak{B}} \rho_0 \mathbf{N}^T \mathbf{N} dV.\end{aligned}\tag{90}$$

Note that the trial functions depend on space and time.

In the Hamiltonian framework, the admissible trial functions  $\tilde{\varphi}$  and  $\tilde{\phi}$  are required to be piecewise continuous, but they must be continuous along the interelement boundaries. They may be represented by a combination of interpolation functions and nodal variables:

$$\begin{aligned}\tilde{\varphi}(\mathbf{X}, t) &= \tilde{\varphi}^h(\mathbf{X}, t) = \sum_{i=1}^{n_{\text{node}}} N_i^h(\mathbf{X}) \tilde{\varphi}_i^h(t) = \mathbf{N} \mathbf{q}, \quad \tilde{\phi}(\mathbf{X}, t) = \tilde{\phi}^h(\mathbf{X}, t) = \sum_{i=1}^{n_{\text{node}}} N_i^h(\mathbf{X}) \tilde{\phi}_i^h(t) = \rho_0 \mathbf{N} \dot{\mathbf{q}}, \\ \mathbf{q}(t) &= \{\tilde{\varphi}_1^h(t) \dots \tilde{\varphi}_{n_{\text{node}}}^h(t)\}^T \in Q \subset \mathbb{R}^{3n_{\text{node}}}, \quad \mathbf{p}(t) = \mathbf{M} \dot{\mathbf{q}}(t) \in \mathbf{T}_q^* Q \subset \mathbb{R}^{3n_{\text{node}}}, \quad \mathbf{M} = \int_{\mathfrak{B}} \rho_0 \mathbf{N}^T \mathbf{N} dV.\end{aligned}\tag{91}$$

In continuum dynamics, a body can be approximated by a finite number of subdomains, say finite elements. Therefore, the whole domain is assumed to consist of an assemblage of finite elements. Directly starting the discretization process via the rate given in (50), (62) and (72), we may choose the same admissible trial functions in (90) and (91) as the assumed displacement field functions, without involving

test or weighting functions when the discrete total energy or Lagrangian differential operator, which is discussed below, is employed to obtain the semidiscrete second order in time differential equations.

In addition, we may choose the same admissible trial functions in (91) as the assumed displacement and canonical momentum field functions, without involving test or weighting functions when the discrete Hamiltonian differential operator, which is also discussed below, is employed to obtain the semidiscrete first order in time differential equations. For simplicity, we introduce a phase space with generalized coordinates and canonical momenta, denoted by  $T^*Q = \bigcup_{q \in Q} T_q^*Q$ , that is,

$$T^*Q := \left\{ (q, p) \mid \begin{array}{l} q(t) = \{\tilde{\varphi}_1^h(t) \dots \tilde{\varphi}_{n_{\text{node}}}^h(t)\}^T \in Q \subset \mathbb{R}^{n_{\text{dof}}=3n_{\text{node}}}, \\ p(t) = M\dot{q}(t) \in T_q^*Q \subset \mathbb{R}^{n_{\text{dof}}=3n_{\text{node}}}, \quad M = \int_{\mathcal{B}} \rho_0 N^T N dV \end{array} \right\}. \quad (92)$$

Upon substituting (90) into (50), the rate of the total energy can be discretized in space as follows

$$\frac{d\mathcal{E}^h(\tilde{\varphi}^h, \dot{\tilde{\varphi}}^h)}{dt} = \frac{d}{dt} \left\{ \int_{\mathcal{B}} \rho_0 \dot{\tilde{\varphi}}^h \cdot \dot{\tilde{\varphi}}^h dV - \mathcal{L}^h(\tilde{\varphi}^h, \dot{\tilde{\varphi}}^h) \right\} = 0, \quad (93)$$

where the autonomous space-discrete total energy for finite-dimensional systems is given by

$$\mathcal{E}^h(\tilde{\varphi}^h, \dot{\tilde{\varphi}}^h) = \int_{\mathcal{B}} \bar{\mathcal{E}}^h(\tilde{\varphi}^h, \dot{\tilde{\varphi}}^h, \tilde{F}^h) dV - \int_{\partial\mathcal{B}_\sigma} \bar{T}(X) \cdot \tilde{\varphi}^h(X, t) dA = \mathcal{E}^h(q, \dot{q}), \quad (94)$$

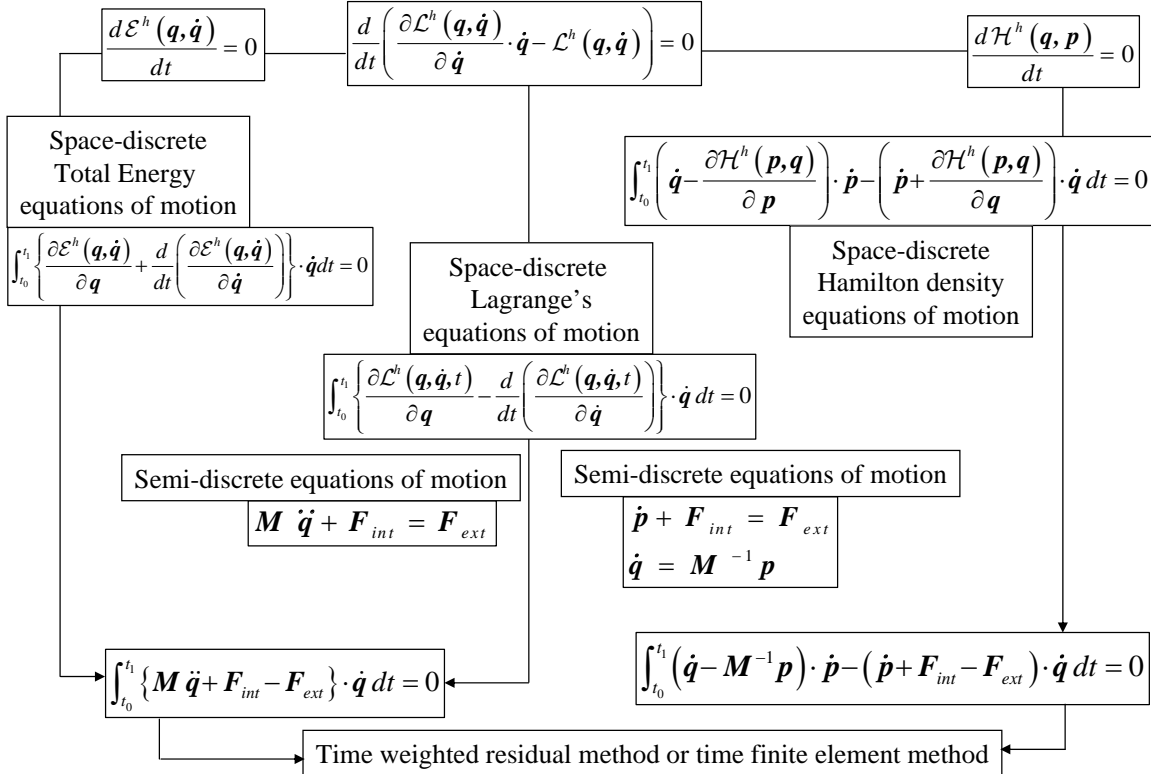


**Figure 3.** Space-discrete finite element formulation in the Lagrangian, Hamiltonian, and Total Energy frameworks, and their equivalence.

while the autonomous space-discrete Lagrangian for finite-dimensional systems is simply constructed as

$$\mathcal{L}^h(\tilde{\boldsymbol{\varphi}}^h, \dot{\tilde{\boldsymbol{\varphi}}^h}) = \int_{\mathcal{B}} \overline{\mathcal{L}}^h(\tilde{\boldsymbol{\varphi}}^h, \dot{\tilde{\boldsymbol{\varphi}}^h}, \tilde{\mathbf{F}}^h) dV + \int_{\partial\mathcal{B}_\sigma} \overline{\mathbf{T}}(\mathbf{X}) \cdot \dot{\tilde{\boldsymbol{\varphi}}^h}(\mathbf{X}, t) dA = \mathcal{L}^h(\mathbf{q}, \dot{\mathbf{q}}). \quad (95)$$

In terms of generalized coordinates within the total energy framework, (93) can be rewritten as

$$\frac{d\mathcal{E}^h(\mathbf{q}, \dot{\mathbf{q}})}{dt} = \left\{ \frac{\partial\mathcal{E}^h(\mathbf{q}, \dot{\mathbf{q}})}{\partial\mathbf{q}} + \frac{d}{dt} \left( \frac{\partial\mathcal{E}^h(\mathbf{q}, \dot{\mathbf{q}})}{\partial\dot{\mathbf{q}}} \right) \right\} \cdot \dot{\mathbf{q}} = 0, \quad (96)$$

where the space-discrete total energy in the direct notation is given by

$$\begin{aligned} \mathcal{E}^h(\mathbf{q}, \dot{\mathbf{q}}) &= \frac{1}{2} \dot{\mathbf{q}} \cdot \mathbf{M} \dot{\mathbf{q}} + \Pi_{\text{int}}^h - \mathbf{q} \cdot \mathbf{F}_{\text{ext}}, & \Pi_{\text{int}}^h &= \int_{\mathcal{B}} \rho_0 \Psi(\mathbf{F}^h) dV & \mathbf{M} &= \int_{\mathcal{B}} \rho_0 \mathbf{N}^T \mathbf{N} dV, \\ \frac{\partial\mathcal{E}^h(\mathbf{q}, \dot{\mathbf{q}})}{\partial\mathbf{q}} &= \mathbf{F}_{\text{int}} - \mathbf{F}_{\text{ext}} & \mathbf{F}_{\text{int}} &= \int_{\mathcal{B}} \overline{\mathbf{B}}^T \mathbf{P} dV, & \mathbf{F}_{\text{ext}} &= \int_{\mathcal{B}} \rho_0 \mathbf{N}^T \mathbf{B} dV + \int_{\partial\mathcal{B}_\sigma} \mathbf{N}^T \overline{\mathbf{T}} dA, \end{aligned} \quad (97)$$

where  $\overline{\mathbf{B}}$  denotes the strain matrix and  $\mathbf{N}$  the interpolation matrix.

Within the Lagrangian framework, in lieu of (96), we have

$$\frac{d}{dt} \left\{ \frac{\partial\mathcal{L}^h(\mathbf{q}, \dot{\mathbf{q}})}{\partial\dot{\mathbf{q}}} \cdot \dot{\mathbf{q}} - \mathcal{L}^h(\mathbf{q}, \dot{\mathbf{q}}) \right\} = \left\{ \frac{\partial\mathcal{L}^h(\mathbf{q}, \dot{\mathbf{q}})}{\partial\mathbf{q}} - \frac{d}{dt} \left( \frac{\partial\mathcal{L}^h(\mathbf{q}, \dot{\mathbf{q}})}{\partial\dot{\mathbf{q}}} \right) \right\} \cdot \dot{\mathbf{q}}(t) = 0, \quad (98)$$

where the space-discrete autonomous Lagrangian is constructed as follows

$$\begin{aligned} \mathcal{L}^h(\mathbf{q}, \dot{\mathbf{q}}) &= \frac{1}{2} \dot{\mathbf{q}} \cdot \mathbf{M} \dot{\mathbf{q}} - \Pi_{\text{int}}^h + \mathbf{q} \cdot \mathbf{F}_{\text{ext}}, & \Pi_{\text{int}}^h &= \int_{\mathcal{B}} \rho_0 \Psi(\mathbf{F}^h) dV, & \mathbf{M} &= \int_{\mathcal{B}} \rho_0 \mathbf{N}^T \mathbf{N} dV, \\ \frac{\partial\mathcal{L}^h(\mathbf{q}, \dot{\mathbf{q}})}{\partial\mathbf{q}} &= \mathbf{F}_{\text{ext}} - \mathbf{F}_{\text{int}}, & \mathbf{F}_{\text{int}} &= \int_{\mathcal{B}} \overline{\mathbf{B}}^T \mathbf{P} dV, & \mathbf{F}_{\text{ext}} &= \int_{\mathcal{B}} \rho_0 \mathbf{N}^T \mathbf{B} dV + \int_{\partial\mathcal{B}_\sigma} \mathbf{N}^T \overline{\mathbf{T}} dA. \end{aligned} \quad (99)$$

The admissible trial functions we used previously to discretize the rate of the total energy or Jacobi's integral are of class  $C^{m-1}(\mathcal{B})$ , like the trial functions applied to the principle of virtual work in (A.3). Because Equations (96) and (98) are equivalent to the discretization of the principle of virtual work in (A.3), discretizing the rate of the total energy or Jacobi's integral via admissible trial functions leads to the minimization of the errors arising from imposing the admissible trial functions into the weak form.

We next consider the Hamiltonian framework. Upon substituting (91) into (72), the rate of the Hamiltonian can be discretized in space as follows

$$\frac{d\mathcal{H}^h(\tilde{\boldsymbol{\varphi}}^h, \tilde{\boldsymbol{\varphi}}^h)}{dt} = 0, \quad (100)$$

where the space-discrete autonomous Hamiltonian for finite-dimensional systems can be simply constructed utilizing the Hamiltonian density function:

$$\mathcal{H}^h(\tilde{\boldsymbol{\varphi}}^h, \tilde{\boldsymbol{\varphi}}^h) = \int_{\mathcal{B}} \overline{\mathcal{H}}^h(\tilde{\boldsymbol{\varphi}}^h, \tilde{\boldsymbol{\varphi}}^h, \mathbf{F}^h) dV - \int_{\partial\mathcal{B}_\sigma} \overline{\mathbf{T}}(\mathbf{X}) \cdot \tilde{\boldsymbol{\varphi}}^h(\mathbf{X}, t) dA = \mathcal{H}^h(\mathbf{q}, \mathbf{p}). \quad (101)$$



In terms of the generalized coordinates and canonical momenta, (100) can be rewritten as

$$\frac{d\mathcal{H}^h(\mathbf{q}, \mathbf{p})}{dt} = \left( \dot{\mathbf{p}} + \frac{\partial \mathcal{H}^h}{\partial \mathbf{q}} \right) \cdot \dot{\mathbf{q}} - \left( \dot{\mathbf{q}} - \frac{\partial \mathcal{H}^h}{\partial \mathbf{p}} \right) \cdot \dot{\mathbf{p}} = 0, \quad (102)$$

where the space-discrete autonomous Hamiltonian consists of the space-discrete autonomous kinetic and potential energies:

$$\begin{aligned} \mathcal{H}^h(\mathbf{q}, \mathbf{p}) &= \mathcal{K}^h(\mathbf{p}) + \mathcal{U}^h(\mathbf{q}), & \mathcal{K}^h(\mathbf{p}) &= \frac{1}{2} \mathbf{p} \cdot \mathbf{M}^{-1} \mathbf{p}, & \mathcal{U}^h(\mathbf{q}) &= \Pi_{\text{int}}^h - \mathbf{q} \cdot \mathbf{F}_{\text{ext}}, \\ \Pi_{\text{int}}^h &= \int_{\mathcal{B}} \rho_0 \Psi(\mathbf{F}^h) dV, & \frac{\partial \mathcal{H}^h}{\partial \mathbf{q}} &= \mathbf{F}_{\text{int}} - \mathbf{F}_{\text{ext}}, & \mathbf{M} &= \int_{\mathcal{B}} \rho_0 \mathbf{N}^T \mathbf{N} dV, \\ \mathbf{F}_{\text{int}} &= \int_{\mathcal{B}} \bar{\mathbf{B}}^T \mathbf{P} dV, & \mathbf{F}_{\text{ext}} &= \int_{\mathcal{B}} \rho_0 \mathbf{N}^T \mathbf{B} dV + \int_{\partial \mathcal{B}_\sigma} \mathbf{N}^T \bar{\mathbf{T}} dA. \end{aligned} \quad (103)$$

Here  $\mathbf{P}$  is the first Piola–Kirchhoff stress tensor,  $\mathbf{B}$  the strain matrix, and  $\mathbf{N}$  the interpolation matrix. Note that the admissible trial functions we used previously to discretize the rate of the Hamiltonian are of class  $C^{m-1}(\mathcal{B})$  as the trial functions applied to the principle of virtual work in Equation (A.5) of the Appendix. We stress again that the discretization of the rate of the Hamiltonian as given in (100) corresponds to the discretization of the principle of virtual work in (A.6). Therefore, discretizing the rate of the Hamiltonian by the admissible trial functions automatically leads to the minimization of the errors arising from the approximating functions in association. The expression in (97), (99) and (103) holds regardless of whether material/geometric nonlinearity of the body exists or not.

In contrast to traditional practices (see the Appendix via the three formalisms but with “density forms of representation”, instead of standard Newton-based Cauchy equations of motion, as a starting point), for space discretization we simply adopt the following procedure. In view of (96), we introduce the discrete total energy differential operator

$$\mathfrak{E}_D = \frac{d}{dt} \frac{\partial}{\partial \dot{\mathbf{q}}} + \frac{\partial}{\partial \mathbf{q}} \quad (104)$$

by which the space-discrete finite element equations of motion can be readily obtained after constructing the space-discrete total energy which only entails the use of trial functions. Upon substituting the space-discrete total energy into the discrete total energy differential operator, we obtain

$$\mathfrak{E}_D(\mathcal{E}^h) = 0 \Rightarrow \frac{d}{dt} \frac{\partial \mathcal{E}^h}{\partial \dot{\mathbf{q}}} + \frac{\partial \mathcal{E}^h}{\partial \mathbf{q}} = 0, \quad (105)$$

where the dependent state variable is the space-discrete total energy. Likewise, in view of (98), we first introduce the discrete Lagrangian differential operator

$$\mathfrak{L}_D = \frac{d}{dt} \frac{\partial}{\partial \dot{\mathbf{q}}} - \frac{\partial}{\partial \mathbf{q}}; \quad (106)$$

upon substituting this operator into the discrete Lagrangian differential operator, we obtain

$$\mathfrak{L}_D(\mathcal{L}^h) = 0 \Rightarrow \frac{d}{dt} \frac{\partial \mathcal{L}^h}{\partial \dot{\mathbf{q}}} - \frac{\partial \mathcal{L}^h}{\partial \mathbf{q}} = 0, \quad (107)$$

where the dependent state variable is the space-discrete Lagrangian. *The discrete total energy and Lagrangian differential operators above imply that errors associated with governing equations and natural boundary conditions are implicitly minimized when the admissible trial functions satisfying the essential boundary conditions are chosen.* Thus, we readily have the space discrete finite element equations of motion governing the mechanical dynamic behavior of the continuous-body within the total energy and Lagrangian frameworks:

$$\mathbf{M}\ddot{\mathbf{q}} + \mathbf{F}_{\text{int}} - \mathbf{F}_{\text{ext}} = 0. \quad (108)$$

In view of (102), we introduce the discrete Hamiltonian differential operators

$$\mathfrak{H}_{D1} = \dot{\mathbf{p}} + \frac{\partial}{\partial \mathbf{q}}, \quad \mathfrak{H}_{D2} = \dot{\mathbf{q}} - \frac{\partial}{\partial \mathbf{p}} \quad (109)$$

and use them to obtain the space-discrete finite element equations of motion can be after constructing the space-discrete Hamiltonian, which again only entails the use of trial functions. Upon substituting the space-discrete Hamiltonian into the discrete Hamiltonian differential operator, we have

$$\mathfrak{H}_{D1}(\mathcal{H}^h) = 0 \Rightarrow \dot{\mathbf{p}} + \frac{\partial \mathcal{H}^h}{\partial \mathbf{q}} = 0, \quad \mathfrak{H}_{D2}(\mathcal{H}^h) = 0 \Rightarrow \dot{\mathbf{q}} - \frac{\partial \mathcal{H}^h}{\partial \mathbf{p}} = 0, \quad (110)$$

where the dependent state variable is the space-discrete autonomous Hamiltonian. This discussion shows that *errors associated with governing equations and natural boundary conditions are implicitly minimized when the admissible trial functions satisfying the essential boundary conditions are chosen.* The space-discrete finite element equations of motion governing the mechanical dynamic behavior of the continuous-body within the Hamiltonian framework are then

$$\dot{\mathbf{p}} + \mathbf{F}_{\text{int}} - \mathbf{F}_{\text{ext}} = 0, \quad \dot{\mathbf{q}} - \mathbf{M}^{-1} \mathbf{p} = 0. \quad (111)$$

In contrast, for elastostatics, the corresponding discrete differential operators are simply  $\mathfrak{E}_S = \partial/\partial \mathbf{q}$ ,  $\mathfrak{L}_S = -\partial/\partial \mathbf{q}$ ,  $\mathfrak{H}_S = \partial/\partial \mathbf{q}$ , and the finite element static equilibrium equations become

$$\mathfrak{E}_S(\mathcal{E}^h) = 0 \Rightarrow \frac{\partial \mathcal{E}^h}{\partial \mathbf{q}} = 0, \quad \mathfrak{L}_S(\mathcal{L}^h) = 0 \Rightarrow -\frac{\partial \mathcal{L}^h}{\partial \mathbf{q}} = 0, \quad \mathfrak{H}_S(\mathcal{H}^h) = 0 \Rightarrow \frac{\partial \mathcal{H}^h}{\partial \mathbf{q}} = 0. \quad (112)$$

These equations describe the now familiar representation with the generalized coordinates corresponding to the Ritz coefficients. The same remark about optimization made after (110) applies.

Integrating both sides of (96), (98) and (102) over  $t \in \mathbb{I} = [t_1, t_2]$ , we have

$$\begin{aligned} \mathcal{E}^h(\mathbf{q}, \dot{\mathbf{q}})|_{t=t_1} - \mathcal{E}^h(\mathbf{q}, \dot{\mathbf{q}})|_{t=t_2} &= \int_{t_1}^{t_2} (\mathbf{F}_{\text{ext}} - \mathbf{F}_{\text{int}} - \mathbf{M}\ddot{\mathbf{q}}) \cdot \dot{\mathbf{q}} dt = 0, \\ \left( \frac{\partial \mathcal{L}^h(\mathbf{q}, \dot{\mathbf{q}})}{\partial \dot{\mathbf{q}}} \cdot \dot{\mathbf{q}} - \mathcal{L}^h(\mathbf{q}, \dot{\mathbf{q}}) \right) \Big|_{t=t_1} - \left( \frac{\partial \mathcal{L}^h(\mathbf{q}, \dot{\mathbf{q}})}{\partial \dot{\mathbf{q}}} \cdot \dot{\mathbf{q}} - \mathcal{L}^h(\mathbf{q}, \dot{\mathbf{q}}) \right) \Big|_{t=t_2} &= \int_{t_1}^{t_2} (\mathbf{F}_{\text{ext}} - \mathbf{F}_{\text{int}} - \mathbf{M}\ddot{\mathbf{q}}) \cdot \dot{\mathbf{q}} dt = 0, \\ \mathcal{H}^h(\mathbf{q}, \mathbf{p})|_{t=t_2} - \mathcal{H}^h(\mathbf{q}, \mathbf{p})|_{t=t_1} &= \int_{t_1}^{t_2} ((\dot{\mathbf{p}} + \mathbf{F}_{\text{int}} - \mathbf{F}_{\text{ext}}) \cdot \dot{\mathbf{q}} - (\dot{\mathbf{q}} - \mathbf{M}^{-1} \mathbf{p}) \cdot \dot{\mathbf{p}}) dt = 0. \end{aligned} \quad (113)$$

The first two of these equations have the Bubnov–Galerkin weighted residual form in time, while the last has the hybrid weighted residual form in time. Instead of the virtual displacement, the equations in (113) take the generalized velocity as the weighting function. Hence, (113) can be used as a critical equation

to discretize the time domain. The first two equations in (113) may be regarded as an unconstrained generalized velocity formulation with a single dependent field variable in the time domain; thus we have the single-field generalized velocity problem within the total energy or Lagrangian framework. The last equation in (113) may be regarded as an unconstrained formulation with two dependent field variables in the time domain; thus we have the hybrid two-field problem within the Hamiltonian framework. In general, the time weighted-residual method [Tamma et al. 2000; Masuri et al. 2009a; 2009b] or the time finite element procedure [Simkins 1981; Aharoni and Bar-Yoseph 1992] can be applied to (113) for developing time stepping schemes.

In the presence of nonconservative forces such as contact forces on the contact boundary surfaces of nonholonomic systems, we have

$$\begin{aligned} \frac{d\mathcal{E}^h(\tilde{\boldsymbol{\varphi}}^h, \dot{\tilde{\boldsymbol{\varphi}}^h})}{dt} \text{ or } \frac{d}{dt} \left\{ \int_{\mathcal{B}} \rho_0 \dot{\tilde{\boldsymbol{\varphi}}^h} \cdot \dot{\tilde{\boldsymbol{\varphi}}^h} dV - \mathcal{L}^h(\tilde{\boldsymbol{\varphi}}^h, \dot{\tilde{\boldsymbol{\varphi}}^h}) \right\} \text{ or } \frac{d\mathcal{H}^h(\tilde{\boldsymbol{\varphi}}^h, \tilde{\boldsymbol{\phi}}^h)}{dt} \\ = \int_{\partial\mathcal{B}_\sigma} \bar{\mathbf{T}}(\mathbf{X}, t) \cdot \dot{\tilde{\boldsymbol{\varphi}}^h}(\mathbf{X}, t) dA + \int_{\partial\mathcal{B}_c} (\mathbf{P}_c^A - \mathbf{P}_c^B) \cdot \hat{\mathbf{N}}_c^A \cdot \dot{\tilde{\boldsymbol{\varphi}}^h} dA. \end{aligned} \quad (114)$$

Hence, Equations (96), (98) and (102) can be rewritten as

$$\begin{aligned} \frac{d\mathcal{E}^h(\mathbf{q}, \dot{\mathbf{q}})}{dt} &= \frac{d}{dt} \left( \frac{\partial \mathcal{E}^h}{\partial \dot{\mathbf{q}}} \right) + \frac{\partial \mathcal{E}^h}{\partial \mathbf{q}} = (\mathbf{F}_{\text{ext}} + \mathbf{F}_{\text{contact}}) \cdot \dot{\mathbf{q}}, \\ \frac{d}{dt} \left( \frac{\partial \mathcal{L}^h(\mathbf{q}, \dot{\mathbf{q}})}{\partial \dot{\mathbf{q}}} \cdot \dot{\mathbf{q}} - \mathcal{L}^h(\mathbf{q}, \dot{\mathbf{q}}) \right) &= \left( \frac{\partial \mathcal{L}^h(\mathbf{q}, \dot{\mathbf{q}})}{\partial \mathbf{q}} - \frac{d}{dt} \frac{\partial \mathcal{L}^h(\mathbf{q}, \dot{\mathbf{q}})}{\partial \dot{\mathbf{q}}} \right) \cdot \dot{\mathbf{q}} = (\mathbf{F}_{\text{ext}} + \mathbf{F}_{\text{contact}}) \cdot \dot{\mathbf{q}}, \\ \frac{d\mathcal{H}^h(\mathbf{q}, \mathbf{p})}{dt} &= \left( \dot{\mathbf{p}} + \frac{\partial \mathcal{H}^h}{\partial \mathbf{q}} \right) \cdot \dot{\mathbf{q}} - \left( \dot{\mathbf{q}} - \frac{\partial \mathcal{H}^h}{\partial \mathbf{p}} \right) \cdot \dot{\mathbf{p}} = (\mathbf{F}_{\text{ext}} + \mathbf{F}_{\text{contact}}) \cdot \dot{\mathbf{q}}, \end{aligned} \quad (115)$$

where  $\mathbf{F}_{\text{contact}}$  denotes the contact force vector. Integrating for both sides of each equation over  $t \in \mathbb{I} = [t_1, t_2]$  leads to

$$\begin{aligned} \mathcal{E}^h(\mathbf{q}, \dot{\mathbf{q}})|_{t=t_2} - \mathcal{E}^h(\mathbf{q}, \dot{\mathbf{q}})|_{t=t_1} &= \int_{t_1}^{t_2} ((\mathbf{M}\ddot{\mathbf{q}} + \mathbf{F}_{\text{int}}) \cdot \dot{\mathbf{q}}) dt = \int_{t_1}^{t_2} (\mathbf{F}_{\text{ext}} + \mathbf{F}_{\text{contact}}) \cdot \dot{\mathbf{q}} dt, \\ \left( \frac{\partial \mathcal{L}^h(\mathbf{q}, \dot{\mathbf{q}})}{\partial \dot{\mathbf{q}}} \cdot \dot{\mathbf{q}} - \mathcal{L}^h(\mathbf{q}, \dot{\mathbf{q}}) \right) \Big|_{t=t_2} - \left( \frac{\partial \mathcal{L}^h(\mathbf{q}, \dot{\mathbf{q}})}{\partial \dot{\mathbf{q}}} \cdot \dot{\mathbf{q}} - \mathcal{L}^h(\mathbf{q}, \dot{\mathbf{q}}) \right) \Big|_{t=t_1} \\ &= \int_{t_1}^{t_2} ((\mathbf{M}\ddot{\mathbf{q}} + \mathbf{F}_{\text{int}}) \cdot \dot{\mathbf{q}}) dt = \int_{t_1}^{t_2} (\mathbf{F}_{\text{ext}} + \mathbf{F}_{\text{contact}}) \cdot \dot{\mathbf{q}} dt, \\ \mathcal{H}^h(\mathbf{q}, \mathbf{p})|_{t=t_2} - \mathcal{H}^h(\mathbf{q}, \mathbf{p})|_{t=t_1} &= \int_{t_1}^{t_2} ((\dot{\mathbf{p}} + \mathbf{F}_{\text{int}}) \cdot \dot{\mathbf{q}} - (\dot{\mathbf{q}} - \mathbf{M}^{-1}\mathbf{p}) \cdot \dot{\mathbf{p}}) dt = \int_{t_1}^{t_2} (\mathbf{F}_{\text{ext}} + \mathbf{F}_{\text{contact}}) \cdot \dot{\mathbf{q}} dt. \end{aligned} \quad (116)$$

The first two of these equations above can be recast as

$$\int_{t_1}^{t_2} ((\mathbf{M}\ddot{\mathbf{q}} + \mathbf{F}_{\text{int}} - \mathbf{F}_{\text{ext}} - \mathbf{F}_{\text{contact}}) \cdot \dot{\mathbf{q}}) dt = 0, \quad (117)$$

which has the Bubnov–Galerkin weighted residual form in time. The weighting function is still the generalized velocity. Hence, (117) can be used as a critical equation to discretize the time domain.

Similarly, the last equation in (116) yields

$$\int_{t_1}^{t_2} ((\dot{\mathbf{p}} + \mathbf{F}_{\text{int}} - \mathbf{F}_{\text{ext}} - \mathbf{F}_{\text{contact}}) \cdot \dot{\mathbf{q}} - (\dot{\mathbf{q}} - \mathbf{M}^{-1} \mathbf{p}) \cdot \dot{\mathbf{p}}) dt = 0, \quad (118)$$

which has the hybrid weighted residual form in time. The weighting functions are the rates of the canonical coordinates. Hence, (118) can be also used as a critical equation to discretize the time domain [Aharoni and Bar-Yoseph 1992].

## 8. Numerical examples and illustrations

We consider two examples, the rotating bar and the Timoshenko beam, to illustrate the concepts discussed. We assume the systems are conservative and the materials undergo perfectly elastic deformations without producing entropy.

**8.1. Rotating bar.** Consider the dynamical behavior of a rotating bar described by the function  $J(x)$ , the polar moment of area about the center of the cross-section. As the dependent variable, we take the angle  $\theta(x, t)$  of rotation about the axial axis. The kinetic energy is purely rotational:

$$\mathcal{K}(\dot{\theta}) = \frac{1}{2} \int_l \rho J(x) \dot{\theta}^2 dx. \quad (119)$$

Let  $G$  be the shear modulus. The torque  $M_T(x, t)$  causing the bar to rotate can be written as

$$M_T(x, t) = GJ(x)\theta'(x, t), \quad \theta'(x, t) = \frac{\partial \theta(x, t)}{\partial x}. \quad (120)$$

The total potential energy of the bar subject to the distributed torque  $\bar{m}(x, t)$  is given by

$$\begin{aligned} \mathcal{U}(\theta) &= \frac{1}{2} \int_l M_T(x, t) \theta'(x, t) dx - \int_l \bar{m}_T(x) \theta(x, t) dx \\ &= \frac{1}{2} \int_l GJ(x) (\theta'(x, t))^2 dx - \int_l \bar{m}_T(x) \theta(x, t) dx. \end{aligned} \quad (121)$$

In view of (119) and (121), the Lagrangian is

$$\mathcal{L}(\theta, \dot{\theta}) = \int_l \bar{\mathcal{L}}(\theta, \dot{\theta}, \theta') dx + \int_l \bar{m}_T(x) \theta(x, t) dx, \quad (122)$$

where the Lagrangian density function is defined as

$$\bar{\mathcal{L}}(\theta, \dot{\theta}, \theta') = \frac{1}{2} \rho J(x) \dot{\theta}^2 - \frac{1}{2} GJ(x) (\theta'(x, t))^2. \quad (123)$$

The total energy is

$$\mathcal{E}(\theta, \dot{\theta}) = \int_l \bar{\mathcal{E}}(\theta, \dot{\theta}, \theta') dx - \int_l \bar{m}_T(x) \theta(x, t) dx, \quad (124)$$

where the total energy density function is defined as

$$\bar{\mathcal{E}}(\theta, \dot{\theta}, \theta') = \frac{1}{2} \rho J(x) \dot{\theta}^2 + \frac{1}{2} GJ(x) (\theta'(x, t))^2. \quad (125)$$

The total time derivative of the total energy is therefore

$$\frac{d\mathcal{E}(\theta, \dot{\theta}, \theta')}{dt} = \int_1 \frac{d\bar{\mathcal{E}}(\theta, \dot{\theta}, \theta')}{dt} dx - \int_1 \bar{m}_T(x) \theta(x, t) dx = 0, \quad (126)$$

or equivalently,

$$\frac{d\mathcal{E}(\theta, \dot{\theta}, \theta')}{dt} = \int_1 \left( \frac{\partial \bar{\mathcal{E}}}{\partial \theta} + \frac{d}{dt} \frac{\partial \bar{\mathcal{E}}}{\partial \dot{\theta}} - \frac{\partial}{\partial x} \frac{\partial \bar{\mathcal{E}}}{\partial \theta'} - \bar{m}_T(x) \right) \dot{\theta} dx + \frac{\partial \bar{\mathcal{E}}}{\partial \theta'} \dot{\theta} \Big|_0^l = 0. \quad (127)$$

Therefore, the governing equation is

$$\frac{d}{dt} \frac{\partial \bar{\mathcal{E}}}{\partial \dot{\theta}} = \frac{\partial}{\partial x} \frac{\partial \bar{\mathcal{E}}}{\partial \theta'} - \frac{\partial \bar{\mathcal{E}}}{\partial \theta} + \bar{m}_T(x), \quad (128)$$

subject to the boundary condition

$$\left( \frac{\partial \bar{\mathcal{E}}}{\partial \theta'} \dot{\theta} \right) \Big|_0^l = 0. \quad (129)$$

Turning now to the Lagrangian framework, the rate of Jacobi's integral is

$$\int_1 \left( \frac{d}{dt} \left( \frac{\partial \bar{\mathcal{L}}}{\partial \dot{\theta}} \right) \dot{\theta} - \frac{\partial \bar{\mathcal{L}}}{\partial \theta'} \dot{\theta}' \right) dx - \int_1 \bar{m}_T(x) \dot{\theta} dx = 0, \quad (130)$$

or equivalently

$$\int_1 \left( \frac{d}{dt} \frac{\partial \bar{\mathcal{L}}}{\partial \dot{\theta}} + \frac{\partial}{\partial x} \frac{\partial \bar{\mathcal{L}}}{\partial \theta'} - \bar{m}_T(x) \right) \dot{\theta} dx - \frac{\partial \bar{\mathcal{L}}}{\partial \theta'} \dot{\theta} \Big|_0^l = 0. \quad (131)$$

Therefore, the governing equation is

$$\frac{d}{dt} \frac{\partial \bar{\mathcal{L}}}{\partial \dot{\theta}} + \frac{\partial}{\partial x} \frac{\partial \bar{\mathcal{L}}}{\partial \theta'} - \bar{m}_T(x) = 0 \quad (132)$$

subject to the boundary condition

$$\left( \frac{\partial \bar{\mathcal{L}}}{\partial \theta'} \dot{\theta} \right) \Big|_0^l = 0. \quad (133)$$

Substituting the total energy or Lagrangian density function into the corresponding governing equations, we obtain the equation of motion

$$\rho J(x) \ddot{\theta} = \frac{\partial}{\partial x} \left( GJ(x) \frac{\partial \theta(x, t)}{\partial x} \right) + \bar{m}_T(x), \quad (134)$$

subject to the boundary condition

$$GJ(x) \frac{\partial \theta(x, t)}{\partial x} \dot{\theta}(x, t) \Big|_0^l = 0. \quad (135)$$

Within the Hamiltonian framework, the generalized momentum can be written

$$\phi = \frac{\partial \bar{L}}{\partial \dot{\theta}} = \rho J(x) \dot{\theta}. \quad (136)$$

We find the Hamiltonian density function by Legendre transformation:

$$\bar{\mathcal{H}}(\theta, \phi, \theta') = \phi \dot{\theta} - \bar{\mathcal{L}}(\theta, \dot{\theta}, \theta'). \quad (137)$$

The continuous Hamiltonian is therefore

$$\mathcal{H}(\theta, \phi) = \int_l \bar{\mathcal{H}}(\theta, \phi, \theta') dx - \int_l \bar{m}_T(x) \theta(x, t) dx. \quad (138)$$

and its total time derivative is

$$\frac{d\mathcal{H}(\theta, \phi)}{dt} = \int_l \frac{d\bar{\mathcal{H}}(\theta, \phi, \theta')}{dt} dx - \int_l \bar{m}_T(x) \theta(x, t) dx. \quad (139)$$

The total time derivative of the autonomous Hamiltonian can be rewritten as

$$\frac{d\mathcal{H}(\theta, \phi)}{dt} = \int_l \left\{ \left( \frac{\partial}{\partial x} \frac{\partial \bar{\mathcal{H}}}{\partial \theta'} - \frac{\partial \bar{\mathcal{H}}}{\partial \theta} - \frac{d\phi}{dt} + \bar{m}_T(x) \right) \dot{\theta} + \left( \dot{\theta} - \frac{\partial \bar{\mathcal{H}}}{\partial \phi} \right) \dot{\phi} \right\} dx + \left( \frac{\partial \bar{\mathcal{H}}}{\partial \theta'} \dot{\theta} \right) \Big|_0^l = 0. \quad (140)$$

Thus, the governing equations are

$$\frac{d\phi}{dt} = \frac{\partial}{\partial x} \frac{\partial \bar{\mathcal{H}}}{\partial \theta'} - \frac{\partial \bar{\mathcal{H}}}{\partial \theta} + \bar{m}_T(x), \quad \text{and} \quad \dot{\theta} - \frac{\partial \bar{\mathcal{H}}}{\partial \phi} = 0, \quad (141)$$

subject to the boundary condition

$$\left( \frac{\partial \bar{\mathcal{H}}}{\partial \theta'} \dot{\theta} \right) \Big|_0^l = 0. \quad (142)$$

Substituting the Hamiltonian density function (137) into (141), we obtain the equations of motion, a set of first-order differential equations:

$$\dot{\phi} = \frac{\partial}{\partial x} \left( GJ(x) \frac{\partial \theta(x, t)}{\partial x} \right) + \bar{m}_T(x), \quad \dot{\theta} = \frac{\phi}{\rho J(x)}, \quad (143)$$

subject to the boundary condition

$$GJ(x) \frac{\partial \theta(x, t)}{\partial x} \dot{\theta}(x, t) \Big|_0^l = 0. \quad (144)$$

Next, we discuss the development of semidiscrete differential equations of motion in the three formalisms. The trial functions are approximated as

$$\begin{aligned} \theta^h(x, t) &= \mathbf{N}(x) \cdot \mathbf{q}(t), & \dot{\theta}^h(x, t) &= \mathbf{N}(x) \cdot \dot{\mathbf{q}}(t), & \frac{\partial \theta^h(x, t)}{\partial x} &= \mathbf{B}(x) \cdot \mathbf{q}(t), \\ \boldsymbol{\phi}^h(x, t) &= \rho J(x) \mathbf{N}(x) \cdot \dot{\mathbf{q}}(t), & \mathbf{M} &= \frac{1}{2} \int_l \rho J(x) \mathbf{N}^T(x) \mathbf{N}(x) dx, & \\ \mathbf{q}(t) &= (\theta_1^h(t), \theta_2^h(t), \dots, \theta_{n_{\text{node}}}^h(t)), & \dot{\mathbf{q}}(t) &= (\dot{\theta}_1^h(t), \dot{\theta}_2^h(t), \dots, \dot{\theta}_{n_{\text{node}}}^h(t)), & \mathbf{p} &= \mathbf{M} \dot{\mathbf{q}}(t). \end{aligned} \quad (145)$$

Then, we have the space-discrete kinetic and potential energies given by

$$\mathcal{K}^h(\dot{\mathbf{q}}) = \frac{1}{2} \dot{\mathbf{q}}(t) \cdot \mathbf{M} \dot{\mathbf{q}}(t) \quad \text{or} \quad \mathcal{K}^h(\mathbf{p}) = \frac{1}{2} \mathbf{p}(t) \cdot \mathbf{M}^{-1} \mathbf{p}(t), \quad \mathcal{U}^h(\mathbf{q}) = \frac{1}{2} \mathbf{q}(t) \cdot \mathbf{K}(x) \mathbf{q}(t) - \mathbf{q}(t) \cdot \mathbf{F}_{\text{ext}}, \quad (146)$$

where the stiffness matrix and the external force are

$$\mathbf{K}(x) = \int_l GJ(x) \mathbf{B}^T(x) \mathbf{B}(x) dx \quad \text{and} \quad \mathbf{F}_{\text{ext}} = \int_l \mathbf{N}^T(x) \bar{m}_T(x) dx. \quad (147)$$

Hence, the space-discrete autonomous Lagrangian, Hamiltonian and total energy are given by

$$\mathcal{L}^h(\mathbf{q}, \dot{\mathbf{q}}) = \mathcal{K}^h(\dot{\mathbf{q}}) - \mathcal{U}^h(\mathbf{q}) = \frac{1}{2}\dot{\mathbf{q}}(t) \cdot \mathbf{M}\dot{\mathbf{q}}(t) - \frac{1}{2}\mathbf{q}(t) \cdot \mathbf{K}(x)\mathbf{q}(t) + \mathbf{q}(t) \cdot \mathbf{F}_{\text{ext}}, \quad (148)$$

$$\mathcal{E}^h(\mathbf{q}, \dot{\mathbf{q}}) = \mathcal{K}^h(\dot{\mathbf{q}}) + \mathcal{U}^h(\mathbf{q}) = \frac{1}{2}\dot{\mathbf{q}}(t) \cdot \mathbf{M}\dot{\mathbf{q}}(t) + \frac{1}{2}\mathbf{q}(t) \cdot \mathbf{K}(x)\mathbf{q}(t) - \mathbf{q}(t) \cdot \mathbf{F}_{\text{ext}}, \quad (149)$$

$$\mathcal{H}^h(\mathbf{q}, \mathbf{p}) = \mathcal{K}^h(\mathbf{p}) + \mathcal{U}^h(\mathbf{q}) = \frac{1}{2}\mathbf{p}(t) \cdot \mathbf{M}^{-1}\mathbf{p}(t) + \frac{1}{2}\mathbf{q}(t) \cdot \mathbf{K}(x)\mathbf{q}(t) - \mathbf{q}(t) \cdot \mathbf{F}_{\text{ext}}. \quad (150)$$

Substituting  $\mathcal{L}^h(\mathbf{q}, \dot{\mathbf{q}})$  and  $\mathcal{E}^h(\mathbf{q}, \dot{\mathbf{q}})$  into the corresponding discrete differential operators given by (106) and (104) we get the semidiscrete equations of motion:

$$\mathcal{L}_D(\mathcal{L}^h) \equiv \mathfrak{E}_D(\mathcal{E}^h) = 0 \Rightarrow \mathbf{M}\ddot{\mathbf{q}} + \mathbf{K}\mathbf{q} - \mathbf{F}_{\text{ext}} = 0. \quad (151)$$

Similarly, substituting  $\mathcal{H}^h(\mathbf{q}, \mathbf{p})$  into the discrete Hamiltonian differential operators defined by (109) yields the semidiscrete equations of motion

$$\mathfrak{H}_{D1}(\mathcal{H}^h) = 0 \Rightarrow \dot{\mathbf{p}} + \mathbf{K}\mathbf{q} - \mathbf{F}_{\text{ext}} = 0, \quad \mathfrak{H}_{D2}(\mathcal{H}^h) = 0 \Rightarrow \dot{\mathbf{q}} - \mathbf{M}^{-1}\mathbf{p} = 0. \quad (152)$$

**8.2. Timoshenko beam.** As an illustration typical of a more complicated numerical example in the class of structural dynamical systems, we consider the dynamical behavior of the Timoshenko beam with  $A(x)$ , the cross-sectional area and  $I(x)$ , the area moment per unit length about the neutral axis of the cross-section. It is governed by two differential equations, because of the presence of two dependent variables such as the transverse deflection  $y(x, t)$  and the angle of rotation  $\varphi(x, t)$  due to bending moment acting on the beam subject to transverse distributed load  $\bar{\omega}(x)$ . The reason for us to illustrate the Timoshenko beam problem is that the mechanics of the beam reflects the effect of rotary inertia of the beam mass as well as the translational kinetic motion effect. Thus, the proposed space-discrete formulation readily facilitates a simple and straightforward derivation of the space-discrete finite element equations of motion over the traditional principle of virtual work.

In matrix and vector notation, the continuous total energy of the Timoshenko beam can be written

$$\mathcal{E}(\mathbf{u}, \dot{\mathbf{u}}) = \int_l \bar{\mathcal{E}}(\mathbf{u}, \dot{\mathbf{u}}, \mathbf{u}') dx - \int_l \bar{\omega}(x)\mathbf{a} \cdot \mathbf{u} dx, \quad \mathbf{u}'^T = \left( \frac{\partial y(x, t)}{\partial x}, \frac{\partial \varphi(x, t)}{\partial x} \right), \quad \mathbf{a}^T = (1, 0), \quad (153)$$

where the total energy density function can be defined as

$$\begin{aligned} \bar{\mathcal{E}}(\mathbf{u}, \dot{\mathbf{u}}, \mathbf{u}') &= \frac{1}{2}\dot{\mathbf{u}} \cdot \rho\dot{\mathbf{u}} + \frac{1}{2}\boldsymbol{\kappa} \cdot \mathbf{D}_b\boldsymbol{\kappa} + \frac{1}{2}\boldsymbol{\gamma} \cdot \mathbf{G}_s\boldsymbol{\gamma}, \quad \boldsymbol{\kappa} = \left[ \frac{\partial \varphi}{\partial x} \right], \quad \mathbf{D}_b = [EI(x)], \\ \boldsymbol{\gamma} &= \left[ \frac{\partial y(x, t)}{\partial x} - \varphi(x, t) \right], \quad \mathbf{G}_s = [\kappa GA(x)]. \end{aligned} \quad (154)$$

In the context of the Lagrangian framework, the continuous Lagrangian of the Timoshenko beam is

$$\mathcal{L}(\mathbf{u}, \dot{\mathbf{u}}) = \int_l \bar{\mathcal{L}}(\mathbf{u}, \dot{\mathbf{u}}, \mathbf{u}') dx + \int_l \bar{\omega}(x)\mathbf{a} \cdot \mathbf{u} dx, \quad (155)$$

where the Lagrangian density function can be defined as

$$\bar{\mathcal{L}}(\mathbf{u}, \dot{\mathbf{u}}, \mathbf{u}') = \frac{1}{2}\dot{\mathbf{u}} \cdot \rho\dot{\mathbf{u}} - \frac{1}{2}\boldsymbol{\kappa} \cdot \mathbf{D}_b\boldsymbol{\kappa} - \frac{1}{2}\boldsymbol{\gamma} \cdot \mathbf{G}_s\boldsymbol{\gamma}. \quad (156)$$

Then, the rate of the total energy gives

$$\frac{d\bar{\mathcal{E}}(\mathbf{u}, \dot{\mathbf{u}})}{dt} = \int_l \frac{d\bar{\mathcal{E}}(\mathbf{u}, \dot{\mathbf{u}}, \mathbf{u}')}{dt} dx - \int_l \bar{\omega}(x) \mathbf{a} \cdot \dot{\mathbf{u}} dx = 0. \quad (157)$$

Within the Lagrangian framework, the rate of Jacobi's integral can be expressed

$$\frac{d}{dt} (2\bar{\mathcal{H}}(\dot{\mathbf{u}}) - \bar{\mathcal{L}}(\mathbf{u}, \dot{\mathbf{u}})) = \int_l \frac{d}{dt} \left\{ \frac{\partial \bar{\mathcal{L}}(\mathbf{u}, \dot{\mathbf{u}}, \mathbf{u}')}{\partial \dot{\mathbf{u}}} \cdot \dot{\mathbf{u}} - \bar{\mathcal{L}}(\mathbf{u}, \dot{\mathbf{u}}, \mathbf{u}') \right\} dx - \int_l \bar{\omega}(x) \mathbf{a} \cdot \dot{\mathbf{u}} dx = 0. \quad (158)$$

Consequently, (157) and (158) result in respectively

$$\begin{aligned} \int_l \left\{ \left( \frac{\partial \bar{\mathcal{E}}}{\partial \mathbf{u}} + \frac{d}{dt} \frac{\partial \bar{\mathcal{E}}}{\partial \dot{\mathbf{u}}} - \frac{\partial}{\partial x} \frac{\partial \bar{\mathcal{E}}}{\partial \mathbf{u}'} - \bar{\omega}(x) \mathbf{a} \right) \cdot \dot{\mathbf{u}} \right\} dx + \left( \frac{\partial \bar{\mathcal{E}}}{\partial \mathbf{u}'} \cdot \dot{\mathbf{u}} \right) \Big|_0^l &= 0, \\ \int_l \left\{ \left( \frac{\partial \bar{\mathcal{L}}}{\partial \mathbf{u}} - \frac{d}{dt} \frac{\partial \bar{\mathcal{L}}}{\partial \dot{\mathbf{u}}} - \frac{\partial}{\partial x} \frac{\partial \bar{\mathcal{L}}}{\partial \mathbf{u}'} + \bar{\omega}(x) \mathbf{a} \right) \cdot \dot{\mathbf{u}} \right\} dx + \left( \frac{\partial \bar{\mathcal{L}}}{\partial \mathbf{u}'} \cdot \dot{\mathbf{u}} \right) \Big|_0^l &= 0, \end{aligned} \quad (159)$$

where both governing equations and natural boundary conditions are included. The governing equations in terms of the Lagrangian and total energy density functions are

$$\frac{\partial \bar{\mathcal{L}}}{\partial \mathbf{u}} - \frac{d}{dt} \frac{\partial \bar{\mathcal{L}}}{\partial \dot{\mathbf{u}}} - \frac{\partial}{\partial x} \frac{\partial \bar{\mathcal{L}}}{\partial \mathbf{u}'} + \bar{\omega}(x) \mathbf{a} = 0 \quad \text{and} \quad \frac{\partial \bar{\mathcal{E}}}{\partial \mathbf{u}} + \frac{d}{dt} \frac{\partial \bar{\mathcal{E}}}{\partial \dot{\mathbf{u}}} - \frac{\partial}{\partial x} \frac{\partial \bar{\mathcal{E}}}{\partial \mathbf{u}'} - \bar{\omega}(x) \mathbf{a} = 0, \quad (160)$$

subject to the natural boundary conditions

$$\frac{\partial \bar{\mathcal{L}}}{\partial \mathbf{u}'} \cdot \dot{\mathbf{u}} \Big|_0^l = 0 \quad \text{and} \quad \left( \frac{\partial \bar{\mathcal{E}}}{\partial \mathbf{u}'} \cdot \dot{\mathbf{u}} \right) \Big|_0^l = 0. \quad (161)$$

In the Hamiltonian framework, the components of the canonical momenta  $\boldsymbol{\phi}^T(x, t) = (\boldsymbol{\phi}_1(x, t), \boldsymbol{\phi}_2(x, t))$  are

$$\boldsymbol{\phi} = \frac{\partial \bar{\mathcal{L}}(\mathbf{u}, \dot{\mathbf{u}}, \mathbf{u}')}{\partial \dot{\mathbf{u}}}. \quad (162)$$

The Legendre transformation gives

$$\bar{\mathcal{H}}(\mathbf{u}, \boldsymbol{\phi}, \mathbf{u}') = \boldsymbol{\phi}(x, t) \cdot \dot{\mathbf{u}}(x, t) - \bar{\mathcal{L}}(\mathbf{u}, \dot{\mathbf{u}}, \mathbf{u}') = \frac{1}{2} \boldsymbol{\phi} \cdot \rho^{-1} \boldsymbol{\phi} + \frac{1}{2} \boldsymbol{\kappa} \cdot D_b \boldsymbol{\kappa} + \frac{1}{2} \boldsymbol{\gamma} \cdot G_s \boldsymbol{\gamma}. \quad (163)$$

Hence, the rate of the continuous Hamiltonian, which is autonomous, yields

$$\frac{d\bar{\mathcal{H}}(\mathbf{u}, \boldsymbol{\phi})}{dt} = 0, \quad (164)$$

where the continuous Hamiltonian of the Timoshenko beam can be obtained as

$$\bar{\mathcal{H}}(\mathbf{u}(x, t), \boldsymbol{\phi}(x, t)) = \int_l \bar{\mathcal{H}}(\mathbf{u}(x, t), \boldsymbol{\phi}(x, t), \mathbf{u}'(x, t)) dx - \int_l \bar{\omega}(x) \mathbf{a} \cdot \mathbf{u} dx. \quad (165)$$

Hence, (164) leads to

$$\frac{d\bar{\mathcal{H}}(\mathbf{u}, \boldsymbol{\phi})}{dt} = \int_l \left\{ \left( \dot{\mathbf{u}} - \frac{\partial \bar{\mathcal{H}}}{\partial \boldsymbol{\phi}} \right) \cdot \dot{\boldsymbol{\phi}} + \left( \frac{\partial}{\partial x} \frac{\partial \bar{\mathcal{H}}}{\partial \mathbf{u}'} - \frac{\partial \bar{\mathcal{H}}}{\partial \mathbf{u}} - \frac{d\boldsymbol{\phi}}{dt} + \bar{\omega}(x) \mathbf{a} \right) \cdot \dot{\mathbf{u}} \right\} dx - \frac{\partial \bar{\mathcal{H}}}{\partial \mathbf{u}'} \cdot \dot{\mathbf{u}} \Big|_0^l = 0, \quad (166)$$



where both governing equations and natural boundary conditions are included. The governing equations in terms of the Hamiltonian density function can be given by

$$\frac{\partial}{\partial x} \frac{\partial \bar{\mathcal{H}}}{\partial \mathbf{u}'} - \frac{\partial \bar{\mathcal{H}}}{\partial \mathbf{u}} - \frac{d\boldsymbol{\phi}}{dt} + \bar{\omega}(x)\mathbf{a} = 0, \quad \dot{\mathbf{u}} - \frac{\partial \bar{\mathcal{H}}}{\partial \boldsymbol{\phi}} = 0 \quad (167)$$

subject to the natural boundary conditions

$$\frac{\partial \bar{\mathcal{H}}}{\partial \mathbf{u}'} \cdot \dot{\mathbf{u}} \Big|_0^l = 0. \quad (168)$$

Consequently, we have shown the derivation of the two governing equations of motion with the traction boundary condition via the theorem of expended power. In contrast to following traditional practices, instead of substituting the admissible functions into the Bubnov–Galerkin weighted residual forms in (159) and (166), alternatively we construct first the space-discrete Lagrangian, Hamiltonian and total energy. The admissible trial functions are given by

$$\begin{aligned} y^h(x, t) &= \mathbf{H}_y(x)\mathbf{q}(t), & \boldsymbol{\phi}^h(x, t) &= \mathbf{H}_\phi(x)\mathbf{q}(t), \\ \mathbf{H}_y(x) &= [N_y(x) \ 0], & \mathbf{H}_\phi(x) &= [0 \ N_\phi(x)], \\ \mathbf{u} &= \mathbf{H}(x)\mathbf{q}(t), & \dot{\mathbf{u}} &= \mathbf{H}(x)\dot{\mathbf{q}}(t), & \mathbf{H}^T(x) &= [\mathbf{H}_y^T(x) \ \mathbf{H}_\phi^T(x)], \\ \mathbf{q}(t) &= (y_1^h(t), y_2^h(t), \dots, y_{n_{\text{node}}}^h(t), \boldsymbol{\phi}_1^h(t), \boldsymbol{\phi}_2^h(t), \dots, \boldsymbol{\phi}_{n_{\text{node}}}^h(t)), \\ \dot{\mathbf{q}}(t) &= (\dot{y}_1^h(t), \dot{y}_2^h(t), \dots, \dot{y}_{n_{\text{node}}}^h(t), \dot{\boldsymbol{\phi}}_1^h(t), \dot{\boldsymbol{\phi}}_2^h(t), \dots, \dot{\boldsymbol{\phi}}_{n_{\text{node}}}^h(t)). \end{aligned} \quad (169)$$

The space-discrete Lagrangian, Hamiltonian and total energy may be written as

$$\begin{aligned} \mathcal{L}^h(\mathbf{q}, \dot{\mathbf{q}}) &= \frac{1}{2}\dot{\mathbf{q}}(t) \cdot \mathbf{M}\dot{\mathbf{q}}(t) - \frac{1}{2}\mathbf{q}(t) \cdot \mathbf{K}\mathbf{q}(t) + \mathbf{q}(t) \cdot \mathbf{F}_{\text{ext}}, \\ \mathcal{E}^h(\mathbf{q}, \dot{\mathbf{q}}) &= \frac{1}{2}\dot{\mathbf{q}}(t) \cdot \mathbf{M}\dot{\mathbf{q}}(t) + \frac{1}{2}\mathbf{q}(t) \cdot \mathbf{K}\mathbf{q}(t) - \mathbf{q}(t) \cdot \mathbf{F}_{\text{ext}}, \\ \mathcal{H}^h(\mathbf{q}, \mathbf{p}) &= \frac{1}{2}\mathbf{p}(t) \cdot \mathbf{M}^{-1}\mathbf{p}(t) + \frac{1}{2}\mathbf{q}(t) \cdot \mathbf{K}\mathbf{q}(t) - \mathbf{q}(t) \cdot \mathbf{F}_{\text{ext}}, \\ \mathbf{M} &= \frac{1}{2} \int_l \mathbf{H}(x)^T \rho \mathbf{H}(x) dx, & \mathbf{p}(t) &= \mathbf{M}\dot{\mathbf{q}}(t), \\ \mathbf{K}_b &= \int_l \mathbf{B}_b^T(x) \mathbf{D}_b \mathbf{B}_b(x) dx, & \mathbf{K}_s &= \int_l \mathbf{B}_s^T(x) \mathbf{G}_s \mathbf{B}_s(x) dx, & \mathbf{K} &= \mathbf{K}_b + \mathbf{K}_s, \\ \mathbf{B}_b &= \left[ \frac{\partial \mathbf{H}_\phi(x)}{\partial x} \right], & \mathbf{B}_s &= \left[ \frac{\partial \mathbf{H}_y(x)}{\partial x} - \mathbf{H}_\phi(x) \right], & \mathbf{F}_{\text{ext}} &= \int_l \bar{\omega}(x) \mathbf{H}_y^T(x) dx, \end{aligned} \quad (170)$$

where  $E$  denotes Young's modulus,  $\kappa$  the shear correction factor, and  $G$  the shear modulus. Substituting the space-discrete Lagrangian total energy, and Hamiltonian into the corresponding discrete differential operators (104), (106), (109) leads to the space-discrete finite element equations of motion within the corresponding frameworks:

$$\begin{aligned} \mathfrak{L}_D(\mathcal{L}^h) &\equiv \mathfrak{E}_D(\mathcal{E}^h) = 0 \Rightarrow \mathbf{M}\ddot{\mathbf{q}} + \mathbf{K}\mathbf{q} - \mathbf{F}_{\text{ext}} = 0, \\ \mathfrak{H}_{D1}(\mathcal{H}^h) &= 0 \Rightarrow \dot{\mathbf{p}} + \mathbf{K}\mathbf{q} - \mathbf{F}_{\text{ext}} = 0, & \mathfrak{H}_{D2}(\mathcal{H}^h) &= 0 \Rightarrow \dot{\mathbf{q}} - \mathbf{M}^{-1}\mathbf{p} = 0. \end{aligned} \quad (171)$$

## 9. Conclusions

In most renowned textbooks, and historically, the finite element method for elastodynamics applications has been explained in the sense of the principle of virtual work involving the concept of variations from various viewpoints. Traditional variational practices and Newton based formulations stemming from the Cauchy equations of motion cannot readily establish the various symmetries for the semidiscrete system. In contrast, alternate developments via differential calculus were described involving the theorem of expended power and scalar representations which provide an improved physical interpretation, and for also ensuring that the semidiscretized system also inherits the same physics as in the continuous system by capitalizing on theorems' such as Noether. In this work, we introduced and showed that the theorem of expended power involving three distinct frameworks, namely, the Total Energy, the Lagrangian, and the Hamiltonian density functions is a consistent and viable alternative for deriving the governing equations with boundary conditions for both  $N$ -body and continuous-body scleronomic dynamical systems. In addition, in contrast to traditional practices, which, after obtaining the model governing equations, seek to employ the weak form or principle of virtual work with trial and test functions to enacting the discretization process, we proposed a space-discrete Total Energy, Lagrangian, and Hamiltonian finite element formulation involving only trial functions to directly discretize the theorem of extended power, without resorting to traditional practices resulting in the space discrete finite element equations of motion for continuum-dynamical systems. Extensions to account for non-holonomic constraints were also described. The equivalence of the three frameworks in terms of the strong and weak forms were established in relation to describing Newton's second law and the underlying equation of motion, and illustrative examples of the rotating bar and Timoshenko beam were demonstrated to describe the basic ideas.

### Appendix: Space discretization via density formalisms and finite element formulation

Alternatively, we herein describe the evolution of traditional practices using as a starting point, the theorem of expended power within the total energy density formalism and framework, followed by the Lagrangian and Hamiltonian frameworks via the corresponding density formalisms. In view of (54) and (56), the rate of the total energy easily yields the weak form in the sense of the space

$$\frac{d\mathcal{E}(\boldsymbol{\varphi}, \dot{\boldsymbol{\varphi}})}{dt} = \int_{\mathcal{B}} \frac{d}{dt} \left( \frac{\partial \bar{\mathcal{E}}}{\partial \dot{\boldsymbol{\varphi}}} \right) \cdot \dot{\boldsymbol{\varphi}} dV + \int_{\mathcal{B}} \frac{\partial \bar{\mathcal{E}}}{\partial \mathbf{F}} \cdot \dot{\mathbf{F}} dV + \int_{\mathcal{B}} \frac{\partial \bar{\mathcal{E}}}{\partial \boldsymbol{\varphi}} \cdot \dot{\boldsymbol{\varphi}} dV - \int_{\partial \mathcal{B}_\sigma} \bar{\mathbf{T}}(\mathbf{X}) \cdot \dot{\boldsymbol{\varphi}} dA = 0. \quad (\text{A.1})$$

We know that this equation can be obtained when the virtual displacement in the principle of virtual work is replaced by the generalized velocity. This is the so-called the single field problem; the dependent variable is the displacement, and one can follow traditional practices of discretization in space and time. Likewise, the rate of Jacobi's integral gives the weak form in terms of the Lagrangian density function

$$\int_{\mathcal{B}} \frac{d}{dt} \left( \frac{\partial \bar{\mathcal{L}}}{\partial \dot{\boldsymbol{\varphi}}} \right) \cdot \dot{\boldsymbol{\varphi}}(\mathbf{X}, t) dV - \int_{\mathcal{B}} \frac{\partial \bar{\mathcal{L}}}{\partial \mathbf{F}} \cdot \dot{\mathbf{F}} dV - \int_{\mathcal{B}} \frac{\partial \bar{\mathcal{L}}}{\partial \boldsymbol{\varphi}} \cdot \dot{\boldsymbol{\varphi}}(\mathbf{X}, t) dV - \int_{\partial \mathcal{B}_\sigma} \bar{\mathbf{T}}(\mathbf{X}) \cdot \dot{\boldsymbol{\varphi}}(\mathbf{X}, t) dA = 0. \quad (\text{A.2})$$

Note that the essential boundary conditions become nodal position vectors on nodal points. This is the conventional process for the Galerkin finite element method [Hughes 1987; Reddy 2006]. Consequently,

substituting appropriate trial and test functions into (A.1) and (A.2), yields the semidiscrete second order in time differential equations of motion as

$$\sum_{i=1}^{n_{\text{elem}}} \left( \int_{\mathcal{B}_i} \rho \ddot{\tilde{\boldsymbol{\varphi}}^h} \cdot \dot{\tilde{\boldsymbol{\varphi}}^h} dV + \int_{\mathcal{B}_i} \tilde{\mathbf{P}}^h \cdot \dot{\tilde{\mathbf{F}}}^h dV - \int_{\mathcal{B}_i} \rho_0 \mathbf{B}(\mathbf{X}) \cdot \dot{\tilde{\boldsymbol{\varphi}}^h} dV - \int_{\partial \mathcal{B}_{i\sigma}} \bar{\mathbf{T}}(\mathbf{X}) \cdot \dot{\tilde{\boldsymbol{\varphi}}^h} dA \right) = 0, \quad (\text{A.3})$$

where  $\mathcal{B}_i$  stands for the  $i$ -th element domain. Notice that (A.3) gives a set of simultaneous  $N$  ordinary time differential equations to be discretized subsequently in time. Therefore, the weak form is the most important equation to which one must apply both the admissible trial functions  $\tilde{\boldsymbol{\varphi}}(\mathbf{X}, t)$  and the admissible test functions  $\dot{\tilde{\boldsymbol{\varphi}}}(\mathbf{X}, t)$  to discretize the domain of interest. From (A.3), we obtain the semidiscrete second order differential equations, that is, the finite element equations of motion resulting as follows for the total energy and Lagrangian frameworks:

$$\mathbf{M}\ddot{\mathbf{q}} + \mathbf{F}_{\text{int}} - \mathbf{F}_{\text{ext}} = 0. \quad (\text{A.4})$$

In addition, within the Hamiltonian framework, the rate of the Hamiltonian yields the weak form in the sense of the space:

$$\begin{aligned} \int_{\mathcal{B}} \dot{\boldsymbol{\phi}} \cdot \dot{\boldsymbol{\phi}} dV + \int_{\mathcal{B}} \frac{\partial \bar{\mathcal{H}}}{\partial \mathbf{F}} \cdot \dot{\mathbf{F}} dV + \int_{\mathcal{B}} \frac{\partial \bar{\mathcal{H}}}{\partial \boldsymbol{\varphi}} \cdot \dot{\boldsymbol{\varphi}} dV - \int_{\partial \mathcal{B}_{i\sigma}} \bar{\mathbf{T}}(\mathbf{X}) \cdot \dot{\boldsymbol{\phi}} dA = 0, \\ \int_{\mathcal{B}} \left( \dot{\boldsymbol{\phi}} - \frac{\partial \bar{\mathcal{H}}}{\partial \boldsymbol{\phi}} \right) \cdot \dot{\boldsymbol{\phi}} dV = 0. \end{aligned} \quad (\text{A.5})$$

Finally, substituting appropriate trial and test functions into (A.5), we obtain the semidiscrete first order differential equations of motion:

$$\begin{aligned} \sum_{i=1}^{n_{\text{elem}}} \left( \int_{\mathcal{B}_i} \dot{\tilde{\boldsymbol{\varphi}}^h} \cdot \dot{\tilde{\boldsymbol{\varphi}}^h} dV + \int_{\mathcal{B}_i} \left( \frac{\partial \bar{\mathcal{H}}}{\partial \tilde{\mathbf{F}}} \right)^h \cdot \dot{\tilde{\mathbf{F}}}^h dV + \int_{\mathcal{B}_i} \left( \frac{\partial \bar{\mathcal{H}}}{\partial \tilde{\boldsymbol{\varphi}}} \right)^h \cdot \dot{\tilde{\boldsymbol{\varphi}}^h} dV - \int_{\partial \mathcal{B}_{i\sigma}} \bar{\mathbf{T}}(\mathbf{X}) \cdot \dot{\tilde{\boldsymbol{\varphi}}^h} dA \right) t = 0, \\ \sum_{i=1}^{n_{\text{elem}}} \left( \int_{\mathcal{B}_i} \dot{\tilde{\boldsymbol{\varphi}}^h} \cdot \dot{\tilde{\boldsymbol{\varphi}}^h} dV - \int_{\mathcal{B}_i} \left( \frac{\partial \bar{\mathcal{H}}}{\partial \tilde{\boldsymbol{\varphi}}} \right)^h \cdot \dot{\tilde{\boldsymbol{\varphi}}^h} dV \right) = 0 \end{aligned} \quad (\text{A.6})$$

which yields

$$\dot{\mathbf{p}} + \mathbf{F}_{\text{int}} - \mathbf{F}_{\text{ext}} = 0, \quad \dot{\mathbf{q}} - \mathbf{M}^{-1} \mathbf{p} = 0. \quad (\text{A.7})$$

For nonholonomic or nonconservative systems involving contact, (A.1) and (A.2) should be modified:

$$\begin{aligned} \int_{\mathcal{B}} \frac{d}{dt} \left( \frac{\partial \bar{\mathcal{E}}}{\partial \dot{\boldsymbol{\phi}}} \right) \cdot \dot{\boldsymbol{\phi}} dV + \int_{\mathcal{B}} \frac{\partial \bar{\mathcal{E}}}{\partial \mathbf{F}} \cdot \dot{\mathbf{F}} dV + \int_{\mathcal{B}} \frac{\partial \bar{\mathcal{E}}}{\partial \boldsymbol{\varphi}} \cdot \dot{\boldsymbol{\varphi}} dV - \int_{\partial \mathcal{B}_{i\sigma}} \bar{\mathbf{T}}(\mathbf{X}, t) \cdot \dot{\boldsymbol{\phi}} dA = \int_{\partial \mathcal{B}_c} (\mathbf{P}_c^A - \mathbf{P}_c^B) \cdot \hat{\mathbf{N}}_c^A \cdot \dot{\boldsymbol{\phi}} dA, \\ \int_{\mathcal{B}} \frac{d}{dt} \left( \frac{\partial \bar{\mathcal{L}}}{\partial \dot{\boldsymbol{\phi}}} \right) \cdot \dot{\boldsymbol{\phi}} dV - \int_{\mathcal{B}} \frac{\partial \bar{\mathcal{L}}}{\partial \mathbf{F}} \cdot \dot{\mathbf{F}} dV - \int_{\mathcal{B}} \frac{\partial \bar{\mathcal{L}}}{\partial \boldsymbol{\varphi}} \cdot \dot{\boldsymbol{\varphi}} dV - \int_{\partial \mathcal{B}_{i\sigma}} \bar{\mathbf{T}}(\mathbf{X}, t) \cdot \dot{\boldsymbol{\phi}} dA = \int_{\partial \mathcal{B}_c} (\mathbf{P}_c^A - \mathbf{P}_c^B) \cdot \hat{\mathbf{N}}_c^A \cdot \dot{\boldsymbol{\phi}} dA. \end{aligned}$$

The discretization of these equations gives

$$\begin{aligned} \sum_{i=1}^{n_{\text{elem}}} \left( \int_{\mathcal{B}_i} \rho \ddot{\boldsymbol{\phi}}^h \cdot \dot{\boldsymbol{\phi}}^h dV + \int_{\mathcal{B}_i} \tilde{\mathbf{P}}^h \cdot \dot{\mathbf{F}}^h dV - \int_{\mathcal{B}_i} \rho_0 \mathbf{B}(\mathbf{X}) \cdot \dot{\boldsymbol{\phi}}^h dV - \int_{\partial \mathcal{B}_{i\sigma}} \bar{\mathbf{T}}(\mathbf{X}, t) \cdot \dot{\boldsymbol{\phi}}^h dA \right) \\ = \sum_{i=1}^{n_{\text{elem}}} \left( \int_{\partial \mathcal{B}_{ic}} (\mathbf{P}_c^A - \mathbf{P}_c^B) \cdot \hat{\mathbf{N}}_c^A \cdot \dot{\boldsymbol{\phi}}^h dA \right) \end{aligned} \quad (\text{A.8})$$

which finally reduces to

$$\mathbf{M} \ddot{\mathbf{q}} + \mathbf{F}_{\text{int}} - \mathbf{F}_{\text{ext}} = \mathbf{F}_{\text{contact}}. \quad (\text{A.9})$$

Further, within the Hamiltonian framework, (A.5) should be modified to read

$$\begin{aligned} \int_{\mathcal{B}} \dot{\boldsymbol{\phi}} \cdot \dot{\boldsymbol{\phi}} dV + \int_{\mathcal{B}} \frac{\partial \bar{\mathcal{H}}}{\partial \mathbf{F}} \cdot \dot{\mathbf{F}} dV + \int_{\mathcal{B}} \frac{\partial \bar{\mathcal{H}}}{\partial \boldsymbol{\phi}} \cdot \dot{\boldsymbol{\phi}} dV - \int_{\partial \mathcal{B}_{\sigma}} \bar{\mathbf{T}}(\mathbf{X}, t) \cdot \dot{\boldsymbol{\phi}} dA = \int_{\partial \mathcal{B}_c} (\mathbf{P}_c^A - \mathbf{P}_c^B) \cdot \hat{\mathbf{N}}_c^A \cdot \dot{\boldsymbol{\phi}} dA, \\ \int_{\mathcal{B}} \left( \dot{\boldsymbol{\phi}} - \frac{\partial \bar{\mathcal{H}}}{\partial \boldsymbol{\phi}} \right) \cdot \dot{\boldsymbol{\phi}} dV = 0. \end{aligned}$$

Discretization yields

$$\begin{aligned} \sum_{i=1}^{n_{\text{elem}}} \left( \int_{\mathcal{B}_i} \dot{\boldsymbol{\phi}}^h \cdot \dot{\boldsymbol{\phi}}^h dV + \int_{\mathcal{B}_i} \left( \frac{\partial \bar{\mathcal{H}}}{\partial \tilde{\mathbf{F}}} \right)^h \cdot \dot{\mathbf{F}}^h dV + \int_{\mathcal{B}_i} \left( \frac{\partial \bar{\mathcal{H}}}{\partial \boldsymbol{\phi}} \right)^h \cdot \dot{\boldsymbol{\phi}}^h dV - \int_{\partial \mathcal{B}_{i\sigma}} \bar{\mathbf{T}}(\mathbf{X}, t) \cdot \dot{\boldsymbol{\phi}}^h dA \right) \\ = \sum_{i=1}^{n_{\text{elem}}} \left( \int_{\partial \mathcal{B}_{ic}} (\mathbf{P}_c^A - \mathbf{P}_c^B) \cdot \hat{\mathbf{N}}_c^A \cdot \dot{\boldsymbol{\phi}}^h dA \right) \end{aligned} \quad (\text{A.10})$$

and

$$\sum_{i=1}^{n_{\text{elem}}} \left( \int_{\mathcal{B}_i} \dot{\boldsymbol{\phi}}^h \cdot \dot{\boldsymbol{\phi}}^h dV - \int_{\mathcal{B}_i} \left( \frac{\partial \bar{\mathcal{H}}}{\partial \boldsymbol{\phi}} \right)^h \cdot \dot{\boldsymbol{\phi}}^h dV \right) = 0, \quad (\text{A.11})$$

which reduce to

$$\dot{\mathbf{p}} + \mathbf{F}_{\text{int}} - \mathbf{F}_{\text{ext}} = \mathbf{F}_{\text{contact}}, \quad \dot{\mathbf{q}} - \mathbf{M}^{-1} \mathbf{p} = 0. \quad (\text{A.12})$$

Equations (A.8), (A.10) and (A.11) represent the semidiscrete finite element equations of motion for nonholonomic or nonconservative systems with contact.

## References

- [ABAQUS 2002] *ABAQUS/Explicit user's manual*, Hibbit, Karlsson and Sorenson, Pawtucket, RI, 2002. Version 6.2.
- [Aharoni and Bar-Yoseph 1992] D. Aharoni and P. Bar-Yoseph, "Mixed finite element formulations in the time domain for solution of dynamic problems", *Comput. Mech.* **9**:5 (1992), 359–374.
- [Arnold 1989] V. I. Arnold, *Mathematical methods of classical mechanics*, Springer, New York, 1989.
- [Asaro and Lubarda 2006] R. J. Asaro and V. A. Lubarda, *Mechanics of solids and materials*, Cambridge University Press, Cambridge, 2006.
- [Bailey 1975] C. D. Bailey, "Application of Hamilton's law of varying action", *AIAA J.* **13**:9 (1975), 1154–1157.
- [Bathe 1982] K. J. Bathe, *Finite element procedures in engineering analysis*, Prentice Hall, Englewood Cliffs, NJ, 1982.
- [Belytschko et al. 2000] T. Belytschko, W. K. Liu, and B. Moran, *Nonlinear finite elements for continua and structures*, Wiley, New York, 2000.

- [Byers 1996] N. Byers, “The life and times of Emmy Noether: contributions of Emmy Noether to particle physics”, pp. 945–964 in *History of original ideas and basic discoveries in particle physics*, edited by H. B. Newman and T. Ypsilantis, Plenum, New York, 1996.
- [Byers 1999] N. Byers, “E. Noether’s discovery of the deep connection between symmetries and conservation laws”, *Isr. Math. Conf. Proc.* **12** (1999), 67–82.
- [Carini and Genna 1998] A. Carini and F. Genna, “Some variational formulations for continuum nonlinear dynamics”, *J. Mech. Phys. Solids* **46**:7 (1998), 1253–1277.
- [Castro 2000] A. S. de Castro, “Exploring a rheonomic system”, *Eur. J. Phys.* **21**:1 (2000), 23–26.
- [Coleman and Noll 1963] B. D. Coleman and W. Noll, “The thermodynamics of elastic materials with heat conduction and viscosity”, *Arch. Ration. Mech. An.* **13**:1 (1963), 167–178.
- [Cook et al. 2002] R. D. Cook, D. S. Malkus, M. E. Plesha, and R. J. Witt, *Concepts and applications of finite element analysis*, 4th ed., Wiley, New York, 2002.
- [Goldstein et al. 2002] H. Goldstein, C. Poole, and J. Safko, *Classical mechanics*, 3rd ed., Addison-Wesley, San Francisco, 2002.
- [Greenwood 1977] D. T. Greenwood, *Classical dynamics*, Prentice-Hall, Englewood Cliffs, NJ, 1977.
- [Gurtin 1964a] M. E. Gurtin, “Variational principles for linear initial value problems”, *Quart. Appl. Math.* **22** (1964), 252–256.
- [Gurtin 1964b] M. E. Gurtin, “Variational principles for linear elastodynamics”, *Arch. Ration. Mech. An.* **16**:1 (1964), 34–50.
- [Gurtin 1972] M. E. Gurtin, “The linear theory of elasticity”, pp. 1–295 in *Mechanics of solids*, edited by C. A. Truesdell, *Handbuch der Physik VIa/2*, Springer, Berlin, 1972.
- [Hallquist 1998] J. O. Hallquist, *LS-DYNA theoretical manual*, Livermore Software Technology Corporation, Livermore, CA, 1998.
- [Hallquist et al. 1985] J. O. Hallquist, G. L. Goudreau, and D. J. Benson, “Sliding interfaces with contact-impact in large-scale Lagrangian computations”, *Comput. Methods Appl. Mech. Eng.* **51**:1–3 (1985), 107–137.
- [Hand and Finch 1998] L. H. Hand and J. D. Finch, *Analytical mechanics*, Cambridge University Press, Cambridge, 1998.
- [Har and Tamma 2009] J. Har and K. K. Tamma, “Total energy framework, finite elements, and discretization via Hamilton’s law of varying action”, *Acta Mech.* (2009).
- [Hibbitt et al. 1970] H. D. Hibbitt, P. V. Marcal, and J. R. Rice, “A finite element formulation for problems of large strain and large displacement”, *Int. J. Solids Struct.* **6**:8 (1970), 1069–1086.
- [Holzapfel 2000] G. A. Holzapfel, *Nonlinear solid mechanics: a continuum approach for engineering*, Wiley, New York, 2000.
- [Hughes 1987] T. J. R. Hughes, *Finite element method: linear static and dynamic finite element analysis*, Prentice-Hall, Englewood Cliffs, NJ, 1987.
- [Lanczos 1970] C. Lanczos, *The variational principles of mechanics*, University of Toronto Press, Toronto, 1970.
- [Laursen 2002] T. A. Laursen, *Computational contact and impact mechanics: fundamentals of modeling interfacial phenomena in nonlinear finite element analysis*, Springer, Heidelberg, 2002.
- [Lee 1969] E. H. Lee, “Elastic-plastic deformations at finite strains”, *J. Appl. Mech. (ASME)* **36** (1969), 1–6.
- [Lee and Liu 1967] E. H. Lee and D. T. Liu, “Finite-strain elastic-plastic theory with application to plane-wave analysis”, *J. Appl. Phys.* **38**:1 (1967), 19–27.
- [Malvern 1969] L. E. Malvern, *Introduction to the mechanics of a continuous medium*, Prentice-Hall, Englewood Cliffs, NJ, 1969.
- [Marsden and Hughes 1983] J. E. Marsden and T. J. R. Hughes, *Mathematical foundations of elasticity*, Prentice-Hall, Englewood Cliffs, NJ, 1983.
- [Masuri et al. 2009a] S. Masuri, A. Hoitink, X. Zhou, and K. K. Tamma, “Algorithms by design, II: A novel normalized time weighted residual methodology and design of a family of symplectic-momentum conserving algorithms for nonlinear structural dynamics”, *Int. J. Comput. Methods Eng. Sci. Mech.* **10**:1 (2009), 27–56.
- [Masuri et al. 2009b] S. U. Masuri, A. Hoitink, X. Zhou, and K. K. Tamma, “Algorithms by design: a new normalized time-weighted residual methodology and design of a family of energy-momentum conserving algorithms for non-linear structural dynamics”, *Int. J. Numer. Methods Eng.* (2009). (In Press).

- [Meirovitch 2003] L. Meirovitch, *Methods of analytical dynamics*, Dover, Mineola, NY, 2003.
- [Mikhlin 1964] S. G. Mikhlin, *Variational methods in mathematical physics*, Macmillan, New York, 1964.
- [Nemat-Nasser 1982] S. Nemat-Nasser, “On finite deformation elasto-plasticity”, *Int. J. Solids Struct.* **18**:10 (1982), 857–872.
- [Noether 1918] E. Noether, “Invariante Variationsprobleme”, *Nachr. v. d. Ges. d. Wiss. (Göttingen)* **2** (1918), 235–257. Translated in *Transport Theory Stat. Mech.* **1**:3, (1971), 183–207. Original and translation available at <http://www.physics.ucla.edu/~cwp/articles/noether.trans>.
- [Papadopoulos et al. 1995] P. Papadopoulos, R. E. Jones, and J. M. Solberg, “A novel finite element formulation for frictionless contact problems”, *Int. J. Numer. Methods Eng.* **38**:15 (1995), 2603–2617.
- [Pars 1965] L. A. Pars, *A treatise on analytical dynamics*, Wiley, New York, 1965.
- [Reddy 2006] J. N. Reddy, *An introduction to the finite element method*, 3rd ed., McGraw-Hill, New York, 2006.
- [Simkins 1981] T. E. Simkins, “Finite elements for initial value problems in dynamics”, *AIAA J.* **19**:10 (1981), 1357–1362.
- [Simo and Hughes 1998] J. C. Simo and T. J. R. Hughes, *Computational inelasticity*, Springer, New York, 1998.
- [Simo et al. 1992] J. C. Simo, N. Tarnow, and K. K. Wong, “Exact energy-momentum conserving algorithms and symplectic schemes for nonlinear dynamics”, *Comput. Methods Appl. Mech. Eng.* **100**:1 (1992), 63–116.
- [Tamma et al. 2000] K. K. Tamma, X. Zhou, and D. Sha, “The time dimension: a theory towards the evolution, classification, characterization and design of computational algorithms for transient/dynamic applications”, *Arch. Comput. Methods Eng.* **7**:2 (2000), 67–290.
- [Tonti 1973] E. Tonti, “On the variational formulation for linear initial value problems”, *Ann. Mat. Pura Appl.* **95**:1 (1973), 331–359.
- [Tonti 1984] E. Tonti, “Variational formulation for every nonlinear problem”, *Int. J. Eng. Sci.* **22**:11–12 (1984), 1343–1371.
- [Tonti 2001a] E. Tonti, “A direct discrete formulation of field laws: the cell method”, *Comput. Model. Eng. Sci.* **2**:2 (2001), 237–258.
- [Tonti 2001b] E. Tonti, “A direct discrete formulation for the wave equation”, *J. Comput. Acoust.* **9**:4 (2001), 1355–1382.
- [Truesdell and Noll 2004] C. Truesdell and W. Noll, *The non-linear field theories of mechanics*, 3rd ed., Springer, Berlin, 2004.
- [Wriggers 2006] P. Wriggers, *Computational contact mechanics*, 2nd ed., Springer, Berlin, 2006.
- [Zienkiewicz et al. 2005] O. C. Zienkiewicz, R. L. Taylor, and J. Z. Zhu, *The finite element method: its basis and fundamentals*, 6th ed., Elsevier Butterworth-Heinemann, Amsterdam, 2005.

Received 1 Oct 2008. Revised 19 Dec 2008. Accepted 19 Jan 2009.

JASON HAR: [jason.har@gmail.com](mailto:jason.har@gmail.com)

*Department of Mechanical Engineering, University of Minnesota, 111 Church Street SE, Minneapolis, MN 55455*

KUMAR K. TAMMA: [ktamma@gmail.com](mailto:ktamma@gmail.com)

*Department of Mechanical Engineering, University of Minnesota, 111 Church Street SE, Minneapolis, MN 55455*

## STATIC BENDING ANALYSIS OF LAMINATED CYLINDRICAL PANELS WITH VARIOUS BOUNDARY CONDITIONS USING THE DIFFERENTIAL CUBATURE METHOD

S. MAHMOUD MOUSAVI AND MOHAMAD M. AGHDAM

This paper deals with the application of the differential cubature method (DCM) to the bending analysis of laminated cylindrical panels. Symmetric and unsymmetric laminate, with various combinations of clamped, simply supported and free boundary conditions, are considered, with either uniform or sinusoidal transversely distributed loads. Using first-order shear deformation theory, fifteen first-order partial differential equations are obtained, containing as many unknowns in terms of displacements, rotations, moments, and forces. Comparison of the results obtained by DCM shows very good agreement with those of other numerical and analytical methods, with decreased computational effort. Further, in this method, a free boundary condition and unsymmetric laminates do not violate the accuracy of the results.

*A list of symbols can be found starting on page 519.*

### 1. Introduction

Considerable research has been conducted to investigate the response of thin/thick laminated cylindrical panels, as one of the fundamental parts of engineering structures. Since only particular elasticity problems can be studied using analytical methods, numerical techniques have been developed to obtain solutions for different structural components subjected to various types of loading and boundary conditions. Among the methods employed we mention the finite difference [Smith 2000], finite element [Qatu and Algothani 1994; Reddy 2004], boundary element [Jianqiao 1988], dynamic relaxation [Ramesh and Krishnamoorthy 1995], and extended Kantorovich methods [Yuan et al. 1998; Alijani et al. 2008], meshless methods [Alavi et al. 2006], and the differential quadrature (DQ) [Artioli et al. 2005], generalized differential quadrature (GDQ) [Aghdam et al. 2006], and differential cubature methods (DCM) [Civan 1994; Liew and Liu 1997; 1998; Teo and Liew 2002; Wu and Liu 2005].

In the literature of the static bending analysis of shells and plates, the free boundary condition has been a major problem and usually the methods lose their accuracy when there is even one free edge. Although this is more of a problem with analytical methods than numerical ones, only a few numerical methods—such as GDQ [Aghdam et al. 2006], FEM [Bhaskar and Varadan 1991], and state space [Khdeir et al. 1989]—can be assumed safe for dealing with static problems involving shells and plates with free edges. Naturally, then, the development of new methods usable for unsymmetric shells with some free edges is a desirable goal.

The DCM was presented in [Civan 1994] as an efficient procedure to obtain solutions for partial differential equations with a relatively small number of grid points and less computational effort. However, reported applications of the DCM in the open literature are restricted to analyses of plates, including

*Keywords:* cylindrical panel, unsymmetric laminates, differential cubature method, bending analysis.

bending [Liew and Liu 1997; 1998; Teo and Liew 2002] and vibration [Wu and Liu 2005]. Nothing was found in the open literature for other structural elements, such as shells and panels.

Here we perform a bending analysis of laminated cylindrical panels with various loading boundary conditions using the DCM. The complete form of the governing partial differential equations of the problem based on first-order shear deformation theory is considered. All panel variables including displacements, rotations, moment, and force resultants are presented in the governing equations. The presence of all variables provides an easy way to satisfy different boundary conditions.

The solution to the governing equations provides direct predictions of all variables with the same order of accuracy. Both governing equations and solution domain are discretized using DCM. As with most other numerical techniques, this yields a system of linear algebraic equations. Comparison of the predictions for stress resultants and displacement components shows very good agreement with results of other analytical and numerical techniques. The lamination sequence of the examples are symmetric, unsymmetric, cross-ply and angle-ply. There is no restriction to using this method for panels with free edges.

## 2. Governing equations

As a test case for the capabilities of the DCM and the accuracy of its results, we consider a moderately thick laminated cylindrical shell panel with length  $a$ , thickness  $h$ , and mid-surface radius  $R$  (Figure 1). Using the principle of minimum potential energy and the assumptions of first-order shear deformation theory (FSDT), one obtains the fifteen first-order PDEs listed in Table 1, which constitute the general form of the governing partial differential equations of the problem; see [Toorani and Lakis 2000] for details. (These governing equations have been used and verified in some recent surveys such as [Aghdam et al. 2006; Toorani and Lakis 2001].)

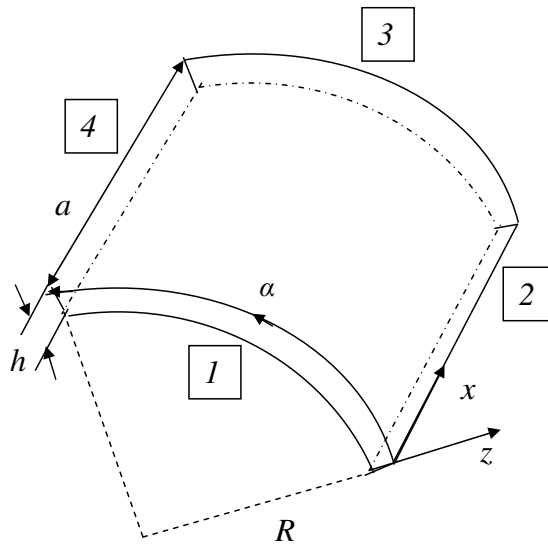


**Figure 1.** Shell geometry and coordinate system.



$$\begin{aligned}
 N_{xx} - G_{11} \frac{\partial u_x}{\partial x} - G_{16} \frac{\partial u_\theta}{\partial x} - \frac{A_{12}}{R} \left( \dot{w} + \frac{\partial u_\theta}{\partial \theta} \right) - \frac{A_{16}}{R} \frac{\partial u_x}{\partial \theta} - H_{11} \frac{\partial \beta_x}{\partial x} - H_{16} \frac{\partial \beta_\theta}{\partial x} - \frac{B_{12}}{R} \frac{\partial \beta_\theta}{\partial \theta} - \frac{B_{16}}{R} \frac{\partial \beta_x}{\partial \theta} &= 0, \\
 N_{x\theta} - G_{61} \frac{\partial u_x}{\partial x} - G_{66} \frac{\partial u_\theta}{\partial x} - \frac{A_{62}}{R} \left( w + \frac{\partial u_\theta}{\partial \theta} \right) - \frac{A_{66}}{R} \frac{\partial u_x}{\partial \theta} - H_{61} \frac{\partial \beta_x}{\partial x} - H_{66} \frac{\partial \beta_\theta}{\partial x} - \frac{B_{62}}{R} \frac{\partial \beta_\theta}{\partial \theta} - \frac{B_{66}}{R} \frac{\partial \beta_x}{\partial \theta} &= 0, \\
 N_{\theta\theta} - A_{21} \frac{\partial u_x}{\partial x} - A_{26} \frac{\partial u_\theta}{\partial x} - \frac{G'_{22}}{R} \left( w + \frac{\partial u_\theta}{\partial \theta} \right) - \frac{G'_{26}}{R} \frac{\partial u_x}{\partial \theta} - B_{21} \frac{\partial \beta_x}{\partial x} - B_{26} \frac{\partial \beta_\theta}{\partial x} - \frac{H'_{22}}{R} \frac{\partial \beta_\theta}{\partial \theta} - \frac{H'_{26}}{R} \frac{\partial \beta_x}{\partial \theta} &= 0, \\
 N_{\theta x} - A_{61} \frac{\partial u_x}{\partial x} - A_{66} \frac{\partial u_\theta}{\partial x} - \frac{G'_{62}}{R} \left( w + \frac{\partial u_\theta}{\partial \theta} \right) - \frac{G'_{66}}{R} \frac{\partial u_x}{\partial \theta} - B_{61} \frac{\partial \beta_x}{\partial x} - B_{66} \frac{\partial \beta_\theta}{\partial x} - \frac{H'_{62}}{R} \frac{\partial \beta_\theta}{\partial \theta} - \frac{H'_{66}}{R} \frac{\partial \beta_x}{\partial \theta} &= 0, \\
 M_{xx} - H_{11} \frac{\partial u_x}{\partial x} - H_{16} \frac{\partial u_\theta}{\partial x} - \frac{B_{12}}{R} \left( w + \frac{\partial u_\theta}{\partial \theta} \right) - \frac{B_{16}}{R} \frac{\partial u_x}{\partial \theta} - J_{11} \frac{\partial \beta_x}{\partial x} - J_{16} \frac{\partial \beta_\theta}{\partial x} - \frac{D_{12}}{R} \frac{\partial \beta_\theta}{\partial \theta} - \frac{D_{16}}{R} \frac{\partial \beta_x}{\partial \theta} &= 0, \\
 M_{x\theta} - H_{61} \frac{\partial u_x}{\partial x} - H_{66} \frac{\partial u_\theta}{\partial x} - \frac{B_{62}}{R} \left( w + \frac{\partial u_\theta}{\partial \theta} \right) - \frac{B_{66}}{R} \frac{\partial u_x}{\partial \theta} - J_{61} \frac{\partial \beta_x}{\partial x} - J_{66} \frac{\partial \beta_\theta}{\partial x} - \frac{D_{62}}{R} \frac{\partial \beta_\theta}{\partial \theta} - \frac{D_{66}}{R} \frac{\partial \beta_x}{\partial \theta} &= 0, \\
 M_{\theta\theta} - B_{21} \frac{\partial u_x}{\partial x} - B_{26} \frac{\partial u_\theta}{\partial x} - \frac{H'_{22}}{R} \left( w + \frac{\partial u_\theta}{\partial \theta} \right) - \frac{H'_{26}}{R} \frac{\partial u_x}{\partial \theta} - D_{21} \frac{\partial \beta_x}{\partial x} - D_{26} \frac{\partial \beta_\theta}{\partial x} - \frac{J'_{22}}{R} \frac{\partial \beta_\theta}{\partial \theta} - \frac{J'_{26}}{R} \frac{\partial \beta_x}{\partial \theta} &= 0, \\
 M_{\theta x} - B_{61} \frac{\partial u_x}{\partial x} - B_{66} \frac{\partial u_\theta}{\partial x} - \frac{H'_{62}}{R} \left( w + \frac{\partial u_\theta}{\partial \theta} \right) - \frac{H'_{66}}{R} \frac{\partial u_x}{\partial \theta} - D_{61} \frac{\partial \beta_x}{\partial x} - D_{66} \frac{\partial \beta_\theta}{\partial x} - \frac{J'_{62}}{R} \frac{\partial \beta_\theta}{\partial \theta} - \frac{J'_{66}}{R} \frac{\partial \beta_x}{\partial \theta} &= 0, \\
 Q_x - K_s G_{55} \left( \frac{\partial w}{\partial x} + \beta_x \right) + \frac{A_{54}}{R} \left( u_\theta - R\beta_\theta - \frac{\partial w}{\partial \theta} \right) &= 0, \\
 Q_\theta - A_{45} \left( \frac{\partial w}{\partial x} + \beta_x \right) + K_s \frac{G'_{44}}{R} \left( u_\theta - R\beta_\theta - \frac{\partial w}{\partial \theta} \right) &= 0, \\
 \frac{\partial N_{xx}}{\partial x} + \frac{1}{R} \frac{\partial N_{\theta x}}{\partial \theta} = -q_x, \quad \frac{\partial N_{x\theta}}{\partial x} + \frac{1}{R} \frac{\partial N_{\theta\theta}}{\partial \theta} + \frac{Q_\theta}{R} = -q_\theta, \quad \frac{\partial Q_x}{\partial x} + \frac{1}{R} \frac{\partial Q_\theta}{\partial \theta} + \frac{N_{\theta\theta}}{R} = q_x, \\
 \frac{\partial M_{xx}}{\partial x} + \frac{1}{R} \frac{\partial M_{\theta x}}{\partial \theta} - Q_x = 0, \quad \frac{\partial M_{x\theta}}{\partial x} + \frac{1}{R} \frac{\partial M_{\theta\theta}}{\partial \theta} - Q_\theta = 0,
 \end{aligned}$$

**Table 1.** Governing equations for the system in Figure 1.

Here  $Q_i$ ,  $N_{ij}$ , and  $M_{ij}$  represent shear and normal forces and moments,  $u_x$ ,  $u_\theta$ ,  $w$  are the components of the displacement in cylindrical coordinates, and  $\beta_x$ ,  $\beta_\theta$  are rotations of the tangents to the reference surface along the  $x$  and  $\theta$  axis. We also denote by  $\theta$  the counterclockwise orientation angle between the fiber direction and the panel coordinate system, and we set  $m = \cos \theta$ ,  $n = \sin \theta$ . Other panel constants are

$$\begin{aligned}
 A_{ij} &= \sum_{k=1}^N (\bar{Q}_{ij})_k (h_k - h_{k-1}), & B_{ij} &= \frac{1}{2} \sum_{k=1}^N (\bar{Q}_{ij})_k (h_k^2 - h_{k-1}^2), & D_{ij} &= \frac{1}{3} \sum_{k=1}^N (\bar{Q}_{ij})_k (h_k^3 - h_{k-1}^3), \\
 G_{ij} &= A_{ij} + a_1 B_{ij} + a_2 D_{ij}, & H_{ij} &= B_{ij} + a_1 D_{ij} + a_2 E_{ij}, & J_{ij} &= D_{ij} + a_1 E_{ij} + a_2 F_{ij}, \\
 G'_{ij} &= A_{ij} + b_1 B_{ij} + b_2 D_{ij}, & H'_{ij} &= B_{ij} + b_1 D_{ij} + b_2 E_{ij}, & J'_{ij} &= D_{ij} + b_1 E_{ij} + b_2 F_{ij},
 \end{aligned} \tag{1}$$

where for cylindrical panels  $a_1 = b_1 = 1/R$ ,  $a_2 = 0$ , and  $b_2 = 1/R^2$ . Although some of their values are very small for the problems considered below, these coefficients are all preserved, to achieve better

accuracy and do justice to the capability of the differential cubature method. The  $\bar{Q}_{ij}$  are defined as

$$\begin{aligned}
\bar{Q}_{11} &= Q_{11}m^4 + 2(Q_{12} + 2Q_{66})m^2n^2 + Q_{22}n^4, \\
\bar{Q}_{12} &= (Q_{11} + Q_{22} - 4Q_{66})m^2n^2 + Q_{12}(m^4 + n^4), \\
\bar{Q}_{22} &= Q_{11}n^4 + 2(Q_{12} + 2Q_{66})m^2n^2 + Q_{22}m^4, \\
\bar{Q}_{45} &= (Q_{55} - Q_{44})mn, \\
\bar{Q}_{16} &= (Q_{11} - Q_{12} - 2Q_{66})m^3n + (Q_{12} - Q_{22} + 2Q_{66})mn^3, \\
\bar{Q}_{26} &= (Q_{11} - Q_{12} - 2Q_{66})mn^3 + (Q_{12} - Q_{22} + 2Q_{66})m^3n, \\
\bar{Q}_{44} &= Q_{44}m^2 + Q_{55}n^2, \\
\bar{Q}_{55} &= Q_{44}n^2 + Q_{55}m^2, \\
\bar{Q}_{66} &= (Q_{11} + Q_{22} - 2Q_{12} - 2Q_{66})m^2n^2 + Q_{66}(m^4 + n^4),
\end{aligned} \tag{2}$$

while the  $Q_{ij}$  denote the elastic stiffness in the material coordinates (local axes) and are defined by

$$\begin{aligned}
Q_{11} &= E_1/\Delta, & Q_{12} &= E_1\nu_{21}/\Delta, & Q_{22} &= E_2/\Delta, & Q_{44} &= G_{23}, \\
Q_{55} &= G_{13}, & Q_{66} &= G_{12}, & \Delta &= 1 - \nu_{12}\nu_{21},
\end{aligned} \tag{3}$$

where  $E_i$ ,  $G_{ij}$  and  $\nu_{ij}$  are, respectively, the Young's moduli of elasticity in the principal directions, the shear moduli of each lamina, and Poisson's ratios characterizing the transverse contraction (expansion) under tension (compression) in the directions of the coordinate axes.

The boundary conditions for the panel can be any combination of

$$\text{Free (F):} \quad \begin{cases} N_{xx} = N_{x\theta} = Q_x = M_{xx} = M_{x\theta} = 0 & \text{for } x \text{ constant,} \\ N_{\theta x} = N_{\theta\theta} = Q_\theta = M_{\theta x} = M_{\theta\theta} = 0 & \text{for } \theta \text{ constant;} \end{cases} \tag{4}$$

$$\text{Simply supported (S):} \quad \begin{cases} N_{xx} = u_\theta = w = M_{xx} = \beta_\theta = 0 & \text{for } x \text{ constant,} \\ u_x = N_{\theta\theta} = w = \beta_x = M_{\theta\theta} = 0 & \text{for } \theta \text{ constant;} \end{cases} \tag{5}$$

$$\text{Clamped (C):} \quad u_x = u_\theta = w = \beta_x = \beta_\theta = 0 \quad \text{for } x \text{ constant and for } \theta \text{ constant.} \tag{6}$$

Since there are ten derivatives in the fifteen equations, five boundary conditions is available and also enough in each edge.

### 3. Application of the DCM

The first step to apply the DCM is to form a nondimensional version of the governing equations in Table 1. To do so, we let  $q_0$  be the uniform load or the amplitude of a sinusoidally distributed load, and introduce the dimensionless parameters

$$\begin{aligned}
w^* &= w \times E_1 h^3 / q_0 a^4, & u_i^* &= u_i \times E_1 h^3 / q_0 a^4, & \beta_i^* &= \beta_i \times E_1 h^3 / q_0 a^3, \\
M_{ij}^* &= M_{ij} / q_0 a^2, & N_{ij}^* &= N_{ij} / q_0 a, & Q_i^* &= Q_i / q_0 a,
\end{aligned} \tag{7}$$

where  $i, j = 1, 2$ . It is obvious that in the isotropic panel,  $E_1$  in (7) should be replaced by  $E$ . Then, for instance, the first equation in Table 1 becomes

$$N_{xx}^* - G_{11} \frac{a^2}{E_1 h^3} \frac{\partial u_x^*}{\partial x^*} - G_{16} \frac{a^2}{E_1 h^3} \frac{\partial u_\theta^*}{\partial x^*} - \frac{A_{12}}{R} \frac{a^3}{E_1 h^3} \left( w + \frac{\partial u_\theta}{\partial \theta} \right) - \frac{A_{16}}{R} \frac{a^3}{E_1 h^3} \frac{\partial u_x}{\partial \theta} - H_{11} \frac{a}{E_1 h^3} \frac{\partial \beta_x}{\partial x^*} - H_{16} \frac{a}{E_1 h^3} \frac{\partial \beta_\theta^*}{\partial x^*} - \frac{B_{12}}{R} \frac{a^2}{E_1 h^3} \frac{\partial \beta_\theta^*}{\partial \theta} - \frac{B_{16}}{R} \frac{a^2}{E_1 h^3} \frac{\partial \beta_x^*}{\partial \theta} = 0. \quad (8)$$

The next step is to choose a grid for the panel domain. A particular procedure should be used for node generation and their numbering in the DCM; details are given in [Civan 1994; Liew and Liu 1997; 1998; Teo and Liew 2002; Wu and Liu 2005]. For example, Figure 2 shows the entire panel with 61 nodes and their numbers. This method for grid generation and node numbering minimizes computational efforts. For other kinds of structures such as rectangular panel, the same numbering pattern for square panel is used in a scaled format.

It is then necessary to discretize the dimensionless governing equations. In the DCM, any linear operation such as a continuous function or various orders of partial derivatives of a multivariable function can be expressed as a weighted linear sum of discrete functions chosen within the overall domain of the problem [Civan 1994]. For instance, in a two-dimensional problem, the cubature approximation at the  $i$ -th discrete node is given by

$$\Re\{f(x, y)\}_i \cong \sum_{j=1}^n c_{ij} f(x_j, y_j) \quad i = 1, 2, \dots, n, \quad (9)$$

where  $\Re$  denotes a linear differential operator which can be any order of partial derivatives or combinations of these partial derivatives,  $i$  is the index of arbitrarily sequenced grid points for the two-dimensional solution domain,  $n$  is the total number of discrete points within the domain, and the  $c_{ij}$  are the  $n \times n$

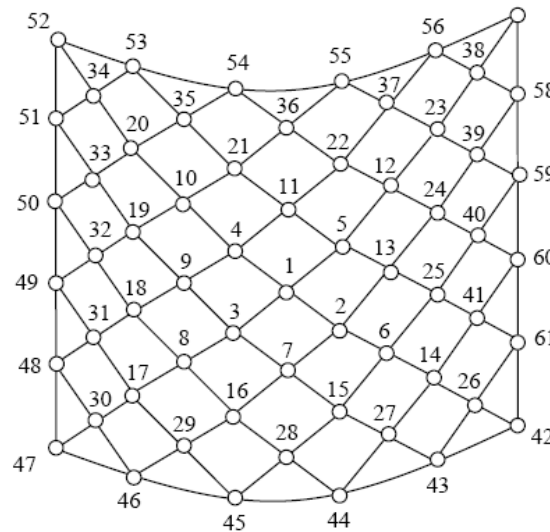


**Figure 2.** Grid generation and node numbering based on the DCM.

cubature weighting coefficients, to be determined. In order to find these coefficients, one uses a set of monomials in the form

$$F(x, y) = x^{m-n}y^n; \quad m = 0, 1, 2, \dots, k-1; \quad n = 0, 1, 2, \dots, m. \quad (10)$$

The number of these monomials should be equal to the total number  $n$  of grid points. The appropriate value of  $k$  in Equation (10) can be determined to satisfy this condition. For instance, for the case with 41 nodes, all of the monomials up to  $k = 8$  should be used. However, for  $k = 8$  there are only  $k(k+1)/2 = 36$  monomials. Therefore, five more monomials from the value of  $k = 9$  should be added to complete 41 monomials. The selection of these five monomials among those from  $k = 9$  does not influence the results. Once the monomials in (10) are constructed, one can reach  $n$  equations by substituting these monomials into (9). Introducing the  $n$  equations obtained to all grid points leads to  $n \times n$  equations, which are then used to calculate the  $n \times n$  unknowns  $c_{ij}$  in (9).

This process should be done for all of the operators in the governing equations and boundary conditions if necessary. Having determined all the coefficients for the operators in the governing equations, one can substitute them according to (9) into the equations of Table 1 to reach a set of linear equations.

The last step is to apply boundary conditions to the main equations. As with other numerical methods, various techniques can be used for this purpose. In this study, the discretized forms of the boundary conditions are added to the main system of equations. This leads to an over-determined system, whose (approximate) solution is obtained using the least-squares method [Toorani and Lakis 2000].

#### 4. Numerical results and discussions

The accuracy, convergence rate and performance of the presented DCM in obtaining solutions for the bending of laminated cylindrical panels are studied using seven test cases. Comparisons with results of other analytical and numerical studies available in the literature are provided in each case. To facilitate the comparison of our results with those in the literature, different definitions for dimensionless deflection of the panel are used in each case; the appropriate parameter definitions are mentioned both in the text and above the tables. Two kinds of loading conditions are used: uniform and sinusoidal distributed loads. To refer to the various boundary conditions, a number from 1 to 4 is assigned to each edge of the panel; see Figure 1. Thus, FSFC refers to a panel with free edges on the curved boundaries 1 and 3, simply supported on edge 2 and clamped on edge 4.

**Case 1: SSSS panels with uniform loading.** The first example is a SSSS cylindrical panel subjected to uniform loading  $q_0$ . Three types of panels are considered: isotropic, [0/90/0] and [0/90]. The panel is made of a square platform with side  $a$ . The ratio  $a/h$  of side length to thickness is chosen as 100, and the ratio  $a/R$  of side length to radius as 0.5. The Poisson's ratio for the isotropic panel is 0.3, while the material properties of the orthotropic layers are taken from [Qatu and Algothani 1994]:

$$E_1/E_2 = 15.4, \quad G_{12}/E_2 = 0.79, \quad \nu_{12} = 0.3. \quad (11)$$

Table 2 reports the predictions of the DCM for dimensionless central deflection, moments, and forces as defined in (7). Only 81 nodes are used to reach final convergence for DCM. Included in the table are also results of analytical and finite element method reported in [Qatu and Algothani 1994]. It is

	Model	$10^3 w^*$	$10N_x^*$	$10N_\theta^*$	$10N_{x\theta}^*$	$10^3 M_x^*$	$10^3 M_\theta^*$	$10^3 M_{x\theta}^*$
Isotropic ( $\nu = 0.3$ )	Analytic	179	-278	-248	0	6	-13	0
	FEM	177	-274	-250	0	5	-12	0
	DCM	179.41	-278.49	-247.96	0.000708	5.7191	-13.079	0.0003283
[0/90/0]	Analytic	86	-214	-248	0	50	-19	0
	FEM	89	-215	-252	0	53	-15	0
	DCM	86.09	-214.37	-247.66	0.000558	50.26	-18.814	0.0001531
[0/90]	Analytic	110	-268	-247	0	-40	38	0
	FEM	109	-264	-247	0	-40	42	0
	DCM	110.54	-268.83	-246.79	0.000655	-40.122	37.551	0.0004902

**Table 2.** Dimensionless central deflection and stress resultants of SSSS cylindrical panels under uniform load. Analytic and FEM results from [Qatu and Algotani 1994].

seen from the table that the DCM predictions for deflection, forces and moments are much closer to the analytical results than those of the FEM, although the DCM computation used 81 grid points, versus 100 eight-node elements used in the FEM results.

**Case 2: Symmetric SSSS panel under sinusoidal loading.** This example deals with two kinds of symmetric cross-ply laminated cylindrical panels: [0/90/0] and [90/0/90]. The geometric parameters are length  $a = 4$ , total angle  $\alpha = \pi/4$  and radius  $R = 1$ . The material properties of the layers are

$$E_1/E_2 = 25, \quad G_{12}/E_2 = 0.5, \quad G_{23}/E_2 = 0.2, \quad \nu_{12} = 0.25 \quad (12)$$

and we use the sinusoidal loading condition

$$q = q_0 \sin \frac{\pi x}{a} \sin \frac{\pi \theta}{\alpha}. \quad (13)$$

The predictions of the presented model for normalized deflection of symmetric panels are tabulated in Table 3 for the [0/90/0] panel and in the top half of Table 4 for the [90/0/90] panel. For comparison, the table lists the normalized deflection  $\bar{w}_1$  and the nondimensional deflection  $\bar{w}_2$ , defined by

$$\bar{w}_1 = 10wE_1/q_0s^3, \quad \bar{w}_2 = 10wE_1/q_0Rs^3; \quad s = R/h. \quad (14)$$

$s = R/h$	DCM			FEM
	$n = 25$	$n = 41$	$n = 61$	[Reddy 2004]
50	0.2350	0.5458	0.5459	0.5458
100	0.1500	0.4718	0.4718	0.4718
500	0.0342	0.1028	0.1026	0.1028

**Table 3.** Normalized central deflection  $\bar{w}_1 = 10wE_1/q_0s^3$  of a [0/90/0] symmetric SSSS cylindrical panel under sinusoidal loading.

[90/0/90] unsymmetric pannel							
$s = R/h$	DCM			FEM	FEM	TSDT	FSDT
	$n = 25$	$n = 41$	$n = 61$	Bhaskar	Cheng	Reddy	Reddy
4	2.8742	3.7792	3.8197	4.0090	3.6067	4.0816	3.7990
10	0.6992	1.0589	1.0752	1.2230	1.2033	1.1835	1.0713
50	0.2350	0.5425	0.5459	0.5495	0.5486	0.5504	0.5457
100	0.1500	0.4702	0.4718	0.4715	0.4711	0.4727	0.4718
500	0.0342	0.1025	0.1026	0.1027	0.1027	0.1028	0.1028

[0/90] unsymmetric pannel							
$s = R/h$	DCM			FEM	FEM	TSDT	FSDT
	$n = 25$	$n = 41$	$n = 61$	Bhaskar	Cheng	Reddy	Reddy
4	4.7670	6.8671	6.9548	6.1000	5.0970	6.6698	7.3282
10	2.0527	3.4692	3.5066	3.3300	3.1658	3.4498	3.6715
50	0.1572	2.2558	2.2641	2.2420	2.2371	2.2627	2.2865
100	0.1718	1.3665	1.3737	1.3670	1.3667	1.3738	1.3781
500	0.0435	0.1007	0.1005	0.1005	0.1005	0.1006	0.1006

**Table 4.** Normalized central deflection  $\bar{w}_2 = 10w E_1/q_0 R s^3$  of a [90/0/90] symmetric SSSS cylindrical panel (top) and a [0/90] unsymmetric SSSS cylindrical panel (bottom) under sinusoidal loading. The columns marked “Bhaskar”, “Cheng” and “Reddy” are taken from [Bhaskar and Varadan 1991], [Cheng et al. 2000] and [Reddy and Arciniega 2004].

We validate the model with the FEM results from [Reddy 2004; Reddy and Arciniega 2004; Bhaskar and Varadan 1991], and the results from [Cheng et al. 2000], which are based on a new imperfect-interface model. Considering that the loading is nonuniform in this example, the agreement is encouraging: with only 61 grid points we get highly accurate predictions for deflection of the panel when compared with FEM. The results for [0/90/0] deviate by less than 0.2% from those obtained in [Reddy 2004], which is quite satisfactory.

**Case 3: Unsymmetric SSSS panel under sinusoidal loading.** Table 4, bottom, deals with the results for an unsymmetric panel under the same loading condition and having the same material and geometric properties as in case 2. The laminate arrangement is [0/90]. Verification is done with the results in [Reddy and Arciniega 2004; Bhaskar and Varadan 1991; Cheng et al. 2000], and the nondimensional deflection  $\bar{w}_2$  defined in (14) is used. We see that even for an unsymmetric panel, the DCM provides acceptable predictions. For lower values of  $s = R/h$ , the DCM results are closer to the third-order shear deformation theory (TSDT) predictions.

**Case 4: Symmetric panel with different boundary conditions.** Next we consider a symmetric [0/90/0] cylindrical panel made from a square platform of side  $a$ , choosing the ratios  $a/h = 10$  and  $a/R = 0.2$ .

	DCM					HSDT	CST
	$n = 25$	$n = 41$	$n = 61$	$n = 85$	$n = 113$		
FSFS	6.8906	5.7138	5.7997	5.7910	5.8390	5.7912	5.5270
SSFS	3.4831	3.0705	3.2503	3.3308	3.3760	3.3519	3.1130
CSFS	1.3319	1.4614	1.5225	1.5490	1.5609	1.5809	1.1945
SSSS	0.8818	0.9428	0.9440	0.9440	0.9436	0.9650	0.7615
CSSS	0.5563	0.6103	0.6118	0.6119	0.6117	0.6337	0.3659
CSCS	0.3876	0.4346	0.4357	0.4357	0.4357	0.4540	0.2047

**Table 5.** Dimensionless central deflection  $\bar{w}_3 = 100wE_2h^3/q_0a^4$  of  $[0/90/0]$  cylindrical panel with various boundary conditions under sinusoidal loading. Our DCM calculations are based on FSDT assumptions, while the comparison results, taken from [Bhaskar and Varadan 1991], are obtained using higher-order shear deformation theory (HSDT) and classical shell theory (CST).

The two straight edges of the panel are simply supported, while the curved edges can be free, simply supported or clamped. The panel is subjected to sinusoidal loading given by (13), and the material properties of the layers are

$$E_1 = 19.2 \times 10^6 \text{ psi}, \quad E_2 = 1.56 \times 10^6 \text{ psi}, \quad G_{12} = 0.82 \times 10^6 \text{ psi}, \quad G_{23} = 0.523 \times 10^6 \text{ psi}, \quad \nu_{12} = 0.24. \quad (15)$$

Comparison of the dimensionless central deflection of the panel with FEM [Bhaskar and Varadan 1991] is reported in Table 5. Following that paper, the dimensionless form of the deflection reported is  $\bar{w}_3 = 100wE_2h^3/q_0a^4$ .

Clearly the DCM results are closer to the HSDT predictions than the CST results. Furthermore, the results show rapid convergence of the method; only minor differences are observed between the predictions with 41 grid points and higher numbers.

**Case 5: Unsymmetric panel with different boundary conditions.** The next case differs from Case 4 only in that it deals with an unsymmetric  $[0/90]$  cylindrical panel. Table 6 presents the results for the dimensionless central deflection  $\bar{w}_3 = 100wE_2h^3/q_0a^4$ . The predictions are compared with the results of CST, FSDT and HSDT reported in [Khdeir et al. 1989]. We see that the FSDT results obtained by DCM are in very good agreement with FSDT predictions reported in that reference, with a discrepancy never exceeding 1.3%. The results for shells with free boundary condition show slightly higher discrepancy than those without free edges. For instance, in comparison with the FSDT results of [Khdeir et al. 1989], the differences for FSFS, SSFS and CSFS are 1.24%, 1.18%, and 0.95%, respectively, whereas for SSSS, CSSS, and CSCS they are 0.63%, 0.47%, and 0.35%.

**Case 6: A symmetric SSSS angle-ply  $[\theta/-\theta/\theta/-\theta/\theta]$  panel.** The next example is a symmetric angle-ply  $[\theta/-\theta/\theta/-\theta/\theta]$  cylindrical panel made of a square platform with side length of  $a$ . choosing the ratios  $a/h = 10$  and  $a/R = \frac{1}{3}$ . All edges are simply supported and the transverse load is assumed to be uniform. The material properties of the layers are the same as in case 2; see (12).

Table 7 shows the predictions for the dimensionless central deflection  $\bar{w}_3 = 100wE_2h^3/q_0a^4$  of the panel, for various orientation angles  $\theta$ , together with FSDT- and HSDT-based results from [Bhaskar and

	DCM					CST	FSDT	HSDT
	$n = 25$	$n = 41$	$n = 61$	$n = 85$	$n = 113$			
FSFS	3.1259	2.9997	2.9720	2.9483	2.9576	2.6933	2.9213	2.9061
SSFS	2.3134	2.3003	2.3033	2.3062	2.3170	2.1053	2.2899	2.2791
CSFS	1.2296	1.5853	1.6198	1.6288	1.6364	1.4163	1.6210	1.6154
SSSS	1.2361	1.5666	1.5712	1.5714	1.5712	1.4211	1.5614	1.5550
CSSS	0.7472	1.0911	1.0994	1.1000	1.1002	0.9221	1.0951	1.0914
CSCS	0.4304	0.7886	0.7964	0.7971	0.7974	0.6148	0.7946	0.7925

**Table 6.** Dimensionless central deflection  $\bar{w}_3 = 100wE_2h^3/q_0a^4$  of  $[0/90]$  cylindrical panel with various boundary conditions under sinusoidal loading. The comparison results on the right are taken from [Khdeir et al. 1989].

	DCM					HSDT	FSDT
	$n = 25$	$n = 41$	$n = 61$	$n = 85$	$n = 113$		
$\theta = 15^\circ$	0.7896	0.8334	0.8481	0.8531	0.8552	0.8507	0.7802
$\theta = 30^\circ$	0.6179	0.7062	0.7233	0.7262	0.7199	0.7393	0.6386
$\theta = 45^\circ$	0.4516	0.5958	0.6234	0.6245	0.6471	0.6514	0.5561
$\theta = 60^\circ$	0.5781	0.7352	0.7421	0.7505	0.7516	0.7525	0.6517
$\theta = 75^\circ$	0.6181	0.8846	0.8812	0.8873	0.8893	0.8769	0.8053

**Table 7.** Dimensionless central deflection  $\bar{w}_3 = 100wE_2h^3/q_0a^4$  of a  $[\theta/-\theta/\theta/-\theta/\theta]$  SSSS cylindrical panel under uniform load. The comparison results are from [Bhaskar and Varadan 1991].

Varadan 1991]. It can be seen that discrepancies of the results for angle-ply laminated shells are higher than those of cross ply laminates.

**Case 7: Symmetric  $[0/90/0]$  square plate under sinusoidal loading.** The governing equations and solution procedure discussed here can also be employed for the bending analysis of rectangular plates, by making the panel radius  $R$  and the total angle  $\alpha$  correspondingly small. If the dimensions of the plate are  $a$  and  $b$ , we take  $a$  as before and  $\alpha = b/R$ .

The last example includes a fully simply supported symmetric  $[0/90/0]$  square plate subjected to sinusoidal load; see Equation (13). Material properties of all layers are the same as (12). Predictions for the dimensionless central deflection  $\bar{w}_4 = wE_2h^3/q_0a^4$  of the square plate are tabulated in Table 8. Again, comparisons with the results of analytical solutions [Whitney and Pagano 1970] and the generalized differential quadrature (GDQ) method [Aghdam et al. 2006] demonstrate good agreement. As can be concluded from the table, in the GDQ method results are obtained with 121 nodes while the DCM reaches the same level of accuracy by employing only 61 nodes. This might potentially mean that DCM requires less computation time than GDQ, for results of similar quality.



$a/h$	DCM				GDQ $11 \times 11$ Aghdam	Analytic Whitney
	$n = 13$	$n = 25$	$n = 41$	$n = 61$		
2	3.6450	5.2116	5.2288	5.2294	5.2293	5.2293
4	1.0174	1.7719	1.7750	1.7758	1.7758	1.7758
10	0.2086	0.6672	0.6683	0.6693	0.6693	0.6693
20	0.0556	0.4574	0.4923	0.4920	0.4921	0.4921
50	0.0021	0.1893	0.4406	0.4406	0.4411	0.4411
100	0.0001	0.1456	0.4310	0.4326	0.4337	0.4337

**Table 8.** Dimensionless central deflection  $\bar{w}_4 = wE_2h^3/q_0a^4$  of an SSSS [0/90/0] square plate under sinusoidal loading. The columns marked “Aghdam” and “Whitney” are taken from [Aghdam et al. 2006] and [Whitney and Pagano 1970].

## 5. Conclusion

We studied the performance of the differential cubature method in the static analysis of laminated cylindrical panels subject to uniform and sinusoidal loadings. The formulation presented allows the treatment of any type of lamination, whether symmetric or unsymmetric, and any combination of clamped, simply supported and free boundary conditions on the edges. Starting from the governing equations for cylindrical panels based on first-order shear deformation theory (fifteen first-order partial differential equations in the same number of unknowns), we proceed by discretizing the solution domain, governing equations and related boundary conditions, according to the DCM procedure. The results show that DCM can provide reasonably accurate predictions with relatively few grid points, and so may require less computational time than other numerical techniques, for a given accuracy level. The method provides the same order of accuracy for all stress and displacement variables within the solution domain. Comparison of calculated stress resultants and displacement components shows good agreement with results obtained using other analytical and numerical techniques.

## List of symbols

$R$	radius	$a$	side length
$h$	thickness	$s$	radius-to-thickness ratio
$\alpha$	total angle (Figure 1)	$q_0$	uniform load or the maximum of sinusoidally distributed load
$\theta$	orientation angle	$Q_i$	shear force
$N_{ij}$	normal force	$M_{ij}$	moment
$u_x, u_\theta, w$	displacement components	$\beta_x, \beta_\theta$	rotations of the tangents
$Q_{ij}$	elastic stiffness in the material	$E_i$	Young's moduli
	coordinates (local axes)	$\nu_{ij}$	Poisson's ratios
$G_{ij}$	shear moduli	$\bar{w}_2$	nondimension deflection
$\bar{w}_1$	normalized deflection	$M_{ij}^*, N_{ij}^*, Q_i^*$	dimensionless parameters
$w^*, u_i^*, \beta_i^*$	dimensionless parameters		

## References

- [Aghdam et al. 2006] M. M. Aghdam, M. R. N. Farahani, M. Dashty, and S. M. Rezaei Niya, "Application of generalized differential quadrature method to the bending of thick laminated plates with various boundary conditions", *Appl. Mech. Mater.* **5-6** (2006), 407–414.
- [Alavi et al. 2006] S. M. Alavi, M. M. Aghdam, and A. Eftekhari, "Three-dimensional elasticity analysis of thick rectangular laminated composite plates using meshless local Petrov-Galerkin (MLPG) method", *Appl. Mech. Mater.* **5-6** (2006), 331–338.
- [Alijani et al. 2008] F. Alijani, M. M. Aghdam, and M. Abouhamze, "Application of the extended Kantorovich method to the bending of clamped cylindrical panels", *Eur. J. Mech. A Solids* **27**:3 (2008), 378–388.
- [Artioli et al. 2005] E. Artioli, P. L. Gould, and E. Viola, "A differential quadrature method solution for shear-deformable shells of revolution", *Eng. Struct.* **27**:13 (2005), 1879–1892.
- [Berghaus 2001] D. G. Berghaus, *Numerical methods for experimental mechanics*, Kluwer, Boston, 2001.
- [Bhaskar and Varadan 1991] K. Bhaskar and T. K. Varadan, "A higher-order theory for bending analysis of laminated shells of revolution", *Comput. Struct.* **40**:4 (1991), 815–819.
- [Cheng et al. 2000] Z. Q. Cheng, L. H. He, and S. Kitipornchai, "Influence of imperfect interfaces on bending and vibration of laminated composite shells", *Int. J. Solids Struct.* **37**:15 (2000), 2127–2150.
- [Civan 1994] F. Civan, "Solving multivariable mathematical models by the quadrature and cubature methods", *Numer. Meth. Partial Differential Eq.* **10**:5 (1994), 545–567.
- [Jianqiao 1988] Y. Jianqiao, "A new approach for the bending problem of shallow shell by the boundary element method", *Appl. Math. Model.* **12**:5 (1988), 467–470.
- [Khdeir et al. 1989] A. A. Khdeir, L. Librescu, and D. Frederick, "A shear deformable theory of laminated composite shallow shell-type panels and their response analysis, II: static response", *Acta Mech.* **77**:1-2 (1989), 1–12.
- [Liew and Liu 1997] K. M. Liew and F. L. Liu, "Differential cubature method: a solution technique for Kirchhoff plates of arbitrary shape", *Comput. Methods Appl. Mech. Eng.* **145**:1-2 (1997), 1–10.
- [Liu and Liew 1998] F. L. Liu and K. M. Liew, "Differential cubature method for static solutions of arbitrarily shaped thick plates", *Int. J. Solids Struct.* **35**:28–29 (1998), 3655–3674.
- [Qatu and Algothani 1994] M. S. Qatu and A. Algothani, "Bending analysis of laminated plates and shells by different methods", *Comput. Struct.* **52**:3 (1994), 529–539.
- [Ramesh and Krishnamoorthy 1995] G. Ramesh and C. S. Krishnamoorthy, "Geometrically non-linear analysis of plates and shallow shells by dynamic relaxation", *Comput. Methods Appl. Mech. Eng.* **123**:1-4 (1995), 15–32.
- [Reddy 2004] J. N. Reddy, *Mechanics of laminated composite plates and shells: theory and analysis*, 2nd ed., CRC Press, Boca Raton, FL, 2004.
- [Reddy and Arciniega 2004] J. N. Reddy and R. A. Arciniega, "Shear deformation plate and shell theories: from Stavsky to present", *Mech. Adv. Mater. Struct.* **11**:6 (2004), 535–582.
- [Smith 2000] T. A. Smith, "Finite difference analysis of rotationally symmetric shells using variable node point spacings", *J. Sound Vib.* **230**:5 (2000), 1119–1145.
- [Teo and Liew 2002] T. M. Teo and K. M. Liew, "Differential cubature method for analysis of shear deformable rectangular plates on Pasternak foundations", *Int. J. Mech. Sci.* **44**:6 (2002), 1179–1194.
- [Toorani and Lakis 2000] M. H. Toorani and A. A. Lakis, "General equations of anisotropic plates and shells including transverse shear deformations, rotary inertia and initial curvature effects", *J. Sound Vib.* **237**:4 (2000), 561–615.
- [Toorani and Lakis 2001] M. H. Toorani and A. A. Lakis, "Shear deformation in dynamic analysis of anisotropic laminated open cylindrical shells filled with or subjected to a flowing fluid", *Comput. Methods Appl. Mech. Eng.* **190**:37-38 (2001), 4929–4966.
- [Whitney and Pagano 1970] J. M. Whitney and N. J. Pagano, "Shear deformation in heterogeneous anisotropic plates", *J. Appl. Mech. (ASME)* **37**:4 (1970), 1031–6.
- [Wu and Liu 2005] L. Wu and J. Liu, "Free vibration analysis of arbitrary shaped thick plates by differential cubature method", *Int. J. Mech. Sci.* **47**:1 (2005), 63–81.

[Yuan et al. 1998] S. Yuan, Y. Jin, and F. W. Williams, "Bending analysis of Mindlin plates by extended Kantorovich method", *J. Eng. Mech. (ASCE)* **124**:12 (1998), 1339–1345.

Received 12 Oct 2008. Revised 21 Mar 2009. Accepted 25 Mar 2009.

S. MAHMOUD MOUSAVI: [s\\_mousavi@aut.ac.ir](mailto:s_mousavi@aut.ac.ir)

*Department of Mechanical Engineering, Amirkabir University of Technology, 424 Hafez Avenue, Tehran 15875–4413, Iran*

MOHAMAD M. AGHDAM: [semahmoudmousavi@yahoo.com](mailto:semahmoudmousavi@yahoo.com)

*Department of Mechanical Engineering, Amirkabir University of Technology, 424 Hafez Avenue, Tehran 15875–4413, Iran*



## INDENTATION ANALYSIS OF FRACTIONAL VISCOELASTIC SOLIDS

ROUZBEH SHAHSAVARI AND FRANZ-JOSEF ULM

The constitutive differential equations governing the time-dependent indentation response for axisymmetric indenters into a fractional viscoelastic half-space are derived, together with indentation creep and relaxation functions suitable for the backanalysis of fractional viscoelastic properties from indentation data. These novel fractional viscoelastic indentation relations include, as a subset, classical integer-type viscoelastic models such as the Maxwell model or Zener model. Using the correspondence principle of viscoelasticity, it is found that the differential order of the governing equations of the indentation response is higher than the one governing the material level. This difference in differential order between the material scale and indentation scale is more pronounced for the viscoelastic shear response than for the viscoelastic bulk response, which translates, into fractional derivatives, the well-known fact that an indentation test is rather a shear test than a hydrostatic test. By way of example, an original method for the inverse analysis of fractional viscoelastic properties is proposed and applied to experimental indentation creep data of polystyrene. The method is based on fitting the time-dependent indentation data (in the Laplace domain) to the fractional viscoelastic model response. Applied to polystyrene, it is shown that the particular time-dependent response of this material is best captured by a bulk-and-deviator fractional viscoelastic model of the Zener type.

### 1. Introduction

The aim of indentation analysis is to link indentation data, typically an indentation force versus indentation depth curve,  $F-h$ , to meaningful mechanical properties of the indented material. It is common practice to condense the indentation data into two quantities, the hardness  $H$  and the indentation modulus  $M$ , which are related to measured indentation data, namely the maximum indentation force  $F_{\max}$ , the initial slope (or indentation stiffness)  $S$  of the unloading curve, and the projected contact area  $A_c$  by

$$H \stackrel{\text{def}}{=} \frac{F_{\max}}{A_c}, \quad S = \left. \frac{dF}{dh} \right|_{h=h_{\max}} \stackrel{\text{def}}{=} \frac{2}{\sqrt{\pi}} M \sqrt{A_c}. \quad (1)$$

Traditionally, for metals, the hardness  $H$  was early on recognized to relate to strength properties of the indented material [Brinell 1901; Tabor 1951], and recent developments in indentation analysis have extended those approaches to account for strain hardening [Cheng and Cheng 2004], cohesive-frictional strength behavior [Ganneau et al. 2006], and the effect of porosity on the strength behavior [Cariou et al. 2008]. The investigation of the link between the unloading slope  $S$  and the elasticity properties of the indented material is more recent, requiring depth sensing indentation techniques that provide a continuous

---

*Keywords:* fractional viscoelasticity, indentation analysis, creep, relaxation, correspondence principle, polystyrene.

This work was supported by Schoettler Fellowship Program at MIT, and Schlumberger–Doll Research, Cambridge, MA. The experimental data on Polystyrene was provided by Dr. Catherine Tweedie and Prof. Krystyn J. Van Vliet, of MIT's Department of Material Science and Engineering.

Indenter shape	$n$	$B$	$\phi$	$F$ - $h$ relation
Cone	1	$\cot \theta$	$\frac{2 \tan \theta}{\pi}$	$F = \frac{2M \tan \theta}{\pi} h^2$
Sphere	2	$1/2R$	$\frac{4\sqrt{R}}{3}$	$F = \frac{4M\sqrt{R}}{3} h^{1.5}$
Flat punch	$\rightarrow \infty$	$1/a^n$	$2a$	$F = 2Mah$

**Table 1.**  $F$ - $h$  equations for different indenter shapes.  $\theta$  is the half-cone angle,  $R$  and  $a$  are the sphere radius and the flat cylinder punch, respectively.

record of the  $F$ - $h$  curve during loading and unloading in an indentation test [Tabor 1951; Doerner and Nix 1986; Oliver and Pharr 1992; Bulychev 1999]. Relation (1)<sub>2</sub> is an exact relation for linear elastic materials. For non-elastic materials, (1)<sub>2</sub> becomes an approximate relation and  $S$  may be affected by the residual stress field and by adhesion of materials [Borodich and Galanov 2008]. Application of the depth sensing indentation techniques in indentation analysis confirmed the link provided by classical linear elastic contact mechanics solutions [Hertz 1882; Boussinesq 1885; Love 1939; Galin 1961; Sneddon 1965; Borodich and Keer 2004] for a rigid indenter of axysmmetric shape that can be described by a monomial function of the form  $z = Br^n$ :

$$F = \phi M h^{1+1/n}, \quad (2)$$

where  $r$  and  $z$  are, respectively, the first and the third cylindrical coordinates of the surface of the tip,  $\phi$  (of dimension  $[\phi] = L^{1-1/n}$ ), condenses the indenter specific geometry parameters,

$$\phi = \frac{2}{(\sqrt{\pi} B)^{1/n}} \frac{n}{n+1} \left[ \frac{\Gamma(n/2 + 1/2)}{\Gamma(n/2 + 1)} \right]^{1/n}, \quad (3)$$

$B$  is the shape function of the indenter at unit radius,  $n \geq 0$  is the degree of the homogeneous function,  $\Gamma(x)$  is the Euler Gamma function,  $\Gamma(x) = \int_0^\infty t^{x-1} \exp(-t) dt$ . Table 1 develops expression (2) for some common indenter shapes. Finally,  $M$  is the indentation modulus. The indentation modulus  $M$  provides a snapshot of the elasticity of the indented material. In the isotropic case,  $M$  relates to the bulk and shear modulus ( $K$ ,  $G$ ) of the indented half-space by

$$M = 4G \frac{3K + G}{3K + 4G}. \quad (4)$$

Based on the adaptation for indentation analysis of the method of functional equations [Lee and Radok 1960], closed-form solutions for indentation in various linear viscoelastic solids became recently available for a variety of indenter shapes: flat punch indentation [Cheng et al. 2000], spherical indentation [Cheng et al. 2005; Oyen 2005], and conical indentation [Vandamme and Ulm 2006; Oyen 2006], which have been synthesized into viscoelastic indentation creep and relaxation functions for any indenter of axysmmetric shape [Vandamme and Ulm 2007]. Those linear viscoelastic approaches are relevant for materials whose behavior can be described by the classical *integer-type* time-dependent differential equation of

linear viscoelasticity [Bland 1960],

$$\sigma + \sum_{i=1}^I P_i \frac{d^i \sigma}{dt^i} = E' \left( \varepsilon + \sum_{j=1}^J Q_j \frac{d^j \varepsilon}{dt^j} \right), \quad (\text{for } i = 1, 2, \dots, I; j = 1, 2, \dots, J), \quad (5)$$

where  $\sigma$  and  $\varepsilon$  are stress and strain,  $P_i$  and  $Q_j$  stand for relaxation and retardation time, respectively, and  $E'$  is the relaxed elasticity modulus. The restriction to integer-type time derivatives to describe the ‘real’ stress relaxation and creep behavior of polymers and other materials has been recognized as a drawback for material characterization [Rossikhin and Shitikova 2004] and can be removed by the introduction of fractional derivatives in the time-dependent differential equation. The application of fractional viscoelastic material models in indentation analysis is the focus of this paper. The paper is structured as follows: Following a brief review of the basic concepts of fractional derivatives, we derive a general differential representation of the time-dependent indentation response of a fractional viscoelastic material half-space using the correspondence principle. The general solution is then adapted to derive creep and relaxation functions that potentially allow the determination of meaningful viscous material properties from time-dependent experimental indentation data.

## 2. Elements of fractional order derivatives

Fractional calculus is an old mathematical topic, but its application in physics and engineering is more recent. For instance, in viscoelasticity and hereditary solid mechanics [Bagley and Torvik 1983], electromagnetic systems [Engheta 1996], and diffusion phenomena in inhomogeneous media [Arkhincheev 1993], fractional order derivatives have been used to describe the system behavior. From a mathematical perspective, fractional derivatives are an extension of ordinary derivatives, and possess mathematical definitions and properties that stem from ordinary derivatives. Some definitions of fractional derivatives can be found in [Podlubny 1999] and [Kilbas et al. 2006]. The Riemann–Liouville definition is the simplest one. According to this definition, the  $\alpha$ -th order fractional derivative of a function  $f(t)$  with respect to  $t$  is

$$D^\alpha f(t) = \frac{\partial^\alpha}{\partial t^\alpha} f(t) = \frac{1}{\Gamma(m-\alpha)} \frac{\partial^m}{\partial t^m} \int_a^t \frac{f(\tau)}{(t-\tau)^{\alpha+1-m}} d\tau, \quad m-1 \leq \alpha < m, \quad (6)$$

where  $m$  is the first integer larger than  $\alpha$ , and  $a$  is the lower limit related to the operation of fractional differentiation. Following [Ross 1977], we call  $a$  the lower terminal value and set  $a = 0$  for all fractional definitions in this article. We also use the short hand notation  $D^\alpha f(t) = \frac{\partial^\alpha}{\partial t^\alpha} f(t)$ . The Laplace transform of the Riemann–Liouville derivative is given by

$$\widehat{D^\alpha f(t)} = s^\alpha \widehat{f(s)} - \sum_{k=0}^{m-1} s^k D^{\alpha-k-1} f(0), \quad m-1 \leq \alpha < m, \quad (7)$$

where  $s$  is the Laplace parameter and  $\widehat{f(s)}$  stands for the Laplace transform of  $f(t)$ . Applying this definition to solve initial value problems requires knowledge of the non-integer derivatives of the initial conditions at  $t = 0$ . Despite the fact that mathematically these problems can be solved successfully, their solution is practically meaningless because there is no physical interpretation available for such

initial conditions. A solution to this conflict was proposed by Caputo [1967; 1969]. Caputo's fractional derivative (for a zero terminal value) can be written as

$$D^\alpha f(t) = \frac{1}{\Gamma(m-\alpha)} \int_0^t \frac{f^{(m)}(\tau)}{(t-\tau)^{\alpha+1-m}} d\tau, \quad m-1 < \alpha < m, \quad (8)$$

where  $f^{(m)}(\tau) = \frac{\partial^m}{\partial \tau^m} f(\tau)$ . The Laplace transform of (8) is given by

$$\widehat{D^\alpha f(t)} = s^\alpha \widehat{f(s)} - \sum_{k=0}^{m-1} s^{\alpha-1-k} f^{(k)}(0), \quad m-1 < \alpha \leq m, \quad (9)$$

where in (9), only ordinary derivatives are acted upon initial conditions. Another main difference between the two definitions is that the Caputo derivative (8) of a constant  $C$  is zero,

$$D^\alpha C = 0, \quad (10)$$

whereas in the cases of a finite lower terminal value, the Riemann–Liouville fractional derivative (6) of a constant  $C$  is not zero but is given by [Podlubny 1999]

$$D^\alpha C = \frac{Ct^{-\alpha}}{\Gamma(1-\alpha)}. \quad (11)$$

It can be shown that for  $\alpha \rightarrow m$ , Caputo's fractional derivative becomes a conventional  $m$ -th derivative [Podlubny 1999; Kilbas et al. 2006],

$$D^\alpha f(t) = f^{(m)}(t). \quad (12)$$

Similar to integer-order differentiation, Caputo's fractional differentiation is a linear operation,

$$D^\alpha (\lambda f(t) + \mu g(t)) = \lambda D^\alpha f(t) + \mu D^\alpha g(t), \quad (13)$$

where  $\lambda$  and  $\mu$  are constants. Analogous to [Schuessel et al. 1995], by using Caputo's fractional derivative, the well-known Hookian spring relation,  $\sigma(t) = E\varepsilon(t)$ , and Newtonian dashpot relation,  $\sigma(t) = \eta d\varepsilon(t)/dt$ , can be generalized to

$$\sigma(t) = E\tau^\alpha \frac{d^\alpha \varepsilon(t)}{dt^\alpha} = E\tau^\alpha D^\alpha \varepsilon(t), \quad 0 < \alpha < 1. \quad (14)$$

In (14), the parameter  $\tau$  with units of time is employed to non-dimensionalize the fractional derivative of  $\varepsilon$ , which helps to obtain a meaningful physical relation between stress and strain. Note that here, since  $0 < \alpha < 1$ , Eq (8) reduces to

$$D^\alpha f(t) = \frac{1}{\Gamma(1-\alpha)} \int_0^t \frac{f^{(1)}(\tau)}{(t-\tau)^\alpha} d\tau, \quad 0 < \alpha < 1. \quad (15)$$

Throughout this work, we will exclusively refer to Caputo's definition when using the term fractional derivatives. A full discussion on differences between Caputo and Riemann–Liouville fractional derivatives, and the conditions when they both become equivalent, can be found in [Podlubny 1999]. The introduction of the integrodifferential operator (15) in (14) offers a number of interesting perspectives for modeling viscoelastic behavior. From a mathematical perspective, due to the convolution with  $t^{-\alpha}$ ,  $\sigma(t)$  has a fading memory [Baker et al. 1996]. To illustrate this behavior, consider a simple rod in uniaxial



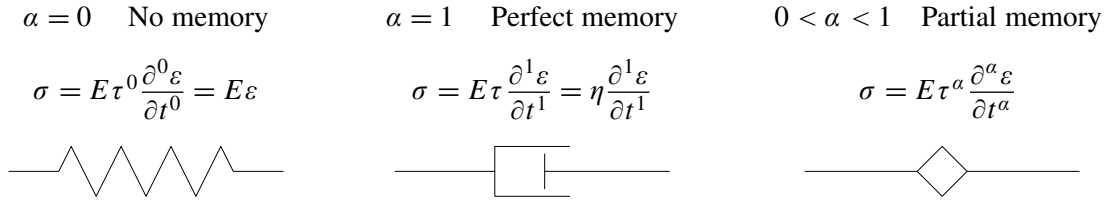


**Figure 1.** Illustration of integer and fractional models.

extension by a strain  $\varepsilon$ . In the limit cases, if  $\alpha = 0$ ,  $D^\alpha \varepsilon = \varepsilon$ , and if  $\alpha = 1$ ,  $D^\alpha \varepsilon = \dot{\varepsilon}$  (this can be proved by integration by parts). Thus, by multiplying a constant,  $E\tau^\alpha$ , to  $D^\alpha \varepsilon$ , depending on the value of  $\alpha$ , one obtains either the elastic force (spring model) or the damping force (dashpot model). In other words,  $\alpha = 0$  corresponds to a system with no memory since the stress depends only on the instantaneous magnitude of  $\varepsilon$  (Figure 1, left), while  $\alpha = 1$  corresponds to a system with perfect memory since the time history and the particular way the system has reached its current position becomes important for derivative calculations (Figure 1, middle). For any  $0 < \alpha < 1$ , the system has partial memory, and consequently the derived stress is a combination of dashpot and spring models (symbolized by a square in Figure 1, right). Relative to discrete (integer) derivatives, therefore, fractional derivatives offer a wide range for modeling the rate of change of the time-dependent behavior of viscoelastic materials in a continuous fashion. Figure 2 displays a simple function along with its half-derivative and first derivative, showing that fractional derivatives are usually sandwiched in between the closest lower and upper integer-derivatives. This allows one to monitor changes in a much smoother and compact fashion than offered by integer derivatives.

While spring and dashpot models can be recognized by only one material property parameter ( $E$  and  $\eta$ , respectively), introducing a fractional element requires three parameters, called  $\alpha$ ,  $\tau$ , and  $E$ . A fractional element with only three parameters is mathematically and physically equivalent to an infinite number of simple springs and dashpots connected through a certain hierarchical arrangement [Schuessel and Blumen 1993]. Thus, capturing the continuous rate of change in time by means of integer-type models requires

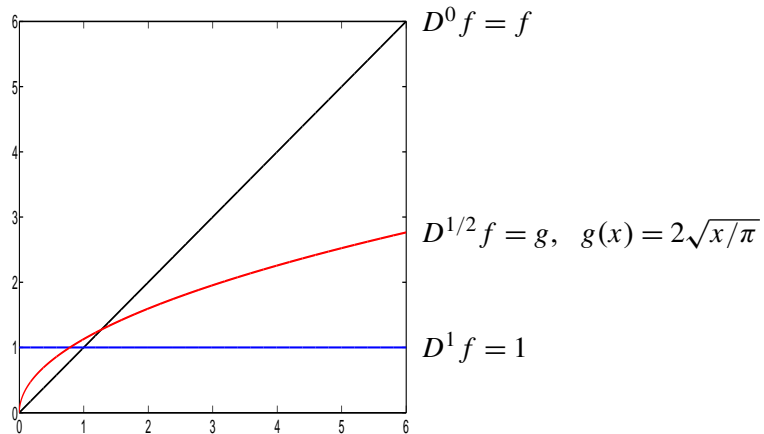


**Figure 2.** Derivatives of  $f(x) = x$  of order 0 (black),  $\frac{1}{2}$  (red) and 1 (blue).

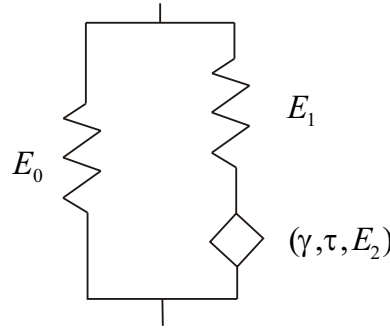


**Figure 3.** Fractional Zener model with identical fractional order derivatives on stress and strain.

generally many higher integer-order derivative terms in (5) to achieve a similar accuracy. With the above preliminary explanations, the extension of (5) to fractional derivatives can be written as

$$\sigma + \sum_{i=1}^I P_i \tau^{\alpha_i} D^{\alpha_i} \sigma = E' \left( \varepsilon + \sum_{j=1}^J Q_j \tau^{\beta_j} D^{\beta_j} \varepsilon \right), \quad (\text{for } i = 1, 2, \dots, I; j = 1, 2, \dots, J), \quad (16)$$

where  $\alpha_i, \beta_j \in [0, 1]$ . Each fractional term in (16) can be considered as a replacement of a system made of many conventional springs and dashpots.

By way of application, consider a fractional Zener viscoelastic material, shown in Figure 3, in which the dashpot of the conventional Zener model is replaced by a fractional element. As shown below, this model is described by a fractional differential equation in which only the first fractional derivative terms ( $I = J = 1$ ) are present in each series in (16), and in which the fractional derivative of stress and strain is identical ( $\alpha_1 = \beta_1$ ). There are five independent parameters in this model, called  $E_0, E_1, E_2, \gamma, \tau$ . Indeed, the total strain on the right branch is

$$\varepsilon = \varepsilon_s + \varepsilon_f, \quad (17)$$

where subscripts  $s, f$  refer to the spring element and the fractional element, respectively. As these elements are connected in series, their stresses are equal,

$$\sigma_R = E_1 \varepsilon_s = E_2 \tau^\gamma D^\gamma \varepsilon_f. \quad (18)$$

We now take advantage of the linearity property of the fractional operator (13). By taking the  $\gamma$ -th derivative of (17) and using (18) (assuming  $E_1, E_2$  and  $\tau$  are constants), we obtain

$$\sigma_R + \frac{E_2 \tau^\gamma}{E_1} D^\gamma \sigma_R = E_2 \tau^\gamma D^\gamma \varepsilon, \quad (19)$$

where we let

$$\tau_0 = \left( \frac{E_2 \tau^\gamma}{E_1} \right)^{1/\gamma}, \quad S = E_2 \left( \frac{\tau}{\tau_0} \right)^\gamma. \quad (20)$$

Equation (19) simplifies to

$$\sigma_R + \tau_0^\gamma D^\gamma \sigma_R = S \tau_0^\gamma D^\gamma \varepsilon. \quad (21)$$

Equation (21), which describes the behavior of the right branch of the model in Figure 3, turns out to be the constitutive fractional differential equation of a Maxwell model in which the conventional dashpot is replaced by the fractional element.

The total stress in the parallel system is

$$\sigma = \sigma_L + \sigma_R, \quad (22)$$

where  $\sigma_L$  is the elastic stress in the left branch of the model displayed in Figure 3

$$\sigma_L = E_0 \varepsilon. \quad (23)$$

Then, take the  $\gamma$ -th derivative of (22) and multiply the result with  $\tau_0^\gamma$ :

$$\tau_0^\gamma D^\gamma \sigma = \tau_0^\gamma D^\gamma \sigma_L + \tau_0^\gamma D^\gamma \sigma_R. \quad (24)$$

Finally, by adding (24) and (22), and using (23) and (21), we obtain

$$\sigma + \tau_0^\gamma D^\gamma \sigma = E_0 \varepsilon + (E_0 + S) \tau_0^\gamma D^\gamma \varepsilon. \quad (25)$$

Equation (25) is recognized as the one-dimensional constitutive equation of the fractional Zener model shown in Figure 3. It is characterized by identical fractional order derivatives on stress and strain. This is an important requirement for thermodynamic stability of the model described by (25).<sup>1</sup> More generalized constitutive equations including different fractional order derivatives on stress and strain can be found in [Schiessel et al. 1995]. In what follows, we employ the fractional Zener model in indentation analysis.

### 3. Time-dependent indentation response of fractional viscoelastic materials

In general, the time-dependent behavior of hereditary materials, for which the stress depends nonlinearly on the strain history, can be described by the volterra integral equations [Rabotnov 1980]. Most viscoelastic indentation solutions originate from the method of functional equations developed for linear viscoelastic contact problems by Radok [1957] and completed by Lee and Radok [1960]. The method of functional equations consists of solving the viscoelastic problem from the elastic solution by replacing the elastic moduli with their corresponding viscoelastic operators. The method of functional equations can be seen as an extension of the Laplace transform method, as formulated by Lee [1955]. The Laplace transform method consists of eliminating the explicit time dependence of the viscoelastic problem by applying the Laplace transform to the time-dependent moduli and solving the corresponding elasticity problem in the Laplace domain. The Laplace method, however, is restricted to boundary value problems in which the displacement and stress boundary conditions are fixed in time. This is generally not the case in indentation problems (except for the flat punch problem), in which the contact area changes with time, hence changing a part of the stress boundary outside the contact area into a displacement boundary inside the contact area and *vice versa*. This drawback of the Laplace transform was lifted in [Radok 1957; Lee and Radok 1960], which introduced and developed the method of functional equations, valid for linear viscoelastic problems with time-dependent boundary conditions. Galanov [1982] established

<sup>1</sup>There is a special case in which (25), with different fractional derivatives on stress and strain, can be thermodynamically stable. That is, when the fractional derivative acting on strain is greater than that acting on stress, and only below a certain limiting frequency [Glöckle and Nonnenmacher 1991].

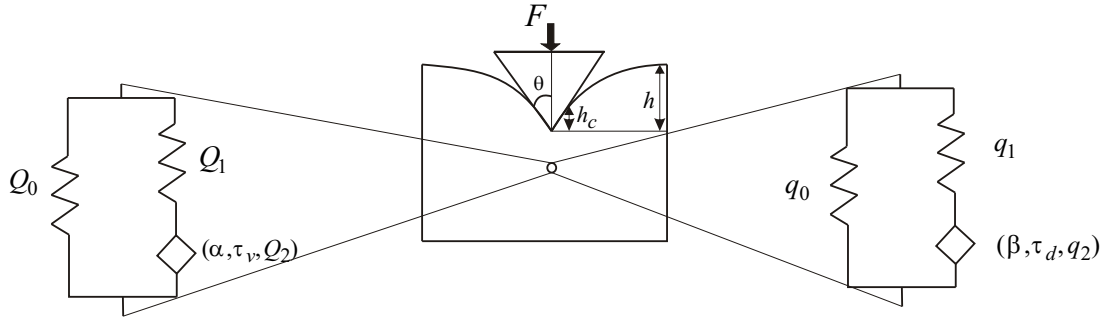


**Figure 4.** A rigid conical indenter on a fractional viscoelastic half-space material (middle) can be studied with a fractional Zener model describing volumetric behavior in indentation (left) or one describing deviatoric behavior in indentation (right).

self-similarity of the contact problem for some viscoelastic solids and gave dimensionless distributions for stresses under Vickers and Berkovich indenters. For indentation problems, the method of functional equations remains valid as long as the contact area (or, equivalently, for viscoelastic materials, the penetration depth) increases monotonically [Lee and Radok 1960]. We shall adopt this method for indentation analysis of fractional viscoelastic materials.

We consider the fractional Zener model shown in Figure 3, whose one-dimensional behavior is described by (25).<sup>2</sup> We employ this model separately for the volumetric and deviatoric part of the three-dimensional stress tensor and strain tensors of the material response to indentation. For the volumetric part with parameters  $Q_0, Q_1, Q_2, \alpha, \tau_v$ , by setting, similarly to (20),

$$\zeta_v = \left( \frac{Q_2 \tau_v^\alpha}{Q_1} \right)^{1/\alpha}, \quad K_0 = Q_2 \left( \frac{\tau_v}{\zeta_v} \right)^\alpha, \quad (26)$$

the fractional differential equation governing the time-dependent spherical isotropic material response reads (Figure 4, left),

$$\sigma_v + \zeta_v^\alpha D^\alpha \sigma_v = Q_0 \epsilon_v + (Q_0 + K_0) \zeta_v^\alpha D^\alpha \epsilon_v, \quad (27)$$

where  $\sigma_v = \frac{1}{3}(\text{tr } \boldsymbol{\sigma}) \mathbf{1}$ ,  $\epsilon_v = \frac{1}{3}(\text{tr } \boldsymbol{\epsilon}) \mathbf{1}$ , are the volumetric parts of the second order stress tensor  $\boldsymbol{\sigma}$  and second order strain tensor  $\boldsymbol{\epsilon}$ , respectively. Similarly, for the deviatoric part with parameters  $q_0, q_1, q_2, \beta, \tau_d$ , by setting

$$\zeta_d = \left( \frac{q_2 \tau_d^\beta}{q_1} \right)^{1/\beta}, \quad G_0 = q_2 \left( \frac{\tau_d}{\zeta_d} \right)^\beta, \quad (28)$$

the fractional differential equation governing the time-dependent deviatoric isotropic material response reads (Figure 4, right)

$$\sigma_d + \zeta_d^\beta D^\beta \sigma_d = q_0 \epsilon_d + (q_0 + G_0) \zeta_d^\beta D^\beta \epsilon_d. \quad (29)$$

Here  $\sigma_d$  and  $\epsilon_d$  are, respectively, the deviatoric parts of the second order stress and strain tensors,  $\boldsymbol{\sigma}$  and  $\boldsymbol{\epsilon}$ . From basic tensor algebra, relations  $\boldsymbol{\sigma} = \sigma_v + \sigma_d$ ,  $\boldsymbol{\epsilon} = \epsilon_v + \epsilon_d$  hold. Thus, as Figure 4 shows, based

<sup>2</sup>For a general nonlinear stress-strain behavior in solids, the fractional calculus can be integrated into the volterra equations [Rabotnov 1980].

on our chosen models, there are in total 10 independent parameters  $Q_0, Q_1, Q_2, \alpha, \tau_v, q_0, q_1, q_2, \beta, \tau_d$  that describe the volumetric and deviatoric material behavior (five for each behavior). For simplicity in notation and avoiding carrying too many parameters in our analytical derivations, we rewrite (27) and (29) as

$$\sigma_v(t) + PD^\alpha \sigma_v(t) = Q_0 \boldsymbol{\varepsilon}_v(t) + QD^\alpha \boldsymbol{\varepsilon}_v(t), \quad (30)$$

$$\sigma_d(t) + pD^\beta \sigma_d(t) = q_0 \boldsymbol{\varepsilon}_d(t) + qD^\beta \boldsymbol{\varepsilon}_d(t), \quad (31)$$

where we let

$$P = \zeta_v^\alpha, \quad Q = (Q_0 + K_0)\zeta_v^\alpha, \quad (32)$$

$$p = \zeta_d^\beta, \quad q = (q_0 + G_0)\zeta_d^\beta. \quad (33)$$

Using (9), the Laplace transforms of (30) and (31) are readily obtained:

$$\begin{aligned} (1 + Ps^\alpha)\widehat{\sigma}_v(s) - Ps^{\alpha-1}\sigma_v(0) &= (Q_0 + Qs^\alpha)\widehat{\boldsymbol{\varepsilon}}_v(s) - Qs^{\alpha-1}\boldsymbol{\varepsilon}_v(0), \\ (1 + ps^\beta)\widehat{\sigma}_d(s) - ps^{\beta-1}\sigma_d(0) &= (q_0 + qs^\beta)\widehat{\boldsymbol{\varepsilon}}_d(s) - qs^{\beta-1}\boldsymbol{\varepsilon}_d(0), \end{aligned} \quad (34)$$

where  $\widehat{\sigma}_v(s), \widehat{\sigma}_d(s), \widehat{\boldsymbol{\varepsilon}}_v(s), \widehat{\boldsymbol{\varepsilon}}_d(s)$  denote the Laplace transforms of  $\sigma_v(t), \sigma_d(t), \boldsymbol{\varepsilon}_v(t), \boldsymbol{\varepsilon}_d(t)$ , whereas  $\sigma_v(0), \sigma_d(0), \boldsymbol{\varepsilon}_v(0), \boldsymbol{\varepsilon}_d(0)$  represent the stress and strain initial conditions at  $t = 0$ . We remind ourselves of the classical Laplace transformations of the stress convolution integrals of linear isotropic viscoelasticity [Christensen 1971]:

$$\begin{aligned} \sigma_v(t) &= \int_{-\infty}^t 3K(t-\tau) \frac{d}{d\tau} \boldsymbol{\varepsilon}_v(\tau) d\tau \rightarrow \widehat{\sigma}_v(s) = 3s\widehat{K}(s)\widehat{\boldsymbol{\varepsilon}}_v(s), \\ \sigma_d(t) &= \int_{-\infty}^t 2G(t-\tau) \frac{d}{d\tau} \boldsymbol{\varepsilon}_d(\tau) d\tau \rightarrow \widehat{\sigma}_d(s) = 2s\widehat{G}(s)\widehat{\boldsymbol{\varepsilon}}_d(s), \end{aligned} \quad (35)$$

where  $K(t)$  and  $G(t)$  are the time-dependent bulk and shear modulus, respectively. Then, by comparing (34) and (35), one obtains the following relations for bulk and shear response of the fractional material:

$$3s\widehat{K}(s) = \frac{Q_0 + Qs^\alpha}{1 + Ps^\alpha}, \quad 2s\widehat{G}(s) = \frac{q_0 + qs^\beta}{1 + ps^\beta}, \quad (36)$$

and

$$P\sigma_v(0) = Q\boldsymbol{\varepsilon}_v(0), \quad p\sigma_d(0) = q\boldsymbol{\varepsilon}_d(0). \quad (37)$$

Equations (37) indicate that the initial conditions acting upon stress and strain are not completely independent, and relations such as (37) must be satisfied. These constraints do not appear only in fractional viscoelastic models. Analogous constraints on initial conditions also exist for integer-order viscoelastic models [Christensen 1971; Shahsavari and Ostoja-Starzewski 2005].

Similarly, application of the correspondence principle to the elastic indentation modulus  $M$  defined by (4) yields [Vandamme and Ulm 2006]

$$M \rightarrow s\widehat{M}(s) = 4s\widehat{G}(s) \frac{3s\widehat{K}(s) + s\widehat{G}(s)}{3s\widehat{K}(s) + 4s\widehat{G}(s)}. \quad (38)$$

Next, analogously to (35), the application of the correspondence principle of viscoelasticity to the elastic indentation force relation (2) yields

$$F(t) = \phi \int_{-\infty}^t M(t-\tau) \frac{d}{d\tau} h^{1+1/n}(\tau) d\tau \implies \widehat{F}(s) = \phi s \widehat{M}(s) \widehat{h^{1+1/n}}(s). \quad (39)$$

In (39), we a priori assumed the geometry parameter  $\phi$  is a time-independent parameter, following [Lee and Radok 1960]. By substituting (36) in (38) and then in (39), one obtains the viscoelastic relation between  $\widehat{F}(s)$  and  $\widehat{h^{1+1/n}}$  in the transformed Laplace space. Next, by extensively rearranging the terms and using the relation (9) along with the linearity property (13) for the fractional order terms, the constitutive differential equation governing the time-dependent indentation response becomes

$$D_F(F(t)) = 2\phi D_h(h^{1+1/n}(t)). \quad (40)$$

This is a differential equation with constant coefficients involving the operators

$$\begin{aligned} D_F &= c_0 + c_1 D^\alpha + c_2 D^\beta + c_3 D^{\alpha+\beta} + c_4 D^{\alpha+2\beta} + c_5 D^{2\beta}, \\ D_h &= l_0 + l_1 D^\alpha + l_2 D^\beta + l_3 D^{\alpha+\beta} + l_4 D^{\alpha+2\beta} + l_5 D^{2\beta} \end{aligned} \quad (41)$$

with coefficients

$$\begin{aligned} c_0 &= Q_0 + 2q_0, & l_0 &= \frac{1}{2}q_0^2 + q_0Q_0, \\ c_1 &= Q + 2Pq_0, & l_1 &= q_0Q + \frac{1}{2}Pq_0^2, \\ c_2 &= 2Q_0p + 2q + 2pq_0, & l_2 &= q_0pQ_0 + qq_0 + qQ_0, \\ c_3 &= 2Qp + 2Pq + 2Ppq_0, & l_3 &= q_0pQ + Pqq_0 + qQ, \\ c_4 &= Qp^2 + 2Ppq, & l_4 &= qpQ + \frac{1}{2}Pq^2, \\ c_5 &= Q_0p^2 + 2pq, & l_5 &= qpQ_0 + \frac{1}{2}q^2. \end{aligned} \quad (42)$$

Note that in view of (37) the following relations between initial conditions hold:

$$c_i F(0) = 2\phi l_i \Omega(0), \quad (i = 1, 2, \dots, 5), \quad (43)$$

$$c_i F^{(1)}(0) = 2\phi l_i \Omega^{(1)}(0), \quad (i = 3, 4, 5), \quad (44)$$

$$c_4 F^{(2)}(0) = 2\phi l_4 \Omega^{(2)}(0), \quad (45)$$

where we have set  $\Omega(0) = h^{1+1/n}(0)$ . Considering the initial conditions above, the use of Caputo's derivative results in five integer-order relations in (43) and four inter-order derivatives in (44) and (45). In order for (44) to hold with  $i = 3$ , we must have  $\alpha + \beta > 1$ ; the same relation with  $i = 4$  and  $i = 5$  requires  $\alpha + 2\beta > 1$  and  $2\beta > 1$ , respectively. Similarly, (45) requires that  $\alpha + 2\beta > 2$ . If any of these conditions is not met, the corresponding relation in (44)–(45) does not exist.

The following observations deserve attention:

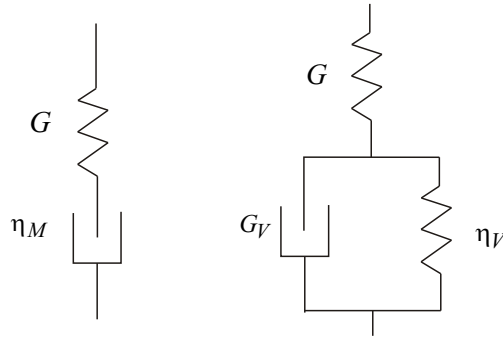


**Figure 5.** Left: Maxwell model. Right: Zener model.

(i) For  $\alpha = \beta = 0$ , which corresponds to the case of a material with no memory (Figure 1, left), Equation (40) reduces to the elastic indentation relation (2), with

$$M = \frac{2l_0}{c_0} = 2q_0 \frac{Q_0 + \frac{1}{2}q_0}{Q_0 + 2q_0}, \quad K = \frac{1}{3}Q_0, \quad G = \frac{1}{2}q_0. \quad (46)$$

(ii) Letting  $\alpha = 0$  corresponds to the case of a pure deviatoric creep, a case which was extensively studied in integer-type viscoelastic indentation analysis (for example, [Cheng and Cheng 2004; Cheng et al. 2000; 2005; Vandamme and Ulm 2006]). In this case  $\beta = 1$ , and one obtains

$$(c_0 + (c_2 + c_3)D^1 + (c_4 + c_5)D^2)F(t) = 2\phi(l_0 + (l_2 + l_3)D^1 + (l_4 + l_5)D^2)h^{1+1/n}(t). \quad (47)$$

Note that a deviatoric creep behavior described at a material level by a *first*-order differential equation (see (31) for  $\beta = 1$ ), yields a *second*-order differential equation that governs the  $F(t) - h(t)$  indentation response. This includes, as integer subset models, the three-parameter deviator creep Maxwell model and the four-parameter deviator creep Kelvin–Voigt or Zener model (Figure 5), for which the constant coefficients read as follows:

	$P$	$Q_0$	$Q$	$p$	$q_0$	$q$
Maxwell	0	$3K$	0	$\eta_M/G$	0	$2\eta_M$
Zener	0	$3K$	0	$\frac{\eta_V}{G+G_V}$	$2\frac{GG_V}{G+G_V}$	$2\frac{G}{G+G_V}\eta_V$

Here  $\eta_M$  and  $\eta_V$  stand for the viscosity in the respective models. Use of (48) in (42) and then in (47) yields the following differential equations for the two particular integer-type viscoelastic models:

$$\text{Maxwell: } F(t) + \frac{c_2}{c_0} \frac{\partial F}{\partial t} + \frac{c_5}{c_0} \frac{\partial^2 F}{\partial t^2} = 2\phi \left( \frac{l_2}{c_0} \frac{\partial h^{1+1/n}}{\partial t} + \frac{l_5}{c_0} \frac{\partial^2 h^{1+1/n}}{\partial t^2} \right), \quad (49)$$

$$\text{Zener: } F(t) + \frac{c_2}{c_0} \frac{\partial F}{\partial t} + \frac{c_5}{c_0} \frac{\partial^2 F}{\partial t^2} = 2\frac{l_0}{c_0} \phi \left( h^{1+1/n} + \frac{l_2}{l_0} \frac{\partial h^{1+1/n}}{\partial t} + \frac{l_5}{l_0} \frac{\partial^2 h^{1+1/n}}{\partial t^2} \right). \quad (50)$$

(iii) The difference in differential order between the material and the indentation scale becomes even more apparent for  $\alpha = \beta = 1$ , which converts the fractional model into an integer-type model governed

by a third-order differential equation:

$$(c_0 + (c_1 + c_2)D^1 + (c_3 + c_5)D^2 + c_4D^3)F(t) = 2\phi(l_0 + (l_1 + l_2)D^1 + (l_3 + l_5)D^2 + l_4D^3)h^{1+1/n}(t). \quad (51)$$

Setting  $\alpha = \beta$  reduces the model to the often considered case of a material with time independent Poisson's ratio [Gao and Ogden 2003], which is obtained by letting  $P = p$ ,  $q = bQ$ , and  $q_0 = bQ_0$  for any non-negative value of  $b$  in (30)–(31) and (42). This concept is similar to using two same-type integer viscoelastic models with the aforementioned relations between their parameters which lead to a constant Poisson's ratio [Tschöegl et al. 2002].

(iv) This difference in differential order between the material and the indentation scale holds true for fractional materials; that is, because of the definition of the differential operators in (41), the order of the fractional derivatives at the indentation scale given by (40), is always greater than the one of the material level defined by (30)–(31). For example, for a deviatoric fractional creep model,  $\alpha = 0$ , the differential equation (31) governing the material behavior is of order  $0 < \beta < 1$ , while the indentation response is of order  $2\beta$ , and can thus be greater than unity:

$$(c_0 + (c_2 + c_3)D^\beta + (c_4 + c_5)D^{2\beta})F(t) = 2\phi(l_0 + (l_2 + l_3)D^\beta + (l_4 + l_5)D^{2\beta})h^{1+1/n}(t). \quad (52)$$

The specification of (52) for a fractional deviatoric Maxwell material ( $P = Q = q_0 = 0$ ) and a fractional deviatoric Zener material ( $P = Q = 0$ ) reads as follows:

$$\text{Maxwell: } F(t) + \frac{c_2}{c_0} \frac{\partial^\beta F}{\partial t^\beta} + \frac{c_5}{c_0} \frac{\partial^{2\beta} F}{\partial t^{2\beta}} = 2\phi \left( \frac{l_2}{c_0} \frac{\partial^\beta h^{1+1/n}}{\partial t^\beta} + \frac{l_5}{c_0} \frac{\partial^{2\beta} h^{1+1/n}}{\partial t^{2\beta}} \right), \quad (53)$$

$$\text{Zener: } F(t) + \frac{c_2}{c_0} \frac{\partial^\beta F}{\partial t^\beta} + \frac{c_5}{c_0} \frac{\partial^{2\beta} F}{\partial t^{2\beta}} = 2 \frac{l_0}{c_0} \phi \left( h^{1+1/n} + \frac{l_2}{l_0} \frac{\partial^\beta h^{1+1/n}}{\partial t^\beta} + \frac{l_5}{l_0} \frac{\partial^{2\beta} h^{1+1/n}}{\partial t^{2\beta}} \right), \quad (54)$$

where the coefficients  $c_0, \dots, c_5$  and  $l_0, \dots, l_5$  are still given by (42). Their dimensionality, however, changes due to the application of non-integer time derivatives. For instance, we have  $[c_2/c_0] = [l_2/l_0] = T^\beta$ , while  $[c_5/c_0] = [l_5/l_0] = T^{2\beta}$ , and so on. Still, analogously to (19)–(20), one can define parameters similar to  $\tau_0$  with the dimension of time and replace the the fractional dimension of  $c_2/c_0$ , etc.

(v) The operators (41) are not symmetric with respect to  $\alpha$  and  $\beta$ ; that is, in contrast to  $\alpha$ , which is the fractional exponent for the volumetric viscoelastic response (30), there are some extra terms that involve higher derivatives of order  $2\beta$ , which is the fractional exponent for the viscoelastic shear response (31). This observation translates, into fractional derivatives, the well-known fact that an indentation test is a shear test than a hydrostatic test. For this reason, the effect of  $\beta$  dominates over the effect of  $\alpha$  in the fractional derivatives that define the indentation response (40). This dominance of shear over bulk exists for conventional viscoelastic materials in indentation, but it is hidden in the constitutive equations.

#### 4. Indentation creep and relaxation functions

A convenient way to analyze time-dependent experimental indentation data is in the form of indentation creep and relaxation functions, derived for a step force loading or step displacement loading, respectively. It is also a formidable illustration of the use of the fractional model developed here before.



**4.1. Indentation creep compliance.** Consider a Heaviside step loading  $F(t) = F_{\max} \mathcal{H}(t)$ , where  $F_{\max}$  is the maximum load, and  $\mathcal{H}(t)$  the Heaviside step function. We recall the Laplace transform  $\widehat{F}(s)$  of the Heaviside load function:

$$F(t) = F_{\max} \mathcal{H}(t) \iff \widehat{F}(s) = \frac{F_{\max}}{s}. \quad (55)$$

Then, a substitution of (55) in (39) along with a substitution of (55) in Laplace transform of (40) can be developed in the form

$$\widehat{L}(s) = \frac{\widehat{\phi h^{1+1/n}}(s)}{F_{\max}} = \frac{1}{s^2 \widehat{M}(s)} = \frac{\widehat{D}_F(s)}{2s \widehat{D}_h(s)}, \quad (56)$$

where  $D_F(s)$  and  $D_h(s)$  are the Laplace transforms of the operators (41) according to definition (9):<sup>3</sup>

$$\widehat{D}_F(s) = c_0 + c_1 s^\alpha + c_2 s^\beta + c_3 s^{\alpha+\beta} + c_4 s^{\alpha+2\beta} + c_5 s^{2\beta}, \quad (57)$$

$$\widehat{D}_h(s) = l_0 + l_1 s^\alpha + l_2 s^\beta + l_3 s^{\alpha+\beta} + l_4 s^{\alpha+2\beta} + l_5 s^{2\beta}. \quad (58)$$

Note that the inverse Laplace transform of (56),  $L(t)$ , has dimension of compliance  $[L] = 1/(L^{-1}MT^{-2})$ , and can therefore be appropriately called an indentation creep compliance function. As discussed in detail for integer-type viscoelasticity models in [Vandamme and Ulm 2007], the indentation creep compliance is independent of the indenter-shape. The right-hand side of (56), therefore, is representative of the material response of the considered fractional viscoelastic material. The inverse transform of (56) exists, is real, and continuous. The following statements are derived in the Appendix:

(i) For a ‘double’ Zener model (Zener bulk and Zener deviatoric creep model), the inverse Laplace transform of (56) yields the following expression of the time-dependent indentation creep compliance:

$$\begin{aligned} L(t) &= \frac{\phi h^{1+1/n}(t)}{F_{\max}} \\ &= \frac{c_0}{2l_0} + \frac{1}{\pi} \operatorname{Im} \int_0^\infty \frac{\widehat{D}_F(re^{-i\pi})}{2re^{-i\pi} \widehat{D}_h(re^{-i\pi})} \exp(-rt) dr + \sum_j \lim_{s \rightarrow \lambda_j^m} (s - \lambda_j^m) \frac{\widehat{D}_F(\lambda_j^m) \exp(\lambda_j^m t)}{2\lambda_j^m \widehat{D}_h(\lambda_j^m)}, \quad (59) \end{aligned}$$

where  $m$  is the smallest common denominator of the fractional numbers  $\alpha$  and  $\beta$ . Note that  $\lambda^m$  is a complex number with negative real part. Thus, as  $t \rightarrow \infty$ , the second and the third terms on the right-hand side of (59) vanish and  $L(t)$  converges to a constant  $c_0/2l_0$ . This is because in Zener-type models (either fractional or integer; see Figure 5, right), there is a spring parallel to the rest of the system that prevents infinite deformation.

<sup>3</sup>Initial conditions in the Laplace transform of a derivative of a Heaviside function are zero, since  $0^-$  (and not  $0^+$ ) is taken as a lower limit of Laplace integration for a Heaviside function. More details can be found in [Flügge 1967].

(ii) For a ‘double’ Maxwell model, the expression of the inverse Laplace transform is the same one as (59), except for the first term on the right:

$$L(t) = \frac{\phi h^{1+1/n}(t)}{F_{\max}} = \frac{1}{2(k-1)!} \frac{\partial^{k-1}}{\partial u^{k-1}} [f(u) \exp(u^m t)]_{u=0} + \frac{1}{\pi} \operatorname{Im} \int_0^\infty \frac{D_F(\widehat{r e^{-i\pi}})}{2r e^{-i\pi} D_h(\widehat{r e^{-i\pi}})} \exp(-rt) dr + \sum_j \lim_{s \rightarrow \lambda_j^m} (s - \lambda_j^m) \frac{D_F(\lambda_j^m) \exp(\lambda_j^m t)}{2\lambda_j^m D_h(\lambda_j^m)}, \quad (60)$$

where  $k = m(1 + \beta)$  is an integer, and

$$f(u) = \frac{c_1 + c_2 u^{m(\beta-\alpha)} + c_3 u^{m\beta} + c_4 u^{2m\beta} + c_5 u^{m(2\beta-\alpha)}}{2(l_3 + l_4 u^{m\beta} + l_5 u^{m(\beta-\alpha)}), \quad \alpha \leq \beta, \quad (61)$$

$$f(u) = \frac{c_1 u^{m(\alpha-\beta)} + c_2 + c_3 u^{m\alpha} + c_4 u^{m(\alpha+\beta)} + c_5 u^{m\beta}}{2(l_3 u^{m(\alpha-\beta)} + l_4 u^{m\alpha} + l_5), \quad \alpha > \beta.$$

Specification of (60) for a fractional deviatoric Maxwell material ( $P = Q = q_0 = 0, \alpha = 0$ ) and of (59) for a fractional deviatoric Zener material ( $P = Q = 0, \alpha = 0$ ) yields

$$\text{Maxwell: } L(t) = \frac{1}{2(k-1)!} \frac{\partial^{k-1}}{\partial u^{k-1}} \left[ \frac{Q_0 + (2Q_0 p + 2q)u^{m\beta} + (Q_0 p^2 + 2pq)u^{2m\beta}}{qQ_0 + (qpQ_0 + \frac{1}{2}q^2)u^{m\beta}} \exp(u^m t) \right]_{u=0} + \frac{1}{\pi} \operatorname{Im} \int_0^\infty \frac{Q_0 + (2Q_0 p + 2q)r^\beta e^{-i\pi\beta} + (Q_0 p^2 + 2pq)r^{2\beta} e^{-2i\pi\beta}}{2r^{1+\beta} e^{-i\pi(1+\beta)} (qQ_0 + (qpQ_0 + \frac{1}{2}q^2)r^\beta e^{-i\pi\beta})} \exp(-rt) dr + \sum_j \lim_{s \rightarrow \lambda_j^m} (s - \lambda_j^m) \frac{Q_0 + (2Q_0 p + 2q)\lambda_j^{\beta m} + (Q_0 p^2 + 2pq)\lambda_j^{2\beta m}}{2\lambda_j^{m(1+\beta)} (qQ_0 + (qpQ_0 + \frac{1}{2}q^2)s^\beta)} \exp(\lambda_j^m t), \quad (62)$$

$$\text{Zener: } L(t) = \frac{\frac{1}{2}Q_0 + q_0}{\frac{1}{2}q_0^2 + q_0 Q_0} + \frac{1}{\pi} \operatorname{Im} \int_0^\infty \frac{(Q_0 + 2q_0 + (2Q_0 p + 2q + 2pq_0)r^\beta e^{-i\pi\beta} + (Q_0 p^2 + 2pq)r^{2\beta} e^{-2i\pi\beta}) \exp(-rt)}{2r e^{-i\pi} (\frac{1}{2}q_0^2 + q_0 Q_0 + (q_0 p Q_0 + q q_0 + q Q_0)r^\beta e^{-i\pi\beta} + (qpQ_0 + \frac{1}{2}q^2)r^{2\beta} e^{-2i\pi\beta})} dr + \sum_j \lim_{s \rightarrow \lambda_j^m} (s - \lambda_j^m) \frac{Q_0 + 2q_0 + (2Q_0 p + 2q + 2pq_0)\lambda_j^{\beta m} + (Q_0 p^2 + 2pq)\lambda_j^{2\beta m}}{2\lambda_j^m (\frac{1}{2}q_0^2 + q_0 Q_0 + (q_0 p Q_0 + q q_0 + q Q_0)s^\beta + (qpQ_0 + \frac{1}{2}q^2)s^{2\beta})} \exp(\lambda_j^m t). \quad (63)$$

(iii) For  $\beta = 1$ , since  $e^{-i\pi} = -1$ , the imaginary part of the integrand in the middle terms of both (62) and (63) become zero and hence the middle terms vanish. In this case, the other two terms in (62) and (63) are found to reduce to the known indentation creep compliance functions of the integer-type deviatoric models as follows [Vandamme and Ulm 2007]:

$$\text{Maxwell: } L(t) = \frac{1}{M} + \frac{t}{4\eta_M} + \frac{(1-2\nu)^2}{4E} \left( 1 - \exp\left(-\frac{E}{3\eta_M} t\right) \right), \quad (64)$$

$$\text{Zener: } L(t) = \frac{1}{M} + \frac{1}{4G_V} \left( 1 - \exp\left(-\frac{G_V}{\eta_V} t\right) \right) + \frac{(1-2\nu)^2}{4(E+3G_V)} \left( 1 - \exp\left(-\frac{E+3G_V}{3\eta_V} t\right) \right). \quad (65)$$

Here we have used the notation (42) and (42) along with the well known elasticity relations

$$E = \frac{9KG}{3K + G}, \quad \nu = \frac{3K - 2G}{2(3K + G)}.$$

(iv) Finally, the indentation creep compliance function can be used to study the time-dependent indentation response  $h(t)$  for any prescribed monotonically increasing indentation load history  $F(t) = F_{max}\mathcal{F}(t)$ , in both the Laplace and time domain [Vandamme and Ulm 2007]:

$$\frac{\phi h^{1+1/n}(s)}{F_{max}} = s\widehat{L}(s)\widehat{\mathcal{F}}(s) \implies \frac{\phi h^{1+1/n}(t)}{F_{max}} = \int_{-\infty}^t L(t - \tau) \frac{d}{d\tau} \mathcal{F}(\tau) d\tau, \quad (66)$$

where  $\widehat{\mathcal{F}}(s)$  is the Laplace transform of the normalized loading history  $\mathcal{F}(t) = F(t)/F_{max}$ , satisfying  $(d\mathcal{F}/dt)(t) \geq 0$ .

**4.2. Indentation relaxation modulus.** For a Heaviside displacement loading  $h^{1+1/n}(t) = h_{max}^{1+1/n}\mathcal{H}(t)$ , one can principally proceed in a similar way as for the indentation creep compliance. Alternatively, one can make use of the link between indentation creep compliance  $L(t)$  and indentation relaxation modulus  $M(t)$ , given by (see [Vandamme and Ulm 2007])

$$(s\widehat{M}(s))^{-1} = s\widehat{L}(s). \quad (67)$$

The expression of the relaxation modulus in the Laplace space thus becomes

$$\widehat{M}(s) = \frac{\widehat{F}(s)}{\phi h_{max}^{1+1/n}} = \frac{1}{s^2\widehat{L}(s)} = \frac{2\widehat{D}_h(s)}{s\widehat{D}_F(s)}. \quad (68)$$

The inverse Laplace transform for a selected number of models are as follows:

(i) For the ‘double’ Zener material:

$$M(t) = \frac{F(t)}{\phi h_{max}^{1+1/n}} = \frac{2l_0}{c_0} + \frac{1}{\pi} \text{Im} \int_0^\infty \frac{2\widehat{D}_h(s)}{s\widehat{D}_F(s)} \exp(-rt) dr + \sum_j (s - \lambda_j^m) \frac{2\widehat{D}_h(\lambda_j^m) \exp(\lambda_j^m t)}{\lambda_j^m \widehat{D}_F(\lambda_j^m)}. \quad (69)$$

(ii) For the ‘double’ Maxwell material:

$$M(t) = \frac{F(t)}{\phi h_{max}^{1+1/n}} = \frac{1}{(k-1)!} \frac{\partial^{k-1}}{\partial u^{k-1}} [f(u) \exp(u^m t)]_{u=0} + \frac{1}{\pi} \text{Im} \int_0^\infty \frac{2\widehat{D}_h(re^{-i\pi})}{re^{-i\pi} \widehat{D}_F(re^{-i\pi})} \exp(-rt) dr + \sum_j (s - \lambda_j^m) \frac{2\widehat{D}_F(\lambda_j^m) \exp(\lambda_j^m t)}{2\lambda_j^m \widehat{D}_h(\lambda_j^m)}, \quad (70)$$

where  $k = m(1 - \beta)$  is an integer, and

$$f(u) = \frac{2(l_3 + l_4 u^{m\beta} + l_5 u^{m(\beta-\alpha)})}{c_1 + c_2 u^{m(\beta-\alpha)} + c_3 u^{m\beta} + c_4 u^{2m\beta} + c_5 u^{m(2\beta-\alpha)}}, \quad \alpha \leq \beta, \quad (71)$$

$$f(u) = \frac{2(l_3 u^{m(\alpha-\beta)} + l_4 u^{m\alpha} + l_5)}{c_1 u^{m(\alpha-\beta)} + c_2 + c_3 u^{m\alpha} + c_4 u^{m(\alpha+\beta)} + c_5 u^{m\beta}}, \quad \alpha > \beta.$$

The relaxation moduli for fractional deviatoric Maxwell and Zener materials are, respectively,

$$M(t) = \frac{1}{(k-1)!} \frac{\partial^{k-1}}{\partial u^{k-1}} \left[ \frac{Q_0 + (2Q_0p + 2q)u^{m\beta} + (Q_0p^2 + 2pq)u^{2m\beta}}{qQ_0 + (qpQ_0 + \frac{1}{2}q^2)u^{m\beta}} \exp(u^m t) \right]_{u=0} \\ + \frac{1}{\pi} \operatorname{Im} \int_0^\infty \frac{2(Q_0 + (2Q_0p + 2q)r^\beta e^{-i\pi\beta} + (Q_0p^2 + 2pq)r^{2\beta} e^{-2i\pi\beta})}{r^{1+\beta} e^{-i\pi(1+\beta)} (qQ_0 + (qpQ_0 + \frac{1}{2}q^2)r^\beta e^{-i\pi\beta})} \exp(-rt) dr \\ + \sum_j \lim_{s \rightarrow \lambda_j^m} (s - \lambda_j^m) \frac{2(Q_0 + (2Q_0p + 2q)\lambda_j^{\beta m} + (Q_0p^2 + 2pq)\lambda_j^{2\beta m})}{\lambda_j^{m(1+\beta)} (qQ_0 + (qpQ_0 + \frac{1}{2}q^2)s^\beta)} \exp(\lambda_j^m t), \quad (72)$$

$$M(t) = \frac{\frac{1}{2}q_0^2 + q_0Q_0}{\frac{1}{2}Q_0 + q_0} \\ + \frac{1}{\pi} \operatorname{Im} \int_0^\infty \frac{2(\frac{1}{2}q_0^2 + q_0Q_0 + (q_0pQ_0 + qq_0 + qQ_0)r^\beta e^{-i\pi\beta} + (qpQ_0 + \frac{1}{2}q^2)r^{2\beta} e^{-2i\pi\beta}) \exp(-rt)}{r e^{-i\pi} (Q_0 + 2q_0 + (2Q_0p + 2q + 2pq_0)r^\beta e^{-i\pi\beta} + (Q_0p^2 + 2pq)r^{2\beta} e^{-2i\pi\beta})} dr \\ \sum_j \lim_{s \rightarrow \lambda_j^m} (s - \lambda_j^m) \frac{2(\frac{1}{2}q_0^2 + q_0Q_0 + (q_0pQ_0 + qq_0 + qQ_0)\lambda_j^{\beta m} + (qpQ_0 + \frac{1}{2}q^2)\lambda_j^{2\beta m}) \exp(\lambda_j^m t)}{\lambda_j^m (Q_0 + 2q_0 + (2Q_0p + 2q + 2pq_0)s^\beta + (Q_0p^2 + 2pq)s^{2\beta})}, \quad (73)$$

Similar to creep compliances, for  $\beta = 1$ , the previous expressions are found to reduce to the known indentation relaxation modulus expressions of the integer-type deviatoric models [Vandamme and Ulm 2007]:

$$\text{Maxwell: } M(t) = M - \frac{E}{2(1+\nu)} (1 - e^{-\frac{E}{2(1+\nu)\eta_M} t}) - \frac{E}{2(1-\nu)} \left( 1 - \exp\left(-\frac{E}{6(1-\nu)\eta_M} t\right) \right), \quad (74)$$

$$\text{Zener: } M(t) = M - \frac{E^2}{2(1+\nu)(E + 2G(1+\nu))} \left( 1 - \exp\left(-\frac{(E + 2G(1+\nu))t}{2\eta_V(1+\nu)}\right) \right) \\ - \frac{E^2}{2(1-\nu)(E + 6G(1-\nu))} \left( 1 - \exp\left(-\frac{(E + 6G(1-\nu))t}{6\eta_V(1-\nu)}\right) \right). \quad (75)$$

The indentation relaxation modulus functions can be used to study the time-dependent force relaxation history  $F(t)$  for any prescribed monotonically increasing indentation displacement history  $h^{1+1/n}(t) = h_{\max}^{1+1/n} \mathcal{G}(t)$ , in both Laplace and time domain [Vandamme and Ulm 2007]:

$$\frac{\widehat{F}(s)}{\phi h_{\max}^{1+1/n}} = s \widehat{M}(s) \widehat{\mathcal{G}}(s) \implies \frac{F(t)}{\phi h_{\max}^{1+1/n}} = \int_{-\infty}^t M(t-\tau) \frac{d}{d\tau} \mathcal{G}(\tau) d\tau, \quad (76)$$

where  $\widehat{\mathcal{G}}(s)$  is the Laplace transform of  $\mathcal{G}(t) = h^{1+1/n}(t)/h_{\max}^{1+1/n}$ , the normalized displacement loading history, which satisfies  $(d\mathcal{G}/dt)(t) \geq 0$ .

## 5. Application

In this section, we illustrate the application of the above theoretical derivations in indentation analysis of the fractional and viscous parameters of polystyrene (Dupont, Wilmington, DE) under a creep test. Depth-sensing indentation experiment was performed with a Nanotest 600 nanoindenter (MicroMaterials Ltd., Wrexham) with a Berkovich indenter. As is common practice in indentation analysis, the Berkovich

Maximum force [mN]	500	Thermal drift [nm/sec]	< 0.1
Load resolution [nN]	2–3	Machine compliance [nm/mN]	0.3–0.4
Load noise floor [nN]	100	Specimen clamping [nm/mN]	~ 0.01
Maximum depth [ $\mu\text{m}$ ]	15	Feedback control	Open loop
Displacement resolution [nm]	0.05–0.06	Drift correction	No

**Table 2.** Specifications of Nanotest 600 nanoindenter (values provided by the manufacturer and pretesting calibration). See also [Micromaterials 2002; Constantinides 2006].

$F_{\max}$ [mN]	31.45	$h_{\max}$ [nm]	2579
$S$ [mN/nm]	0.0696	$\tau_L$ [sec]	3.12
$M$ [GPa]	4.83	$\tau_H$ [sec]	29.99
$H$ [GPa]	0.19	$\tau_U$ [sec]	4.14

**Table 3.** Indentation data for the Nanotest run.

indenter is assimilated to a cone of half-opening angle  $\theta = 70.32^\circ$ . Table 2 provides more specifications on the nanoindenter device.

The load function is a prescribed trapezoidal force history:

$$F(t) = F_{\max} F(t), \quad F(t) = \begin{cases} t/\tau_L & 0 \leq t \leq \tau_L, \\ 1 & \tau_L \leq t \leq \tau_L + \tau_H, \\ 1 - t/\tau_U & \tau_L + \tau_H \leq t \leq \tau_L + \tau_H + \tau_U. \end{cases} \quad (77)$$

The load was increased linearly up to  $F_{\max}$ , held constant during the creep phase and then decreased to zero linearly. In (77),  $\tau_L$ ,  $\tau_H$ , and  $\tau_U$  are, respectively, loading, holding, and unloading time which are given in Table 3. By monitoring force-indentation depth data (Figure 6), we get  $M$  and  $H$  from (1). Indentation parameters and moduli are summarized in Table 3.

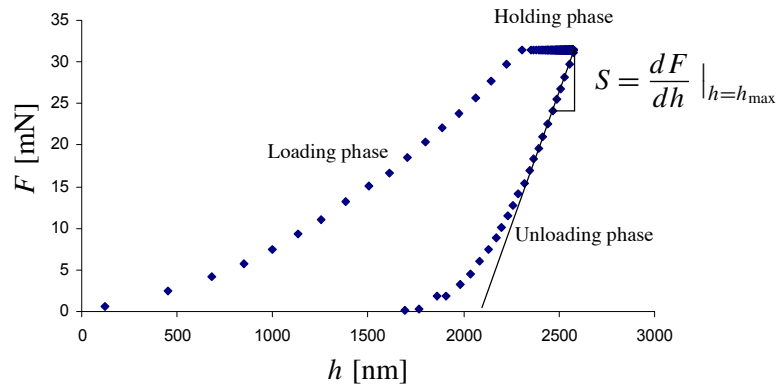


**Figure 6.** Load versus indentation depth for polystyrene.

Theoretical derivations throughout this paper are based on pure viscoelastic deformation. However, the monitored indentation depth is a mixture of elastic and plastic deformations, particular around the tip of the nanoindenter where there is a high stress concentration. Thus, in what follows, we first approximate the elastic indentation depth by removing the plastic indentation. Next, we fit the elastic experimental data to the theoretical creep compliance to identify the fractional model parameters.

**5.1. Correcting for plasticity.** Extensive works on plastic analysis of nanoindentation are available in the literature (see [Cheng and Cheng 2004], for example). Here we use the method proposed by Sakai in [Sakai 1999] and [Shimizu et al. 1999] to approximate the plastic deformations. In this method, the quadratic load-depth relations are experimentally observed through the relation

$$F = k_1 h^2. \quad (78)$$

Here  $k_1$  is a parameter related to hardness  $H$  in (1)<sub>1</sub> and the true hardness  $H_T$ . For loading,  $k_1$  reads

$$k_1 = \frac{gH}{\gamma^2}. \quad (79)$$

In this equation,  $\gamma$  is a geometrical factor which relates the total penetration depth  $h$  and the contact depth  $h_c$  through  $h = \gamma h_c$  (we approximate  $\gamma \approx 1$ ), and  $g$  is the geometrical factor of the indenter that relates to the contact area  $A_c$  by  $g = A_c/h_c^2$ . For a Berkovich indenter,  $g = 24.5$ . Sakai's analysis for elastoplastic indentation deformation is based on a Maxwell model in which  $F = F_e = F_p$  and  $h = h_e + h_p$  (indices  $e$  and  $p$  refer to elastic and plastic, respectively). This model consists of a perfectly elastic component with an elastic modulus  $M$  (as opposed to  $E$ ) connected in series to a perfectly plastic component with true hardness  $H_T$  given by

$$H_T = \frac{k_1}{(\sqrt{g} - \sqrt{2 \cot \theta} \sqrt{k_1/M})^2}. \quad (80)$$

Plastic indentation can be computed from the quadratic relation between  $F_p = F$  and  $h_p$  by

$$h_p(t) = \sqrt{\frac{F(t)}{gH_T}}. \quad (81)$$

Finally,  $h_e(t)$ , based on Sakai's procedure, is straightforward:

$$h_e(t) = h(t) - h_p(t). \quad (82)$$

During a creep test (constant load),  $h_p(t)$  simplifies to a constant. By having indentation moduli in Table 3 and following (79) to (81), the plastic indentation depth during the holding phase is approximated to be  $h_p = 1380$  nm. In fact, it is implicitly assumed that there is no further plasticity during the creep test.

**5.2. Viscoelastic fitting procedure.** Now we consider fitting the approximated elastic data obtained experimentally to the viscoelastic model creep compliance. Direct fitting of the analytical solutions, (59) or (60), to the elastic experimental data in the time domain is a complicated task (because the analytical solutions require parametrically finding the roots of a rational function, Equation (58), with fractional exponents; see the Appendix). However, once the fractional and viscous parameters are known, Equations (59) and (60) are handy to use. In order to find the fractional and viscous parameters, we proceed in the following way, which leads to a curve-fitting in the Laplace domain:

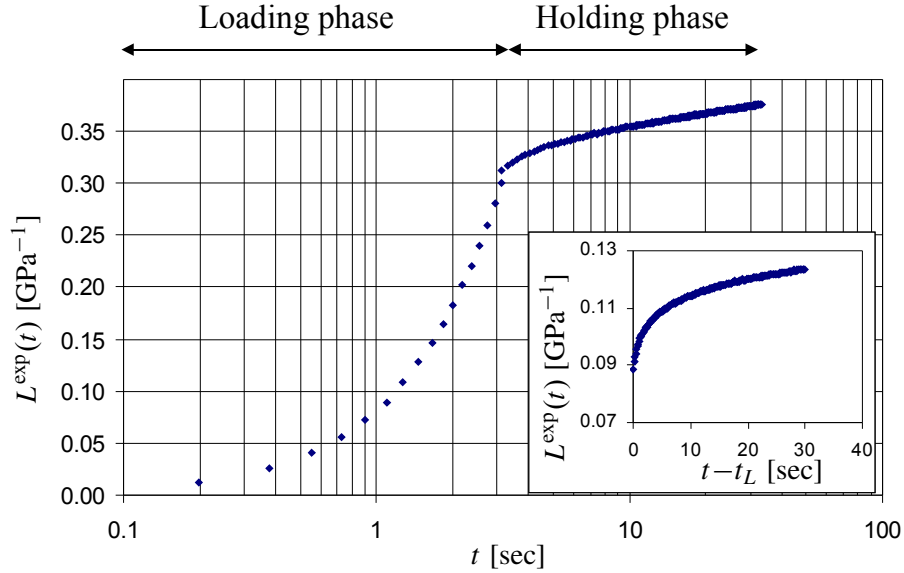


**Figure 7.** Time-dependent compliance  $L(t)$  for polystyrene. The large window indicates  $L^{\text{exp}}(t)$  for the loading and holding phases ( $0 < t < \tau_L + \tau_H$ ) where recorded experimental depth  $h(t)$  is used; The small window shows  $L_e^{\text{exp}}(t)$  for the holding phase ( $\tau_L < t < \tau_L + \tau_H$ ), where an elastic indentation depth  $h_e(t)$  is used.

(i) From the recorded indentation depth  $h(t)$ , determine the experimental indentation creep compliance function  $L^{\text{exp}}$  for the equivalent cone representing the Berkovich indenter ( $n = 1$ ,  $B = \cot \theta$ , see Table 1):

$$L^{\text{exp}}(t) = \frac{\phi h^{1+1/n}(t)}{F_{\text{max}}} = \frac{2 \tan \theta}{\pi F_{\text{max}}} h^2(t). \quad (83)$$

$L^{\text{exp}}(t)$  is shown in the large window in Figure 7 and consists of the loading and the holding phases.

(ii) Focus on the creep response and consider the holding phase  $t > \tau_L = 3.12$  sec where the load is constant. Determine elastic indentation depth  $h_e(t)$  by using (79)–(82), and replace  $h(t)$  by  $h_e(t)$  in (83) to get the elastic compliance function  $L_e^{\text{exp}}(t)$ . This is shown in the small window of Figure 7, and  $L_e^{\text{exp}}(t)$  reads

$$L_e^{\text{exp}}(t) = \frac{\phi h_e^{1+1/n}(t)}{F_{\text{max}}} = \frac{2 \tan \theta}{\pi F_{\text{max}}} h_e^2(t). \quad (84)$$

(iii) Transfer the time-dependent  $L_e^{\text{exp}}(t)$  to the Laplace domain. One can do this either numerically using a Finite Laplace Transform method, or by fitting a continuous function to  $L_e^{\text{exp}}(t)$  and then analytically transforming the fitted function to the Laplace space. We choose the latter procedure. By using a nonlinear optimization algorithm (for example, the `lsqnonlin` function in Matlab v7.4), it turns out that the best fitted function is a power function of the form

$$L_e^{\text{exp}}(t) = at^b + c, \quad (85)$$

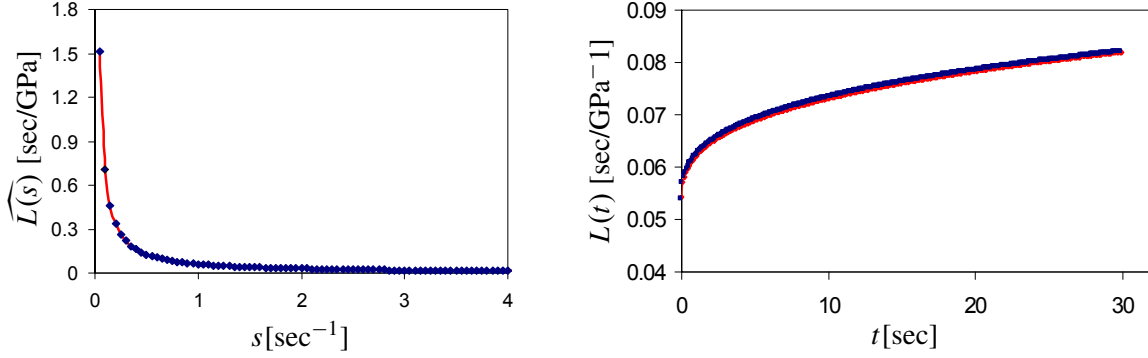


**Figure 8.** Left: curve-fitting in the Laplace domain for the compliance. Blue squares represent Laplace transform of experimental compliance  $\widehat{L}_e^{\text{exp}}(s)$  while the red line represents the Laplace of the theoretical model compliance  $\widehat{L}(s)$ . Right: validation of the curve-fitting in the time domain. Blue squares represent experimental compliance  $L_e^{\text{exp}}(t)$  and the red line represent theoretical model compliance  $L(t)$  which perfectly coincides with  $L_e^{\text{exp}}(t)$ .

where, for the test data in (84),  $a = 0.0102$ ,  $b = 0.318$ , and  $c = 0.052$ . The parameter  $b$  is dimensionless, but  $[a] = LM^{-1}T^{2-b}$  and  $[c] = LM^{-1}T^2$ . The Laplace transform of (85) is

$$\widehat{L}_e^{\text{exp}}(s) = \frac{0.0102\Gamma(1 + 0.318)}{s^{1.318}} + \frac{0.052}{s}. \quad (86)$$

(iv) In Laplace space, fit the transformed elastic compliance response  $\widehat{L}_e^{\text{exp}}(s)$ , given by (86), to the transformed model response  $\widehat{L}(s)$  in (56), involving fractional exponents and parameters. In view of the considered models in Figure 4, this is equivalent to determining 10 independent unknown parameters in  $\widehat{L}(s)$ , namely  $\alpha$ ,  $Q_0$ ,  $Q_1$ ,  $Q_2$ ,  $\tau_v$  for the bulk and  $\beta$ ,  $q_0$ ,  $q_1$ ,  $q_2$ ,  $\tau_d$  for the shear behavior. For the purpose of fitting in the complex plane, we refer to the Identity Theorem in complex analysis (for example, [Carrier et al. 1966; Marsden and Hoffman 1999]) and consider  $s$  as a real variable on the positive real axis. This fitting in the Laplace space does not require any a priori assumption of the particular model (double Maxwell, double Zener, etc.). Therefore, we minimize the quadratic error between the elastic compliance function, (86), and the model function (56) by

$$\min_{\substack{\alpha, \beta: \alpha < \beta, \\ Q_0, Q_1, Q_2, \tau_v, \\ q_0, q_1, q_2, \tau_d}} \sum_{i=1}^{n+1} \left( \widehat{L}_e^{\text{exp}}(s_i) - \frac{\widehat{D}_F(s_i)}{2s_i \widehat{D}_h(s_i)} \right)^2, \quad (87)$$

where the linear constraint  $\alpha < \beta$  renders an account of the fact that the indentation test is more of a shear test, for which reason the effect of shear at the constitutive model is more influential. The result of this minimization yields the following values for the 10 parameters:

$$\begin{aligned} \alpha &= 0.257, & Q_0 &= 3.37 \text{ GPa}, & Q_1 &= 30.85 \text{ GPa}, & Q_2 &= 58.01 \text{ GPa}, & \tau_v &= 3.92 \text{ sec} \\ \beta &= 0.374, & q_0 &= 0.84 \text{ GPa}, & q_1 &= 13.99 \text{ GPa}, & q_2 &= 59.46 \text{ GPa}, & \tau_d &= 4.47 \text{ sec}. \end{aligned} \quad (88)$$



Since all parameters in (88) are nonzero, it is recognized that the tested material, polystyrene, follows best the double fractional Zener model with the sum of quadratic errors being  $0.22 \times 10^{-9}$ . By reducing the unknown parameters down to 8 for the double Maxwell models, this error becomes  $3.1 \times 10^{-9}$ . For validation, after identifying the model parameters of  $\widehat{L}(s)$ , the inverse Laplace transform of  $L(s)$  must match with  $L_e^{\text{exp}}(t)$ , (84), in the time domain. This is numerically confirmed in Figure 8 by using the Talbot algorithm [Abate and Valkó 2004]) for Laplace inversion.

**Remark 1.** Since  $s$  is, in general, a complex number, one may expect that both real and imaginary parts of  $s$  are required for the purpose of curve-fitting in the Laplace domain. But The Identity Theorem for single-valued analytic functions states that if two single-valued functions are analytic in a common region and coincide identically in a subset of that region (for instance, on a segment of a curve) then the two functions coincide identically throughout their common region of analyticity; see, for example, [Carrier et al. 1966; Marsden and Hoffman 1999]. A continuous function is analytic in a region of the complex plane if it is free of singularities in that region. Given that for any linear stable physical system, such as creep in indentation,  $\widehat{L}(s)$  and  $\widehat{L}_e^{\text{exp}}(s)$  are free of singularities in the right-half of the complex plane where  $\text{Re}(s) > 0$  (see the Appendix), then if  $\widehat{L}(s) = \widehat{L}_e^{\text{exp}}(s)$  on the positive real axis of  $s$  (which is a subset of the complex plane in which  $\widehat{L}(s)$  and  $\widehat{L}_e^{\text{exp}}(s)$  are analytic), then directly from the Identity Theorem,  $\widehat{L}(s) = \widehat{L}_e^{\text{exp}}(s)$  throughout all regions of their analyticity in the complex plane. Hence, for fitting  $\widehat{L}(s)$  and  $\widehat{L}_e^{\text{exp}}(s)$  on the complex plane, as long as these functions coincide in a region where  $s$  lies on the positive real axis, there is no need for the imaginary parts of  $s$  to be taken into account. Here we used a relatively large interval up to  $s = 1000 \text{ sec}^{-1}$  (since the exponent of  $e^{st}$  is dimensionless, the dimension of  $s$  is 1/time which indicates that large  $s$  refers to small times and small  $s$  to large times). Increasing this interval is practically insignificant because  $\widehat{L}_e^{\text{exp}}(s)$  approaches zero at around  $s = 4 \text{ sec}^{-1}$  (Figure 8).

**Remark 2.** The optimization problem (87) defined in the Laplace domain involves a ten-dimensional shallow hypersurface for the ten unknown parameters  $(\alpha, Q_0, Q_1, Q_2, \tau_v, \beta, q_0, q_1, q_2, \tau_d)$ , in which there are many local minima. To approach the global minimum, we use ten nested loops over initial parameter guesses, each loop covering the given range of that parameter (we consider  $0 < \alpha, \beta < 1$  and  $0 < \tau_v, \tau_d < 10 \text{ sec}$ ,  $0 < Q_0, Q_1, Q_2, q_0, q_1, q_2 < 70 \text{ GPa}$ ). We then regularly discretize the range of each parameter and repeat the optimization as many times as different combinations of initial parameter guesses exist through the ten nested loops.

**Remark 3.** The optimization algorithm starts from different points within the hypersurface and each time finds a closest local minimum by calling the 'lsqnonlin' subroutine in Matlab v7.4, which uses a subspace trust region method for each set of initial parameter guesses. This subroutine is based on the interior-reflective Newton method [Coleman and Li 1994; 1996], and is set to a maximum of 20,000 iterations and function evaluations. Each iteration in this subroutine involves the approximate solution of the large linear system using the method of preconditioned conjugate gradients (PCG). Over all initial parameter guesses, the criterion for the best fit (or the global minimum among these local minima) will be the one that has the least quadratic error. For a double Zener model, the run time for finding the global minimum was 2 days, and the mean and standard deviation of the minima are  $1.8 \times 10^{-5}$  and  $2.9 \times 10^{-4}$ , respectively.

Given that the quadratic error function for the global minimum is orders of magnitude less than the mean of the minima, the objective function must be highly sensitive to the model parameters. To clarify this dependence we perform a sensitivity analysis.

**5.3. Sensitivity analysis of the model parameters.** Once the model parameters are identified, one can perform a sensitivity analysis to determine the quality of the employed models and the parameters that contribute most to the output variability, which in this case is the objective function (88). Sensitivity analysis also enables us to study the optimal– or instability– regions within the space of each parameter for which the objective function is guaranteed not to jump from the global minimum to the next lowest local minimum. Let's use the symbol  $\Theta$  to indicate the objective function (88). We numerically disturb a model parameter, say  $\alpha$ , from its optimum value while keeping all the other model parameters unchanged. Next, by monitoring the change in  $\Theta$  to a defined tolerance  $\Delta\Theta$ , we can measure the sensitivity of  $\Theta$  with respect to each model parameter. Then, one can simply repeat this procedure for each model parameter and find a tolerance in which  $\Theta$  is assured not to exceed the allowable drift. Here, for a double Zener model, we set  $\Delta\Theta = (0.59 - 0.22) \times 10^{-9} = 0.37 \times 10^{-9}$ , which is the difference between the global minimum  $\Theta$  and its next lowest local minimum. For this case, we obtain

$$\begin{aligned} \Delta\alpha &= \pm 0.0001, \quad \Delta Q_0 = \pm 0.7 \text{ MPa}, \quad \Delta Q_1 = \pm 2.1 \text{ MPa}, \quad \Delta Q_2 = \pm 5.6 \text{ MPa}, \quad \Delta\tau_v = \pm 0.0015 \text{ sec}, \\ \Delta\beta &= \pm 0.00004, \quad \Delta q_0 = \pm 0.2 \text{ MPa}, \quad \Delta q_1 = \pm 0.3 \text{ MPa}, \quad \Delta q_2 = \pm 3.6 \text{ MPa}, \quad \Delta\tau_d = \pm 0.0007 \text{ sec}. \end{aligned} \quad (89)$$

In view of (89), the following observations are in order:

1. All parameters on the second line of (89) which are related to the deviatoric Zener model, are less than their counterpart on the first line, which are related to the volumetric Zener model. This suggests that the creep phenomenon during indentation is more sensitive to the deviatoric (shear) behavior. In other words, the time-dependent response of the shear behavior is more pronounced than that of the bulk behavior.
2. For each of the deviatoric and volumetric Zener models, the fractional parameters  $\alpha$  and  $\beta$ , with the least tolerance, are the most sensitive parameters in the quadratic error function, or, alternatively, the most dominant parameters in the time-dependent response function.
3. Among all the parameters of the two models, the  $\beta$  parameter in the deviatoric model is the most sensitive factor in the error function (equivalently, the most dominant factor for the time-dependent response function), followed by  $\alpha$ , which is the second most dominant (second least sensitive) parameter in the response function.

The results of the sensitivity analysis are in agreement with the observation that the effect of  $\beta$  (or shear) dominates over the effect of  $\alpha$ . In fact,  $\Theta$  is a nonlinear rational function of the independent variable  $s$ , the model parameters  $(\alpha, Q_0, Q_1, Q_2, \tau_v)$  for bulk and  $(\beta, q_0, q_1, q_2, \tau_d)$  for shear behavior. Among these parameters, the fractional parameters  $\alpha, \beta$  have significant influence in determining  $\Theta$ . This is because  $\alpha, \beta$  appear as the exponents of  $s$  in  $\Theta$ . For instance, in the case of shear behavior, in view of (28)<sub>1</sub> and (33), it is readily seen that the other four viscous model parameters appear only as coefficients of  $s$ , and thus their variations are not as critical as  $\beta$ . Then, between  $\alpha$  and  $\beta$ ,  $\beta$ , with greater exponent, is clearly the dominant parameter.

## 6. Conclusions

The fractional viscoelastic model offers new possibilities for the characterization of materials whose time-dependent response may be poorly captured by classical integer-type viscoelastic models. The analysis and method developed in this paper aims at determining the fractional properties from indentation analysis. The following conclusions can be drawn:

- (i) The derived constitutive differential equations governing the indentation response show that the differential order of the constitutive differential equations of the indentation response is higher than the one governing the material level. This difference in differential order between the material scale and indentation scale holds for both fractional and integer-type viscoelastic models, the latter being recognized as a subset of the more general fractional modeling framework. The found difference is more pronounced for the viscoelastic shear response than for the viscoelastic bulk response. This is explicitly shown with higher order derivatives in  $\beta$  than in  $\alpha$  for fractional viscoelastic materials. This observation is in agreement with the sensitivity analysis performed on the error function, and it translates into the well-known fact that an indentation test is rather a shear test than a hydrostatic test.
- (ii) The general constitutive differential equations are readily employed to derive indentation creep and relaxation functions, which, analogously to uniaxial creep compliance and relaxation functions, can be used in fractional indentation analysis for any monotonically increasing force- or depth-load histories applied in indentation testing. On this basis, explicit solutions for specific fractional creep models can be derived, as illustrated for the double Zener, double Maxwell, and deviatoric Maxwell and Zener models.
- (iii) In order to translate time-dependent indentation data into fractional material model properties, we suggest fitting the experimental response to the model response in the Laplace domain. This reduces the mathematical complexity of obtaining properties from indentation data without compromising the accuracy of the fit in the time domain. Our optimization method has two important features: the optimum model parameters do not depend on the initial parameter guesses; and in our curve-fitting on the complex plane, all functions are treated as real functions by making use of the Identity Theorem.

## Appendix

The fractional expression  $\widehat{D}(s)$  can be converted into a polynomial of integer order by

$$\widehat{D}(s) = \sum_j b_j s^{j/m} = \sum_j b_j u^j = X(u), \quad (90)$$

where  $u^j = s^{j/m}$ , and  $m > 0$  is the smallest common denominator of the fractional parameters  $\alpha$  and  $\beta$ . Some of the coefficients  $b_j$  are clearly zero, while any non-zero  $b_j$  corresponds to the coefficient of  $s$  in  $\widehat{D}(s)$  whose exponent becomes equal to  $j/m$ . The inverse transform of a function,  $\widehat{f}(s)$ , exists and is real, continuous, and causal when (i)  $\widehat{f}(s)$  is analytic for  $\text{Re}(s) > 0$ , (ii)  $\widehat{f}(s)$  is real for  $s$  real and positive, (iii)  $\widehat{f}(s)$  is of order  $s^{-\gamma}$ , where  $\gamma > 1$ , for  $|s|$  large in the right half  $s$  plane [Churchill 1958]. One can simply show that  $\widehat{L}(s)$  in (56) satisfies all three conditions. By definition, the inverse Laplace

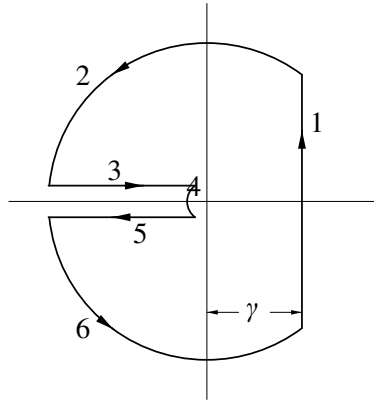


**Figure 9.** Integration contour on the complex  $s$ -plane for the calculation of (91).

transform of (56) is then

$$L(t) = \frac{1}{2\pi i} \int_{\gamma-i\infty}^{\gamma+i\infty} e^{st} \frac{\widehat{D_F(s)}}{2s \widehat{D_h(s)}} ds. \tag{91}$$

One can evaluate this line integral by extending it into a closed contour integration, as in Figure 9. Recall that the residue theorem states that the integral along any closed contour, divided by  $2\pi i$ , is equal to the sum of the residues of poles of the integrand within that contour. The contour in Figure 9, is divided into six segments with arrows which indicate the direction of integration. (Segments 3, 4, 5 are needed since the branch cut of  $s^{1/m}$  lies along the negative real axis.) We thus can write

$$\frac{1}{2\pi i} \int_{C_1} e^{st} \frac{\widehat{D_F(s)}}{2s \widehat{D_h(s)}} ds + \frac{1}{2\pi i} \sum_{k=2}^6 \int_{C_k} e^{st} \frac{\widehat{D_F(s)}}{2s \widehat{D_h(s)}} ds = \sum_j b_j, \tag{92}$$

where  $b_j$  are the residues. Equation (91) is the first term in (92) when its limits are extended to infinity in the negative and positive imaginary directions of the  $s$  plane. The radii of the segments 2 and 6 are increased infinitely to ensure the continuity of the closed contour. Similarly, segments 3 and 5 are stretched to infinity on the negative real axis. When the radius approaches infinity, it can be shown that the integrals along the contours 2 and 6 are zero. By using the following lemma [MacRobert 1962] one can obtain the contour integral along the segment 4,

**Lemma.** *If  $\lim(s - a)f(s) = k$  as  $s \rightarrow a$ , where  $k$  is a constant, then  $\lim \int f(s)ds = i(\theta_2 - \theta_1)k$ , the integral being taken for  $s \rightarrow a$  and  $r \rightarrow 0$  around an arc from  $\theta_1$  to  $\theta_2$  of the circle  $|s - a| = r$ .*

It follows that since  $(\theta_2 - \theta_1) = 0$ ,

$$\int_4 e^{st} \frac{\widehat{D_F(s)}}{2s \widehat{D_h(s)}} ds = 0. \tag{93}$$

One can also show that

$$\int_3 e^{st} \frac{\widehat{D_F(s)}}{2s \widehat{D_h(s)}} ds + \int_5 e^{st} \frac{\widehat{D_F(s)}}{2s \widehat{D_h(s)}} ds = -2i \operatorname{Im} \int_0^\infty e^{-rt} \frac{\widehat{D_F(re^{-i\pi})}}{2s \widehat{D_h(re^{-i\pi})}} dr. \tag{94}$$

Finally, using the conventional technique, the residues are calculated as

$$b_j = \lim_{s \rightarrow \lambda_j^m} (s - \lambda_j^m) \frac{\widehat{D_F(s)}}{2s \widehat{D_h(s)}} e^{st}. \quad (95)$$

Here,  $\lambda_j$  refers to the  $j$ -th root of the integer polynomial  $X(u)$ . In view of equations (90) and (56), the roots of  $X(u)$  correspond to the poles of  $L(t)$ . Lastly, by substituting (93), (94), and (95) into (92), one can find the general solution in the time domain. For specific solutions, we need to consider different models. For a double Zener models, since all the  $c$  and  $l$  coefficients in (42) are nonzero,  $s = 0$  in (56) is a simple pole, and because its exponent is one and an integer number, this pole is on the  $s$ -plane. Thus, its residue via (95) is simply the first term in (59). Other poles of (56)  $\lambda_i$  (those that make  $\widehat{D_h(s)} = 0$ ) were found in the  $s^{1/m}$  plane. Since the Laplace transform is performed in the  $s$ -plane, the poles  $\lambda_i$  should be transformed into  $\lambda_i^m$  to be on the  $s$ -plane. However, that transformation maps some of the original poles onto Riemann surfaces out of the closed contour of integration in the  $s$ -plane. Thus, according to the residue theorem, the residues of such poles do not contribute to the solution. Hence, the summation over the index  $j$  in (59) (and through all equations in this paper) pertains only to those poles that remain in the closed contour's plane after the transformation. This indicates that, for a linear physical system,  $\lambda_i^m$  must have a negative real part in order for the system to be stable.

For double Maxwell models,  $c_0 = l_0 = l_1 = l_2 = 0$ , and (56) simplifies to

$$\widehat{L(s)} = \frac{\widehat{D_F(s)}}{2s \widehat{D_h(s)}} = \frac{c_1 s^\alpha + c_2 s^\beta + c_3 s^{\alpha+\beta} + c_4 s^{\alpha+2\beta} + c_5 s^{2\beta}}{2s(l_3 s^{\alpha+\beta} + l_4 s^{\alpha+2\beta} + l_5 s^{2\beta})}. \quad (96)$$

In the case of  $\alpha \leq \beta$ , after cancelling out  $s^\alpha$ , (96) yields

$$\widehat{L(s)} = \frac{c_1 + c_2 s^{\beta-\alpha} + c_3 s^\beta + c_4 s^{2\beta} + c_5 s^{2\beta-\alpha}}{2s^{1+\beta}(l_3 + l_4 s^\beta + l_5 s^{\beta-\alpha})}. \quad (97)$$

Clearly,  $s = 0$  in (97) is not a simple pole, rather, it is a pole of fractional order  $1 + \beta$ . Consider this fractional number to be  $k/m$ , where  $k$  and  $m$  are two integer numbers. By using the following transformation:

$$s^{1+\beta} = (s^{1/m})^k = u^k, \quad (98)$$

one can convert (97) into quotient of two polynomials as

$$\widehat{L(u)} = \frac{c_1 + c_2 u^{m(\beta-\alpha)} + c_3 u^{m\beta} + c_4 u^{2m\beta} + c_5 u^{m(2\beta-\alpha)}}{2u^k(l_3 + l_4 u^{m\beta} + l_5 u^{m(\beta-\alpha)})}. \quad (99)$$

Now,  $u = 0$  in (99) is a multiple pole of order  $k$ . In order to find its residue, we use the fact that the residue of a function  $f(s) = Q(s)/(s - a)^{n+1}$  at a multiple pole  $a$  of order  $n + 1$  is given by

$$F(s, t) = \frac{1}{n!} \frac{\partial^n}{\partial s^n} [Q(s)e^{st}]_{s=a}.$$

(see [Churchill 1958], for example). Applying this to (99) leads to (61)<sub>1</sub>. Similarly, in the case of  $\alpha > \beta$ , after cancelling out  $s^\beta$ , one can find (61)<sub>2</sub>. The residue theorem in conjunction with fractional-order derivatives has been used in [Bagley and Torvik 1983] and [Ostoja-Starzewski and Shahsavari 2008] in a slightly different way.

## References

- [Abate and Valkó 2004] J. Abate and P. P. Valkó, “Multi-precision Laplace transform inversion”, *Int. J. Numer. Methods Eng.* **60** (2004), 979–993.
- [Arkhincheev 1993] V. E. Arkhincheev, “Anomalous diffusion in inhomogeneous media: some exact results”, *Model. Meas. Control A* **26**:2 (1993), 11–29.
- [Bagley and Torvik 1983] R. L. Bagley and P. J. Torvik, “A theoretical basis for the application of fractional calculus to viscoelasticity”, *J. Rheol.* **27**:3 (1983), 201–210.
- [Baker et al. 1996] W. P. Baker, L. B. Eldred, and A. Palazotto, “Viscoelastic material response with a fractional-derivative constitutive model”, *AIAA J.* **34**:3 (1996), 596–600.
- [Bland 1960] D. R. Bland, *The theory of linear viscoelasticity*, International Series of Monographs on Pure and Applied Mathematics **10**, Pergamon, New York, 1960.
- [Borodich and Galanov 2008] F. M. Borodich and B. A. Galanov, “Non-direct estimations of adhesive and elastic properties of materials by depth-sensing indentation”, *Proc. R. Soc. Lond. A* **464**:2098 (2008), 2759–2776.
- [Borodich and Keer 2004] F. M. Borodich and L. M. Keer, “Contact problems and depth-sensing nanoindentation for frictionless and frictional boundary conditions”, *Int. J. Solids Struct.* **41**:9–10 (2004), 2479–2499.
- [Boussinesq 1885] J. Boussinesq, *Applications des potentiels à l'étude de l'équilibre et du mouvement des solides élastiques*, Gauthier-Villars, Paris, 1885.
- [Brinell 1901] J. A. Brinell, “Mémoire sur les épreuves à bille en acier”, pp. 83–94 in *Communications présentées devant le Congrès International des Méthodes d'Essai des Matériaux de Construction* (Paris, 1900), vol. 2, edited by P. Debray and L. Baclé, Dunod, Paris, 1901.
- [Bulychev 1999] S. I. Bulychev, “Relation between the reduced and unreduced hardness in nanomicroindentation tests”, *Tech. Phys.* **44**:7 (1999), 775–781.
- [Caputo 1967] M. Caputo, “Linear models of dissipation whose  $Q$  is almost frequency independent, Part II”, *Geophys. J. Int.* **13**:5 (1967), 529–539.
- [Caputo 1969] M. Caputo, *Elasticità e dissipazione*, Zanichelli, Bologna, 1969.
- [Cariou et al. 2008] S. Cariou, F.-J. Ulm, and L. Dormieux, “Hardness-packing density scaling relations for cohesive-frictional porous materials”, *J. Mech. Phys. Solids* **56**:3 (2008), 924–952.
- [Carrier et al. 1966] G. F. Carrier, M. Krook, and C. E. Pearson, *Functions of a complex variable: theory and technique*, McGraw-Hill, New York, 1966.
- [Cheng and Cheng 2004] Y.-T. Cheng and C.-M. Cheng, “Scaling, dimensional analysis, and indentation measurements”, *Mater. Sci. Eng. R* **44**:4–5 (2004), 91–149.
- [Cheng et al. 2000] L. Cheng, H. Xia, W. Yu, L. E. Scriven, and W. W. Gerberich, “Flat-punch indentation of viscoelastic materials”, *J. Polym. Sci. B Polym. Phys.* **38**:1 (2000), 10–22.
- [Cheng et al. 2005] L. Cheng, X. Xia, L. E. Scriven, and W. W. Gerberich, “Spherical-tip indentation of viscoelastic material”, *Mech. Mater.* **37**:1 (2005), 213–226.
- [Christensen 1971] R. M. Christensen, *Theory of viscoelasticity: an introduction*, Academic Press, New York, 1971.
- [Churchill 1958] R. V. Churchill, *Operational mathematics*, 2nd ed., McGraw-Hill, New York, 1958.
- [Coleman and Li 1994] T. F. Coleman and Y. Li, “On the convergence of interior-reflective Newton methods for nonlinear minimization subject to bounds”, *Math. Program.* **67**:2, Ser. A (1994), 189–224.
- [Coleman and Li 1996] T. F. Coleman and Y. Li, “An interior trust region approach for nonlinear minimization subject to bounds”, *SIAM J. Optim.* **6**:2 (1996), 418–445.
- [Constantinides 2006] G. Constantinides, *Invariant mechanical properties of Calcium-Silicate-Hydrates (C-S-H) in cement-based materials: instrumented nanoindentation and micromechanical modeling*, Ph.D. thesis, Department of Civil and Environmental Engineering, Massachusetts Institute of Technology, 2006.
- [Doerner and Nix 1986] M. F. Doerner and W. D. Nix, “A method for interpreting the data from depth-sensing indentation instruments”, *J. Mater. Res.* **1**:4 (1986), 601–609.

- [Engheta 1996] N. Engheta, "On fractional calculus and fractional multipoles in electromagnetism", *IEEE Trans. Antenn. Propag.* **44**:4 (1996), 554–566.
- [Flügge 1967] W. Flügge, *Viscoelasticity*, Blaisdell, Waltham, MA, 1967.
- [Galanov 1982] B. A. Galanov, "An approximate method for the solution of some two-body contact problems with creep in the case of an unknown contact area", *Sov. Appl. Mech.* **18**:8 (1982), 711–718.
- [Galín 1961] L. A. Galín, *Contact problems in the theory of elasticity*, edited by I. N. Sneddon, North Carolina State College, Raleigh, NC, 1961.
- [Ganneau et al. 2006] F. P. Ganneau, G. Constantinides, and F.-J. Ulm, "Dual-indentation technique for the assessment of strength properties of cohesive-frictional materials", *Int. J. Solids Struct.* **43**:6 (2006), 1727–1745.
- [Gao and Ogden 2003] D. Y. Gao and R. W. Ogden (editors), *Advances in mechanics and mathematics, Volume II*, Advances in Mechanics and Mathematics **4**, Kluwer Academic, Boston, 2003.
- [Glöckle and Nonnenmacher 1991] W. G. Glöckle and T. F. Nonnenmacher, "Fractional integral operators and Fox functions in the theory of viscoelasticity", *Macromolecules* **24**:24 (1991), 6426–6434.
- [Hertz 1882] H. Hertz, "Über die Bierührung fester elastischer Körper", *J. Reine Angew. Math.* **92** (1882), 156–171. Translated in *Miscellaneous papers by H. Hertz*, Jones and Schott (Eds.), Macmillan, London, 1896.
- [Kilbas et al. 2006] A. A. Kilbas, H. M. Srivastava, and J. J. Trujillo, *Theory and applications of fractional differential equations*, North-Holland Mathematics Studies **204**, Elsevier, Amsterdam, 2006.
- [Lee 1955] E. H. Lee, "Stress analysis in visco-elastic bodies", *Quart. Appl. Math.* **13** (1955), 183–190.
- [Lee and Radok 1960] E. H. Lee and J. R. M. Radok, "The contact problem for viscoelastic bodies", *J. Appl. Mech. (ASME)* **27** (1960), 438–444.
- [Love 1939] A. E. H. Love, "Boussinesq's problem for a rigid cone", *Quart. J. Math. Oxford Ser. (2)* **10**:1 (1939), 161–175.
- [MacRobert 1962] T. M. MacRobert, *Functions of a complex variable*, 5th ed., Macmillan, London, 1962.
- [Marsden and Hoffman 1999] J. E. Marsden and M. J. Hoffman, *Basic complex analysis*, 3rd ed., W. H. Freeman, New York, 1999.
- [Micromaterials 2002] *Micromaterials nanotest user manual*, Micromaterials, Wrexham, 2002.
- [Oliver and Pharr 1992] W. C. Oliver and G. M. Pharr, "An improved technique for determining hardness and elastic modulus using load and displacement sensing indentation experiments", *J. Mater. Res.* **7**:6 (1992), 1564–1583.
- [Ostoja-Starzewski and Shahsavari 2008] M. Ostoja-Starzewski and H. Shahsavari, "Response of a helix made of a fractional viscoelastic material", *J. Appl. Mech. (ASME)* **75**:1 (2008), 011012.
- [Oyen 2005] M. L. Oyen, "Spherical indentation creep following ramp loading", *J. Mater. Res.* **20**:8 (2005), 2094–2100.
- [Oyen 2006] M. L. Oyen, "Analytical techniques for indentation of viscoelastic materials", *Philos. Mag.* **86**:33–35 (2006), 5625–5641.
- [Podlubny 1999] I. Podlubny, *Fractional differential equations*, Mathematics in Science and Engineering **198**, Academic Press, San Diego, CA, 1999.
- [Rabotnov 1980] J. N. Rabotnov, *Elements of hereditary solid mechanics*, Mir, Moscow, 1980.
- [Radok 1957] J. R. M. Radok, "Visco-elastic stress analysis", *Quart. Appl. Math.* **15** (1957), 198–202.
- [Ross 1977] B. Ross, "Fractional calculus", *Math. Mag.* **50**:3 (1977), 115–122. An historical apologia for the development of a calculus using differentiation and antidifferentiation of non-integral orders.
- [Rossikhin and Shitikova 2004] Y. A. Rossikhin and M. V. Shitikova, "Analysis of the viscoelastic rod dynamics via models involving fractional derivatives or operators of two different orders", *Shock Vib. Digest* **36**:1 (2004), 3–26.
- [Sakai 1999] M. Sakai, "The Meyer hardness: a measure for plasticity?", *J. Mater. Res.* **14**:9 (1999), 3630–3639.
- [Schiessel and Blumen 1993] H. Schiessel and A. Blumen, "Hierarchical analogues to fractional relaxation equations", *J. Phys. A Math. Gen.* **26**:19 (1993), 5057–5069.
- [Schiessel et al. 1995] H. Schiessel, R. Metzler, A. Blumen, and T. F. Nonnenmacher, "Generalized viscoelastic models: their fractional equations with solutions", *J. Phys. A Math. Gen.* **28**:23 (1995), 6567–6584.

- [Shahsavari and Ostoja-Starzewski 2005] H. Shahsavari and M. Ostoja-Starzewski, "On elastic and viscoelastic helices", *Philos. Mag.* **85**:33–35 (2005), 4213–4230.
- [Shimizu et al. 1999] S. Shimizu, T. Yanagimoto, and M. Sakai, "Pyramidal indentation-depth curve of viscoelastic materials", *J. Mater. Res.* **14**:10 (1999), 4075–4086.
- [Sneddon 1965] I. N. Sneddon, "The relation between load and penetration in the axisymmetric Boussinesq problem for a punch of arbitrary profile", *Int. J. Eng. Sci.* **3**:1 (1965), 47–57.
- [Tabor 1951] D. Tabor, *Hardness of metals*, Clarendon, Oxford, 1951.
- [Tschoegl et al. 2002] N. W. Tschoegl, W. G. Knauss, and I. Emri, "Poisson's ratio in linear viscoelasticity: a critical review", *Mech. Time-Depend. Mat.* **6**:1 (2002), 3–51.
- [Vandamme and Ulm 2006] M. Vandamme and F.-J. Ulm, "Viscoelastic solutions for conical indentation", *Int. J. Solids Struct.* **43**:10 (2006), 3142–3165.
- [Vandamme and Ulm 2007] M. Vandamme and F.-J. Ulm, "Indenter-shape independent viscoelastic solutions for indentation creep and relaxation testing", *C. R. Mécanique* (2007). Submitted.

Received 12 Oct 2008. Revised 22 Dec 2008. Accepted 4 Feb 2009.

ROUZBEH SHAHSAVARI: [shahs@mit.edu](mailto:shahs@mit.edu)

*Department of Civil and Environmental Engineering, Massachusetts Institute of Technology, 77 Massachusetts Avenue, Cambridge, MA 02139-4307, United States*

FRANZ-JOSEF ULM: [ulm@mit.edu](mailto:ulm@mit.edu)

*Department of Civil and Environmental Engineering, Massachusetts Institute of Technology, 77 Massachusetts Avenue, Cambridge, MA 02139-4307, United States*



## MACROSCALE MODELLING OF MICROSTRUCTURE DAMAGE EVOLUTION BY A RIGID BODY AND SPRING MODEL

SIRO CASOLO

A mechanistic approach is presented for macroscale modelling of a structured solid material. The model consists of an assemblage of rigid mass-elements connected to each other by normal and shear line-springs at each side. The characteristics of these springs govern the macroscopic behaviour of the model that is able to incorporate an internal length and a polarity, in analogy with an orthotropic Cosserat solid material. The present numerical implementation addresses the in-plane modelling of a masonry-like composite whose main macroscopic constitutive aspects are: very low tensile strength, texture-dependent evolution of the damage, and orthotropy of shear strength and internal friction. The constitutive rules are assigned by following a heuristic approach, based on the main in-plane damage mechanisms that are identified at the mesoscale, on a representative volume element of the composite solid material. In particular, specific separate constitutive laws for the normal and the shear springs are adopted. Two numerical tests compare the present macroscale approach with a detailed finite element micromodelling, and demonstrate the capability of the proposed model to describe the main microstructure features of the damaging process with very few degrees of freedom.

### 1. Introduction

The mechanical response and damage evolution of a composite material made with a periodic texture are strictly related to its internal geometry and to the ratio between the microstructure characteristic length and the global size of the system. In the present study, attention is focused on the postelastic macroscale response of a plane masonry-like material that is composed of blocks jointed by mortar layers where the strain tends to localise and the main part of the mechanical degradation occurs. It is well known that the texture geometry produces perceivable effects at the macroscale that tend to evolve and to become more evident with the progressive degradation of the material. In particular, the different topology of the continuous horizontal mortar joints with respect to the vertical joints, interrupted by the blocks, causes a marked orthotropy of the macroscopic shear response, as also shown by specific laboratory experiment [Malyszko 2005].

Experiments as well as numerical and analytical studies have shown that often the damage behaviour of a masonry-like material can be described on the basis of a limited number of mesoscale mechanisms [Dhanasekar et al. 1985; Zucchini and Lourénço 2002]. At the macroscale level, most of these damage mechanisms can be modelled in the frame of a Cauchy solid continuum approach [Lourénço et al. 1997; Pietruszczak and Ushaksaraei 2003; Massart et al. 2004; Milani et al. 2006]. Nevertheless, there are cases in which microscale effects need to be explicitly considered and the description of the mechanical degradation entails taking into account the local rotation of the blocks and the orthotropy of shear

---

*Keywords:* RBSM, rigid, spring, macroscale, microstructure, heuristic, Cosserat.

strength. Dealing with regular textures, the micro/mesoscale transition can thus be performed toward an enriched generalised continuum, which retains some information on the microstructure and internal length [Masiani et al. 1995; Sulem and Mühlhaus 1997; Forest and Sab 1998]. More recently, the relationship between the micro and macroscale for the specific case of masonry-like periodic rigid block assemblies has also been handled by resorting to a multiscale strategy [Trovalusci and Masiani 2005; Brasile et al. 2007].

An alternative computational approach that adopts a specific *mechanistic* model was proposed in [Casolo 2004]. In this case, the heterogeneous solid material is imaged as a mechanism consisting of rigid masses connected by simple elastic-plastic damaging springs, in the spirit of the rigid body spring model (RBSM) [Kawai 1978; Griffiths and Mustoe 2001; Ostoja-Starzewski 2002] and somewhat in the vast family of discrete element models [Lemos 2007]. Given a representative volume of the periodic heterogeneous solid material, the core of the proposed model is a macroscopic mechanical device consisting of 4 masses connected by springs, as shown in Figure 1. This discrete mechanical device should possess the relevant macroscopic properties of the periodic microstructured solid material, and we tentatively name it the *representative macroscopic segment* or *heuristic molecule*. The linear elastic characteristics of the three line springs that connect the elements at each side can be defined either by the relationship with a corresponding continuum or by a direct computational approach [Casolo 2006]. To describe the mean damage evolution of the material, a heuristic approach was initially proposed in [Boffi and Casolo 1998], and then in [Casolo and Peña 2007], based on the phenomenological consideration of the main in-plane damage mechanisms that can be described at the mesoscale.

The sequel of such research is presented in this paper, with the emphasis now placed on discerning the impact of material texture on the orthotropic damage evolution at the macroscale level. As a case study, a masonry-like material made of three material components is considered: the blocks, and the horizontal and vertical mortar joints. The load is applied on an area whose size is comparable with the internal microstructure length of the periodic arrangement. In this case the orthotropy of the shear response and the local rotation of the blocks play an important role in the development of damage, also at the

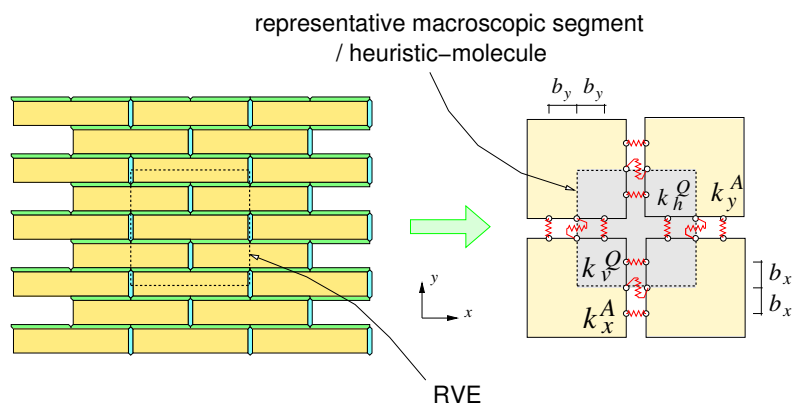


**Figure 1.** Heuristic representation of the correspondence between an RVE (representative volume element) of the composite material and the representative macroscopic segment, or heuristic molecule, made of rigid masses and springs.

macroscale. The numerical application presented at the end of the paper will investigate and compare the proposed mechanistic model with a finite element continuum model that describes the masonry-like texture with a microscale level of detail, assuming a modified Drucker–Prager plasticity model for the three material components [ABAQUS 2007].

## 2. The macroscale rigid body and spring model

**2.1. Discrete formulation of the kinematics.** The masonry-like composite material is modelled as a plane solid body partitioned into  $m$  quadrilateral mass-elements  $\omega^i$  such that no vertex of one quadrilateral lies on the edge of another quadrilateral [Casolo 2006]. Given a global reference frame  $\{O, x, y\}$ , the deformed configuration of the discrete model is described by the displacements and rotation  $\{u_i, v_i, \psi_i\}$  of the local reference frames  $\{o^i, \zeta^i, \eta^i\}$  fixed in each element's barycentre  $o^i$ . These  $3m$  variables are assembled into the vector of Lagrangian coordinates  $\{u\}$  that is conjugated in virtual work with the corresponding vector of external loads  $\{p\}$  (see Figure 2a), as

$$\{u\}^T = \{u_1, v_1, \psi_1, u_2, v_2, \psi_2, \dots, u_m, v_m, \psi_m\}, \quad \{p\}^T = \{p_1, q_1, \mu_1, p_2, q_2, \mu_2, \dots, p_m, q_m, \mu_m\}.$$

Three line springs connect each couple of adjoining mass-elements in correspondence of points  $P$ ,  $Q$  and  $R$ , placed along the common side as shown in Figure 2b.<sup>1</sup> Then, average strain measures are associated with these connecting devices: the axial strains,  $\varepsilon^P$  and  $\varepsilon^R$ , are associated with the volumes of pertinence  $V^P$  and  $V^R$ , while the shear strain  $\varepsilon^Q$  is associated with the volume  $V^Q$ , defined by  $V^Q = V^P + V^R$ . Considering a discrete model with  $r$  sides that connect all the elements, the generalised strain vector  $\{\varepsilon\}$  and the diagonal matrix of volumes of pertinence  $[V]$  are defined as

$$\begin{aligned} \{\varepsilon\}^T &= \{\varepsilon_1^P, \varepsilon_1^Q, \varepsilon_1^R, \varepsilon_2^P, \varepsilon_2^Q, \varepsilon_2^R, \dots, \varepsilon_r^P, \varepsilon_r^Q, \varepsilon_r^R\}, \\ [V] &= \text{diag}\{V_1^P, V_1^Q, V_1^R, V_2^P, V_2^Q, V_2^R, \dots, V_r^P, V_r^Q, V_r^R\}. \end{aligned} \quad (1)$$

Under the assumption of small displacements, the strain-displacement relation can be expressed by considering a  $3r \times 3m$  matrix  $[B]$  as  $\{\varepsilon\} = [B]\{u\}$  (see Appendix A for a specific example).

**2.2. Incremental formulation of the balance laws.** A measure of stress, conjugated in virtual work with the strain associated to each connecting device, is introduced, and the corresponding vector of generalised stress  $\{\sigma\}$  is assembled as  $\{\sigma\}^T = \{\sigma_1^P, \sigma_1^Q, \sigma_1^R, \sigma_2^P, \sigma_2^Q, \sigma_2^R, \dots, \sigma_r^P, \sigma_r^Q, \sigma_r^R\}$ . Out of the linear elastic field, the stress  $\sigma$  and the tangent stiffness  $k$  of each spring depend on the whole past deformation history (designated by the symbol  $\star$ ) which is subdivided into discrete time intervals. Given the stress  $\sigma^0$  for a generic spring at instant  $t_i$ , the following linear expression is adopted for predicting the stress at instant  $t \in [t_i, t_{i+1}]$ :  $\sigma(t, \star) = \sigma^0(t_i, \star) + k(t_i, \star)\Delta\varepsilon$ , with  $\Delta\varepsilon$  being the evaluated strain increment in the spring. The local tangent stiffness matrix  $[D_t]$  of all the connecting springs is

$$[D_t] = \text{diag}\{k_1^P, k_1^Q, k_1^R, k_2^P, k_2^Q, k_2^R, \dots, k_r^P, k_r^Q, k_r^R\}. \quad (2)$$

<sup>1</sup>The absence of the axial springs that connect the rigid elements along the diagonals of the heuristic molecule limits the present RBSM to behaving at the macroscale like a solid material with a Poisson's ratio of zero. This has been assumed for simplicity, after considering the limited importance of the Poisson effect for the main damaging mechanisms of a masonry-like composite material. In general, a range of different values for the macroscopic Poisson's coefficient can be obtained by combining different types of spring (axial, shear, or rotational) and by an appropriate definition of the lattice geometry [Stakgold 1950; Ostoja-Starzewski 2002].

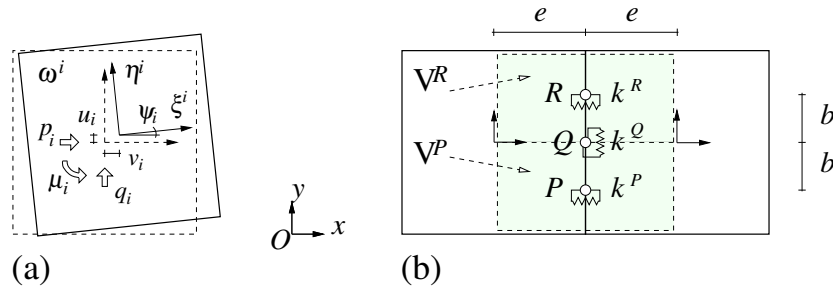


**Figure 2.** Notation adopted and disposition of the connecting springs [Casolo and Peña 2007].

Thus, the internal virtual work done by the elastic-plastic springs is

$$\delta^e W^i = \{\delta \varepsilon\}^T [V] \{\sigma^0\} + \{\delta \varepsilon\}^T [V] [D_t] \{\Delta \varepsilon\} = \{\delta u\}^T (\{f^0\} + [K_t] \{\Delta u\}), \tag{3}$$

where  $\{f^0\}$  is the vector of generalised forces and  $[K_t]$  is the generalised tangent stiffness matrix, defined as  $\{f^0\}^T = \{\sigma^0\}^T [V] [B]$ , and  $[K_t] = [B]^T [V] [D_t] [B]$ , respectively. On the other hand, the virtual work done by the external forces is simply  $\delta^e W^e = \{\delta u\}^T \{p\}$ . Then, by means of the balance of virtual works  $\delta^e W^i = \delta^e W^e, \forall \{\delta u\}$ , the following system of incremental static equations is obtained:

$$\{f^0\} + [K_t] \{\Delta u\} = \{p\}. \tag{4}$$

This is solved adopting the full Newton–Raphson iteration scheme until numerical convergence is attained [Zienkiewicz and Taylor 1991].

**2.3. Constitutive laws: linear elastic field.** A computational approach based on the five elemental loading tests sketched in Figure 3 is adopted, in the linear elastic field, to identify the four spring stiffness  $k_x^P, k_y^P, k_x^Q,$  and  $k_y^Q$ , and the two distances  $b_x$  and  $b_y$  [Casolo 2004]. Alternatively, these six parameters can also be obtained by a direct relation with the elastic tensor  $C$  of an “equivalent” orthotropic

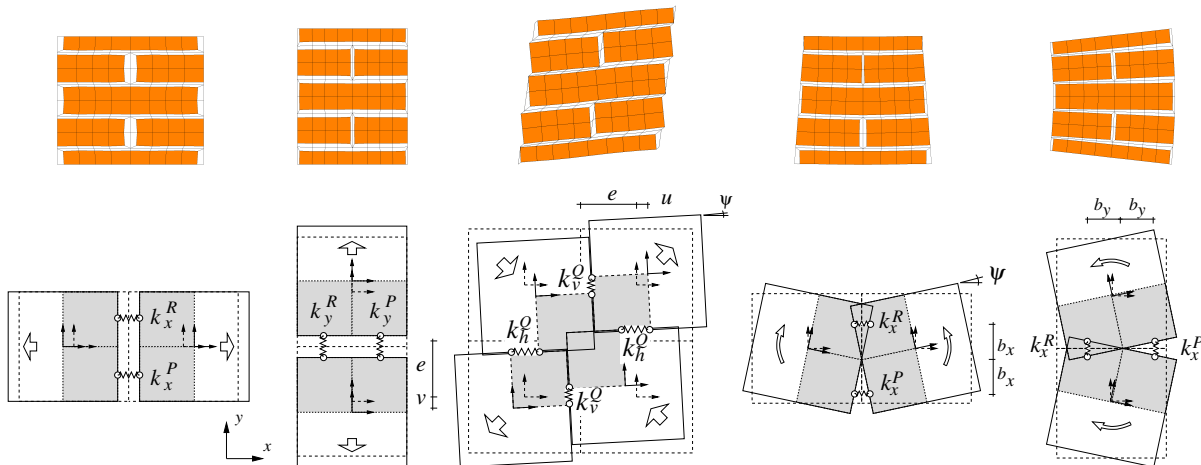


**Figure 3.** Scheme of the deformed shape of the five elemental tests of loading. The finite element model of the RVE (top row) and the the corresponding rigid element schemes (bottom row).

Cosserat continuum,<sup>2</sup> as explained in [Casolo 2006] and summarised in Appendix B. The microscale model adopts a very common masonry-like texture, with a typical Italian brick geometry for the blocks:  $2l \times 2h = 25 \times 5.5$  cm. The case of single leaf masonry is considered here for the sake of clarity as a first approach, with a depth of 12 cm. The reference RVE is a  $26 \times 26$  cm square domain made by finite elements. Homogeneity, isotropy, and perfect bonding are assumed for the three components of the heterogeneous masonry-like material. The elastic modulus of the blocks is  $E_b = 10000$  MPa, the elastic moduli of the horizontal and the vertical mortar joints are  $E_h = 2000$  MPa and  $E_v = 1000$  MPa, respectively, while the Poisson's coefficient is fixed as  $\nu = 0.1$  for all the components.

The stiffness of the axial springs can be directly computed by considering the RVE subjected to simple normal loading acting parallel to a material principal direction and traction-free boundary condition along the other two sides (the first and second loading cases, in the left part of Figure 3). Given the generalised axial strains  $\varepsilon_x = u/e$  and  $\varepsilon_y = v/e$ , and the corresponding average elastic energy densities  ${}^0u_x^A$  and  ${}^0u_y^A$ , then the axial stiffnesses per unit volume to be attributed to the normal connecting devices are

$$k_x^P = \frac{2{}^0u_x^A}{\varepsilon_x^2}, \quad k_y^P = \frac{2{}^0u_y^A}{\varepsilon_y^2}. \quad (5)$$

The evaluation of the shear response requires some more attention. In fact, in addition to the mean shear deformation  $E_s$  it is necessary to select a criterion for measuring the mean local rotation  $\psi$  of the blocks [Casolo 2006]. A direct test can be made, in which the RVE is subjected to periodic displacement boundary conditions and loaded by shear actions along the four boundaries that have equal absolute value  $S_{12} = S_{21}$  (this is the loading case shown in the centre of Figure 3). The average symmetric shear strain is  $\varepsilon_s = (u + v)/2e$ , while the average local rotation measured on the blocks is directly assigned to the rigid elements. The generalised shear strains for the vertical and the horizontal connecting devices are then

$$\varepsilon_v = \varepsilon_s - \psi = \varepsilon_s(1 - \rho), \quad \varepsilon_h = \varepsilon_s + \psi = \varepsilon_s(1 + \rho), \quad (6)$$

with the local rigid rotation ratio  $\rho = \psi/\varepsilon_s$ . The equilibrium of the shear stresses implies that the stiffnesses of the shear connecting devices of the vertical and horizontal sides must be related by the following equation:

$$\frac{k_h^Q}{k_v^Q} = \frac{\varepsilon_v}{\varepsilon_h} = \frac{1 - \rho}{1 + \rho}. \quad (7)$$

Thus, a generalized symmetric shear stiffness  $k_s$  can be defined, such as

$$k_v^Q = (1 + \rho)k_s, \quad k_h^Q = (1 - \rho)k_s.$$

Finally,  $k_s$  is defined as a function of the average elastic energy  ${}^0u_s$  per unit volume stored in the volume of pertinence:

$$k_s = \frac{{}^0u_s}{(1 - \rho^2)\varepsilon_s^2} \quad (8)$$

<sup>2</sup>Clearly, the reduction from eight to six parameters in the passage from the plane orthotropic Cosserat continuum to the present RBSM implies a loss of information about the axial and shear coupling effects. The correspondence would be ideal in the case of an equivalent Cosserat continuum with a *diagonal* elastic tensor as proposed in [Masiani et al. 1995; Sulem and Mühlhaus 1997].

The distances  $b_x$  and  $b_y$  of the axial springs from the mid-point of each side are evaluated by means of the two in-plane bending tests, shown in Figure 3 on the right. After measuring the average elastic energy densities  ${}^0u_x^F$  and  ${}^0u_y^F$  from the RVE finite element model, we have

$$\beta_x = \frac{b_x}{e} = \frac{1}{\psi} \sqrt{\frac{2{}^0u_x^F}{k_x^P}}, \quad \beta_y = \frac{b_y}{e} = \frac{1}{\psi} \sqrt{\frac{2{}^0u_y^F}{k_y^P}}. \quad (9)$$

The six values identified for the springs in the linear-elastic field are as follows:<sup>3</sup>

$$\begin{aligned} k_x^P &= 5650 \text{ MPa} & k_h^Q &= 3520 \text{ MPa} & \beta_x &= 0.61 \\ k_y^P &= 7600 \text{ MPa} & k_v^Q &= 11780 \text{ MPa} & \beta_y &= 0.57 \end{aligned} \quad (10)$$

#### 2.4. Constitutive laws: elastic-plastic field.

**2.4.1. Overview of the heuristic approach.** Modelling the mechanical degradation when the effects at the microstructure level entail taking the local rotation of the blocks and the orthotropy of shear strength into account is the focus of this contribution. To do this, the main hypothesis of the proposed constitutive model is that the damage evolution can be described using a limited number of mesoscale mechanisms that are strictly related with the internal microstructure geometry [Malyszko 2005; Trovalusci and Masiani 2005].

The five basic mesoscale elemental mechanisms are sketched in Figure 4:

- (i) cracking of vertical joints with sliding of bed-joint under horizontal tension;
- (ii) global crushing and local splitting of joints under horizontal compression;
- (iii) bed-joints cracking and opening under vertical tension;
- (iv) global crushing given by simultaneous splitting of blocks and cracking of vertical joints under vertical compression; and
- (v) shear sliding of mortar joints along a stepwise pattern under shear loading with *local* rotation of the blocks.

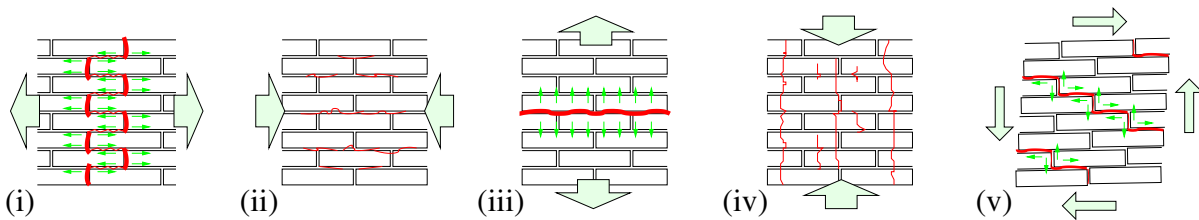


**Figure 4.** Heuristic description of the five types of damage mechanism considered at the mesoscale.

<sup>3</sup>Note that the size effect can significantly affect the macroscopic response of microstructured materials. Ideally, when the size of the discrete elements is much larger than the characteristic length of the RVE, then the parameters that govern the microstructure effects must become negligible at the macroscale level. The present RBSM is designed to deal with this aspect by progressively reducing the orthotropy of the shear springs and by making  $\beta_x$  and  $\beta_y$  tend to  $1/\sqrt{3}$ , as described in [Casolo 2004].

Mechanisms (i) and (v) are those for which the effect of the texture on the global response is more significant. In fact, in the first case the tensile strength is strictly related to the aspect ratio of the blocks, in combination with the friction coefficient of the horizontal mortar joints and the presence of a vertical compressive stress. On the other hand, in the last mechanism the mean local rotation of the blocks as well as the orthotropy of the shear response is also strictly related to the shape and disposition of the blocks. Moreover, it is evident that the presence of a mean compression stress has an impact on the strength characteristics that is orthotropic and depends on the texture geometry.

The proposed constitutive model exploits the observation that the mesoscale damage mechanisms are limited, by associating a particular damage pattern almost exclusively to each type of spring. The model works at the macroscale, without the need of describing the effective texture geometry with the mesh; this is the essential difference with respect to the classical continuum approach usually adopted in finite element models, which generally require to describing the geometry of the material microstructure, except when adopting a generalised continuum [Masiani et al. 1995]. Clearly, in the present formulation the springs should be as much as possible aligned with the principal axes of the material texture, otherwise a good approximation cannot be taken for granted. Furthermore, at present no particular steps have been taken to deal with the localisation and the mesh objectivity which are a consequence of strain-softening material behaviour [Lour en o et al. 1997; de Borst 2001]. As a rule of thumb, the model should be composed by units whose size is approximately comparable to the size of the RVE. In any case, the tests presented in the following section will reveal a limited sensitivity with respect to mesh size.

Even if the present work is focused on the monotonic response, this notwithstanding the RBSM is implemented into a computer code that is designed to perform dynamic analyses. Thus, the constitutive laws also include the hysteretic response, with different rules for strength and stiffness degradation of the axial and shear springs, as is schematically shown in Figure 5, by following the paths indicated by the points labelled 1–9. The skeleton curves degrade depending on the maximum positive and maximum negative deformation reached during the loading history. The degradation of loading stiffness, unloading stiffness, and strength also depends on the maximum deformation reached. Out of the range of deformation defined by the interval  $[S^-, S^+]$ , the skeleton curves are horizontal and correspond to a residual strength which is assumed to remain constant until the ultimate deformation is reached. These hysteretic rules are strictly derived from those already described with more detail in [Casolo 2000; Casolo and Pe a 2007], based on phenomenological evidence [Naraine and Sinha 1991; Binda et al. 1992; Magenes

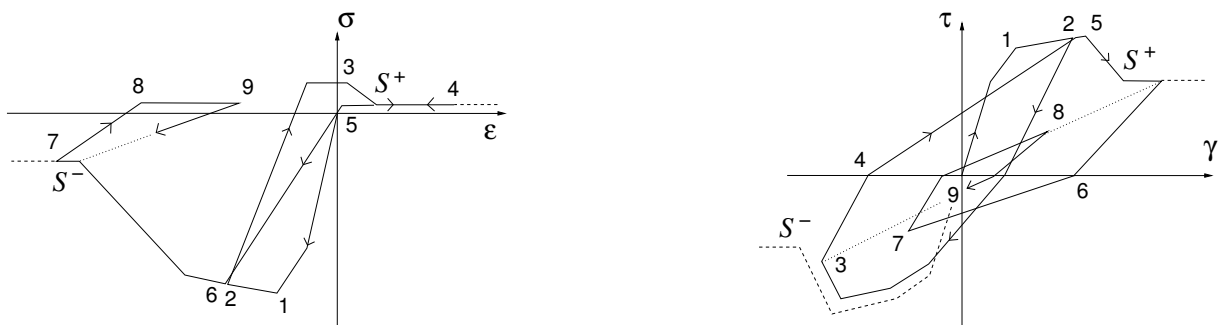


**Figure 5.** Hysteretic behaviour of the axial (left) and shear (right) connecting springs.

	$p_t _0$ (MPa)	$\phi$ (°)	$\vartheta$ (°)
Brick	0.425	30	5
Horizontal mortar	0.10	30	5
Vertical mortar	0.05	30	5

**Table 1.** Parameters assigned to the material components of the masonry-like RVE:  $p_t|_0$  is the initial hydrostatic tension strength of the material, while  $\phi$  and  $\vartheta$  are the material angle of friction and the dilatation angle, respectively.

and Calvi 1992; Anthoine et al. 1995], while in the following sections attention will be only devoted to define the parameters that govern the monotonic response.

**2.4.2. Monotonic tests on the finite element RVE.** The RVE is made by 4-node bilinear generalised plane strain finite elements that adopt the Drucker–Prager plasticity material model available within [ABAQUS 2007]. The hyperbolic yield criterion has been assigned to the three material components: the bricks, and the horizontal and vertical mortar joints. This criterion is a continuous combination of the maximum tensile stress condition of Rankine (tensile cut-off) and the linear Drucker–Prager condition at high confining stress:

$$F = \sqrt{(d'|_0 - p_t|_0 \tan \phi)^2 + q^2} - p \tan \phi - d' = 0, \quad (11)$$

where  $d'$  is the hardening parameter,  $p_t|_0$  is the initial hydrostatic tension strength of the material,  $\phi$  is the material angle of friction,  $q$  is the von Mises equivalent stress, and  $p$  is the equivalent pressure stress.<sup>4</sup> In the present application, the hardening parameter is

$$d' = \sqrt{(d|_0 - p_t|_0 \tan \phi)^2 + d^2}, \quad (12)$$

and it is defined by the cohesion yield stress,  $d = \sqrt{3}\tau$ , data (where  $\tau$  is the yield stress in a shear test) as a function of the equivalent shear plastic strain

$$\bar{\varepsilon}^{pl} = \frac{\gamma^{pl}}{\sqrt{3}}.$$

The values assigned to  $p_t|_0$ ,  $\phi$ , and the dilatation angle  $\vartheta$  in the  $p - q$  plane at high confining pressure are reported in Table 1, while the hardening behaviour of the three elemental materials is shown in Figure 6, left, in terms of a simple shear test.<sup>5</sup> The finite element mesh of the composite RVE is shown in Figure 6, right. The thickness of the mortar joints is  $t = 1$  cm, and the vertical head-joints, interrupted by the bricks, are considered as weaker than the horizontal continuous bed-joints.

<sup>4</sup>In more detail, according with the notation of the [ABAQUS 2007] manual,  $p = -\frac{1}{3} \text{tr}[S]$  and  $q = \sqrt{\frac{2}{3} [S^d] : [S^d]}$ , where  $[S]$  is the Cauchy stress tensor.

<sup>5</sup>The flow potential is  $G = \sqrt{(0.1d|_0 \tan \vartheta)^2 + q^2} - p \tan \vartheta$ , with  $d|_0$  the initial cohesion yield stress. This flow potential is continuous and smooth and ensures that the flow direction is always uniquely defined. This function approaches the linear Drucker–Prager flow potential asymptotically at high confining pressure stress and intersects the hydrostatic pressure axis at  $90^\circ$  [ABAQUS 2007].



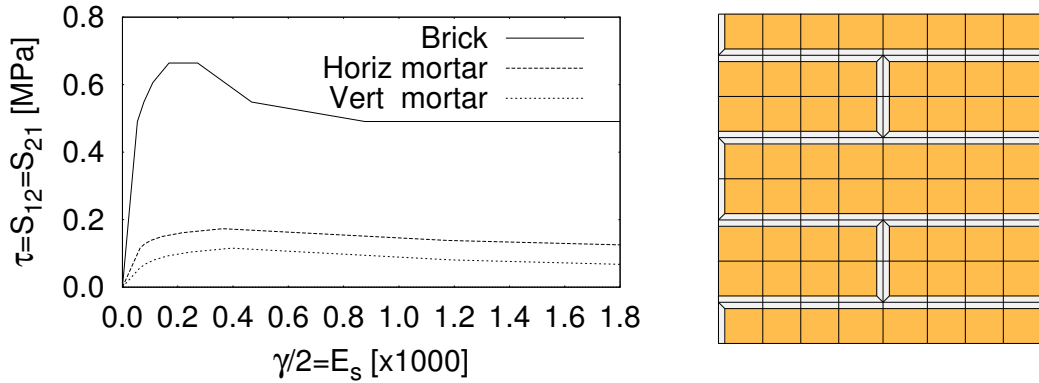


**Figure 6.** Left: Hardening behaviour in a shear test for the three elemental materials. Right: Finite element mesh of the RVE.

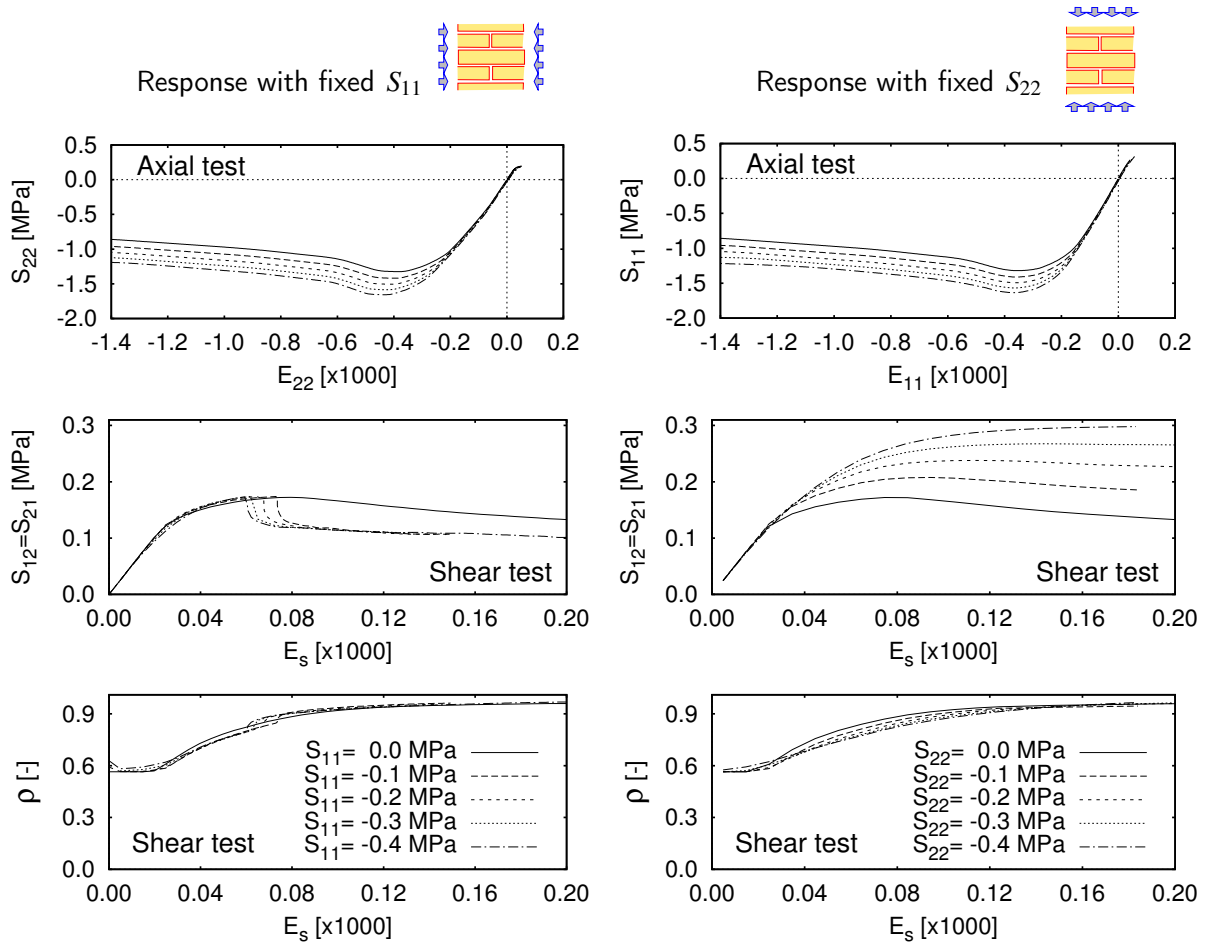


**Figure 7.** Macroscale results of the monotonic tests on the finite element RVE.

Four sets of elemental computational tests were considered on the basis of the heuristic description already sketched in Figure 4. At the macroscale, the effect of the internal friction is evaluated by considering tests with a different level of mean compression along the horizontal and vertical principal directions. The responses, written in terms of mean stress-strain relations, are reported in detail in Figure 7. The following synthetic observations can be made:

- *Tension*: In this case the strength is very low and the calculated response appears to be completely brittle due to the lack of numerical convergence of the computer code. Note that the strength along the horizontal direction (top right) is higher than along the vertical direction (top left) because the vertical joints are interrupted by the blocks.
- *Compression*: In this case the material exhibits its maximum bearing capacity with a progressive mechanical degradation once the peak value of the strength is reached. In the present case the response is almost isotropic.
- *Shear*: This case is governed by the response of the mortar joints. The residual shear strength is enhanced by a vertical compression, obeying a Coulomb-type relation, while the presence of a horizontal mean compression produces a global instability.
- *Local rotation*: In the case of symmetric shear loading the texture effects are evident, involving the local rotation of the blocks, measured by the angle  $\psi$ . The ratio  $\rho = \psi/\varepsilon_s$  is reported in Figure 7 as a function of the symmetric shear deformation  $E_s$ , where  $E_s = (E_{12} + E_{21})/2$ .

**2.4.3. Definition of the constitutive laws of the springs.** The elastic-plastic characteristics given to the connecting springs descend from the identification tests made on the RVE, summarized in Figure 7.

In the macroscopic compression region the constitutive laws of the axial springs are directly related to the axial responses of the reference RVE, as shown in the top row of Figure 8, while for simplicity  $\beta_x$  and  $\beta_y$  have the fixed values reported in (10) on page 556. In the tensile region, on the other hand, the completely brittle response of this RVE at the macroscopic level is mainly due to a global lack of numerical convergence of the computer code. In fact, when adopting uneven loading conditions the tensile behaviour exhibits some strain softening at the local level. Unfortunately this effect is not easily quantifiable, since it depends on the size of the specimen as well as on the different boundary conditions. Thus, a softening behaviour has been tentatively given to the axial springs under tensile loading by assigning a negative slope that is in accord with the negative slope of the compression branch, as shown in Figure 8.

The definition of the horizontal and vertical shear springs requires fitting both the macroscale response in terms of the symmetric shear stress-strain relation and the evolution of the local rotation ratio  $\rho$  as a function of the mean shear strain  $E_s = \varepsilon_s = (\varepsilon_h + \varepsilon_v)/2$ . To do this, different constitutive laws are assigned to the vertical and horizontal shear springs, as shown in the middle row of Figure 8, according with the criterion already explained in [Casolo 2004]. A partial validation of the combined effect of these assignments on the global shear behaviour is shown in the bottom row of Figure 8, where the macroscopic responses of the RBSM heuristic molecule in terms of  $\tau_s(\varepsilon_s)$  and  $\rho_s(\varepsilon_s)$  are compared with the finite element RVE.

Since the macroscale shear strength is enhanced by the presence of vertical compression, it is also assumed that the shear skeleton curve translates as a function of the mean vertical axial stress  $\bar{\sigma}_v$  in the

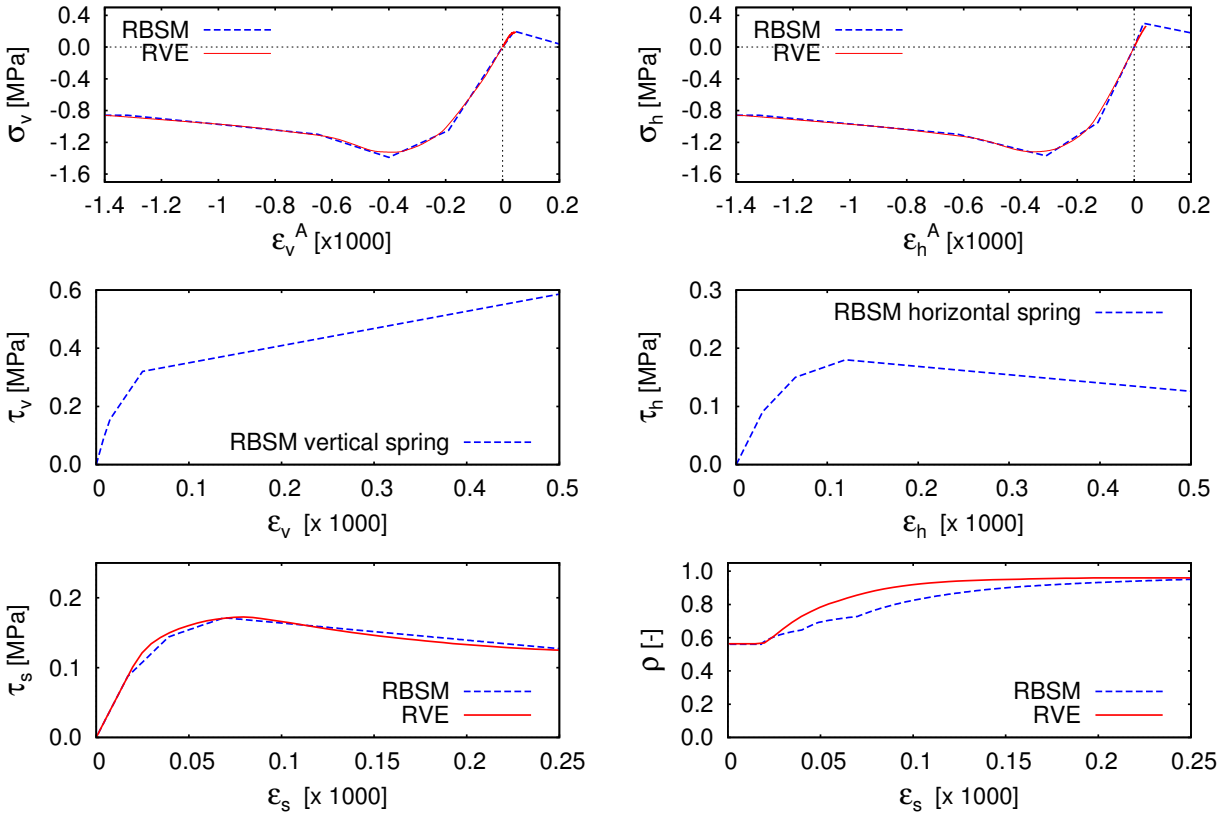


**Figure 8.** Elastic-plastic characteristics of the rigid element springs. The the characteristics of the axial springs (top row), and the characteristics of the shear springs and the corresponding local rotation ratio  $\rho$  (middle and bottom rows).

corresponding volume of pertinence  $V^Q$ , as shown in Figure 9. From the results of the shear test with fixed  $S_{22}$ , the value  $\phi = 0.3$  has been given to this Coulomb-type internal friction coefficient. At present, the model assumes that the influence of the shear on the response of the axial springs is negligible.

Up to now, no specific steps have been taken to deal with localisation and mesh objectivity, which are consequences of strain-softening material behaviour [Lour en o et al. 1997; de Borst 2001].

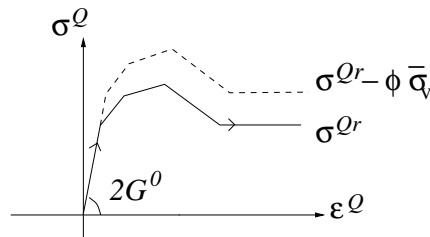


**Figure 9.** Variation of the skeleton curve of a shear spring as a function of the mean vertical stress  $\bar{\sigma}_v$ .

### 3. The case study

To evaluate the performance of the present approach, a situation where the microstructure effects are significant has been investigated in depth. The case study is a square plane domain subjected to two boundary and loading conditions that cause a highly nonhomogeneous stress-strain field, also at the macroscale. The vertical and the horizontal load are monotonically applied over a distributed small volume, as shown in the scheme of Figure 10, left. The parts drawn with dotted line hatching indicate a kinematic boundary condition of full clamping. Note that the block size is not far from the macroscale characteristic length of the problem.

**3.1. Response of the reference FE wall.** The microscale model adopted as the reference wall is made by means of a refined mesh of 3600 plane 4-node bilinear finite elements as shown in Figure 10, right, for a total of 7425 degrees of freedom.

Figure 11 shows the maps of the deformed shape and of the equivalent plastic strain (called PEEQ in ABAQUS) for a loading configuration close to the collapse. The response of this FE model clearly reveals the role played by the masonry-like texture that produces quite different kinematics of the two collapse mechanisms. This is due to the combined effect of the texture geometry with the internal friction, that enhances the shear strength of the horizontal joints in the presence of a vertical pressure. In the case of vertical applied load, the collapse mechanism involves a significant local rotation of the blocks, while in the case of horizontal load the kinematics can be mainly described in terms of horizontal relative translation of the blocks. As a first consequence, the distribution of the plastic strain evidences a diffused damaged area in the first case, while the damage is concentrated in few horizontal layers of mortar with the horizontal load. At the macroscale, the final consequence is that we have a very different bearing capacity, with a maximum vertical load that is 83% higher than the maximum horizontal load

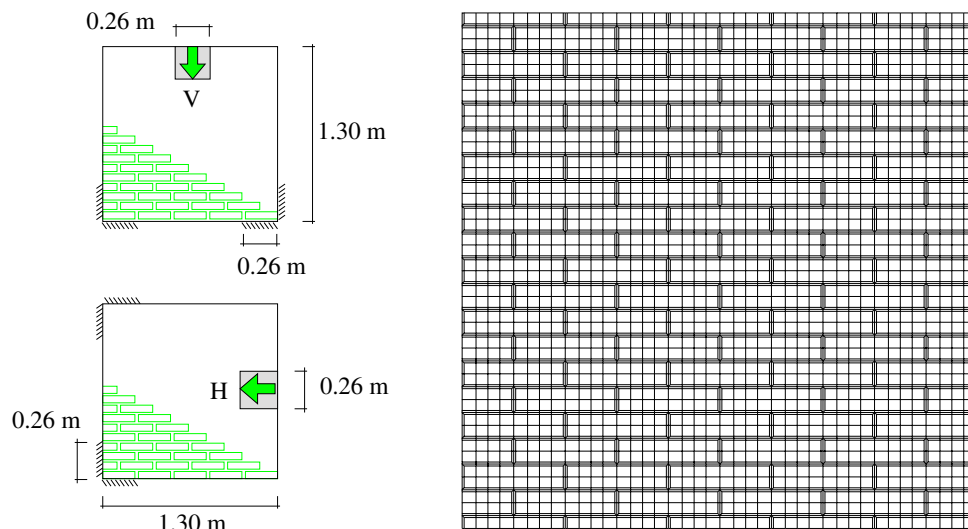


**Figure 10.** Left: scheme of the masonry walls used as reference. Right: finite element mesh for the microscale reference model.

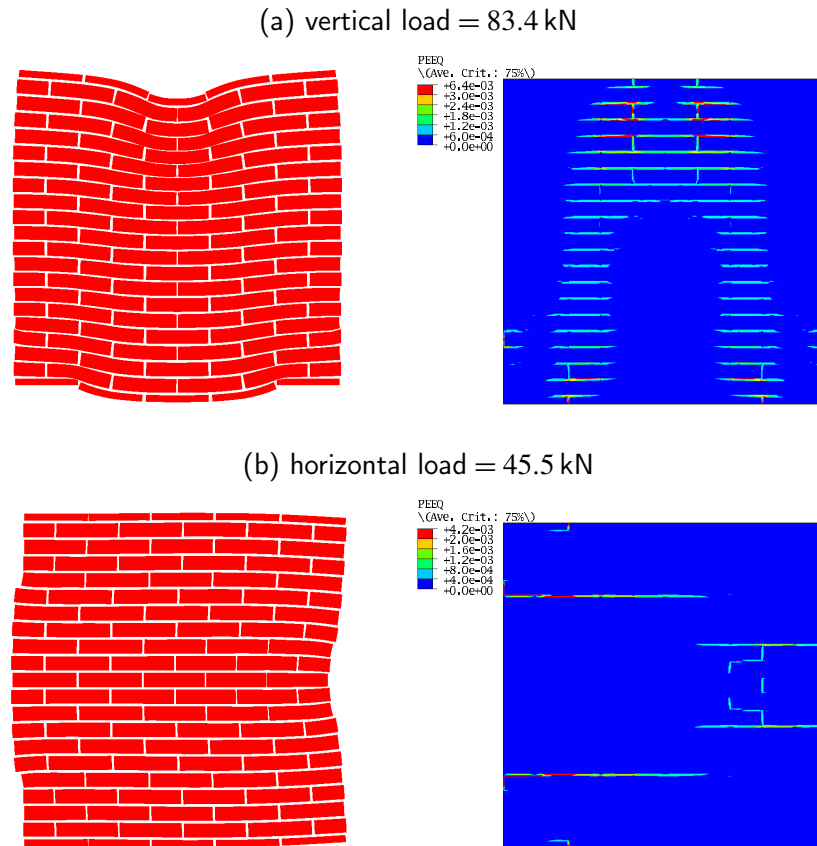


**Figure 11.** Deformed shape and equivalent plastic strain (peeq) for the microscale finite element model for a configuration close to collapse. The vertical (a) and horizontal (b) applied loads.

( $\sim 84$  kN versus  $\sim 46$  kN).<sup>6</sup> Also quite different is the trend of the decay of the stiffness as a function of the increasing displacement at the point of application of the load.

**3.2. Response of the RBSM.** The response of the RBSM is here presented making reference to regular meshes of  $5 \times 5$ ,  $10 \times 10$  and  $20 \times 20$  square elements (hence 75, 300 and 1200 degrees of freedom). With this model, the fully clamped boundary condition should be intended in the sense that the border elements are connected to a solid base that is completely rigid. Ideally, this base could be also modelled by a rigid body and springs that have infinite stiffness. In practice, the connecting springs placed along the clamped boundary have an effective length that is half that of the internal ones, while the strength remains unchanged.

<sup>6</sup>It is interesting to recall that in the laboratory experiment by Malyszko [2005] the orthotropic shear strengths were evaluated by arranging the boundary conditions as to obtain a predetermined single plane of failure: (i) for a loading  $H$  tangential to the bed joints, and (ii) for a loading  $V$  normal to the bed joints. In the first case the global strength was related to the shear strength of the horizontal mortar joint, while in the second case the collapse mechanics was more complex and the shear strength of the bricks was also determinant. The ratio of the two shear strengths was  $V/H = 1.65$ .

First, the capability of the present model to account for the specific microstructure effects can be appreciated from the maps shown in Figure 12, which report the responses of the two RBSMs subjected to the same value of load, equal to 35 kN, along the vertical and horizontal directions. This load produces some mechanical degradation in these models, with a decay of  $\sim 10\%$  of the global stiffness in the case of vertical load, and a decay of  $\sim 30\%$  in the case of horizontal load. In this test, it is noticeable that the central part of the model subjected to the vertical load presents horizontal stripes of alternate positive and negative axial stress  $\sigma_h$ , which indicates the presence of a *local in-plane* flexural mechanism. Clearly, this effect is strictly related to the specific RBSM capability of retaining memory of the original internal texture. In fact, this behaviour is correctly absent in the case of a horizontal applied load. From these

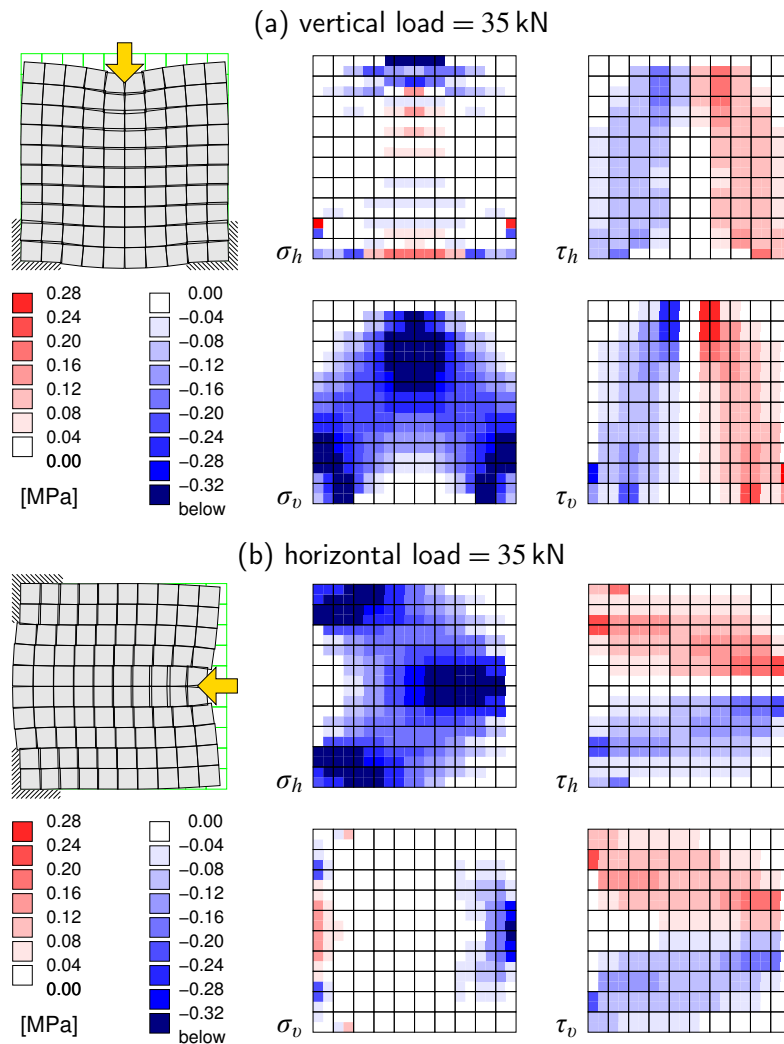


**Figure 12.** Deformed shape and maps of the generalised stresses in the axial springs ( $\sigma_h$ ,  $\sigma_v$ ) and in the shear springs ( $\tau_h$ ,  $\tau_v$ ) as obtained by means of the nonlinear rigid element model subjected to a vertical load (a) and a horizontal load (b).

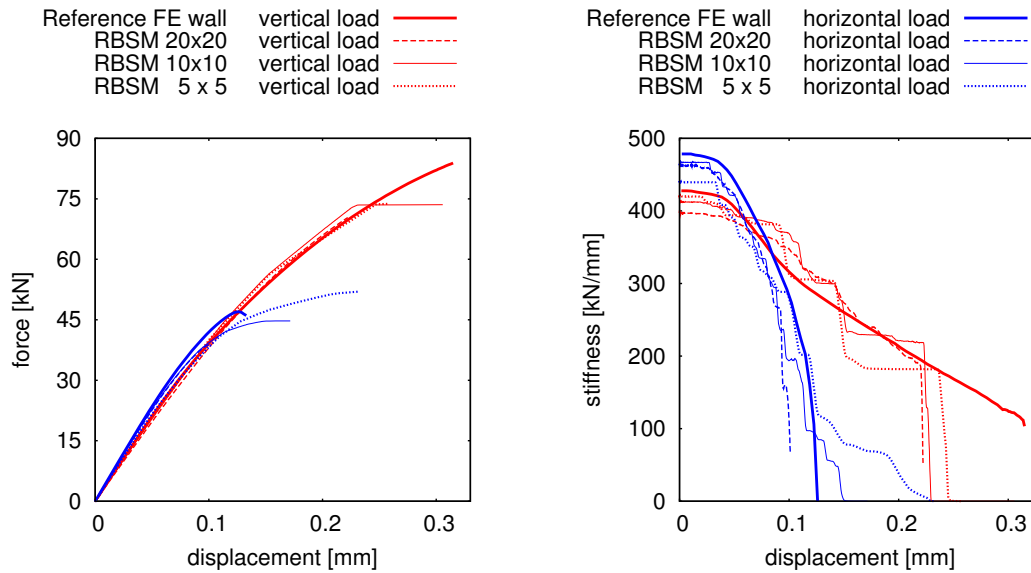


**Figure 13.** Force-displacement response curve and stiffness decay. The displacements are evaluated as the average in the loaded area.

maps it is also evident that the orthotropy of the shear springs favours the bearing capacity in the case of a vertical load, in conjugation with the presence of a prevailing situation of vertical compression stress.

The RBSM responses in terms of global variables are compared with the reference FE models in the graphs of Figure 13, where the results obtained with three different mesh refinements are shown together. The force-displacements curves are given on the left side, for both vertical (red lines) and horizontal (blue lines) loads. The corresponding curves of decay of the global stiffnesses are plotted on the right side Figure 13. They are evaluated by calculating the average slope of the previous curves. Globally, the performance can be judged as quite good, with the exception of the small underestimation of the bearing capacity in the vertical loading case.<sup>7</sup> The responses in terms of force show an acceptable sensitivity to the mesh size, being in the range 70.4–74.6 kN for the vertical load, and in the range 40.0–51.9 kN for the horizontal load. Note that the lower values are obtained with the finest mesh, for which there is a clear problem of localisation due to the fact that the element size is too small with respect to the internal characteristic length of the periodic material. The responses in terms of varying stiffness show the more pronounced stepped decay of the coarse meshes. It is worth noting that the RBSM is able to predict the very different bearing capacity of the two loading cases, as well as the completely different kinematics of the two collapse mechanisms, as shown in the enlarged detail of Figure 14. This capability is essentially related with the specific nonsymmetric characteristics of the shear springs and with the choice of adopting couples of axial springs placed at distances  $b_x \neq b_y$ . As a counter-check, when adopting a RBSM that does not have the present specific microstructure characteristics (i.e., the shear springs are symmetric and  $\beta_x = \beta_y = 1/\sqrt{3}$ ), then the maximum loads are  $\sim 40$  kN and  $\sim 45$  kN for the vertical and horizontal

<sup>7</sup>In this connection, it is possible to enhance the model by introducing a specific rule for varying  $\beta_x$  as a function of the increasing damage. This would be in accord with the results obtained in [Casolo 2006], because  $\beta_x$  tends to increase as a function of the ratio between the elastic modulus of the blocks and of the mortar, while  $\beta_y$  tends to remain constant.

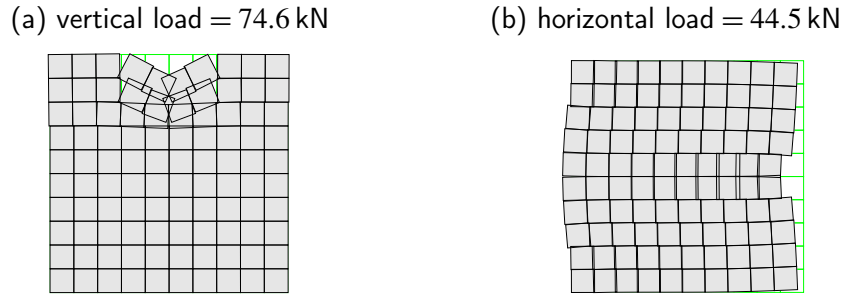


**Figure 14.** Enlarged detail of the collapse kinematics in the load application area with the  $10 \times 10$  mesh.

loads respectively (note that in this case the vertical maximum load would be completely wrong, and even smaller than the horizontal). This performance seems particularly interesting when considering the results obtained with the coarsest mesh, for which a single element has the same size of the composite RVE.

**3.3. Effects of mesh distortion on the RBSM.** As already stated, each type of spring is associated almost exclusively with a definite damage pattern. Thus, the heuristic molecules should be regular, and as much as possible aligned in accord with the principal axes of the material texture, in order to grant a good performance. On the other hand, realistic applications sometimes require dealing with irregular geometries, even if a masonry-like material is usually laid down with a certain degree of regularity due to the presence of the horizontal mortar layers. In the linear-elastic case, this issue has already been considered in [Casolo 2004].<sup>8</sup> Now, the points that define the skeleton curve of an inclined spring must also be recalculated in order to account for the strength orthotropy. Given the couple of strengths ( $\hat{\sigma}_v$  and  $\hat{\sigma}_h$ ), along the vertical and horizontal directions, the most simple trigonometric rule has been chosen for evaluating the strength along a direction of inclination  $\alpha$ :  $\hat{\sigma}(\alpha) = \hat{\sigma}_h \cos^2 \alpha + \hat{\sigma}_v \sin^2 \alpha$ . The performance of the RBSM has been tested by means of the meshes shown in Figure 15. The mesh on the right side has been named the bad mesh because of the high distortion of some elements, that are close to being triangles.

These meshes have been subjected to the same loading conditions described in the previous section, and Figure 16 shows graphs that compare the corresponding responses. It is evident that the performance can be judged as acceptable in the case of a limited distortion, while the bad mesh suffers for some problems of numerical convergence. It also tends to underestimate the bearing capacity of the reference wall in both situations.

<sup>8</sup>Given the angle of inclination  $\alpha$ , the following expressions are adopted for the normal spring stiffness  $k^P$  and shear spring stiffness  $k^Q$ :

$$k^P(\alpha) = k_x^P \cos^4 \alpha + k_y^P \sin^4 \alpha + 4 \frac{k_v^Q k_h^Q}{k_v^Q + k_h^Q} \cos^2 \alpha \sin^2 \alpha, \quad k^Q(\alpha) = \frac{2(k_x^P + k_y^P) \cos^2 \alpha \sin^2 \alpha + 2 \frac{k_v^Q k_h^Q}{k_v^Q + k_h^Q} (\cos^2 \alpha - \sin^2 \alpha)^2}{1 - \frac{k_v^Q - k_h^Q}{k_v^Q + k_h^Q} (\cos^2 \alpha - \sin^2 \alpha)}.$$

Moreover we take  $\beta(\alpha) = \beta_x \cos^2 \alpha + \beta_y \sin^2 \alpha$ .



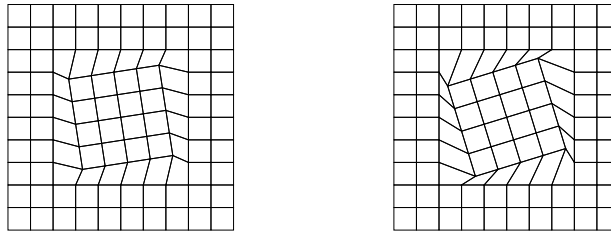


**Figure 15.** Meshes adopted to test the response in the case of geometric distortion. The reasonable (left) and the bad (right) meshes.

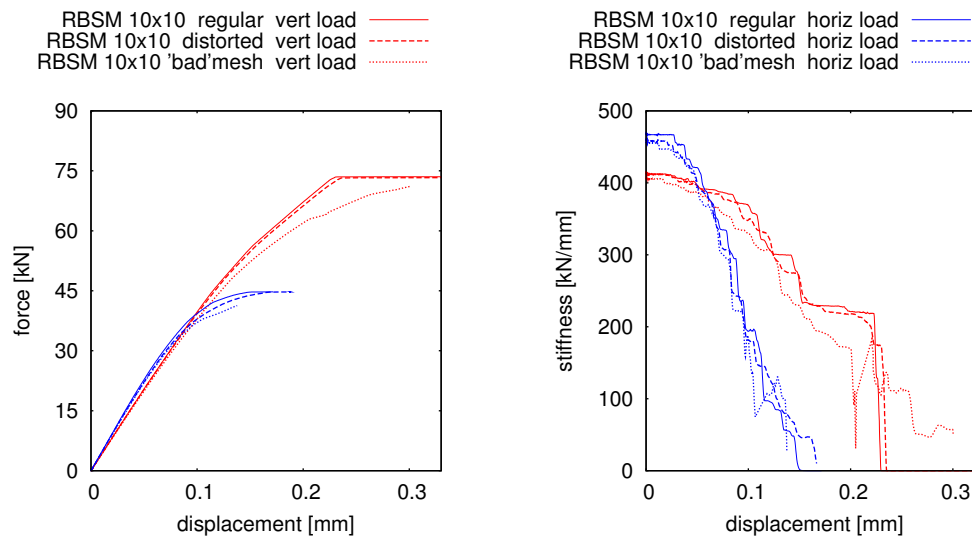


**Figure 16.** Comparison of the force-displacement response curve and stiffness decay when adopting distorted meshes.

#### 4. Final remarks

The present contribution is part of a research project that has the objective of modelling the nonlinear response of masonry-like materials by a macroscale mechanistic approach. The core of the proposed rigid body and spring model (RBSM) is a specific heuristic molecule, or representative macroscopic segment made by four rigid elements, which has the capability of describing the fundamental damage mechanisms at the mesoscale, also including some mechanical effects that are strictly related with the internal microstructure. The parameters that govern the model can be obtained by relatively simple tests that consider the macroscale response of a RVE of the original microstructured material. The computer tests gave good results, in particular when considering the terrific reduction of the required degrees of freedom. At present, the idea is implemented into a specific Fortran computer code that has its natural engineering application in the field of the dynamics of structures made by complex nonlinear materials, as in the case of the seismic analysis of masonry monuments.

### Appendix A: Matrix $[B]$ for the case of square elements

The geometric strain-displacement relationship for the representative macroscopic segment, also called the heuristic molecule, is reported as an example (see Figure 17):

$$\begin{Bmatrix} \varepsilon_1^P \\ \varepsilon_1^Q \\ \varepsilon_1^R \\ \varepsilon_2^P \\ \varepsilon_2^Q \\ \varepsilon_2^R \\ \varepsilon_3^P \\ \varepsilon_3^Q \\ \varepsilon_3^R \\ \varepsilon_4^P \\ \varepsilon_4^Q \\ \varepsilon_4^R \end{Bmatrix} = \frac{1}{2e} \begin{bmatrix} 0 & 1 & -b & 0 & 0 & 0 & 0 & -1 & b & 0 & 0 & 0 \\ -1 & 0 & -e & 0 & 0 & 0 & 1 & 0 & -e & 0 & 0 & 0 \\ 0 & 1 & b & 0 & 0 & 0 & 0 & -1 & -b & 0 & 0 & 0 \\ -1 & 0 & -b & 1 & 0 & b & 0 & 0 & 0 & 0 & 0 & 0 \\ 0 & -1 & -e & 0 & 1 & -e & 0 & 0 & 0 & 0 & 0 & 0 \\ -1 & 0 & b & 1 & 0 & -b & 0 & 0 & 0 & 0 & 0 & 0 \\ 0 & 0 & 0 & 0 & 1 & -b & 0 & 0 & 0 & 0 & -1 & b \\ 0 & 0 & 0 & -1 & 0 & -e & 0 & 0 & 0 & 1 & 0 & -e \\ 0 & 0 & 0 & 0 & 1 & b & 0 & 0 & 0 & 0 & -1 & -b \\ 0 & 0 & 0 & 0 & 0 & 0 & -1 & 0 & -b & 1 & 0 & b \\ 0 & 0 & 0 & 0 & 0 & 0 & 0 & -1 & -e & 0 & 1 & -e \\ 0 & 0 & 0 & 0 & 0 & 0 & -1 & 0 & b & 1 & 0 & -b \end{bmatrix} \begin{Bmatrix} u_1 \\ v_1 \\ \psi_1 \\ u_2 \\ v_2 \\ \psi_2 \\ u_3 \\ v_3 \\ \psi_3 \\ u_4 \\ v_4 \\ \psi_4 \end{Bmatrix}.$$

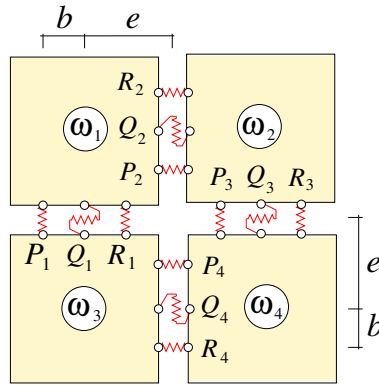


**Figure 17.** Example of a regular representative macroscopic segment, also referred to as a heuristic molecule.

### Appendix B: Relationship with Cosserat continuum elastic moduli

Given the macroscopic axial elastic moduli  $C_{\alpha\alpha\beta\beta}$  that can be evaluated by applying antiperiodic tractions under symmetric periodic boundary conditions [Anthoine 1995], the stiffnesses per unit volume of the axial springs are:

$$k_x^P = k_x^R = \frac{C_{1111}C_{2222} - C_{1122}^2}{C_{2222}}, \quad k_y^P = k_y^R = \frac{C_{1111}C_{2222} - C_{1122}^2}{C_{1111}}.$$

The stiffnesses of the orthotropic shear springs have the following relationship with the macroscopic Cosserat shear moduli  $C_{1212}$ ,  $C_{1221}$ , and  $C_{2121}$ , in accordance with [Casolo 2006]:

$$k_h^Q = \frac{C_{1212}C_{2121} - C_{1221}^2}{C_{2121} - C_{1221}}, \quad k_v^Q = \frac{C_{1212}C_{2121} - C_{1221}^2}{C_{1212} - C_{1221}}.$$

Finally, the distances  $b_x$  and  $b_y$  can be obtained as a function of the in-plane Cosserat flexural stiffnesses as follows [Casolo 2006]:

$$b_x = \beta_x e = \sqrt{\frac{D_{3131}}{k_x^P}}, \quad b_y = \beta_y e = \sqrt{\frac{D_{3232}}{k_y^P}}.$$

## References

- [ABAQUS 2007] ABAQUS, *Abaqus documentation*, Version 6.7, Dassault Systèmes/SIMULIA, Providence, RI, 2007.
- [Anthoine 1995] A. Anthoine, “Derivation of the in-plane elastic characteristics of masonry through homogenization theory”, *Int. J. Solids Struct.* **32**:2 (1995), 137–163.
- [Anthoine et al. 1995] A. Anthoine, G. Magenes, and G. Magonette, “Shear compression testing and analysis of brick masonry walls”, pp. 1657–1662 in *Proceeding of the 10th European Conference on Earthquake Engineering* (Vienna, 1994), edited by G. Duma, A. A. Balkema, Rotterdam, 1995.
- [Binda et al. 1992] L. Binda, G. Gatti, G. Mangano, C. Poggi, and G. Sacchi Landriani, “The collapse of the civic tower of Pavia: a survey of the materials and structure”, *Masonry Int.* **6**:1 (1992), 11–20.
- [Boffi and Casolo 1998] G. Boffi and S. Casolo, “Non-linear dynamic analysis of masonry arches”, pp. 99–108 in *Monument 98: Workshop on Seismic Performance of Monuments* (Lisbon, 1998), Laboratório Nacional de Engenharia Civil, Lisbon, 1998.
- [de Borst 2001] R. de Borst, “Some recent issues in computational failure mechanics”, *Int. J. Numer. Methods Eng.* **52**:1 (2001), 63–95.
- [Brasile et al. 2007] S. Brasile, R. Casciaro, and G. Formica, “Multilevel approach for brick masonry walls, I: A numerical strategy for the nonlinear analysis”, *Comput. Methods Appl. Mech. Eng.* **196**:49–52 (2007), 4934–4951.
- [Casolo 2000] S. Casolo, “Modelling the out-of-plane seismic behaviour of masonry walls by rigid elements”, *Earthquake Eng. Struct. Dyn.* **29**:12 (2000), 1797–1813.
- [Casolo 2004] S. Casolo, “Modelling in-plane micro-structure of masonry walls by rigid elements”, *Int. J. Solids Struct.* **41**:13 (2004), 3625–3641.
- [Casolo 2006] S. Casolo, “Macroscopic modelling of structured materials: relationship between orthotropic Cosserat continuum and rigid elements”, *Int. J. Solids Struct.* **43**:3–4 (2006), 475–496.
- [Casolo and Peña 2007] S. Casolo and F. Peña, “Rigid element model for in-plane dynamics of masonry walls considering hysteretic behaviour and damage”, *Earthquake Eng. Struct. Dyn.* **36**:8 (2007), 1029–1048.
- [Dhanasekar et al. 1985] M. Dhanasekar, A. W. Page, and P. W. Kleeman, “The failure of brick masonry under biaxial stresses”, pp. 295–313 in *Proceedings of the Institution of Civil Engineers, 2: Research and theory*, vol. 79, Thomas Telford, London, 1985.
- [Forest and Sab 1998] S. Forest and K. Sab, “Cosserat overall modeling of heterogeneous materials”, *Mech. Res. Commun.* **25**:4 (1998), 449–454.
- [Griffiths and Mustoe 2001] D. V. Griffiths and G. G. W. Mustoe, “Modelling of elastic continua using a grillage of structural elements based on discrete element concepts”, *Int. J. Numer. Methods Eng.* **50**:7 (2001), 1759–1775.
- [Kawai 1978] T. Kawai, “New discrete models and their application to seismic response analysis of structures”, *Nucl. Eng. Des.* **48**:1 (1978), 207–229.
- [Lemos 2007] J. V. Lemos, “Discrete element modeling of masonry structures”, *Int. J. Archit. Herit.* **1**:2 (2007), 190–213.
- [Lourénço et al. 1997] P. Lourénço, R. de Borst, and J. Rots, “A plane stress softening plasticity model for orthotropic materials”, *Int. J. Numer. Methods Eng.* **40**:21 (1997), 4033–4057.

- [Magenes and Calvi 1992] G. Magenes and G. M. Calvi, “Cyclic behaviour of brick masonry walls”, pp. 3517–3522 in *Proceedings of the 10th World Conference on Earthquake Engineering* (Madrid, 1992), edited by A. Bernal, A. A. Balkema, Rotterdam, 1992.
- [Malyszko 2005] L. Malyszko, “In-plane shear and tensile strength tests of small brickwork specimens”, pp. 291–298 in *Structural analysis of historical constructions: possibilities of numerical and experimental techniques* (Padova, 2004), edited by C. Modena et al., A. A. Balkema, Leiden, 2005.
- [Masiani et al. 1995] R. Masiani, N. Rizzi, and P. Trovalusci, “Masonry as structured continuum”, *Meccanica (Milano)* **30**:6 (1995), 673–683.
- [Massart et al. 2004] T. J. Massart, R. H. J. Peerlings, and M. G. D. Geers, “Mesoscopic modeling of failure and damage-induced anisotropy in brick masonry”, *Eur. J. Mech. A Solids* **23**:5 (2004), 719–735.
- [Milani et al. 2006] G. Milani, P. B. Lourenço, and A. Tralli, “Homogenised limit analysis of masonry walls, I: Failure surfaces”, *Comput. Struct.* **84**:3–4 (2006), 166–180.
- [Naraine and Sinha 1991] K. Naraine and S. Sinha, “Cyclic behavior of brick masonry under biaxial compression”, *J. Struct. Eng. (ASCE)* **117**:5 (1991), 1336–1355.
- [Ostoja-Starzewski 2002] M. Ostoja-Starzewski, “Lattice models in micromechanics”, *Appl. Mech. Rev. (ASME)* **55**:1 (2002), 35–60.
- [Pietruszczak and Ushaksaraei 2003] S. Pietruszczak and R. Ushaksaraei, “Description of inelastic behaviour of structural masonry”, *Int. J. Solids Struct.* **40**:15 (2003), 4003–4019.
- [Stakgold 1950] I. Stakgold, “The Cauchy relations in a molecular theory of elasticity”, *Quart. Appl. Math.* **8**:2 (1950), 169–186.
- [Sulem and Mühlhaus 1997] J. Sulem and H.-B. Mühlhaus, “A continuum model for periodic two-dimensional block structures”, *Mech. Cohes. Frict. Mater.* **2**:1 (1997), 31–46.
- [Trovalusci and Masiani 2005] P. Trovalusci and R. Masiani, “A multifield model for blocky materials based on multiscale description”, *Int. J. Solids Struct.* **42**:21–22 (2005), 5778–5794.
- [Zienkiewicz and Taylor 1991] O. C. Zienkiewicz and R. L. Taylor, *The finite element method*, vol. II, McGraw-Hill, London, 1991.
- [Zucchini and Lourenço 2002] A. Zucchini and P. B. Lourenço, “A micro-mechanical model for the homogenisation of masonry”, *Int. J. Solids Struct.* **39**:12 (2002), 3233–3255.

Received 31 Oct 2008. Revised 10 Feb 2009. Accepted 25 Feb 2009.

SIRO CASOLO: Siro.Casolo@polimi.it

Dipartimento di Ingegneria Strutturale, Politecnico di Milano, Piazza Leonardo da Vinci 32, 20133 Milano, Italy

<http://www.stru.polimi.it/people/casolo/index.plp>

## PERFORMANCE AND PARAMETRIC STUDY OF ACTIVE MULTIPLE TUNED MASS DAMPERS FOR ASYMMETRIC STRUCTURES UNDER GROUND ACCELERATION

CHUNXIANG LI, JINHUA LI, ZHIQIANG YU AND YAN QU

The application of active multiple tuned mass dampers (AMTMD) for suppressing translational and torsional responses is addressed for a simplified two-degree of freedom structure, able to represent the dynamic characteristics of general asymmetric structures subject to ground motions. By employing the developed optimum parameter and effectiveness criteria of the AMTMD, the influences of the normalized eccentricity ratio and the torsional-to-translational frequency ratio of asymmetric structures on the optimum parameters and effectiveness of the AMTMD are investigated in detail. For comparison purposes, the results of a single active tuned mass damper also are taken into consideration.

*A list of symbols can be found starting on page 584.*

### 1. Introduction

Structural vibration control using passive, hybrid, semiactive, and active control strategies is a viable technology for enhancing structural functionality and safety against natural hazards such as strong earthquakes and high wind gusts. Significant strides have been made in recent years toward the development and application of hybrid, semiactive, and active control schemes for vibration control of civil engineering structures (including accounting for nonlinearity) in seismic zones. A multiobjective optimal design of a hybrid control system, consisting of a tuned mass damper (TMD) and an active mass driver (AMD), has been proposed for seismically excited structures by Ahlawat and Ramaswamy [2002a]. To achieve response reductions in smart base isolated buildings in near-fault earthquakes, a new semiactive independently variable damper has been developed by Nagarajaiah and Narasimhan [2007]. For active control systems, either an active tuned mass damper (ATMD) or an AMD can be installed on the top floor of a tall building to alleviate the acceleration response under wind excitations [Yang et al. 2004] or to attenuate the seismic response [Spencer et al. 1998a; 1998b]. In particular, structural control technology aimed at nonlinear structures has received considerable attention from researchers in recent years [Ohtori et al. 2004; Nagarajaiah and Narasimhan 2006; Nagarajaiah et al. 2008; Narasimhan et al. 2006; 2008]. Thus the significance of structural control for inelastic structures under strong earthquakes is well recognized.

The TMD is one of the simplest and most reliable control devices. It consists of a mass, a spring, and a viscous damper attached to the structure. Its mechanism for attenuating undesirable oscillations of a

---

*Keywords:* vibration control, active multiple tuned mass dampers, asymmetric structures, ground acceleration, torsional-to-translational frequency ratio, normalized eccentricity ratio, damping, structural control.

The authors acknowledge the financial contributions received from the innovation project of the Shanghai Board of Education, No. 09-YZ-35.

structure is to transfer the vibration energy of the structure to the TMD and dissipate it there through damping.

To increase the dissipation energy in the TMD, it is very important to determine its optimum parameters. Conversely, a main drawback of TMDs is that performance may worsen due to mistuned frequency or off-optimum damping. A possible remedy for this is to use more than one TMD with different dynamic characteristics. Multiple tuned mass dampers (MTMD) with distributed natural frequencies were proposed by Xu and Igusa [1992], and investigated by many authors [Yamaguchi and Harnpornchai 1993; Abe and Fujino 1994; Kareem and Kline 1995; Jangid 1999; Li 2000; 2006, Gu et al. 2001; Park and Reed 2001; Chen and Wu 2003; Bakre and Jangid 2004; Kwon and Park 2004; Yau and Yang 2004a; 2004b; Hoang and Warnitchai 2005; Li and Li 2005; Li and Zhang 2005; Lin et al. 2005; Han and Li 2006]. MTMDs have been shown to be more effective in the mitigation of oscillations than TMDs.

The effectiveness of TMDs can be further enhanced by introducing an active force to act between the structure and the TMD; this is the principle of the ATMD [Chang and Soong 1980]. However, neither the robustness against change nor the estimation error in the structural natural frequency of ATMDs can be compared with that of MTMDs. Investigations in optimizing the feedback gains and damper characteristics of ATMDs in order to minimize structural displacements and/or accelerations have been carried out, for example, in [Chang and Yang 1995; Ankireddi and Yang 1996; Yan et al. 1999]. However, as a building gets taller and more massive, in order to achieve the required level of response reduction during strong earthquakes or typhoons, a heavier additional mass is required, requiring too much space to be economically practical. With an active control system, a large control force must be created and the power limitations of the actuator prevent this system from being implemented in large buildings. Thus it is of great practical interest to search for control systems that can relax the requirements for masses and control forces.

In view of this, active multiple tuned mass dampers (AMTMD) have been proposed [Li and Liu 2002; Li et al. 2003] to attenuate undesirable oscillations of structures under ground acceleration. In studies on AMTMD, for design purposes it is assumed that a structure vibrates in only one direction or in multiple directions independently, each with its fundamental modal properties, without considering transverse-torsional coupled effects. This assumption simplifies the analysis of a system and the synthesis of a controller. In real structures, however, this assumption is not always appropriate because structures generally possess multidirectional coupled vibration modes and the control performance of controllers will degrade due to parameter variation or spillover induced by the effects of their coupling. Furthermore, there exist not only transverse vibrations but also torsional vibrations in real structures, which generally possess coupling. A real structure is asymmetric to some degree, even with a nominally symmetric plan, and will undergo lateral as well as torsional vibrations simultaneously under purely translational excitations. Consequently, controller design must take into account the effects of transverse-torsional coupled vibration modes in such cases.

For representative studies of TMD, ATMD, MTMD and HMD (hybrid mass damper) design, taking into account the effects of transverse-torsional coupled vibration modes, see [Jangid and Datta 1997; Arfiadi and Hadi 2000; Lin et al. 2000a; 2000b; Ahlawat and Ramaswamy 2002b; 2003; Singh et al. 2002; Pansare and Jangid 2003; Wang and Lin 2005; Li and Qu 2006]. It is well known that structures where the center of mass and center of resistance do not coincide will develop a coupled lateral-torsional response when subjected to earthquake ground motions. For practical applications, it would be important

to include the effects of torsional coupling in consideration when estimating the performance of an AMTMD. Recently, Li and Xiong [2008] investigated AMTMD performance for asymmetric structures using a simplified two-degree of freedom (2-DOF) structure able to represent the dynamic characteristics of general asymmetric structures subject to ground motions. This structure is a generalized 2-DOF system of an asymmetric structure with predominant translational and torsional responses under earthquake excitations using the mode reduced-order method. Depending on the torsional-to-translational eigenfrequency ratio  $\lambda_\omega$  of the asymmetric structure, three cases can be distinguished: torsionally flexible structures (TFS), when  $\lambda_\omega < 1.0$ ; torsionally intermediate stiff structures (TISS), when  $\lambda_\omega \approx 1.0$ ; and torsionally stiff structures (TSS), when  $\lambda_\omega > 1.0$ .

The search criterion for optimum parameters of an AMTMD is the minimization of the minimum values of the maximum translational and torsional displacement dynamic magnification factors (DMF) of an asymmetric structure with an AMTMD. The criterion used for assessing the effectiveness of an AMTMD is the ratio of the minimization of the minimum values of the maximum translational and torsional displacement DMF of the asymmetric structure with an AMTMD to the maximum translational and torsional displacement DMF of the asymmetric structure without an AMTMD. By employing these criteria, a careful examination of the effects of the normalized eccentricity ratio on the effectiveness and robustness of the AMTMD is carried out in the mitigation of both the translational and torsional responses of the asymmetric structure for different values of  $\lambda_\omega$ . Likewise, the effectiveness of a single ATMD with optimum parameters is presented and compared with that of an AMTMD.

Following the direction of [Li and Xiong 2008], we investigate further the optimum performance of AMTMD in attenuating the translational and torsional responses of asymmetric structures under ground acceleration. The chosen optimization criteria are the (separate) minimizations of the translational and torsional displacement variances of the AMTMD-endowed asymmetric structure. The measure of effectiveness we adopt for the AMTMD is the ratio of the minimum translational or torsional displacement variance of AMTMD-endowed structure to the same variances for the structure without an AMTMD.

Using these evaluation criteria, we quantitatively discuss and demonstrate the influence of the normalized eccentricity ratio  $E_R$  and the torsional-to-translational eigenfrequency ratio  $\lambda_\omega$  of an asymmetric structure on the optimum parameters and effectiveness of AMTMDs in the reduction of both the translational and torsional responses of asymmetric structures under ground acceleration.

## 2. Damping of asymmetric structures

We take the structure to be controlled with an AMTMD to be asymmetric, in the sense that the center of resistance (CR) of the structure does not coincide with the center of mass (CM), as shown in Figure 1. The two uncoupled frequencies of the asymmetric structure are defined as

$$\omega_s = \sqrt{\frac{k_s}{m_s}}, \quad \omega_\theta = \sqrt{\frac{k_\theta}{m_s r^2}}, \quad (1)$$

in which  $m_s$  is the mode-generalized mass of the structure;  $k_s = k_{s1} + k_{s2}$  is the mode-generalized lateral stiffness of the structure in the  $x$  direction, where  $k_{s1}$  and  $k_{s2}$  refer to the stiffnesses of the two resisting elements;  $k_\theta = k_{s1}y_{s1}^2 + k_{s2}y_{s2}^2$  represents the mode-generalized torsional stiffness of the structure with respect to the CM, where  $y_{s1}$  and  $y_{s2}$  denote the distances from the CM to the two resisting elements;

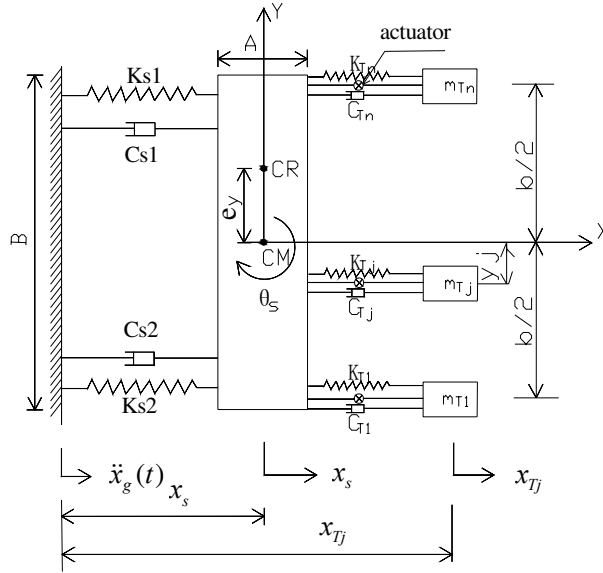


**Figure 1.** Generalized 2-DOF system of an asymmetric structure with the predominant translational and torsional responses set with the AMTMD.

and  $r$  represents the radius of gyration of the deck about the vertical axis through the CM. The equations of motion of the asymmetric structure can be written in matrix form as

$$\begin{bmatrix} m_s & 0 \\ 0 & m_s r^2 \end{bmatrix} \begin{bmatrix} \ddot{x}_s \\ \ddot{\theta}_s \end{bmatrix} + \begin{bmatrix} c_s & c_{s\theta} \\ c_{s\theta} & c_\theta \end{bmatrix} \begin{bmatrix} \dot{x}_s \\ \dot{\theta}_s \end{bmatrix} + \begin{bmatrix} k_s & k_s e_y \\ k_s e_y & k_\theta \end{bmatrix} \begin{bmatrix} x_s \\ \theta_s \end{bmatrix} = - \begin{bmatrix} m_s \\ 0 \end{bmatrix} \ddot{x}_g(t), \quad (2)$$

where  $c_s$ ,  $c_{s\theta}$ , and  $c_\theta$  denote the elements of the damping matrix, to be determined next;  $e_y$  is the eccentricity between the CR and CM, defined as  $e_y = (k_{s1}y_{s1} - k_{s2}y_{s2})/(k_{s1} + k_{s2})$ ; and  $\ddot{x}_g(t)$  is the ground acceleration.

We denote the fundamental and second natural frequencies by  $\omega_{s1}$  and  $\omega_{s2}$  (so  $\omega_{s2} > \omega_{s1}$ ). They can be derived by solving the eigenvalue problem associated with (2) as

$$\frac{\omega_{s1}}{\omega_s} = \sqrt{\frac{1 + \lambda_\omega^2 - \sqrt{(\lambda_\omega^2 - 1)^2 + 4E_R^2}}{2}}, \quad \frac{\omega_{s2}}{\omega_s} = \sqrt{\frac{1 + \lambda_\omega^2 + \sqrt{(\lambda_\omega^2 - 1)^2 + 4E_R^2}}{2}}, \quad (3)$$

in which  $E_R = e_y/r$ , or normalized eccentricity ratio (NER), is the ratio of the eccentricity to the radius of gyration of the deck, and  $\lambda_\omega = \omega_\theta/\omega_s$ , is the uncoupled torsional-to-translational frequency ratio (TFR).

Hypothesizing the same damping ratio  $\zeta_{s1} = \zeta_{s2} = \zeta_s$  for the two modes (in this study,  $\zeta_s = 0.02$ ) and superposing the modal damping matrices, the damping matrix can be expressed in the form

$$\begin{bmatrix} c_s & c_{s\theta} \\ c_{s\theta} & c_\theta \end{bmatrix} = a_0 \begin{bmatrix} m_s & 0 \\ 0 & m_s r^2 \end{bmatrix} + b_0 \begin{bmatrix} k_s & k_s e_y \\ k_s e_y & k_\theta \end{bmatrix}, \quad (4)$$



where

$$a_0 = \frac{2(\zeta_{s2}\omega_{s1} - \zeta_{s1}\omega_{s2})}{\omega_{s1}^2 - \omega_{s2}^2} \omega_{s1}\omega_{s2}, \quad b_0 = \frac{2(\zeta_{s1}\omega_{s1} - \zeta_{s2}\omega_{s2})}{\omega_{s1}^2 - \omega_{s2}^2}. \quad (5)$$

Rearranging (4) yields the elements of the damping matrix

$$c_s = 2a_s m_s \zeta_s \omega_s, \quad c_{s\theta} = 2a_{s\theta} m_s r \zeta_s \omega_s, \quad c_\theta = 2a_\theta m_s r^2 \zeta_s \omega_s, \quad (6)$$

in which

$$a_s = \frac{\frac{\omega_{s1}}{\omega_s} \times \frac{\omega_{s2}}{\omega_s} + 1}{\frac{\omega_{s1}}{\omega_s} + \frac{\omega_{s2}}{\omega_s}}, \quad a_{s\theta} = \frac{E_R}{\frac{\omega_{s1}}{\omega_s} + \frac{\omega_{s2}}{\omega_s}}, \quad a_\theta = \frac{\frac{\omega_{s1}}{\omega_s} \times \frac{\omega_{s2}}{\omega_s} + \lambda_\omega^2}{\frac{\omega_{s1}}{\omega_s} + \frac{\omega_{s2}}{\omega_s}}. \quad (7)$$

### 3. State equations of the AMTMD asymmetric structure system

Referring again to Figure 1, consider an AMTMD evenly placed within the width  $b$ , with its center at the CM; we are interested in its effectiveness in reducing the translational and torsional responses of the asymmetric structure. The ordinate of each ATMD in the AMTMD can be determined by

$$y_j = \left(-\frac{1}{2} + \frac{j-1}{n-1}\right) b \quad (j = 1, 2, \dots, n). \quad (8)$$

When the relative displacements of the structure ( $x_s$ ) and of each ATMD ( $x_{Tj}$ ) with reference to the ground are introduced, the equations of motion for the asymmetric structure with AMTMD under ground acceleration can be formulated as follows:

$$\begin{aligned} m_s \ddot{x}_s + c_s \dot{x}_s + k_s x_s + c_{s\theta} \dot{\theta}_s + k_s e_y \theta_s &= -m_s \ddot{x}_g(t) + \sum_{j=1}^n F_j(t), \\ m_s r^2 \ddot{\theta}_s + c_\theta \dot{\theta}_s + k_\theta \theta_s + c_{s\theta} \dot{x}_s + k_s e_y x_s &= \sum_{j=1}^n y_j F_j(t), \\ m_{Tj} (\ddot{x}_g(t) + \ddot{x}_{Tj}) + c_{Tj} (\dot{x}_{Tj} - (\dot{x}_s + y_j \dot{\theta}_s)) + k_{Tj} (x_{Tj} - (x_s + y_j \theta_s)) &= u_j(t), \\ F_j(t) = c_{Tj} (\dot{x}_{Tj} - (\dot{x}_s + y_j \dot{\theta}_s)) + k_{Tj} (x_{Tj} - (x_s + y_j \theta_s)) - u_j(t). \end{aligned} \quad (9)$$

An active control algorithm is required in order to use the measured responses of the 2-DOF torsionally coupled structure-AMTMD system to calculate an active control force to drive the mass block. The linear quadratic regulator algorithm developed by several authors [Chang and Soong 1980; Abe 1996; Ikeda 1997; Nagashima 2001] may be employed, but here we choose instead the frequency domain design method adopted by some others [Chang and Yang 1995; Ankireddi and Yang 1996; Yan et al. 1999]. In this method one starts with the optimum MTMD configuration, obtained earlier. It is expected that the inertial force of the AMTMD can be increased by feeding back the acceleration of the structure. However, this acceleration feedback will disturb the performance of the optimum MTMD. An alternative approach to this problem is to move the optimum MTMD over to another optimum operating point and feed back the displacement and velocity of the MTMD. In view of this, the active control force can be explicitly expressed as

$$u_j(t) = -m_{Tj} \ddot{x}_s - c_{Tj} (\dot{x}_{Tj} - (\dot{x}_s + y_j \dot{\theta}_s)) + k_{Tj} (x_{Tj} - (x_s + y_j \theta_s)), \quad (10)$$

in which  $m_{Tj}$ ,  $c_{Tj}$ , and  $k_{Tj}$  are the mass, damping, and stiffness, respectively of the  $j$ -th ATMD; and  $m_{Tj}$ ,  $c_{Tj}$ , and  $k_{Tj}$  the gains of the acceleration, velocity, and displacement feedback of the  $j$ -th ATMD.

Here we make the stiffness and damping for all the ATMDs ( $k_{Tj} = k_T$  and  $c_{Tj} = c_T$  for each  $j$ ) but let their masses  $m_{Tj}$  be different. Likewise, the control forces of the AMTMD are generated assuming the displacement and velocity feedback gains are all the same ( $k_{tj} = k_t$  and  $c_{tj} = c_t$  for each  $j$ ) while the acceleration feedback gains  $m_{tj}$  are allowed to differ.

We now define the normalized acceleration feedback gain factor  $\alpha_j = m_{tj}/m_{Tj} = \alpha$ , assumed the same for each  $j$ , and we introduce the further notation

$$\omega_j^2 = \frac{k_{Tj} + k_{tj}}{m_{Tj}} = \frac{k_T + k_t}{m_{Tj}}, \quad \mu_T = \frac{m_T}{m_s} = \sum_{j=1}^n \frac{m_{Tj}}{m_s} = \sum_{j=1}^n \mu_{Tj}, \quad \zeta_j = \frac{c_{Tj} + c_{tj}}{2m_{Tj}\omega_j} = \frac{c_T + c_t}{2m_{Tj}\omega_j},$$

Defining  $\omega_T$ , the average natural frequency of the AMTMD, by  $\omega_T = \sum_{j=1}^n (\omega_j/n)$ , we choose the natural frequency of each ATMD as

$$\omega_j = \omega_T \left( 1 + \left( j - \frac{n+1}{2} \right) \frac{\beta}{n-1} \right) = f \omega_s \left( 1 + \left( j - \frac{n+1}{2} \right) \frac{\beta}{n-1} \right), \quad (11)$$

where  $\beta = (\omega_n - \omega_1)/\omega_T$  is a nondimensional frequency spacing parameter and  $f = \omega_T/\omega_s$  is the tuning frequency ratio of the AMTMD.

From (11), the ratio of the natural frequency of each ATMD to the controlled natural frequency of the structure is seen to be

$$r_j = \frac{\omega_j}{\omega_s} = f \left( 1 + \left( j - \frac{n+1}{2} \right) \frac{\beta}{n-1} \right). \quad (12)$$

Since the damping ratios of the ATMDs are unequal, it is necessary to introduce the average damping ratio  $\zeta_T = \sum_{j=1}^n \zeta_j/n$ . The total mass ratio and the damping ratio of each ATMD is then

$$\mu_T = \sum_{j=1}^n \mu_{Tj} = \left( \sum_{j=1}^n \frac{1}{r_j^2} \right) \mu_{T1} r_1^2 = \left( \sum_{j=1}^n \frac{1}{r_j^2} \right) \mu_{T2} r_2^2 = \cdots = \left( \sum_{j=1}^n \frac{1}{r_j^2} \right) \mu_{Tn} r_n^2, \quad (13)$$

$$\zeta_T = \sum_{j=1}^n \frac{\zeta_j}{n} = \zeta_1 r_1^{-1} f = \zeta_2 r_2^{-1} f = \cdots = \zeta_n r_n^{-1} f; \quad (14)$$

see [Li 2000; Li and Qu 2006]. For the deduction of the state equations, we rewrite (9) and (10) in matrix form as

$$M\ddot{x} + C\dot{x} + Kx = \Gamma\ddot{x}_g(t), \quad (15)$$

where we have set

$$\begin{aligned} x &= [x_s \ r\theta_s \ x_{T1} \ \cdots \ x_{Tj} \ \cdots \ x_{Tn}]^T, & \dot{x} &= [\dot{x}_s \ r\dot{\theta}_s \ \dot{x}_{T1} \ \cdots \ \dot{x}_{Tj} \ \cdots \ \dot{x}_{Tn}]^T, \\ \ddot{x} &= [\ddot{x}_s \ r\ddot{\theta}_s \ \ddot{x}_{T1} \ \cdots \ \ddot{x}_{Tj} \ \cdots \ \ddot{x}_{Tn}]^T, & \Gamma &= [-1 \ 0 \ -\mu_{T1} \ \cdots \ -\mu_{Tj} \ \cdots \ -\mu_{Tn}]^T, \\ M &= \begin{bmatrix} A_1 & 0 & 0_{1 \times n} \\ B_1 & B_2 & 0_{1 \times n} \\ (C_1)_{n \times 1} & (C_2)_{n \times n} & 0_{n \times 1} \end{bmatrix}, & C &= \begin{bmatrix} A_2 & A_3 & (A_4)_{1 \times n} \\ B_3 & B_4 & (B_5)_{1 \times n} \\ (C_3)_{n \times 1} & (C_4)_{n \times 1} & (C_5)_{n \times n} \end{bmatrix}, & K &= \begin{bmatrix} A_5 & A_6 & (A_7)_{1 \times n} \\ B_6 & B_7 & (B_8)_{1 \times n} \\ (C_6)_{1 \times n} & (C_7)_{n \times 1} & (C_8)_{n \times n} \end{bmatrix}, \end{aligned}$$

with

$$\begin{aligned}
A_1 &= 1 - \sum_{j=1}^n \alpha \mu_{Tj}, & A_2 &= 2\omega_s \left( \alpha_s \zeta_s + \sum_{j=1}^n \mu_{Tj} \zeta_j f \left( 1 + \left( j - \frac{n+1}{2} \right) \frac{\beta}{n-1} \right) \right), \\
A_3 &= 2\omega_s \left( a_{s\theta} \zeta_s + \sum_{j=1}^n \mu_{Tj} \zeta_j f \left( \frac{y_j}{r} \right) \left( 1 + \left( j - \frac{n+1}{2} \right) \frac{\beta}{n-1} \right) \right), \\
A_4 &= -2\omega_s \left[ \mu_{T1} \zeta_1 f \left( 1 - \frac{\beta}{2} \right) \dots \mu_{Tj} \zeta_j f \left( 1 + \left( j - \frac{n+1}{2} \right) \frac{\beta}{n-1} \right) \dots \mu_{Tn} \zeta_n f \left( 1 + \frac{\beta}{2} \right) \right], \\
B_1 &= - \sum_{j=1}^n \alpha \mu_{Tj} \left( \frac{y_j}{r} \right), & B_2 &= 1, & B_3 &= A_3, \\
B_4 &= 2\omega_s \left( a_{\theta} \zeta_s + \sum_{j=1}^n \mu_{Tj} \zeta_j f \left( \frac{y_j}{r} \right)^2 \left( 1 + \left( j - \frac{n+1}{2} \right) \frac{\beta}{n-1} \right) \right), \\
B_5 &= -2\omega_s \left[ \mu_{T1} \zeta_1 f \left( \frac{y_j}{r} \right) \left( 1 - \frac{\beta}{2} \right) \dots \mu_{Tj} \zeta_j f \left( \frac{y_j}{r} \right) \left( 1 + \left( j - \frac{n+1}{2} \right) \frac{\beta}{n-1} \right) \dots \mu_{Tn} \zeta_n f \left( \frac{y_j}{r} \right) \left( 1 + \frac{\beta}{2} \right) \right], \\
C_1 &= [\alpha \mu_{T1} \dots \alpha \mu_{Tj} \dots \alpha \mu_{Tn}]^T, \\
C_2 &= \text{diag}[\mu_{T1} \dots \mu_{Tj} \dots \mu_{Tn}], & C_3 &= A_4^T, & C_4 &= B_5^T, \\
C_5 &= 2\omega_s \text{diag} \left[ \mu_{T1} \zeta_1 f \left( 1 - \frac{\beta}{2} \right) \dots \mu_{Tj} \zeta_j f \left( 1 + \left( j - \frac{n+1}{2} \right) \frac{\beta}{n-1} \right) \dots \mu_{Tn} \zeta_n f \left( 1 + \frac{\beta}{2} \right) \right], \\
A_5 &= \omega_s^2 \left( 1 + \sum_{j=1}^n \mu_{Tj} f^2 \left( 1 + \left( j - \frac{n+1}{2} \right) \frac{\beta}{n-1} \right)^2 \right), \\
A_6 &= B_6 = \omega_s^2 \left( E_R + \sum_{j=1}^n \mu_{Tj} f^2 \left( \frac{y_j}{r} \right) \left( 1 + \left( j - \frac{n+1}{2} \right) \frac{\beta}{n-1} \right)^2 \right), \\
A_7 &= -\omega_s^2 \left[ \mu_{T1} f^2 \left( 1 - \frac{\beta}{2} \right)^2 \dots \mu_{Tj} f^2 \left( 1 + \left( j - \frac{n+1}{2} \right) \frac{\beta}{n-1} \right)^2 \dots \mu_{Tn} f^2 \left( 1 + \frac{\beta}{2} \right)^2 \right], \\
B_7 &= \omega_s^2 \left( \lambda_{\omega}^2 + \sum_{j=1}^n \mu_{Tj} f^2 \left( \frac{y_j}{r} \right)^2 \left( 1 + \left( j - \frac{n+1}{2} \right) \frac{\beta}{n-1} \right)^2 \right), \\
B_8 &= -\omega_s^2 \left[ \mu_{T1} f^2 \left( \frac{y_j}{r} \right) \left( 1 - \frac{\beta}{2} \right)^2 \dots \mu_{Tj} f^2 \left( \frac{y_j}{r} \right) \left( 1 + \left( j - \frac{n+1}{2} \right) \frac{\beta}{n-1} \right)^2 \dots \mu_{Tn} f^2 \left( \frac{y_j}{r} \right) \left( 1 + \frac{\beta}{2} \right)^2 \right], \\
C_6 &= A_7^T, & C_7 &= B_8^T, \\
C_8 &= \omega_s^2 \text{diag} \left[ \mu_{T1} f^2 \left( 1 - \frac{\beta}{2} \right)^2 \dots \mu_{Tj} f^2 \left( 1 + \left( j - \frac{n+1}{2} \right) \frac{\beta}{n-1} \right)^2 \dots \mu_{Tn} f^2 \left( 1 + \frac{\beta}{2} \right)^2 \right].
\end{aligned}$$

(Here of course  $\text{diag}[\dots]$  stands for the  $n \times n$  diagonal matrix with the given entries.)

Equation (15) can further be transformed into the state equations

$$\dot{X} = AX + Bw, \quad Y = CX + Dw, \quad (16)$$

where the  $2(n+2) \times 1$  state vector  $X$ , the state matrix  $A$ , the input matrix  $B$ , the output matrix  $C$ , the output vector  $Y$ , and the input  $w$  are as follows ( $E_{(n+2) \times (n+2)}$  being the identity matrix of rank  $n+2$ ):

$$X = \begin{bmatrix} x \\ \dot{x} \end{bmatrix}, \quad A = \begin{bmatrix} 0_{(n+2) \times (n+2)} & E_{(n+2) \times (n+2)} \\ -M^{-1}K & -M^{-1}C \end{bmatrix}, \quad B = \begin{bmatrix} 0_{(n+2) \times 1} \\ M^{-1}\Gamma \end{bmatrix},$$

$$C = \begin{bmatrix} 0_{(n+2) \times (n+2)} & 0_{(n+2) \times (n+2)} \\ 0_{(n+2) \times (n+2)} & E_{(n+2) \times (n+2)} \end{bmatrix}, \quad D = \begin{bmatrix} 0_{(n+2) \times 1} \\ 0_{(n+2) \times 1} \end{bmatrix}, \quad Y = \begin{bmatrix} 0_{(n+2) \times 1} \\ x_{(n+2) \times 1} \end{bmatrix}, \quad w = \ddot{x}_g(t),$$

#### 4. Optimum AMTMD criteria for asymmetric structures

We now assumed fixed the number  $n$  of ATMDs, the normalized width  $b/r$  and structural damping ratio  $\zeta_s$  of the structure, the normalized eccentricity ratio  $E_R$ , the torsional-to-translational frequency ratio  $\lambda_\omega$ , the normalized acceleration feedback gain factor  $\alpha$ , and the total mass ratio  $\mu_T$  of the AMTMD.

The optimization of the three parameters  $f$ ,  $\zeta_T$ , and  $\beta$  is done numerically by the gradient search method (GSM), an iterative method where the objective function and its partial derivatives are evaluated at each step. We now select appropriate objective functions for the optimization.

Based on a single-frequency oscillation  $\ddot{x}_g(t) = X_g e^{-i\omega t}$ , where  $X_g$  represents the displacement transfer function of earthquake ground motions, the translational and torsional displacements of the structure are given by

$$x_s = H_{x_s}(-i\omega)e^{-i\omega t} \quad \text{and} \quad r\theta_s = H_{\theta_s}(-i\omega)e^{-i\omega t},$$

leading to the translational and torsional displacement variances:

$$\sigma_{x_s}^2 = \int_{-\infty}^{+\infty} |H_{x_s}(i\omega)|^2 |X_g(i\omega)|^2 d\omega, \quad \sigma_{r\theta_s}^2 = \int_{-\infty}^{+\infty} |H_{\theta}(i\omega)|^2 |X_g(i\omega)|^2 d\omega. \quad (17)$$

We can also define nondimensionalized variances

$$\sigma_{x_s}^{*2} \quad \text{and} \quad \sigma_{r\theta_s}^{*2} \quad (18)$$

by dividing by the corresponding quantities for the same structure without an AMTMD.

These four variances are the objective functions to be minimized. We thus distinguish four minima:

$$R_I = \min_{f, \zeta_T, \beta} \sigma_{x_s}^2, \quad R_{II} = \min_{f, \zeta_T, \beta} \sigma_{r\theta_s}^2, \quad R_{III} = \min_{f, \zeta_T, \beta} \sigma_{x_s}^{*2}, \quad R_{IV} = \min_{f, \zeta_T, \beta} \sigma_{r\theta_s}^{*2}. \quad (19)$$

We will primarily use  $R_{III}$  and  $R_{IV}$  as our quantitative estimates of the effectiveness of the AMTMD in controlling the translational and torsional displacements of asymmetric structures, respectively.

Note that the normalized acceleration feedback gain factor  $\alpha$  gets smaller as  $n$  increases. The smaller  $\alpha$  is, the less control force is required. Thus the AMTMD is more easily implemented than an ATMD of the same effectiveness, when a large control force must be created.

### 5. Numerical results

The minimization procedure was carried out with the following choices for the parameters:  $n = 5$ ;  $b/r = 1.0$ ;  $\zeta_s = 0.02$ ;  $\alpha = 4$  or  $8$ ;  $E_R = 0, 0.05, 0.1, 0.2, 0.3, 0.4$ ; and  $\mu_T = 0.01, 0.02, 0.03, 0.04, 0.05$ . Further we choose  $\lambda_\omega = 0.5, 1.0$  and  $2.0$  to represent respectively TFS, TISS and TSS (see page 573).  $E_R$  and  $\lambda_\omega$  are the key parameters in quantitatively assessing the effectiveness and robustness of the AMTMD for asymmetric structures.

**Translational response.** Figure 2 displays the optimum parameters and the  $R_{III}$  (translational) effectiveness of the AMTMD for a TFS ( $\lambda_\omega = 0.5$ ), in terms of the values of  $\alpha$ ,  $E_R$ , and  $\mu_T$  just listed. The figure suggests that the influence of  $E_R$  on the optimum tuning frequency ratio is not significant, regardless of the value of  $\alpha$ . The effect of  $E_R$  on the optimum frequency spacing (robustness) of the AMTMD is also not remarkable, regardless of  $\alpha$ . But, in the case of  $\alpha = 4.0$ , a pronounced difference in the optimum average damping ratio can be detected when the total mass ratio is below 0.03.

Comparison of the cases  $\alpha = 4.0$  and  $\alpha = 8.0$  shows that the interrelation between the effectiveness of the AMTMD and the total mass ratio has the same trend:

- (1) For  $E_R = 0.1$ , the effectiveness of the AMTMD for asymmetric structures with  $\lambda_\omega = 0.5$  is almost the same as for symmetric structures ( $E_R = 0$ ).
- (2) For  $E_R > 0.1$ , the effectiveness falls with increasing  $E_R$ , and drastically so when  $E_R = 0.4$ .
- (3) Increasing  $\alpha$  may enhance the effectiveness for asymmetric structures with  $\lambda_\omega = 0.5$ .
- (4) As the total mass ratio increases, the effectiveness initially increases, then remains almost invariant when the total mass ratio is above 0.02.

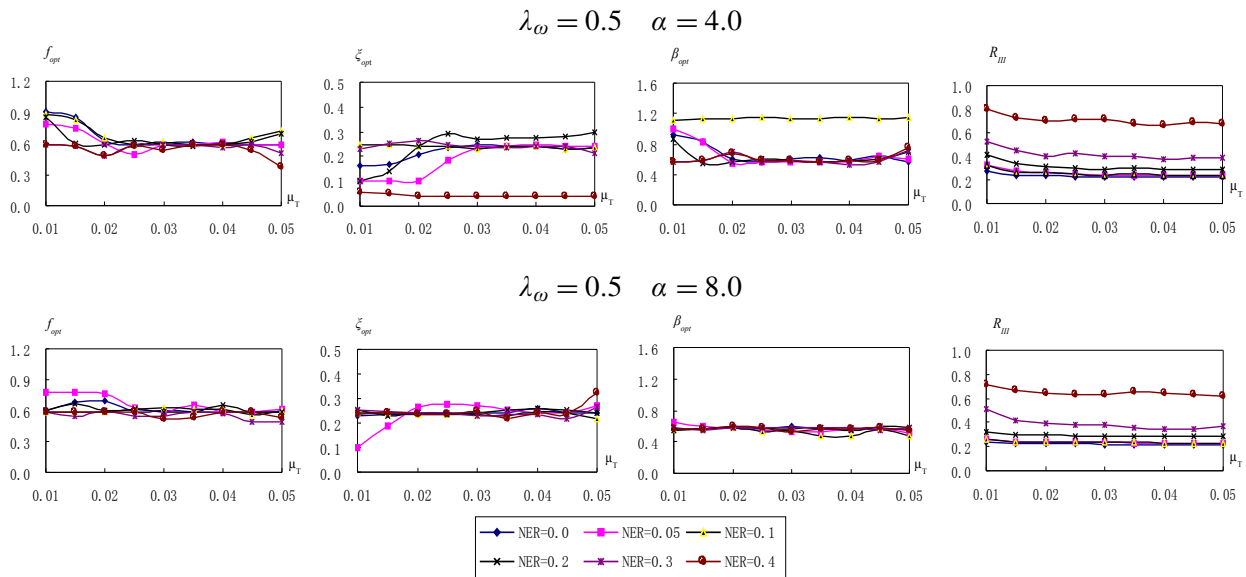


**Figure 2.** Optimum parameters  $f_{opt}$ ,  $\zeta_{opt}$ ,  $\beta_{opt}$  and translational effectiveness  $R_{III}$  as functions of  $\mu_T$ ,  $E_R$ , and  $\alpha$ , for a TFS ( $\lambda_\omega = 0.5$ ). The total number  $n$  of AMTMDs is 5 for all graphs up to Figure 7.

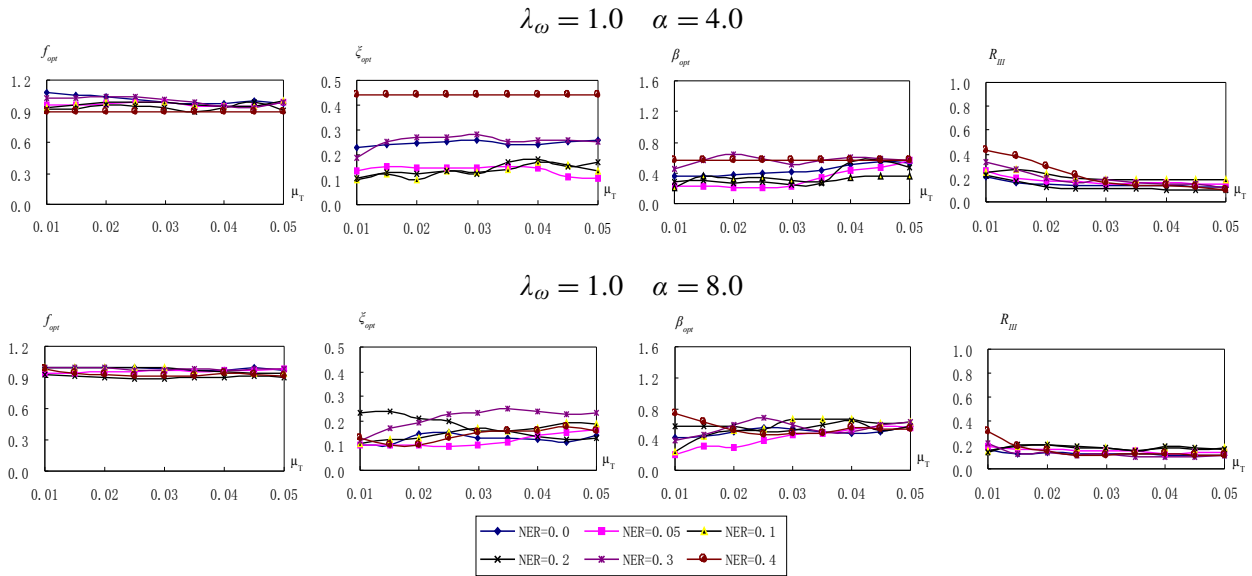


**Figure 3.** Optimum parameters  $f_{opt}$ ,  $\xi_{opt}$ ,  $\beta_{opt}$  and translational effectiveness  $R_{III}$  as functions of  $\mu_T$ ,  $E_R$ , and  $\alpha$ , for a TISS ( $\lambda_\omega = 1.0$ ).

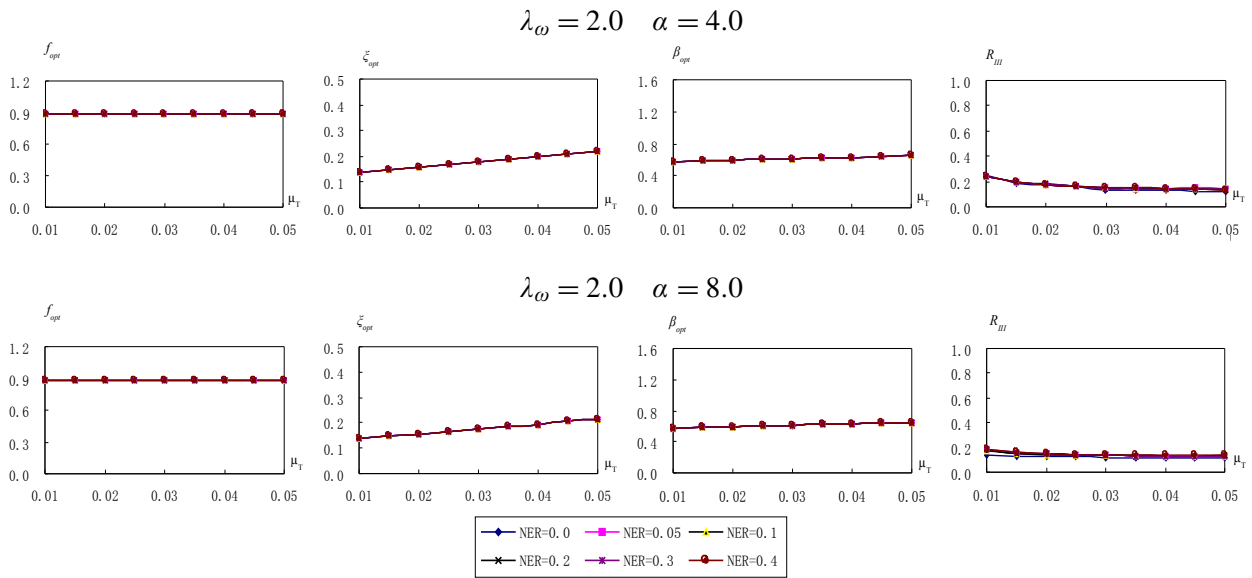
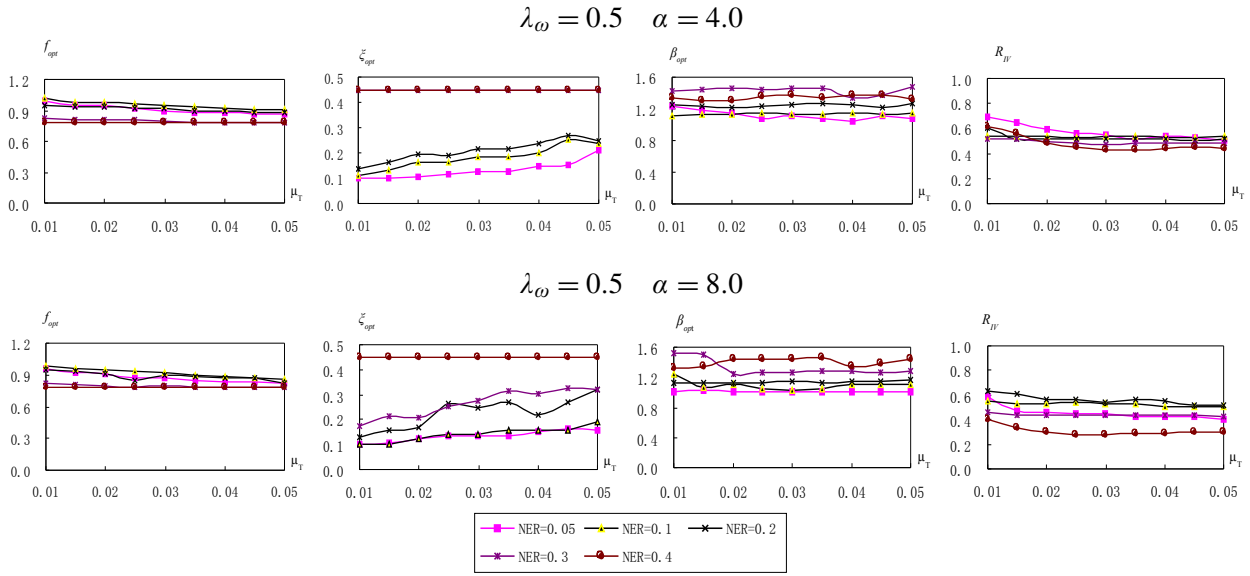


**Figure 4.** Optimum parameters  $f_{opt}$ ,  $\xi_{opt}$ ,  $\beta_{opt}$  and translational effectiveness  $R_{III}$  as functions of  $\mu_T$ ,  $E_R$ , and  $\alpha$ , for a TSS ( $\lambda_\omega = 2.0$ ).

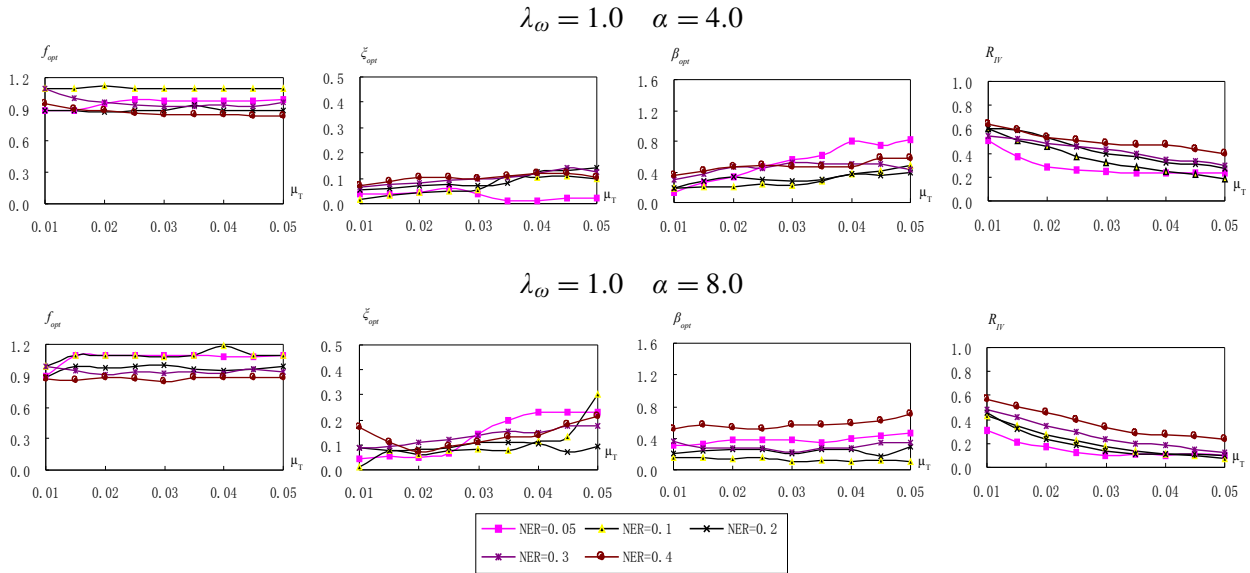
Figure 3 shows the corresponding results for a TISS ( $\lambda_\omega = 1.0$ ). We see that  $E_R$  has an influence on the optimum tuning frequency ratio and the optimum frequency spacing, but it is not great. The value of  $E_R$  has a significant effect on the optimum average damping ratio of the AMTMD, especially for the smaller value of  $\alpha$  (4.0). The effectiveness of the AMTMD for the TFS and the TISS show similar trends, but it is less influenced by  $E_R$  in the TFS.

Figure 4 reports the corresponding results for a TSS ( $\lambda_\omega = 2.0$ ). Here  $E_R$  seems to have very little influence on the optimum parameters and effectiveness.

**Torsional response.** Figure 5 shows the optimum parameters and the  $R_{IV}$  (rotational) effectiveness of the AMTMD for a TFS ( $\lambda_\omega = 0.5$ ), for the same values of  $\alpha$ ,  $E_R$ , and  $\mu_T$  as before (apart from  $E_R = 0$ ).



**Figure 5.** Optimum parameters  $f_{opt}$ ,  $\zeta_{opt}$ ,  $\beta_{opt}$  and torsional effectiveness  $R_{IV}$  as functions of  $\mu_T$ ,  $E_R$ , and  $\alpha$ , for a TFS ( $\lambda_\omega = 0.5$ ).



**Figure 6.** Optimum parameters  $f_{opt}$ ,  $\zeta_{opt}$ ,  $\beta_{opt}$  and torsional effectiveness  $R_{IV}$  as functions of  $\mu_T$ ,  $E_R$ , and  $\alpha$ , for a TISS ( $\lambda_\omega = 1.0$ ).

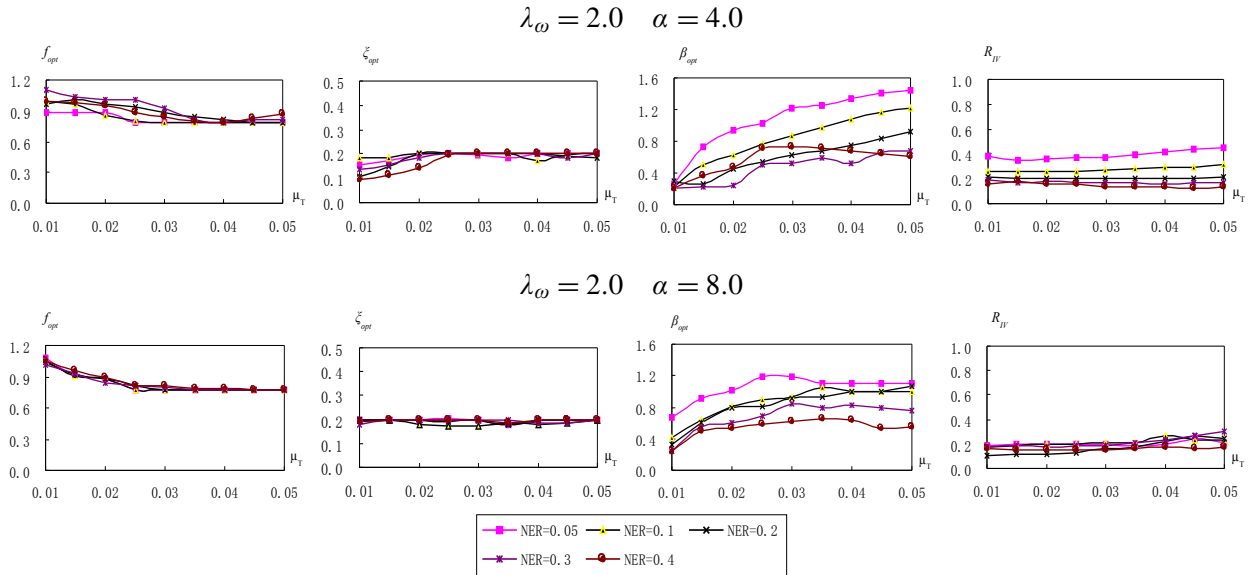


**Figure 7.** Optimum parameters  $f_{opt}$ ,  $\zeta_{opt}$ ,  $\beta_{opt}$  and torsional effectiveness  $R_{IV}$  as functions of  $\mu_T$ ,  $E_R$ , and  $\alpha$ , for a TSS ( $\lambda_\omega = 2.0$ ).

It can be seen that the optimum frequency spacing  $\beta_{opt}$  generally increases somewhat with  $E_R$ . So does the optimal average damping ratio  $\zeta_{opt}$ , albeit in an irregular fashion.

With the lower value of  $\alpha$  (4.0), the effectiveness is somewhat higher than for  $\alpha = 8.0$ , and not very sensitive to  $E_R$ . With the higher  $\alpha$ , the effectiveness varies irregularly with increasing  $E_R$ , decreasing while  $E_R \leq 0.2$  and increasing again when  $E_R \geq 0.3$ .

Figure 6 shows the corresponding data for a TISS ( $\lambda_\omega = 1$ ). In this case  $E_R$  significantly affects the optimum parameters and the effectiveness of the AMTMD. With the exception of the case of  $E_R = 0.4$  and  $\alpha = 8.0$ , the optimum frequency spacing of the AMTMD tends to be greatest for  $E_R = 0.05$ . More importantly, the torsional effectiveness takes on an irregular pattern; it decreases with increasing  $E_R$ .

Figure 7 is the corresponding display for a TSS ( $\lambda_\omega = 2.0$ ). The influence of  $E_R$  on the optimum tuning frequency ratio and average damping ratio is rather negligible here, especially in the case of  $\alpha = 8.0$ . However,  $E_R$  significantly affects the optimum frequency spacing; the two numbers move in opposite directions. The effectiveness decreases with increasing  $E_R$  for  $\alpha = 4.0$ , but is very little affected by  $E_R$  for  $\alpha = 8.0$ .

**Comparison with a single ATMD.** Figure 8 presents the effectivenesses  $R_{III}$  and  $R_{IV}$  of a single ATMD over the same ranges of  $\mu_T$ ,  $\lambda_\omega$ ,  $\alpha$ , and  $E_R$  that we used for the AMTMD calculations. By comparing Figure 8 with the corresponding graphs in Figures 2–7, one sees that, in comparison with a single ATMD, the AMTMD is slightly more effective in reducing the translational response of asymmetric structures, but slightly less effective in controlling the torsional response of asymmetric structures,

## 6. Conclusions

The following major conclusions can be drawn:



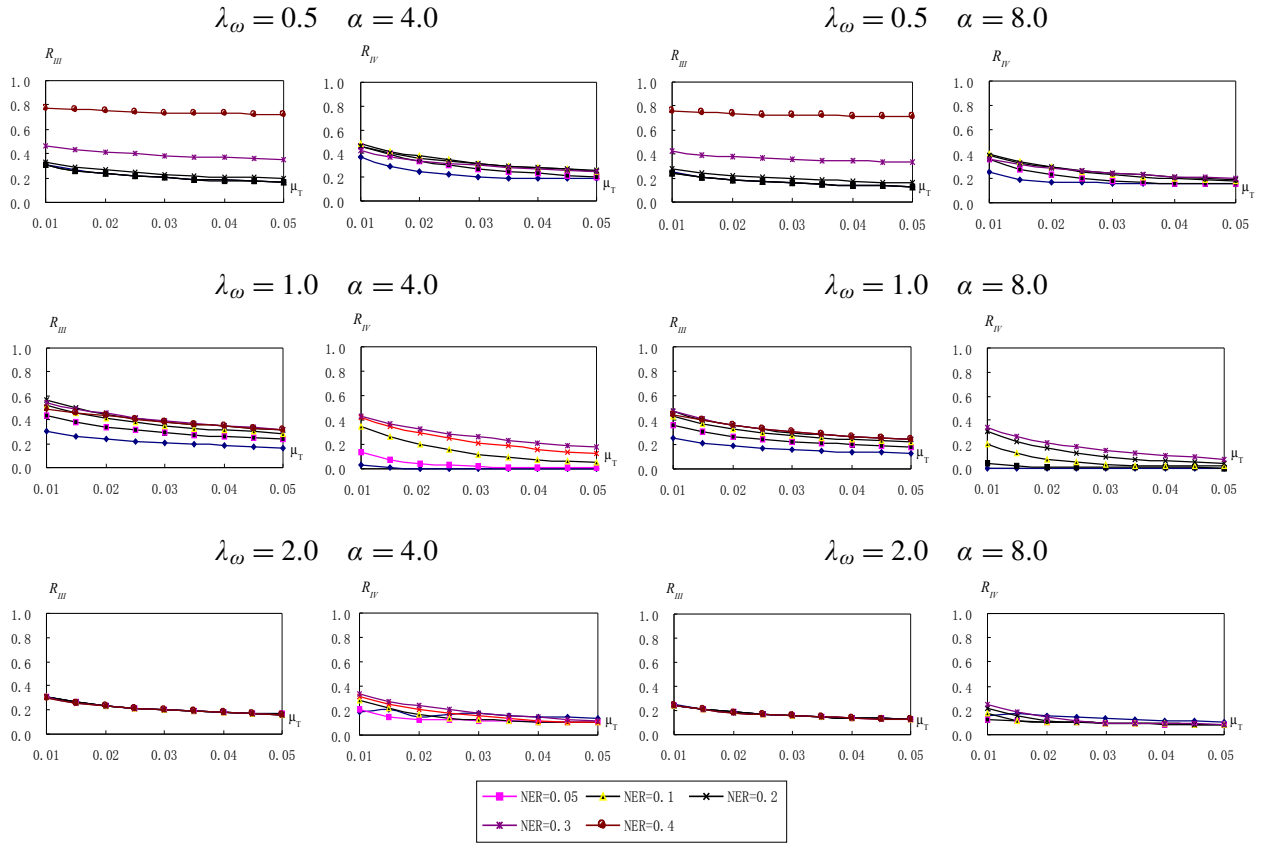


**Figure 8.** Translational effectiveness  $R_{III}$  (first and third columns) and torsional effectiveness  $R_{IV}$  (second and fourth columns) as functions of  $\mu_T$ ,  $E_R$ , and  $\alpha$  for a single ATMD.

- (1) In attenuating the translational response of TFS ( $\lambda_\omega = 0.5$ ), the effect of  $E_R$  on the optimum frequency spacing (robustness) of the AMTMD is not significant; the effectiveness of the AMTMD for asymmetric structures with  $E_R$  smaller than 0.1 is practically equal to that for symmetric structures ( $E_R = 0$ ) and reduces as  $E_R$  increases above 0.1.
- (2) In attenuating the torsional response of TFS, the optimum frequency spacing of the AMTMD generally increases with increasing  $E_R$ . With smaller  $\alpha$ , the effectiveness of the AMTMD improves with increasing  $E_R$ , though this is not very obvious. With higher  $\alpha$ , the effectiveness of the AMTMD decreases with increasing  $E_R$  when  $E_R \leq 0.2$ , and increases with increasing  $E_R$  when  $E_R \geq 0.3$ .
- (3) In controlling the translational response of TISS ( $\lambda_\omega = 1.0$ ),  $E_R$  has influence on the optimum frequency spacing of the AMTMD, but it is not that obvious; the effectiveness of the AMTMD for TISS has similar trends as that for TFS.
- (4) In controlling the torsional response of TISS, the optimum frequency spacing and effectiveness of the AMTMD generally decreases with increasing  $E_R$ .

- (5) In mitigating the translational response of TSS, the AMTMD will take on the same optimum parameters, robustness, and effectiveness, regardless of different  $E_R$  values.
- (6) In reducing the torsional response of TSS, the optimum frequency spacing of the AMTMD generally decreases with increasing  $E_R$ . The effectiveness of the AMTMD with a smaller  $\alpha$ , such as  $\alpha = 4.0$ , decreases as  $E_R$  increases. The influence of  $E_R$  on the effectiveness of the AMTMD with higher  $\alpha$ , such as  $\alpha = 8.0$ , is rather negligible.
- (7) The AMTMD provides slightly higher effectiveness than a single ATMD in reducing the translational response of asymmetric structures.
- (8) The AMTMD are slightly less effective than a single ATMD in controlling the torsional response of asymmetric structures.

We point out that by employing the present approach, which falls into the frequency domain design method of control, Li et al. [2007] have numerically investigated the earthquake resistant performance of AMTMD for asymmetric buildings, so as to further validate the effectiveness and robustness of AMTMD in reducing the translational and torsional responses of asymmetric buildings in the time domain. The SIMULINK analysis has been implemented on a three-story asymmetric steel structure building under various earthquakes, taking into account both the certainty and uncertainty in the structural stiffness. The numerical simulations indicate that AMTMD can effectively control the translational and torsional responses of asymmetric buildings subjected to earthquakes. Likewise, AMTMD generally have better performance than an ATMD for seismically excited asymmetric buildings. More recently, in order to further validate the control force decentralization of AMTMD for the control of wind-induced vibrations of tall buildings in the time-domain, a 22-story steel-frame building is chosen as an example problem [Li et al. 2009]. The numerical results in the time-domain indicate that a large control force can indeed be decentralized into many smaller control forces when using AMTMD. Simultaneously, the effectiveness of AMTMD is a little larger than that of an ATMD based on the DRF and ARF criteria [Li et al. 2009].

### List of symbols

AMTMD	active multiple tuned mass dampers
$\alpha$	normalized acceleration feedback gain factor (NAFGF)
$b/r$	normalized width of an asymmetric structure, here set equal to 1.0
$\beta$	nondimensional frequency spacing
CM	center of mass
CR	center of resistance
$c_s$	mode-generalized damping coefficient
$c_T$	constant damping coefficient of the AMTMD
$c_{Tj}$	damping coefficient of the $j$ -th ATMD in the AMTMD
$c_{tj}$	velocity feedback of the $j$ -th ATMD in the AMTMD
$c_t$	constant velocity feedback of the $j$ -th ATMD in the AMTMD
$E_R$	normalized eccentricity ratio (ratio between eccentricity and gyration radius of the deck)
$e_y$	eccentricity between the CR and CM
$f$	tuning frequency ratio of the AMTMD

$H_{x_s}(-i\omega)$	transfer function for translational displacement
$H_{\theta_s}(-i\omega)$	transfer function for torsional displacement
$j$	number of ATMDs in the AMTMD
$k_s$	mode-generalized lateral stiffness of an asymmetric structure in the translational $x$ direction
$k_T$	constant spring stiffness of the AMTMD
$k_{Tj}$	spring stiffness of the $j$ -th ATMD in the AMTMD
$k_t$	constant displacement feedback of the $j$ -th ATMD in the AMTMD
$k_{tj}$	displacement feedback of the $j$ -th ATMD in the AMTMD
$k_\theta$	mode-generalized torsional stiffness of an asymmetric structure with respect to the CM
$\lambda_\omega$	uncoupled torsional-to-translational frequency ratio (TFR)
MTMD	multiple tuned mass dampers
$m_s$	mode-generalized mass of an asymmetric structure
$m_{Tj}$	mass of the $j$ -th ATMD in the AMTMD
$m_{tj}$	acceleration feedback of the $j$ -th ATMD in the AMTMD
$\mu_{Tj}$	mass ratio of the $j$ -th ATMD in the AMTMD
$\mu_T$	total mass ratio of the AMTMD
$n$	total number of ATMDs in the AMTMD
$R_I$	minimum of translational displacement variance over $f, \zeta_T, \beta$
$R_{II}$	minimum of torsional displacement variance over $f, \zeta_T, \beta$
$R_{III}$	effectiveness of the AMTMD in attenuating the structure's translational response; see (19)
$R_{IV}$	effectiveness of the AMTMD in attenuating the structure's torsional response; see (19)
$r$	radius of gyration of the deck about the vertical axis through the CM
$r_j$	ratio of the natural frequency of the $j$ -th ATMD to the uncoupled translational natural frequency of an asymmetric structure
$\theta_s$	torsional displacement of an asymmetric structure
$\ddot{x}_g(t)$	ground acceleration
$x_s$	translational displacement of an asymmetric structure with respect to the ground
$x_{Tj}$	translational displacement of each ATMD with reference to the ground
$\zeta_j$	damping ratio of the $j$ -th ATMD in the AMTMD
$\zeta_s$	structural damping ratio, which is set equal to 0.02 in this study
$\zeta_T$	average damping ratio of the AMTMD
$y_j$	translational displacement of each ATMD with reference to the ground
$y_{(n+1)/2}$	center of the AMTMD, placement of the $(n + 1)/2$ -th ATMD in the AMTMD
$\omega$	external excitation frequency
$\omega_j$	natural frequency of the $j$ -th ATMD in the AMTMD
$\omega_s$	uncoupled translational natural frequency of an asymmetric structure
$\omega_{s1}$	coupled fundamental natural frequency of an asymmetric structure
$\omega_{s2}$	coupled second natural frequency of an asymmetric structure
$\omega_\theta$	uncoupled torsional natural frequency of an asymmetric structure
$\omega_T$	average natural frequency of the AMTMD

## References

- [Abe 1996] M. Abe, "Rule-based control algorithm for active tuned mass dampers", *J. Eng. Mech. (ASCE)* **122**:8 (1996), 705–713.
- [Abe and Fujino 1994] M. Abe and Y. Fujino, "Dynamic characterization of multiple tuned mass dampers and some design formulas", *Earthquake Eng. Struct. Dyn.* **23**:8 (1994), 813–835.
- [Ahlawat and Ramaswamy 2002a] A. S. Ahlawat and A. Ramaswamy, "Multi-objective optimal design of FLC driven hybrid mass damper for seismically excited structures", *Earthquake Eng. Struct. Dyn.* **31**:7 (2002), 1459–1479.
- [Ahlawat and Ramaswamy 2002b] A. S. Ahlawat and A. Ramaswamy, "Multiobjective optimal FLC driven hybrid mass damper system for torsionally coupled, seismically excited structures", *Earthquake Eng. Struct. Dyn.* **31**:12 (2002), 2121–2139.
- [Ahlawat and Ramaswamy 2003] A. S. Ahlawat and A. Ramaswamy, "Multiobjective optimal absorber system for torsionally coupled seismically excited structures", *Eng. Struct.* **25**:7 (2003), 941–950.
- [Ankireddi and Yang 1996] S. Ankireddi and H. T. Y. Yang, "Simple ATMD control methodology for tall buildings subject to wind loads", *J. Struct. Eng. (ASCE)* **122**:1 (1996), 83–91.
- [Arfiadi and Hadi 2000] Y. Arfiadi and M. N. S. Hadi, "Passive and active control of three-dimensional buildings", *Earthquake Eng. Struct. Dyn.* **29**:3 (2000), 377–396.
- [Bakre and Jangid 2004] S. V. Bakre and R. S. Jangid, "Optimum multiple tuned mass dampers for base-excited damped main system", *Int. J. Struct. Stability Dyn.* **4**:4 (2004), 527–542.
- [Chang and Soong 1980] J. C. H. Chang and T. T. Soong, "Structural control using active tuned mass damper", *J. Eng. Mech. (ASCE)* **106**:6 (1980), 1091–1098.
- [Chang and Yang 1995] C. C. Chang and H. T. Y. Yang, "Control of buildings using active tuned mass dampers", *J. Eng. Mech. (ASCE)* **121**:3 (1995), 355–366.
- [Chen and Wu 2003] G. Chen and J. Wu, "Experimental study on multiple tuned mass dampers to reduce seismic responses of a three-storey building structure", *Earthquake Eng. Struct. Dyn.* **32**:5 (2003), 793–810.
- [Gu et al. 2001] M. Gu, S. R. Chen, and C. C. Chang, "Parametric study on multiple tuned mass dampers for buffeting control of Yangpu Bridge", *J. Wind Eng. Ind. Aerod.* **89**:11-12 (2001), 987–1000.
- [Han and Li 2006] B. Han and C. Li, "Evaluation of multiple dual tuned mass dampers for structures under harmonic ground acceleration", *Int. J. Struct. Stability Dyn.* **6**:1 (2006), 59–75.
- [Hoang and Warnitchai 2005] N. Hoang and P. Warnitchai, "Design of multiple tuned mass dampers by using a numerical optimizer", *Earthquake Eng. Struct. Dyn.* **34**:2 (2005), 125–144.
- [Ikeda 1997] Y. Ikeda, "Effect of weighting a stroke of an active mass damper in the linear quadratic regulator problem", *Earthquake Eng. Struct. Dyn.* **26**:11 (1997), 1125–1136.
- [Jangid 1999] R. S. Jangid, "Optimum multiple tuned mass dampers for base-excited undamped system", *Earthquake Eng. Struct. Dyn.* **28**:9 (1999), 1041–1049.
- [Jangid and Datta 1997] R. S. Jangid and T. K. Datta, "Performance of multiple tuned mass dampers for torsionally coupled system", *Earthquake Eng. Struct. Dyn.* **26**:3 (1997), 307–317.
- [Kareem and Kline 1995] A. Kareem and S. Kline, "Performance of multiple mass dampers under random loading", *J. Struct. Eng. (ASCE)* **121**:2 (1995), 348–361.
- [Kwon and Park 2004] S.-D. Kwon and K.-S. Park, "Suppression of bridge flutter using tuned mass dampers based on robust performance design", *J. Wind Eng. Ind. Aerod.* **92**:11 (2004), 919–934.
- [Li 2000] C. Li, "Performance of multiple tuned mass dampers for attenuating undesirable oscillations of structures under the ground acceleration", *Earthquake Eng. Struct. Dyn.* **29**:9 (2000), 1405–1421.
- [Li 2006] C. Li, "Performance of dual-layer multiple tuned mass dampers for structures under ground excitations", *Int. J. Struct. Stability Dyn.* **6**:4 (2006), 541–557.
- [Li and Li 2005] C. Li and Q. S. Li, "Evaluation of the lever-type multiple tuned mass dampers for mitigating harmonically forced vibration", *Int. J. Struct. Stability Dyn.* **5**:4 (2005), 641–664.

- [Li and Liu 2002] C. Li and Y. Liu, "Active multiple tuned mass dampers for structures under the ground acceleration", *Earthquake Eng. Struct. Dyn.* **31**:5 (2002), 1041–1052.
- [Li and Qu 2006] C. Li and W. Qu, "Optimum properties of multiple tuned mass dampers for reduction of translational and torsional response of structures subject to ground acceleration", *Eng. Struct.* **28**:4 (2006), 472–494.
- [Li and Xiong 2008] C. Li and X. Xiong, "Estimation of active multiple tuned mass dampers for asymmetric structures", *Struct. Eng. Mech.* **29**:5 (2008), 505–530.
- [Li and Zhang 2005] C. Li and J. Zhang, "Evaluation of arbitrary integer based multiple tuned mass dampers for structures", *Int. J. Struct. Stability Dyn.* **5**:3 (2005), 475–488.
- [Li et al. 2003] C. Li, Y. Liu, and Z. Wang, "Active multiple tuned mass dampers: a new control strategy", *J. Struct. Eng. (ASCE)* **129**:7 (2003), 972–977.
- [Li et al. 2007] C. Li, C. Wang, and L. Zhang, "Simulations of earthquake-resistant asymmetric buildings with active multiple tuned mass dampers based on simulink", *Chinese J. Vibration Shock* **26**:9 (2007), 45–50.
- [Li et al. 2009] C. Li, B. Han, J. Zhang, Y. Qu, and J. Li, "Active multiple tuned mass dampers for reduction of undesirable oscillations of structures under wind loads", *Int. J. Struct. Stability Dyn.* **9**:1 (2009), 127–149.
- [Lin et al. 2000a] C. C. Lin, J. M. Ueng, and T. C. Huang, "Seismic response reduction of irregular buildings using passive tuned mass dampers", *Eng. Struct.* **22**:5 (2000), 513–524.
- [Lin et al. 2000b] Y. Y. Lin, C. M. Cheng, and C. H. Lee, "A tuned mass damper for suppressing the coupled flexural and torsional buffeting response of long-span bridges", *Eng. Struct.* **22**:9 (2000), 1195–1204.
- [Lin et al. 2005] C. C. Lin, J. F. Wang, and B. L. Chen, "Train-induced vibration control of high-speed railway bridges equipped with multiple tuned mass dampers", *J. Bridge Eng. (ASCE)* **10**:4 (2005), 398–414.
- [Nagarajaiah and Narasimhan 2006] S. Nagarajaiah and S. Narasimhan, "Smart base-isolated benchmark building, II: phase I sample controllers for linear isolation systems", *Struct. Control Health Monitoring* **13**:2-3 (2006), 589–604.
- [Nagarajaiah and Narasimhan 2007] S. Nagarajaiah and S. Narasimhan, "Seismic control of smart base isolated buildings with new semiactive variable damper", *Earthquake Eng. Struct. Dyn.* **36**:6 (2007), 729–749.
- [Nagarajaiah et al. 2008] S. Nagarajaiah, S. Narasimhan, and E. Johnson, "Structural control benchmark problem, phase II: Nonlinear smart base-isolated building subjected to near-fault earthquakes", *Struct. Control Health Monitoring* **15**:5 (2008), 653–656.
- [Nagashima 2001] I. Nagashima, "Optimal displacement feedback control law for active tuned mass damper", *Earthquake Eng. Struct. Dyn.* **30**:8 (2001), 1221–1242.
- [Narasimhan et al. 2006] S. Narasimhan, S. Nagarajaiah, E. A. Johnson, and H. P. Gavin, "Smart base-isolated benchmark building, I: problem definition", *Struct. Control Health Monitoring* **13**:2-3 (2006), 573–588.
- [Narasimhan et al. 2008] S. Narasimhan, S. Nagarajaiah, and E. Johnson, "Smart base-isolated benchmark building, IV: Phase II sample controllers for nonlinear isolation systems", *Struct. Control Health Monitoring* **15**:5 (2008), 657–672.
- [Ohtori et al. 2004] Y. Ohtori, R. E. Christenson, B. F. Spencer, Jr., and S. J. Dyke, "Benchmark control problems for seismically excited nonlinear buildings", *J. Eng. Mech. (ASCE)* **130**:4 (2004), 366–385.
- [Pansare and Jangid 2003] A. P. Pansare and R. S. Jangid, "Tuned mass dampers for torsionally coupled systems", *Wind Struct.* **6**:1 (2003), 23–40.
- [Park and Reed 2001] J. Park and D. Reed, "Analysis of uniformly and linearly distributed mass dampers under harmonic and earthquake excitation", *Eng. Struct.* **23**:7 (2001), 802–814.
- [Singh et al. 2002] M. P. Singh, S. Singh, and L. M. Moreschi, "Tuned mass dampers for response control of torsional buildings", *Earthquake Eng. Struct. Dyn.* **31**:4 (2002), 749–769.
- [Spencer et al. 1998a] B. F. Spencer, Jr., S. J. Dyke, and H. S. Deoskar, "Benchmark problems in structural control, I: active mass driver system", *Earthquake Eng. Struct. Dyn.* **27**:11 (1998), 1127–1139.
- [Spencer et al. 1998b] B. F. Spencer, Jr., S. J. Dyke, and H. S. Deoskar, "Benchmark problems in structural control, II: active tendon system", *Earthquake Eng. Struct. Dyn.* **27**:11 (1998), 1141–1147.
- [Wang and Lin 2005] J. F. Wang and C. C. Lin, "Seismic performance of multiple tuned mass dampers for soil-irregular building interaction systems", *Int. J. Solids Struct.* **42**:20 (2005), 5536–5554.

- [Xu and Igusa 1992] K. Xu and T. Igusa, “Dynamic characteristics of multiple substructures with closely spaced frequencies”, *Earthquake Eng. Struct. Dyn.* **21**:12 (1992), 1059–1070.
- [Yamaguchi and Harnpornchai 1993] H. Yamaguchi and N. Harnpornchai, “Fundamental characteristics of multiple tuned mass dampers for suppressing harmonically forced oscillations”, *Earthquake Eng. Struct. Dyn.* **22**:1 (1993), 51–62.
- [Yan et al. 1999] N. Yan, C. M. Wang, and T. Balendra, “Optimum damper characteristics of ATMD for buildings under wind loads”, *J. Struct. Eng. (ASCE)* **125**:12 (1999), 1376–1383.
- [Yang et al. 2004] J. N. Yang, A. K. Agrawal, B. Samali, and J. C. Wu, “Benchmark problem for response control of wind-excited tall buildings”, *J. Eng. Mech. (ASCE)* **130**:4 (2004), 437–446.
- [Yau and Yang 2004a] J. D. Yau and Y. B. Yang, “Vibration reduction for cable-stayed bridges traveled by high-speed trains”, *Finite Elem. Anal. Des.* **40**:3 (2004), 341–359.
- [Yau and Yang 2004b] J. D. Yau and Y. B. Yang, “A wideband MTMD system for reducing the dynamic response of continuous truss bridges to moving train loads”, *Eng. Struct.* **26**:12 (2004), 1795–1807.

Received 19 Nov 2008. Revised 12 Jan 2009. Accepted 29 Jan 2009.

CHUNXIANG LI: [li-chunxiang@vip.sina.com](mailto:li-chunxiang@vip.sina.com)

*Department of Civil Engineering, Shanghai University, 149 Yanchang Road, Shanghai 200072, China*

JINHUA LI: *Department of Civil Engineering, Shanghai University, 149 Yanchang Road, Shanghai 200072, China*

ZHIQIANG YU: *Department of Civil Engineering, Shanghai University, 149 Yanchang Road, Shanghai 200072, China*

YAN QU: *Department of Civil Engineering, Shanghai University, 149 Yanchang Road, Shanghai 200072, China*

## EFFECTS OF SURFACE AND INITIAL STRESSES ON THE BENDING STIFFNESS OF TRILAYER PLATES AND NANOFILMS

HANXING ZHU, JIANXIANG WANG AND BHUSHAN KARIHALOO

Simple closed-form analytic solutions have been obtained for the effect of initial residual stress on the bending stiffness of a symmetric trilayer plate/beam and for the combined effect of surface elasticity and initial surface stress on the bending stiffness of a nanofilm/nanobeam. The relative effect of the initial residual stress is generally limited to the range of the material yield strain. For nanofilms and nanobeams, the effect of the surface elasticity reduces with an increase in the thickness, but the initial surface stress effect can be retained at a constant level of up to the limit of elastic strain if it can be controlled, for example by the application of an electrical potential.

### 1. Introduction

Multilayer plate structures are widely used in applications at different size scales ranging from macro civil and mechanical structures down to microelectromechanical systems (MEMS) and nanoelectromechanical systems (NEMS). Elastic and thermal mismatch of individual materials can result in significant internal residual stresses in multilayer systems. As internal residual stresses can influence the overall mechanical properties (such as the stiffness and the natural frequency) and hence the dynamic and stability characteristics of multilayer systems, their determination has long interested material scientists and engineers [Stoney 1909; Freund 2000; Hui et al. 2000; Klein 2000; Dodin et al. 2001; Freund and Johnson 2001; Thompson and Clyne 2001; Donadon et al. 2002; Xu and Zhang 2003; Malzbender 2004; Huang and Zhang 2006; Huang and Zhang 2007]. Both the experimental measurement of internal stresses and the optimal design of multilayer systems rely heavily on the accuracy of the involved correlations. To the best of our knowledge, there is no reliable closed-form solution for the effect of initial residual stress on the bending stiffness of a symmetric trilayer plate structure (Figure 1).

The demand for smaller and faster devices has encouraged technological advances in the production of systems at micro- and nanoscales. While MEMS technology is now a well established area, nanoelectromechanical systems (NEMS) have been attracting more interest lately [Bunch et al. 2007; Masmanidis et al. 2007], as have the mechanical properties of nanomaterials and nanostructures. It has been well recognized that the effect of surface elasticity on the stiffness of nanostructures is size-dependent [He et al. 2004; Lim and He 2004; Cuenot et al. 2004; Zhou and Huang 2004; Duan et al. [2005a; 2005b; 2006]; Chen et al. 2006; Wang et al. 2006; Zhu and Karihaloo 2008]. As the surface to volume ratio is large, the stiffness and deformation of a nanostructure greatly depend on the surface stress, while the latter depends on the electric charge which in turn depends on the applied electric potential [Haiss et al. 1998; Weissmüller et al. 2003; Kramer et al. 2004]. Therefore the deformation of a nanostructure can be controlled by adjusting the applied electric potential [Kramer et al. 2004]. Miller and Shenoy [2000]

*Keywords:* residual stress, bending stiffness, surface effect, nanoplate, nanobeam.

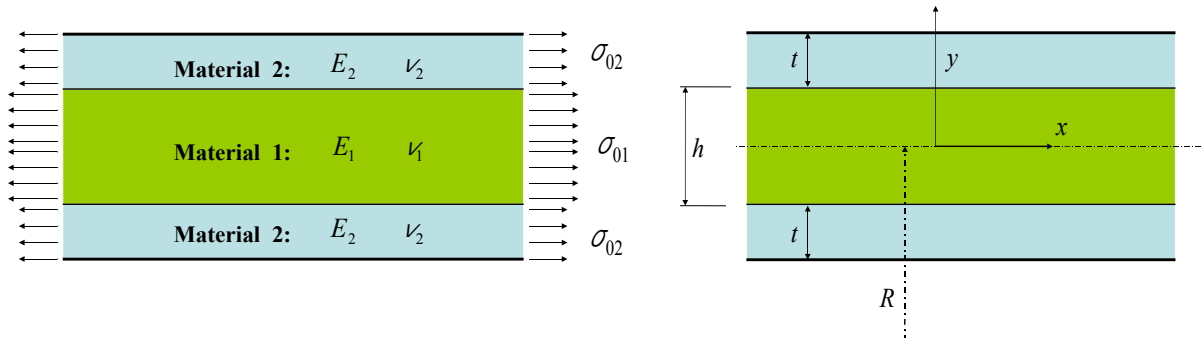


**Figure 1.** Schematic diagram of a prestressed trilayer plate. Left: materials and initial residual stresses. Right: dimensions and coordinate system.

showed that the relative contribution of the surface elastic modulus to the bending stiffness of a nanoplate is  $6S/(Eh)$ , where  $S$  is the surface elastic modulus,  $E$  is the Young's modulus of the bulk material and  $h$  is the thickness of the nanoplate.

However, the effect of the initial residual stresses on the bending stiffness of a nanoplate (or nanobeam) has not yet been considered. Zhu [2008] has considered the combined effects of surface elasticity and initial stresses on the bending stiffness of a core-shell nanowire with a circular cross-section. In this paper we consider the effect of initial stress on the bending stiffness of a symmetric trilayer plate/beam and the combined effects of surface elasticity and the initial stresses on the bending stiffness of a nanoplate/nanobeam with a rectangular or square cross-section.

## 2. Pure bending of a prestressed symmetric trilayer plate/beam

Figure 1 shows the cross-sectional geometry of a trilayer plate. The middle layer of thickness  $h$  is made of material 1 with Young's modulus  $E_1$  and Poisson's ratio  $\nu_1$ . Both the top and bottom layers of thickness  $t$  are made of material 2 with Young's modulus  $E_2$  and Poisson's ratio  $\nu_2$ . The width direction is denoted as  $z$ , which is normal to the  $xy$ -plane. The trilayer plate is initially flat and there is no initial residual stress in the thickness direction (that is, the  $y$  direction). The initial residual stresses in both the  $x$  and the  $z$  directions within the middle and the surface layers are  $\sigma_{01}$  and  $\sigma_{02}$ , respectively. Obviously, they satisfy the equilibrium condition

$$h\sigma_{01} + 2t\sigma_{02} = 0. \quad (1)$$

When the symmetric trilayer plate is bent by a pure moment  $M$ , the radius of the neutral surface is assumed to be  $R$ . To obtain a simple closed-form analytic solution for this problem, the following two assumptions are made: i) the materials are linear elastic and the deformation is very small; ii) the plate thickness does not change and  $R$  is much larger than the plate thickness. When a pure bending moment is applied to the initially flat symmetric trilayer plate, the deformed trilayer plate obviously becomes a cylinder but the initial cross-sectional planes remain plane after bending (as there is no net shear force in cross-sectional planes). As the superposition principle applies to this elastic small deformation problem, all the stresses and strains in the analysis of this paper, unless otherwise mentioned, are their changes from the initial prestressed state resulting from the application of the pure bending moment  $M$ .



When a wide trilayer plate is subjected to pure bending, the change of the strain in the  $z$  direction (which is normal to the  $xy$ -plane of Figure 1)  $\varepsilon_z$  is a constant through the thickness of the three layers and is to be determined. To simplify the analysis, we assume that thickness of the three layers does not change after bending and the neutral surface is always in the middle of the middle layer as the bending deformation is very small. This assumption will be subsequently validated.

We look at the deformation of the top layer first. Hooke's law requires

$$\sigma_2^z(y) = E_2 \varepsilon_z + \nu_2 \sigma_2^x(y) + \nu_2 \sigma_2^y(y) \quad (h/2 \leq y \leq h/2 + t), \quad (2)$$

where  $\sigma_2^z$ ,  $\sigma_2^x$ ,  $\sigma_2^y$  are the stress changes in the  $z$ ,  $x$  and  $y$  directions, respectively and the subscript 2 refers to material 2 of the outer layers (Figure 1, left). All the stress changes are functions of the coordinate  $y$  (Figure 1, right). The equilibrium equation in the radial direction of the bent plate, namely  $d\sigma^r/dr = (\sigma^\theta - \sigma^r)/r$ , requires that

$$d(r\sigma_2^r) = \sigma_2^\theta dr,$$

where  $\sigma_2^\theta = \sigma_2^x + \sigma_{02}$  and  $\sigma_2^r = \sigma_2^y$ . Integrating both sides and making use of the boundary condition  $(r\sigma_2^r)|_{r=R+t+h/2} = 0$ , we get for constant initial residual stress  $\sigma_{02}$  in the outer layers

$$\int_{R+y}^{R+t+h/2} d(r\sigma_2^r) = -(R+y)\sigma_2^y = \int_{R+y}^{R+t+h/2} \sigma_2^\theta dr = \int_y^{t+h/2} (\sigma_2^x + \sigma_{02}) dy.$$

Since the thickness of the trilayer plate is far less than  $R$  (that is,  $|y| \ll R$ ), this can be rewritten as

$$\sigma_2^y(y) = -\frac{1}{R+y} \int_y^{t+h/2} (\sigma_2^x + \sigma_{02}) dy \approx -\frac{1}{R} \int_y^{t+h/2} (\sigma_2^x + \sigma_{02}) dy. \quad (3)$$

Substituting (2) and (3) into Hooke's law

$$\varepsilon_2^x(y) = \frac{y}{R} = \frac{1}{E_2} (\sigma_2^x - \nu_2 \sigma_2^z - \nu_2 \sigma_2^y),$$

gives

$$\frac{yE_2}{R} = (1 - \nu_2^2)\sigma_2^x(y) - \nu_2 E_2 \varepsilon_z + \frac{\nu_2(1 + \nu_2)}{R} \int_y^{t+h/2} (\sigma_2^x(y) + \sigma_{02}) dy. \quad (4)$$

Differentiating both sides with respect to  $y$  leads to

$$(1 - \nu_2^2) \frac{d\sigma_2^x(y)}{dy} - \frac{\nu_2(1 + \nu_2)}{R} (\sigma_2^x(y) + \sigma_{02}) - \frac{E_2}{R} = 0. \quad (5)$$

It should be mentioned that in (3),  $R$  is used to approximate  $r$ ; otherwise, there is an additional term of  $-\nu_2(1 + \nu_2)r^{-2} \int_y^{t+h/2} (\sigma_2^x(y) + \sigma_{02}) dy$  on the left hand side of (5). As  $1/r^2 \approx 1/R^2$  is a higher order small number, the term is ignored in the differential equation (5). The solution of the first order differential equation (5) is

$$\sigma_2^x(y) = A \exp \frac{\nu_2 y}{(1 - \nu_2)R} - \frac{E_2}{\nu_2(1 + \nu_2)} - \sigma_{02} \quad (h/2 \leq y \leq h/2 + t), \quad (6)$$

where  $A$  is a constant of integration to be determined by substituting (6) into (4):

$$\begin{aligned} A &= \left( \frac{\nu_2 E_2 \varepsilon_z}{1 - \nu_2^2} + \sigma_{02} + \frac{E_2}{\nu_2(1 + \nu_2)} + \frac{(h + 2t)E_2}{2R(1 - \nu_2^2)} \right) \exp\left(-\frac{(h + 2t)\nu_2}{2(1 - \nu_2)R}\right) \\ &\approx \frac{\nu_2 E_2 \varepsilon_z}{1 - \nu_2^2} - \frac{\nu_2^2 E_2 \varepsilon_z (h + 2t)}{2(1 - \nu_2)(1 - \nu_2^2)R} + \sigma_{02} + \frac{E_2}{\nu_2(1 + \nu_2)} - \frac{(h + 2t)\nu_2 \sigma_{02}}{2(1 - \nu_2)R}. \end{aligned} \quad (7)$$

The exponential function has been expanded into a polynomial and the terms of order higher than  $1/R$  have been ignored in (7), since  $1/R$  is very small.

It is easy to see that (5) is also the governing differential equation for the stress change in the  $x$  direction within the bottom layer. The solution is therefore

$$\sigma_2^x(y) = B \exp \frac{\nu_2 y}{(1 - \nu_2)R} - \frac{E_2}{\nu_2(1 + \nu_2)} - \sigma_{02} \quad (-h/2 - t \leq y \leq -h/2), \quad (8)$$

where,

$$\begin{aligned} B &= \left( \frac{\nu_2 E_2 \varepsilon_z}{1 - \nu_2^2} + \sigma_{02} + \frac{E_2}{\nu_2(1 + \nu_2)} - \frac{(h + 2t)E_2}{2R(1 - \nu_2^2)} \right) \exp\left(\frac{(h + 2t)\nu_2}{2(1 - \nu_2)R}\right) \\ &\approx \sigma_{02} + \frac{E_2}{\nu_2(1 + \nu_2)} + \frac{(h + 2t)\nu_2 \sigma_{02}}{2(1 - \nu_2)R} + \frac{\nu_2 E_2 \varepsilon_z}{1 - \nu_2^2} + \frac{\nu_2^2 E_2 \varepsilon_z (h + 2t)}{2(1 - \nu_2)(1 - \nu_2^2)R}. \end{aligned} \quad (9)$$

In a similar manner, the governing differential equation for the stress change in the  $x$  direction within the middle layer can be obtained as

$$(1 - \nu_1^2) \frac{d\sigma_1^x(y)}{dy} - \frac{\nu_1(1 + \nu_1)}{R} (\sigma_1^x(y) + \sigma_{01}) - \frac{E_1}{R} = 0 \quad (-h/2 \leq y \leq h/2), \quad (10)$$

where the subscript 1 refers to material 1 of the middle layer. The solution of (10) is

$$\sigma_1^x(y) = C \exp \frac{\nu_1 y}{(1 - \nu_1)R} - \frac{E_1}{\nu_1(1 + \nu_1)} - \sigma_{01} \quad (-h/2 \leq y \leq h/2), \quad (11)$$

where the constant of integration is given by

$$C = \left( \frac{\nu_1 E_1 \varepsilon_z}{1 - \nu_1^2} + \sigma_{01} + \frac{E_1}{\nu_1(1 + \nu_1)} - \frac{t\nu_1}{(1 - \nu_1)R} A + \frac{tE_2\nu_1}{\nu_2(1 + \nu_2)(1 - \nu_1)R} + \frac{hE_1}{2(1 - \nu_1^2)R} \right) \exp\left(-\frac{\nu_1 h}{2(1 - \nu_1)R}\right)$$

for  $0 \leq y \leq h/2$  and by

$$C = \left( \frac{\nu_1 E_1 \varepsilon_z}{1 - \nu_1^2} + \sigma_{01} + \frac{E_1}{\nu_1(1 + \nu_1)} + \frac{t\nu_1}{(1 - \nu_1)R} B - \frac{tE_2\nu_1}{\nu_2(1 + \nu_2)(1 - \nu_1)R} - \frac{hE_1}{2(1 - \nu_1^2)R} \right) \exp\left(-\frac{\nu_1 h}{2(1 - \nu_1)R}\right)$$

for  $-h/2 \leq y \leq 0$ ; in either case, we have

$$C \approx \frac{\nu_1 E_1 \varepsilon_z}{1 - \nu_1^2} + \frac{\nu_1^2 E_1 \varepsilon_z h}{2(1 - \nu_1)(1 - \nu_1^2)R} + \sigma_{01} + \frac{E_1}{\nu_1(1 + \nu_1)} \quad (-h/2 \leq y \leq h/2).$$

(Here we have used (1), (7), (9) and the relationships  $\sigma_1^z(y) = E_1 \varepsilon_z + \nu_1 \sigma_1^x(y) + \nu_1 \sigma_1^y(y)$  (valid for  $-h/2 \leq y \leq h/2$ ) and  $\varepsilon_1^x(y) = y/R = (1/E_1)(\sigma_1^x - \nu_1 \sigma_1^z - \nu_1 \sigma_1^y)$ .)

Therefore, the change of the stress in the  $x$  direction within the symmetric trilayer plate after the application of the external pure bending moment  $M$  is

$$\sigma^x(y) = \begin{cases} A \exp \frac{v_2 y}{(1-v_2)R} - \frac{E_2}{v_2(1+v_2)} - \sigma_{02} & (h/2 \leq y \leq t+h/2), \\ C \exp \frac{v_1 y}{(1-v_1)R} - \frac{E_1}{v_1(1+v_1)} - \sigma_{01} & (-h/2 \leq y \leq h/2), \\ B \exp \frac{v_2 y}{(1-v_2)R} - \frac{E_2}{v_2(1+v_2)} - \sigma_{02} & (-t-h/2 \leq y \leq -h/2), \end{cases} \quad (12)$$

which can be rewritten as

$$\sigma^x(y) = \frac{v_2 E_2 \varepsilon_z}{1-v_2^2} - \frac{v_2^2 E_2 \varepsilon_z (h+2t)}{2(1-v_2)(1-v_2^2)R} + \frac{v_2^2 E_2 \varepsilon_z y}{(1-v_2)(1-v_2^2)R} - \frac{v_2 \sigma_{02}}{(1-v_2)R} \left( \frac{h}{2} + t - y \right) + \frac{E_2 y}{(1-v_2^2)R}$$

for  $h/2 \leq y \leq t+h/2$ ,

$$\sigma^x(y) = \frac{v_1 E_1 \varepsilon_z}{1-v_1^2} + \frac{v_1^2 E_1 \varepsilon_z h}{2(1-v_1)(1-v_1^2)R} + \frac{v_1^2 E_1 \varepsilon_z y}{(1-v_1)(1-v_1^2)R} + \frac{v_1 \sigma_{01}}{(1-v_1)R} y + \frac{E_1 y}{(1-v_1^2)R}$$

for  $-h/2 \leq y \leq h/2$ , and

$$\sigma^x(y) = \frac{v_2 E_2 \varepsilon_z}{1-v_2^2} + \frac{v_2^2 E_2 \varepsilon_z (h+2t)}{2(1-v_2)(1-v_2^2)R} + \frac{v_2^2 E_2 \varepsilon_z y}{(1-v_2)(1-v_2^2)R} + \frac{v_2 \sigma_{02}}{(1-v_2)R} \left( \frac{h}{2} + t + y \right) + \frac{E_2 y}{(1-v_2^2)R}$$

for  $-t-h/2 \leq y \leq -h/2$ .

Now we look at the amplitude of the strain change in the  $z$  direction  $\varepsilon_z$ . The cylindrical bending condition requires a zero resultant force in the  $z$  direction

$$F_z = \int_{R-t-h/2}^{R+t+h/2} r \sigma^z dr = 0. \quad (13)$$

Substituting (2), (12) and  $\sigma_1^z(y) = E_1 \varepsilon_z + v_1 \sigma_1^x(y) + v_1 \sigma_1^y(y)$  into (13), one has

$$\begin{aligned} F_z &= \int_{R-t-h/2}^{R+t+h/2} r \sigma^z dr \\ &= 2t E_2 \varepsilon_z R + h E_1 \varepsilon_z R + v_2 \int_{R-t-h/2}^{R+t+h/2} (\sigma^x + \sigma^y) r dr + (v_1 - v_2) \int_{R-h/2}^{R+h/2} (\sigma_1^x + \sigma_1^y) r dr. \end{aligned} \quad (14)$$

Here  $r = R + y$ . It is easy to verify that

$$v_2 \int_{R-t-h/2}^{R+t+h/2} (\sigma^x + \sigma^y) r dr = v_2 r^2 \sigma^y \Big|_{y=-t-h/2}^{y=t+h/2} = 0, \quad (15)$$

as there is no traction on the outside surface of the top and the bottom layers, and

$$(v_1 - v_2) \int_{R-h/2}^{R+h/2} (\sigma_1^x + \sigma_1^y) r dr = \frac{v_1 - v_2}{2} r^2 \sigma^y \Big|_{y=-h/2}^{y=h/2}. \quad (16)$$

Substituting (14)–(16) into (13) and ignoring the terms of order higher than  $1/R$ , one has

$$\varepsilon_z = \frac{\frac{\nu_2(\nu_1 - \nu_2)(1 + 2t/h)}{1 - \nu_2} \frac{\sigma_{02} t}{E_2 R}}{8t/h + \frac{4E_1}{E_2} - \frac{2\nu_2(1 - \nu_2)t}{(1 - \nu_2^2)R} + \frac{2(\nu_1 - \nu_2)\nu_2^2(1 + 2t/h)t}{(1 - \nu_2)(1 - \nu_2^2)R}} \approx \frac{\nu_2(\nu_1 - \nu_2)(1 + 2t/h)}{(8t/h + 4E_1/E_2)(1 - \nu_2)^2} \cdot \frac{t}{R} \varepsilon_{02}, \quad (17)$$

where  $\varepsilon_{02} = \sigma_{02}(1 - \nu_2)/E_2$  is the initial elastic residual strain in the top or bottom layer before the application of the bending moment  $M$ . Equation (17) shows clearly that  $\varepsilon_z$  is zero if  $\nu_1 = \nu_2$ . As  $t/R$  is very small,  $|\varepsilon_z| \ll |\varepsilon_{02}|$  when  $\nu_1 \neq \nu_2$ , it will be set equal to zero to simplify the analysis that follows.

The total stress in the  $x$  direction within the symmetric trilayer plate after the application of the external pure bending moment  $M$  is given by superposition

$$\Sigma^x(y) = \sigma^x(y) + \begin{cases} \sigma_{02} \\ \sigma_{01} \\ \sigma_{02} \end{cases}$$

$$= \begin{cases} \sigma_{02} - \frac{\nu_2 \sigma_{02}}{(1 - \nu_2)R} \left( \frac{h}{2} + t - y \right) + \frac{E_2 y}{(1 - \nu_2^2)R} & (h/2 \leq y \leq t + h/2), \\ \sigma_{01} + \frac{\nu_1 \sigma_{01}}{(1 - \nu_1)R} y + \frac{E_1 y}{(1 - \nu_1^2)R} & (-h/2 \leq y \leq h/2), \\ \sigma_{02} + \frac{\nu_2 \sigma_{02}}{(1 - \nu_2)R} \left( \frac{h}{2} + t + y \right) + \frac{E_2 y}{(1 - \nu_2^2)R} & (-t - h/2 \leq y \leq -h/2). \end{cases} \quad (18)$$

It is easy to verify the following facts:

- There is no net resultant axial force in the trilayer plate in the  $x$  direction:  $N_x = \int_{-t-h/2}^{t+h/2} \Sigma^x(y) dy = 0$ .
- The stress in the radial direction (the  $y$  direction in Figure 1), given by

$$\sigma^y(y) = -\frac{1}{R} \int_y^{t+h/2} \Sigma^x(y) dy$$

(the equilibrium condition in the  $y$  direction), satisfies the stress continuity condition across the neutral surface and the interfaces between the middle and the surface layers.

- There is no traction in the  $y$  direction on both the top and bottom surfaces; that is,  $\sigma_2^y(t + h/2) = \sigma_2^y(-t - h/2) = 0$ .

For a given bending curvature  $1/R$ , we are now in a position to compute the amplitude of the applied bending moment

$$M = \int_{-t-h/2}^{t+h/2} \Sigma^x(y) y dy. \quad (19)$$

Substituting (18) into (19), the bending stiffness of the prestressed symmetric trilayer plate can be obtained as

$$D = M/(1/R) = \frac{E_2((h + 2t)^3 - h^3)}{12(1 - \nu_2^2)} + \frac{E_1 h^3}{12(1 - \nu_1^2)} + \frac{\nu_1 \sigma_{01} h^3}{12(1 - \nu_1)} - \frac{\nu_2 \sigma_{02} t^2 (3h + 2t)}{6(1 - \nu_2)}. \quad (20)$$

When the initial residual stresses  $\sigma_{02}$  and  $\sigma_{01}$  are absent, the bending stiffness of the symmetric trilayer plate is denoted by

$$D_0 = \frac{E_2((h+2t)^3 - h^3)}{12(1-\nu_2^2)} + \frac{E_1 h^3}{12(1-\nu_1^2)}. \quad (21)$$

From equations (20) and (21), the contribution of the initial residual stresses to the bending stiffness of a symmetric trilayer plate is therefore

$$\begin{aligned} D - D_0 &= \frac{\sigma_{01}}{12} \left( \frac{\nu_1 h^3}{1-\nu_1} + \frac{\nu_2 t h (3h+2t)}{1-\nu_2} \right) = \frac{E_1 \varepsilon_{01}}{12(1-\nu_1)} \left( \frac{\nu_1 h^3}{1-\nu_1} + \frac{\nu_2 t h (3h+2t)}{1-\nu_2} \right) \\ &= -\frac{\sigma_{02}}{6} \left( \frac{\nu_1 t h^2}{1-\nu_1} + \frac{\nu_2 t^2 (3h+2t)}{1-\nu_2} \right) = -\frac{E_2 \varepsilon_{02}}{6(1-\nu_2)} \left( \frac{\nu_1 t h^2}{1-\nu_1} + \frac{\nu_2 t^2 (3h+2t)}{1-\nu_2} \right). \end{aligned} \quad (22)$$

Equation (1) has been used in obtaining (22), where  $\varepsilon_{01} = (1-\nu_1)\sigma_{01}/E_1$  and  $\varepsilon_{02} = (1-\nu_2)\sigma_{02}/E_2$  are the initial residual strains within the middle and extreme layers. Equation (22) shows clearly that an initial tensile residual stress or strain (that is,  $\varepsilon_{01} > 0$ ) in the middle layer increases the bending stiffness of a trilayer plate. If the plate is made of a metallic material, the initial effective residual stresses should be smaller than the yield strength of the metal. According to the von Mises yield criterion, one has

$$|\varepsilon_{01}| = (1-\nu_1)|\sigma_{01}|/E_1 \leq (1-\nu_1)\sigma_{y1}/E_1 = (1-\nu_1)\varepsilon_{y1} \quad (23a)$$

and likewise

$$|\varepsilon_{02}| \leq (1-\nu_1)\varepsilon_{y2}. \quad (23b)$$

Equations (22) and (18) can be used to optimize the design and to determine experimentally the residual stresses or material properties for symmetric trilayer structures such as thermal barrier coated engine blades. Equations (23a) and (23b) give the limits for the possible amplitude of the initial residual elastic strains in symmetric trilayer structures. However, if a trilayer structure is made of a hyper-elastic material, such as a polymer or a rubber, the initial linear elastic residual strain could be as large as a few percent.

Now we consider the pure bending of a symmetric trilayer beam with a rectangular cross-section. The structure, the coordinate system, the initial residual stresses and strains of the unbent symmetric trilayer beam are the same as those of the unbent symmetric trilayer plate. The only difference is its width dimension in the  $z$  direction of Figure 1. When it is bent by a pure moment, the deformation is assumed to satisfy the plane stress condition. Following the above analysis procedure, it can be shown that the total stresses in the  $x$  direction within the trilayer beam are

$$\Sigma^x(y) = \begin{cases} \sigma_{02} - \frac{\nu_2 \sigma_{02}}{R} \left( \frac{h}{2} + t - y \right) + \frac{E_2 y}{R} & (h/2 \leq y \leq t + h/2), \\ \sigma_{01} + \frac{\nu_1 \sigma_{01}}{R} y + \frac{E_1 y}{R} & (-h/2 \leq y \leq h/2), \\ \sigma_{02} + \frac{\nu_2 \sigma_{02}}{R} \left( \frac{h}{2} + t + y \right) + \frac{E_2 y}{R} & (-t - h/2 \leq y \leq -h/2). \end{cases} \quad (24)$$

The bending stiffness of the prestressed beam is therefore

$$D = \frac{E_2((h+2t)^3 - h^3)}{12} + \frac{E_1 h^3}{12} + \frac{\nu_1 \sigma_{01} h^3}{12} - \frac{\nu_2 \sigma_{02} t^2 (3h+2t)}{6}. \quad (25)$$

When the initial residual stresses  $\sigma_{02}$  and  $\sigma_{01}$  are absent, the bending stiffness of the symmetric trilayer beam is denoted as

$$D_0 = \frac{E_2((h+2t)^3 - h^3)}{12} + \frac{E_1 h^3}{12}. \quad (26)$$

The effect of the initial residual stresses on the bending stiffness is

$$D - D_0 = \frac{\nu_1 \sigma_{01} h^3}{12} - \frac{\nu_2 \sigma_{02} t^2 (3h + 2t)}{6}. \quad (27)$$

Obviously, the relative effect of the initial residual stresses on the bending stiffness of a symmetric trilayer beam is at the same level as on that of a symmetric trilayer plate discussed above.

Following the line of the analysis in this paper or in [Zhu 2007], it is possible to obtain the exact closed-form analytical solution for large curvature elastic pure bending of the same structure. However, as the exact solution is a very lengthy function, it is not convenient to use in practice. Although it is easy to obtain a numerical solution for large curvature elastic bending, it is difficult to see the correlations between the different parameters such as the structure dimensions, the material properties and the initial residual stresses (or strains). That is why we have simplified the analysis above to obtain a simple closed-form solution for small curvature.

The simplified closed-form solution is valid not only for macro civil structures, but also for micro- and nanostructures. The schematic symmetric trilayer structure shown in Figure 1 is one of the most typical structures of microactuators. For example, a typical conducting polymeric actuator consists of a polymer membrane (usually, Nafion, Flemion or Aciplex) covered on both faces by a noble metal, generally platinum or gold [Nemat-Nasser 2002; Alici et al. 2005]. When the actuator is stimulated by the application of a small (1–3 V) alternating potential, it undergoes flexural vibrations [Nemat-Nasser 2002]. The precision, resolution and reliability of such a MEMS system mainly depend on its mechanical structure. The outcome of this paper provides an enhanced degree of understanding and predictability in quantifying the actuator's performance and hence paves the way towards the optimal design and precise experimental measurement of such structures.

### 3. Pure bending of a nanoplate/nanobeam

For nanostructures, as the surface to volume ratio is large, the surface elasticity, in addition to any residual surface stresses, plays a very important role in the deformation process [Cuenot et al. 2004; Duan et al. 2005a; 2005b; 2006; Chen et al. 2006; Wang et al. 2006; Zhu and Karihaloo 2008]. In continuum models, nanoplates are usually treated as “sandwich structures” consisting of the bulk material and very thin facets [He et al. 2004; Lim and He 2004; Miller and Shenoy 2000; Lu et al. 2006]. The linear constitutive relation of the surface can be written as [Miller and Shenoy 2000; Cammarata and Sieradzki 1994]

$$\tau_{ij} = \tau_{ij}^0 + S_{ijkl} \varepsilon_{kl}, \quad (28)$$

where  $\tau_{ij}$  is the surface stress after deformation,  $\tau_{ij}^0$  is the initial stress before deformation,  $S_{ijkl}$  is the surface modulus tensor and  $\varepsilon_{kl}$  is the surface strain. The surface stress and surface elastic constants have reduced dimensionality. It has been found that the effect of surface elastic modulus on the stiffness of nanostructures is size-dependent. The effect of surface elasticity on the mechanical properties of materials and structures has been extensively studied [Miller and Shenoy 2000; Lu et al. 2006; Gurtin

and Murdoch 1975], and the relative contribution of the surface elasticity to the bending stiffness of a nanoplate has been found to be  $6S/(Eh)$ , where  $S$  is the surface elastic modulus,  $E$  is the Young's modulus of the bulk material and  $h$  is the thickness of the nanoplate [Miller and Shenoy 2000]. This contribution does not include the effect of any initial surface stress.

For a nanoplate, the surfaces are notionally assumed so only in a mathematical sense, whose thickness  $t$  is much smaller than the thickness  $h$  of the core of the plate. In this case, we still use Figure 1 as the structural model and the stresses are assumed not to change through thickness of the top and the bottom surfaces. Similarly to the macroplate, we assume that when the nanoplate is bent to a very small curvature  $1/R$  ( $R$  is much larger the plate thickness  $h$ ) by a pure bending moment, both the "surface" and the bulk material are linear elastic; and the thickness of the nanoplate remains unchanged. Obviously the original cross-sectional planes remain plane as there is no net shear force in the cross-sectional planes. It is easy to verify that the neutral surface is still in the middle of the bulk plate. Therefore, the stresses in the  $x$  direction in the top and bottom surfaces are respectively

$$\tau_t^x = \tau_0 + \frac{S}{1 - \nu_2^2} \frac{h}{2R} \quad (\text{N/m}) \quad \text{and} \quad \tau_b^x = \tau_0 - \frac{S}{1 - \nu_2^2} \frac{h}{2R} \quad (\text{N/m}), \quad (29)$$

where  $\tau_0$  is the initial surface stress,  $S$  is the surface elastic modulus and  $\nu_2$  is the Poisson ratio of the surfaces.

The stresses in the  $y$  direction on the top and bottom interfaces of bent bulk plate are respectively

$$\sigma_1^y|_{y=h/2} = -\frac{\tau_t^x}{R} \approx -\frac{\tau_0}{R} \quad \text{and} \quad \sigma_1^y|_{y=-h/2} = \frac{\tau_b^x}{R} \approx \frac{\tau_0}{R}. \quad (30)$$

In the similar manner, it is easy to verify that (10) is still the governing differential equation for the stress change in the  $x$  direction within the bulk plate. The solution to the stress change in the  $x$  direction within the bulk plate is the same as (11), but the constant of integration  $C$  is determined by making use of the stress continuity conditions (30) in the radial direction across the top and bottom interfaces,

$$C = \sigma_{01} + \frac{E_1}{\nu_1(1 + \nu_1)} \quad (-h/2 < y < h/2). \quad (31)$$

As before, the exponential function has been replaced by a polynomial function with the terms of order higher than  $1/R$  ignored, and the equilibrium condition  $\sigma_{01} = -\frac{2\tau_0}{h}$  has been used in deriving the solution. Therefore the total stress in the  $x$  direction within the bulk plate after the application of the external pure bending moment  $M$  is given by superposition

$$\Sigma^x(y) = -\frac{2\tau_0}{h} - \frac{2\nu_1\tau_0}{(1 - \nu_1)h} \frac{y}{R} + \frac{E_1 y}{(1 - \nu_1^2)R} \quad (-h/2 < y < h/2). \quad (32)$$

On the top and the bottom surfaces, the surface stresses are given in (29).

The applied pure bending moment can be calculated as

$$M = \frac{Sh^2}{2(1 - \nu_2^2)R} + \int_{-h/2}^{h/2} \Sigma^x(y) y dy$$

and the bending stiffness of a nanoplate is therefore

$$D = \frac{Sh^2}{2(1-\nu_2^2)} + \frac{E_1h^3}{12(1-\nu_1^2)} - \frac{\nu_1\tau_0h^2}{6(1-\nu_1)}. \quad (33)$$

Since  $D_0 = \frac{1}{12}E_1h^3/(1-\nu_1^2)$  is conventionally taken as the bending stiffness of a nanoplate when the surface effect is absent, the relative contribution of the initial residual surface stress  $\tau_0$  and the surface elasticity to the elastic bending capacity is therefore

$$\frac{D-D_0}{D_0} = \frac{6S(1-\nu_1^2)}{(1-\nu_2^2)E_1h} - \frac{2\tau_0\nu_1(1+\nu_1)}{E_1h} = \frac{6(1-\nu_1^2)}{(1-\nu_2^2)} \cdot \frac{\ell_n}{h} + \frac{\nu_1(1+\nu_1)}{1-\nu_1}\varepsilon_{01}, \quad (34)$$

where

$$\varepsilon_{01} = \frac{(1-\nu_1)\sigma_{01}}{E_1} = -\frac{2(1-\nu_1)\tau_0}{E_1h}$$

is the initial elastic residual strain within the core of the nanoplate and  $\ell_n = S/E_1$  is an intrinsic length scale. Since the plate is in an elastic state, according to the Mises yield criterion, (23a) gives the limit for the possible maximum elastic residual strain  $\varepsilon_{01}$  for the plate bulk material. This is because first, the surface stress of a nanoelement depends on the applied electric potential [Haiss et al. 1998]; second, the deformation (hence the bending stiffness) can be controlled by adjusting the applied electric potential [Weissmüller et al. 2003; Kramer et al. 2004]; third, the maximum residual elastic strain (or the maximum residual elastic stress) is limited by the yield strength [Diao et al. 2006].

Equation (34) gives a linear scaling law for the normalized bending stiffness ( $D/D_0$ ) of a nanoplate. Similar scaling has been previously observed in many physical properties at the nanoscale [Wang et al. 2006]. It shows that the thinner a nanoplate is, the larger its normalized bending stiffness will be. The first term of (34) is the relative effect of surface elasticity on the bending stiffness of a nanoplate. If the Poisson ratio of the surface is the same as that of the bulk material (that is,  $\nu_2 = \nu_1$ ), this term is identical to Miller and Shenoy's analytical result for a nanoplate [Miller and Shenoy 2000]. The second term quantifies the relative effect of the initial surface stress on the bending stiffness of a nanoplate.

Equation (34) can be rewritten as

$$\frac{D-D_0}{D_0} = \frac{6S(1-\nu_1^2)}{(1-\nu_2^2)E_1h} - \frac{\tau_0}{E_1h}F(\nu_1),$$

where

$$F(\nu_1) = 2\nu_1(1+\nu_1). \quad (35)$$

For normal metallic nanoplates, the initial surface stress  $\tau_0$  is of the same order of the surface modulus  $S$  [Cammarata and Sieradzki 1994]. Atomistic simulations show that the surface modulus and the initial surface stress of a nanofilm can be either positive or negative [Miller and Shenoy 2000; Gurtin et al. 1976]. Equation (34) shows that an initial tensile surface stress tends to reduce the bending stiffness of a nanoplate.

Based on continuum elasticity, supplemented by surface elasticity [Miller and Shenoy 2000; Gurtin and Murdoch 1975] we have performed a number of numerical simulations on the pure bending of a nanoplate to validate the analytical predictions obtained in this paper. Firstly, we have numerically confirmed that when the initial surface stress is absent the analytical result of (34) (or Miller and Shenoy's



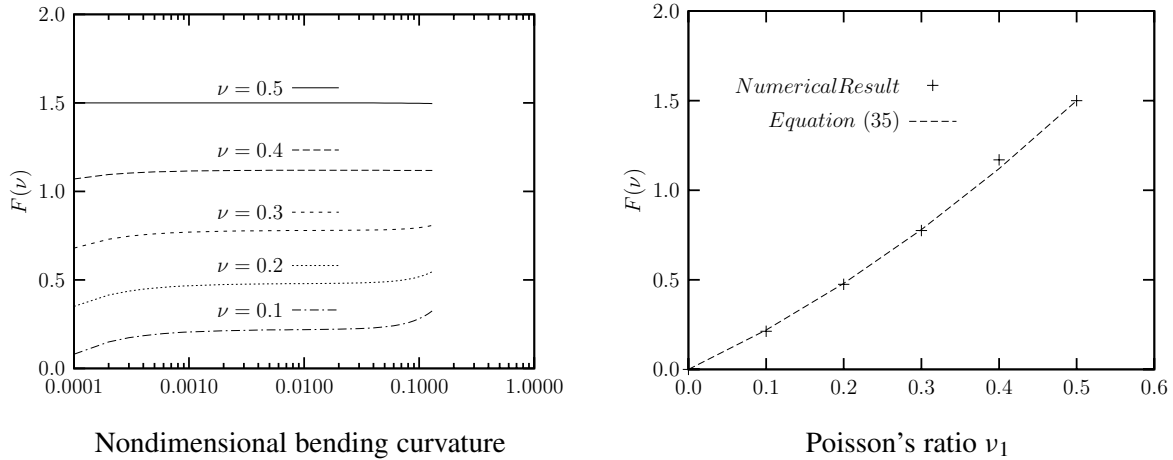


**Figure 2.** Comparison of the simplified analytical prediction with numerical simulations:  $F$  versus nondimensional bending curvature  $1/R$  (left), and versus the Poisson's ratio  $\nu_1$  (right).

analytical result [Miller and Shenoy 2000]) provides exact predictions. Secondly, when the surface elasticity is ignored (that is,  $S = 0$ ) and the Poisson ratio of the core material is fixed ( $\nu_1 > 0$ ), the relative effect of the initial surface stress on the bending stiffness of a nanoplate is proportional to  $\tau_0/(E_1 h)$ , as predicted by (34). Thirdly, when the value of  $\tau_0/(E_1 h)$  is fixed, the relative effect of the initial surface stress  $\tau_0$  on the bending stiffness of a nanoplate is a function of the Poisson ratio of the core material  $\nu_1$ , as shown is in Figure 2. The left half of the figure shows that  $F(\nu_1)$  is almost a constant over the normalized bending curvatures ranging from 0.0005 to 0.05 for a fixed value of  $\nu_1$  (the normalized bending curvature is  $h/R$ ). We see on the right that the numerical result  $F(\nu_1)$  is nearly identical to that of analytical prediction in (35). Although the analytical results obtained in this paper are derived from the small deformation theory, the numerical tests (Figure 2) provide us with sufficient confidence that the analytical results can be used in optimal design or experimental measurements for deformations up to a normalized bending curvature of 0.1 (that is,  $h/R = 0.1$ ). Beyond this value of curvature, deviations occur as a result of the plate thickness reduction [Zhu 2007]. Note that the analytical results obtained in this section can be mathematically deduced from the analysis of the previous section (see Equation (20)) when the thickness  $t$  of the top and the bottom layers tends to zero. However, we have not been tempted by this limiting process as it would require us to relate the bulk elastic constant  $E$  to the surface modulus  $S$ , whereas there is no reason why such a relationship should exist.

For a nanobeam with a rectangular cross-section of thickness  $h$  and width  $b$ , as shown in Figure 3, left, the initial axial residual stress is  $\sigma_0^x = -2\tau_0/h - 2\tau_0/b$ , where  $\tau_0$  is the initial surface stress. When this nanobeam is bent by a pure moment, a plain stress deformation mode is created. Following the above analysis procedure, the total stress within the bulk material of the nanobeam in the axial direction can be calculated as

$$\Sigma^x(y) = \frac{E_1}{R} y - \frac{\nu_1 \tau_0}{R} - \frac{\nu_1 \sigma_0^x}{2R} (h - 2y) + \sigma_0^x \quad (36)$$

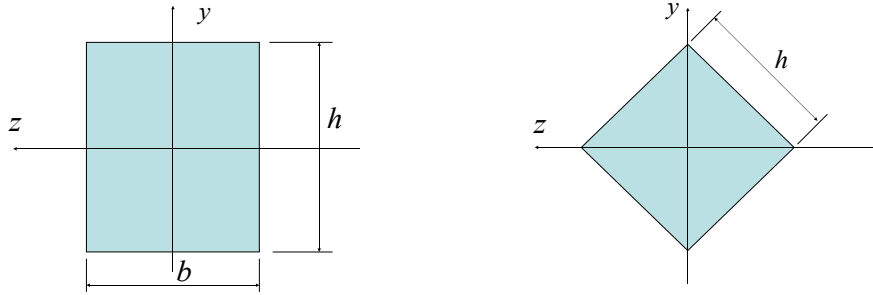


**Figure 3.** Left: a rectangular cross-section with the neutral axis  $z$  parallel to the sides. Right: a square cross-section with the neutral axis  $z$  coincided to the diagonal.

and the total surface stress in the  $x$  direction can be obtained as

$$\tau^x(y, z) = \begin{cases} \tau_0 + Sh/(2R) & (y = h/2 \text{ and } 0 < z < b), \\ \tau_0 + \frac{Sy}{R} - \frac{\nu_1 \tau_0 h}{2R} - \frac{\nu_1 \tau_0}{R} y & (-h/2 \leq y \leq h/2 \text{ and } z = 0 \text{ or } b), \\ \tau_0 - Sh/(2R) & (y = -h/2 \text{ and } 0 < z < b), \end{cases} \quad (37)$$

where the Poisson ratio of the surface is assumed to be the same as that of the bulk material.

The elastic bending capacity is

$$\begin{aligned} M &= \frac{Sbh^2}{2R} + \int_{-h/2}^{h/2} 2 \left( \frac{S}{R} y - \frac{\nu_1 \tau_0}{R} y \right) y dy + \int_{-h/2}^{h/2} \Sigma^x(y) by dy \\ &= \frac{Sbh^2}{2R} + \frac{Sh^3}{6R} - \frac{\nu_1 \tau_0 h^3}{6R} + \frac{E_1 bh^3}{12R} + \frac{\nu_1 \sigma_0^x}{12R} bh^3. \end{aligned} \quad (38)$$

Therefore the bending stiffness of the nanobeam is

$$D = M/(1/R) = \frac{Sbh^2}{2R} + \frac{Sh^3}{6R} - \frac{\nu_1 \tau_0 h^3}{6R} + \frac{E_1 bh^3}{12} + \frac{\nu_1 \sigma_0^x}{12} bh^3. \quad (39)$$

As the bending stiffness of the bulk beam is  $D_0 = E_1 bh^3/12$ , the relative effect of the initial surface stress and the surface elasticity is

$$\begin{aligned} \frac{D - D_0}{D_0} &= \frac{6S}{E_1 h} + \frac{2S}{E_1 b} + \frac{\nu_1 \sigma_0^x}{E_1} - \frac{2\nu_1 \tau_0}{E_1 b} \\ &= \frac{6\ell_n}{h} + \frac{2\ell_n}{b} - \frac{4\nu_1 \tau_0}{E_1 b} - \frac{2\nu_1 \tau_0}{E_1 h} = \frac{6\ell_n}{h} + \frac{2\ell_n}{b} + \frac{(2h+b)\nu_1}{(b+h)(1-\nu_1)} \varepsilon_0^x, \end{aligned} \quad (40)$$

where, as before the internal length parameter  $\ell_n = S/E_1$ , and

$$\varepsilon_0^x = \frac{1}{E_1} (\sigma_0^x - \nu_1 \sigma_0^y - \nu_1 \sigma_0^z) = -\frac{2\tau_0}{E_1 bh} (b+h)(1-\nu_1) \quad (41)$$

is the initial residual elastic strain in the bulk nanobeam in the  $x$  direction. According to the Mises yield criterion,

$$|\varepsilon_0^x| \leq \frac{(b+h)(1-\nu_1)}{\sqrt{b^2+h^2-bh}} \varepsilon_y, \quad (42)$$

where  $\varepsilon_y$  is the uniaxial yield strain of the beam bulk material.

For a nanobeam with a square cross-section (that is,  $b = h$ ), Equation (40) reduces to

$$\frac{D - D_0}{D_0} = \frac{8l_n}{h} - \frac{6\nu_1\tau_0}{E_1h} = \frac{8l_n}{h} + \frac{3\nu_1}{2(1-\nu_1)} \varepsilon_0^x. \quad (43)$$

The first term in (43) is identical to Miller and Shenoy's analytical result (namely  $(D - D_0)/D_0 = 8S/(Eh) = 8\ell_n/h$ ) for a nanobeam with a rectangular cross-section in the absence of the initial stress [Miller and Shenoy 2000]. Metallic nanomaterials can be used to make nanoactuators and the initial surface stress  $\tau_0$  can be controlled by the application of an electric potential [Haiss et al. 1998; Weissmüller et al. 2003; Kramer et al. 2004]. Equations (34) and (40) show that the effect of surface elasticity  $S$  on the bending stiffness of a nanoplate or nanobeam vanishes when its thickness  $h$  reaches about 100 nm, while the effect of the initial residual stress is proportional to  $\varepsilon_0$  which could be retained at a level up to a few percent by the application of an electric potential even for microplates and beams. Equations (34) and (40) provide a reliable estimate of the combined effects of surface elasticity  $S$  and initial surface stress  $\tau_0$  on the bending stiffness (and hence the dynamic characteristics) of nanoplates and nanobeams. It has important applications both in the optimal design of nanostructures and in the measurement of their characteristics.

For completeness, we will also give, without details, the effect of initial surface stress and surface elasticity on the stiffness, if a nanobeam with square section of side length  $h$  is bent about a diagonal plane as shown in Figure 3, right,

$$\frac{D - D_0}{D_0} = \frac{4\sqrt{2}l_n}{h} + \frac{\nu_1\sigma_0^x}{E_1} = \frac{4\sqrt{2}l_n}{h} + \frac{\nu_1}{(1-\nu_1)} \varepsilon_0^x. \quad (44)$$

In this case, the effect of the surface elasticity on the bending stiffness, given by the first term of (44), is smaller than that given by [Miller and Shenoy 2000].

For either a nanoplate/nanobeam or a macro symmetric trilayer plate/beam, we assume that its bending stiffness and natural frequency are respectively  $D_0$  and  $\omega_0$  when the initial residual stress and the surface elasticity (for nanoplate/nanobeam) are absent; and  $D$  and  $\omega$  when the initial residual stress and the surface elasticity (for nanoplate/nanobeam) are present. The combined effect of the initial residual stress and the surface elasticity for nanoplate/nanobeam on its natural frequency therefore scales as

$$\omega/\omega_0 = (D/D_0)^{1/2}. \quad (45)$$

Lagowski et al. [1975] found experimentally that the normal mode of vibration of thin crystals depends strongly on the surface preparation. They related this to the initial surface stress effect, which was treated as an external force. However, Gurtin et al. [1976] argued that the combination of the initial surface stress and the residual stress in the bulk material would cancel their individual effects. They attributed the dependence of the normal mode of vibration of thin crystals on surface preparation to surface elasticity. We have shown conclusively that the dynamic response depends both on the initial

residual stress in the surfaces and the bulk and on surface elasticity at the nanoscale. Wang and Feng [2007] have also considered the combined effects of surface elasticity and residual surface tension on the natural frequency of microbeams. However, as they did not take into account the effect of the residual stress in the bulk material, their result is suspect.

#### 4. Conclusion

A simple closed-form analytical solution identifying the effect of initial residual stresses (or strains) on the bending stiffness of a symmetric trilayer structure or a nanoplate/nanobeam has been obtained. At the macro- and microscales, the relative effect is at the level of the initial elastic residual strain. If the structure is made of a hyperelastic material (such as a conducting polymer) and the initial elastic residual stress (or strain) is controllable, the relative effect of the initial stress (or strain) could reach a few percent. At the nanoscale, if the thickness of the nanoplate/nanobeam is around 10 nm or smaller, then the surface elasticity rather than the initial surface stress generally has a stronger relative effect on the bending stiffness. The surface elasticity effect however reduces with an increase in the plate/beam thickness, but the initial surface stress effect can be retained at a constant level of up to the limit of elastic strain if it can be controlled, for example by the application of an electrical potential.

#### References

- [Alici et al. 2005] G. Alici, P. Metz, and G. M. Spinks, "A mathematical model to describe bending mechanics of polypyrrole (PPy) actuators", pp. 1029–1034 in *Proceedings of the 2005 IEEE/ASME International Conference on Advanced Intelligent Mechatronics* (Monterey, CA, 2005), IEEE, Piscataway, NJ, 2005.
- [Bunch et al. 2007] J. S. Bunch, A. M. Van der Zande, S. S. Verbridge, I. W. Frank, D. M. Tanenbaum, J. M. Parpia, H. G. Craighead, and P. L. McEuen, "Electromechanical resonators from grapheme sheets", *Science* **315**:5811 (2007), 490–493.
- [Cammarata and Sieradzki 1994] R. C. Cammarata and K. Sieradzki, "Surface and interface stresses", *Annu. Rev. Mater. Sci.* **24** (1994), 215–234.
- [Chen et al. 2006] C. Q. Chen, Y. Shi, Y. S. Zhang, J. Zhu, and Y. J. Yan, "Size dependence of Young's modulus in ZnO nanowires", *Phys. Rev. Lett.* **96**:7 (2006), 075505.
- [Cuenot et al. 2004] S. Cuenot, C. Fréty, S. Demoustier-Champagne, and B. Nysten, "Surface tension effect on the mechanical properties of nanomaterials measured by atomic force microscopy", *Phys. Rev. B* **69**:16 (2004), 165410.
- [Diao et al. 2006] J. Diao, K. Gall, M. L. Dunn, and J. A. Zimmerman, "Atomistic simulations of the yielding of gold nanowires", *Acta Mater.* **54**:3 (2006), 643–653.
- [Dodin et al. 2001] M. Dodin, V. Tabard-Cossa, P. Grütter, and P. Williams, "Quantitative surface stress measurements using a microcantilever", *Appl. Phys. Lett.* **79**:4 (2001), 551–553.
- [Donadon et al. 2002] M. V. Donadon, S. F. M. Almeida, and A. R. de Faria, "Stiffening effects on the natural frequencies of laminated plates with piezoelectric actuators", *Compos. B Eng.* **33**:5 (2002), 335–342.
- [Duan et al. 2005a] H. L. Duan, J. Wang, Z. P. Huang, and B. L. Karihaloo, "Eshelby formalism for nano-inhomogeneities", *Proc. R. Soc. Lond. A* **461**:2062 (2005), 3335–3353.
- [Duan et al. 2005b] H. L. Duan, J. Wang, Z. P. Huang, and B. L. Karihaloo, "Size-dependent effective elastic constants of solids containing nano-inhomogeneities with interface stress", *J. Mech. Phys. Solids* **53**:7 (2005), 1574–1596.
- [Duan et al. 2006] H. L. Duan, J. Wang, B. L. Karihaloo, and Z. P. Huang, "Nanoporous materials can be made stiffer than non-porous counterparts by surface modification", *Acta Mater.* **54**:11 (2006), 2983–2990.
- [Freund 2000] L. B. Freund, "Substrate curvature due to thin film mismatch strain in the nonlinear deformation range", *J. Mech. Phys. Solids* **48**:6–7 (2000), 1159–1174.

- [Freund and Johnson 2001] L. B. Freund and H. T. Johnson, "Influence of strain on functional characteristics of nanoelectric devices", *J. Mech. Phys. Solids* **49**:9 (2001), 1925–1935.
- [Gurtin and Murdoch 1975] M. E. Gurtin and A. I. Murdoch, "A continuum theory of elastic material surfaces", *Arch. Ration. Mech. An.* **57**:4 (1975), 291–313.
- [Gurtin et al. 1976] M. E. Gurtin, X. Markenscoff, and R. N. Thurston, "Effect of surface stress on the natural frequency of thin crystals", *Appl. Phys. Lett.* **29**:9 (1976), 529–530.
- [Haiss et al. 1998] W. Haiss, R. J. Nichols, J. K. Sass, and K. P. Charle, "Linear correlation between surface stress and surface charge in anion adsorption on Au(111)", *J. Electroanal. Chem.* **452**:2 (1998), 199–202.
- [He et al. 2004] L. H. He, C. W. Lim, and B. S. Wu, "A continuum model for size-dependent deformation of elastic films of nano-scale thickness", *Int. J. Solids Struct.* **41**:3–4 (2004), 847–857.
- [Huang and Zhang 2006] S. S. Huang and X. Zhang, "Extension of the Stoney formula for film-substrate systems with gradient stress for MEMS applications", *J. Micromech. Microeng.* **16**:2 (2006), 382–389.
- [Huang and Zhang 2007] S. S. Huang and X. Zhang, "Gradient residual stress induced elastic deformation of multilayer MEMS structures", *Sens. Actuators A Phys.* **134**:1 (2007), 177–185.
- [Hui et al. 2000] C. Y. Hui, H. D. Conway, and Y. Y. Lin, "A reexamination of residual stresses in thin films and of the validity of Stoney's estimate", *J. Electron. Packag. (ASME)* **122**:3 (2000), 267–273.
- [Klein 2000] C. A. Klein, "How accurate are Stoney's equation and recent modifications", *J. Appl. Phys.* **88**:9 (2000), 5487–5489.
- [Kramer et al. 2004] D. Kramer, R. N. Viswanath, and J. Weissmüller, "Surface-stress induced macroscopic bending of nanoporous gold cantilevers", *Nano Lett.* **4**:5 (2004), 793–796.
- [Lagowski et al. 1975] J. Lagowski, H. C. Gatos, and E. S. Sproles, Jr., "Surface stress and the normal mode of vibration of thin crystals: GaAs", *Appl. Phys. Lett.* **26**:9 (1975), 493–495.
- [Lim and He 2004] C. W. Lim and L. H. He, "Size-dependent nonlinear response of thin elastic films with nano-scale thickness", *Int. J. Mech. Sci.* **46**:11 (2004), 1715–1726.
- [Lu et al. 2006] P. Lu, L. H. He, H. P. Lee, and C. Lu, "Thin plate theory including surface effects", *Int. J. Solids Struct.* **43**:16 (2006), 4631–4647.
- [Malzbender 2004] J. Malzbender, "Mechanical and thermal stresses in multilayered materials", *J. Appl. Phys.* **95**:4 (2004), 1780–1782.
- [Masmanidis et al. 2007] S. C. Masmanidis, R. B. Karabalin, I. De Vlaminck, G. Borghs, M. R. Freeman, and M. L. Roukes, "Multifunctional nanomechanical systems via tunably coupled piezoelectric actuation", *Science* **317**:5839 (2007), 780–783.
- [Miller and Shenoy 2000] R. E. Miller and V. B. Shenoy, "Size-dependent elastic properties of nanosized structural elements", *Nanotechnology* **11**:3 (2000), 139–147.
- [Nemat-Nasser 2002] S. Nemat-Nasser, "Micromechanics of actuation of ionic polymer-metal composites", *J. Appl. Phys.* **92**:5 (2002), 2899–2915.
- [Stoney 1909] G. G. Stoney, "The tension of metallic films deposited by electrolysis", *Proc. R. Soc. Lond. A* **82** (1909), 172–175.
- [Thompson and Clyne 2001] J. A. Thompson and T. W. Clyne, "The effect of heat treatment on the stiffness of zirconia top coats in plasma-sprayed TBCs", *Acta Mater.* **49**:9 (2001), 1565–1575.
- [Wang and Feng 2007] G.-F. Wang and X.-Q. Feng, "Effects of surface elasticity and residual surface tension on the natural frequency of microbeams", *Appl. Phys. Lett.* **90**:23 (2007), 231904.
- [Wang et al. 2006] J. Wang, H. L. Duan, Z. P. Huang, and B. L. Karihaloo, "A scaling law for properties of nano-structured materials", *Proc. R. Soc. Lond. A* **462**:2069 (2006), 1355–1363.
- [Weissmüller et al. 2003] J. Weissmüller, R. N. Viswanath, D. Kramer, P. Zimmer, R. Würschum, and H. Gleiter, "Charge-induced reversible strain in a metal", *Science* **300**:5617 (2003), 312–315.
- [Xu and Zhang 2003] W.-H. Xu and T.-Y. Zhang, "Mechanical characterization of trilayer thin films by the microbridge testing method", *Appl. Phys. Lett.* **83**:9 (2003), 1731–1733.

- [Zhou and Huang 2004] L. G. Zhou and H. C. Huang, “Are surfaces elastically softer or stiffer?”, *Appl. Phys. Lett.* **84**:11 (2004), 1940–1942.
- [Zhu 2007] H. X. Zhu, “Large deformation pure bending of an elastic plastic power-law-hardening wide plate: analysis and application”, *Int. J. Mech. Sci.* **49**:4 (2007), 500–514.
- [Zhu 2008] H. X. Zhu, “The effects of surface and initial stresses on the bending stiffness of nanowires”, *Nanotechnology* **19**:40 (2008), 405703.
- [Zhu and Karihaloo 2008] H. X. Zhu and B. L. Karihaloo, “Size-dependent bending of thin metallic films”, *Int. J. Plast.* **24**:6 (2008), 991–1007.

Received 1 Dec 2008. Revised 20 Dec 2008. Accepted 31 Dec 2008.

HANXING ZHU: [zhuh3@cf.ac.uk](mailto:zhuh3@cf.ac.uk)

*School of Engineering, Cardiff University, Cardiff CF24 3AA, United Kingdom*

JIANXIANG WANG: [jxwang@pku.edu.cn](mailto:jxwang@pku.edu.cn)

*LTCS and Department of Mechanics and Engineering Science, College of Engineering, Peking University, Beijing 100871, China*

BHUSHAN KARIHALOO: [KarihalooB@cf.ac.uk](mailto:KarihalooB@cf.ac.uk)

*School of Engineering, Cardiff University, Cardiff CF24 3AA, United Kingdom*

## NUMERICAL MODELING OF CRACK PROPAGATION IN ROCKS UNDER TBM DISC CUTTERS

MOHAMMAD FATEHI MARJI, HASAN HOSSEINI NASAB AND AMIN HOSSEIN MORSHEDI

The mechanism of rock fragmentation underneath disc cutters is not fully understood although a number of experimental and numerical investigations have been carried out in this field. Linear elastic fracture mechanics is widely applied for the analysis of crack problems in rock mechanics. In this study, the higher order displacement discontinuity method is modified for the analysis of crack problems using the cubic variations of displacement discontinuities and three special crack tip elements. It is shown how a new formulation of the indirect boundary element method known as the displacement discontinuity method (DDM) can be used to determine the stress intensity factors of the cracks produced in rocks underneath disc cutters of tunnel boring machines (TBMs). Crack initiation angles and propagation paths in the rock can also be predicted using this numerical procedure and a mixed mode fracture criterion (for example, the maximum tensile stress criterion). In this numerical approach, three special crack tip elements are used to increase the accuracy of the displacement discontinuities near the crack tips. This method has been used to find approximately the effect of the specific disc parameters (except speed) on the thrust force, the rolling force, and the specific energy. Crack propagation in rocks under disc cutters is numerically modeled and an optimum ratio of disc spacing to penetration depth of about 10 is obtained, in good agreement with the theoretical and experimental results in the literature.

### 1. Introduction

Tunnel boring machines (TBMs) are usually equipped with disc cutters. The most dominant fracture process involved in cutting by TBMs is due to the subsurface crack propagation and interaction, or subsurface chipping, between adjacent cutters. The chipping process is due to forces from the multiple disc cutters mounted on the cutting head of the machines on the rock face. Several experimental, empirical, analytical and semianalytical models have been used for TBM performance prediction, such as those developed by the Earth Mechanics Institute of the Colorado School of Mines, the University of Trondheim and the Norwegian Institute of Technology, and the Department of Mining Engineering at the Technical University of Istanbul [Lislerud 1988; Nilsen and Ozdemir 1993; Rostami et al. 1994; Johanessen 1995; Bilgin et al. 2000]. Other experimental and theoretical research and work has also been reported for the investigation of the mechanism of rock fragmentation underneath the disc cutters, but its true mechanism is not fully understood yet [Roxborough and Phillips 1975; Howarth and Roxborough 1982; Snowdon et al. 1982; Tan et al. 1996].

---

*Keywords:* crack analysis, cubic elements, semi-infinite problems, displacement discontinuity method, crack tip elements, disc cutters.

Several attempts have been made to use fracture mechanics principles via boundary element methods (especially the displacement discontinuity method), for the simulation of rock fracture mechanics problems [Guo et al. 1992; Whittaker et al. 1992; Shen and Stephansson 1994; Alehossein et al. 2000; Bobet 2001]. In this study, fracture mechanics principles are implemented in the higher order (third order) displacement discontinuity method modified for crack problems. The cubic variations of displacement discontinuity and three special crack tip elements for each crack tip are used for the discretization of the boundary of the problem. The rock breakage mechanism under disc cutters of tunnel boring machines (TBMs) is modeled and studied by the proposed method. The displacement discontinuity solution based on three special crack tip elements is thoroughly explained and the required formulations are derived and given in the text.

Fundamentally, there are three mixed mode fracture criteria: the maximum tangential stress fracture criterion (or  $\sigma$ -criterion), the maximum strain energy release rate fracture criterion (or  $G$ -criterion), and the minimum strain energy density fracture criterion (or  $S$ -criterion) [Erdogan and Sih 1963; Ingraffea 1983; Huang and Wang 1985; Ouchterlony 1988; Broek 1989]. The recent fracture codes, such as FRACOD, which is based on the two-dimensional displacement discontinuity method, uses the modified version of Griffith's  $G$ -criterion (the  $F$ -criterion) to describe the fracture propagation processes [Shen and Stephansson 1994]. All of the mixed mode fracture criteria can be implemented in the proposed higher order displacement discontinuity method. However, the fracture propagation process predicted using the  $\sigma$ -criterion lies between those processes predicted using the other two classic criteria [Ingraffea 1983; Whittaker et al. 1992]: the  $G$ -criterion is more conservative and the  $S$ -criterion is less. (Note that the  $K_{IC}$  predicted by the  $S$ -criterion depends on the material parameter of the Poisson's ratio  $\nu$ .)

In this paper, crack propagation analysis is accomplished by using a suitable mixed mode fracture criterion, the maximum tangential stress criterion (or  $\sigma$ -criterion) of [Erdogan and Sih 1963]. This simple mixed mode criterion, used by several researchers [Ingraffea 1983; Guo et al. 1992; Whittaker et al. 1992; Bobet 2001], compares the computed Mode I and Mode II stress intensity factors  $K_I$  and  $K_{II}$  with  $K_{IC}$  and  $K_{IIC}$ , Mode I and Mode II fracture toughness values under plane strain condition [Erdogan and Sih 1963; Ingraffea 1983; Huang and Wang 1985; Ouchterlony 1988; Broek 1989; Whittaker et al. 1992].

A good deal of research [Stephansson et al. 2001; Stephansson 2002; Backers et al. 2002; 2003; Rao et al. 2003; Backers 2004; Backers et al. 2004; Shen et al. 2004] has shown that the Mode II fracture toughness of rock material is usually higher than the Mode I fracture toughness, especially when the confining pressure increases. It also showed that the rocks are stronger under confining pressure, and that usually crack propagation occurs in Mode II loading under this condition [Backers 2004]. Backers et al. 2002 described a new experimental method for determination of Mode II (shear) fracture toughness of rock,  $K_{IIC}$ , and compared the outcome to results from Mode I (tensile) fracture toughness,  $K_{IC}$ , using the International Society of Rock Mechanics chevron bend test method.

Fracture toughness describes the resistance of rock to fracturing. This parameter is therefore important in estimating the failure of rock and rock structures using rock fracture mechanics principles. In this study, wedge-shaped cracks under mixed mode loading conditions are considered. These cracks are produced on a free surface of a semi-infinite rock mass by forcing the disc cutters onto the rock. As the confining pressure near the rock surface is negligible, the cracks will propagate mostly by mixed mode loading.



The displacement discontinuity solution used in the analysis presented here is of third order, which gives very accurate results of the displacement discontinuity variations along the general boundary elements with only two degrees of freedom. Because of the singularities of the displacement discontinuities at the crack tips, special crack tip elements have been proposed and used in the literature, but in most cases only one or two crack tip elements have been used. To obtain a more accurate result of the near crack tip displacement discontinuities, three or more crack tip elements can be used. This increases computation time, but not to a significant extent for modern computers. Therefore, the displacement discontinuity solution based on three general special crack tip elements is thoroughly explained and given here.

### 2. The cubic variation of displacement discontinuity element

A displacement discontinuity element of length  $2a$  along the  $x$ -axis (Figure 1, left) is characterized by a general displacement discontinuity distribution  $D(\varepsilon)$ . By taking  $D_x$  and  $D_y$  components of the general displacement discontinuity  $D(\varepsilon)$  to be constant in the interval  $(-a, +a)$  as shown in Figure 1, right, the constant element displacement discontinuities  $D_x$  and  $D_y$  are defined as [Crouch 1976]

$$\begin{aligned} D_x &= u_x(x, 0_-) - u_x(x, 0_+), \\ D_y &= u_y(x, 0_-) - u_y(x, 0_+), \end{aligned} \tag{1}$$

where  $u_x(x, 0_-)$ ,  $u_y(x, 0_-)$ ,  $u_x(x, 0_+)$ , and  $u_y(x, 0_+)$  are the  $x$  and  $y$  components of displacements in the negative side of  $y(y = 0_-)$  and positive side of  $y(y = 0_+)$ , respectively.

The general displacement discontinuity method and its formulation for the constant and the higher elements (using equal subelements) are explained in the literature [Crouch 1976; Crawford and Curran 1982; Crouch and Starfield 1983; Shou and Crouch 1995; Fatehi Marji et al. 2006]. In the present paper, the general linear and cubic variations (subelements may or may not be equal) of the displacement discontinuity method are discussed, and their numerical results are compared with each other.

The linear element displacement discontinuity is based on analytical integration of linear collocation shape functions over collinear straight-line displacement discontinuity elements. Figure 2, left, shows the linear displacement discontinuity distribution, which can be written in a general form as

$$D_i(\varepsilon) = N_{1L}(\varepsilon)D_i^1 + N_{2L}(\varepsilon)D_i^2, \quad i = x, y, \tag{2}$$

where  $D_i^1$  and  $D_i^2$  are the linear nodal displacement discontinuities.

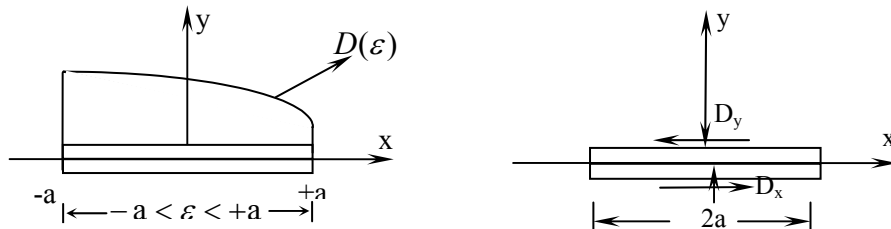


**Figure 1.** Left: Displacement discontinuity element and the distribution of  $u(\varepsilon)$ . Right: Constant element displacement discontinuity and positive sign convention.

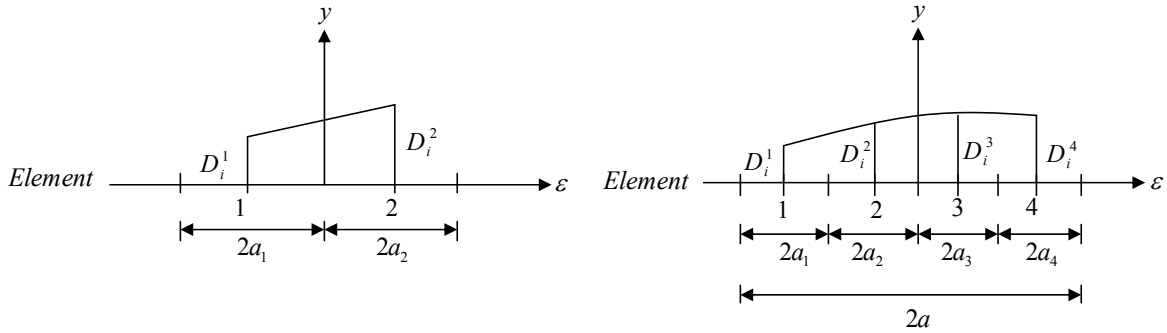


**Figure 2.** Linear (left) and cubic (right) collocations for the higher order displacement discontinuity variations.

The linear shape functions  $N_{1L}(\varepsilon)$  and  $N_{2L}(\varepsilon)$  can be defined as

$$N_{1L}(\varepsilon) = -\frac{\varepsilon - a_2}{a_1 + a_2}, \quad N_{2L}(\varepsilon) = \frac{\varepsilon + a_1}{a_1 + a_2}, \quad (3)$$

which are their linear collocation shape functions. Note that a linear element has two nodes, the centers of its two subelements.

Similarly, the cubic element displacement discontinuity is based on analytical integration of cubic collocation shape functions over collinear straight-line displacement discontinuity elements. Figure 2, right, shows the cubic displacement discontinuity distribution, which can be written as

$$D_i(\varepsilon) = \sum_{j=1}^4 N_j(\varepsilon) D_i^j, \quad i = x, y, \quad (4)$$

where  $D_i^1$ ,  $D_i^2$ ,  $D_i^3$ , and  $D_i^4$  are the cubic nodal displacement discontinuities, and the cubic collocation shape functions  $N_j(\varepsilon)$  can be defined as

$$N_j(\varepsilon) = \sum_{j=1}^4 (A_j + B_j \varepsilon + C_j \varepsilon^2 + D_j \varepsilon^3), \quad (5)$$

where the constants  $A_j$ ,  $B_j$ ,  $C_j$  and  $D_j$  are successively defined by the following equalities:

$$\begin{aligned} A_1 &= a_2 B_1 - a_2^2 C_1 + a_2^3 D_1, & A_2 &= 1 + a_2 B_2 - a_2^2 C_2 + a_2^3 D_2, \\ A_3 &= a_2 B_3 - a_2^2 C_3 + a_2^3 D_3, & A_4 &= a_2 B_4 - a_2^2 C_4 + a_2^3 D_4, \end{aligned}$$

$$\begin{aligned} B_1 &= (a_2 - a_3) C_1 - (a_2^2 - a_2 a_3 + a_3^2) D_1, & B_2 &= -\frac{1}{a_2 + a_3} + (a_2 - a_3) C_2 - (a_2^2 - a_2 a_3 + a_3^2) D_2, \\ B_3 &= \frac{1}{a_2 + a_3} + (a_2 - a_3) C_3 - (a_2^2 - a_2 a_3 + a_3^2) D_3, & B_4 &= (a_2 - a_3) C_4 - (a_2^2 - a_2 a_3 + a_3^2) D_4, \end{aligned}$$

$$C_1 = C_{20}(1 + C_{2D} D_1), \quad C_2 = C_{20}(C_{22} + C_{2D} D_2), \quad C_3 = C_{20}(C_{31} + C_{2D} D_3), \quad C_4 = C_{2D} D_4,$$

$$D_1 = \frac{D_{1N}}{D_D}, \quad D_2 = \frac{D_{2N}}{D_D}, \quad D_3 = \frac{D_{3N}}{D_D}, \quad D_4 = \frac{D_{10}}{D_D}, \quad D_D = 1 - D_{10} D_{1C} C_{10} C_{1D},$$

$$\begin{aligned}
 C_{10} &= \frac{1}{(2a_2+a_1)(a_1+a_2+a_3)-a_2a_3}, & C_{11} &= \frac{a_2}{a_2+a_3}, & C_{12} &= -\frac{2a_2+a_1}{a_2+a_3}, & C_{13} &= \frac{a_1+a_2}{a_2+a_3}, \\
 C_{20} &= \frac{1}{(2a_2+a_1)^2-a_2^2-(a_1+a_2)(a_2-a_3)}, & C_{22} &= -\frac{a_1+2a_2+a_3}{a_2+a_3}, & C_{23} &= \frac{a_1+a_2}{a_2+a_3}, \\
 C_{1D} &= -(2a_2+a_1)((a_2^2-a_2a_3+a_3^2)-(2a_2+a_1)^2), \\
 C_{2D} &= (2a_2+a_1)^3-a_2^3-(a_1+a_2)(a_2^2-a_2a_3+a_3^2),
 \end{aligned}$$

$$\begin{aligned}
 D_{1N} &= D_{10}(D_{11}+D_{1C}C_{10}C_{11}), & D_{2N} &= D_{10}(D_{12}+D_{1C}C_{10}C_{12}), & D_{3N} &= D_{10}(D_{13}+D_{1C}C_{10}C_{13}), \\
 D_{10} &= \frac{1}{(2a_3+a_4)^3+a_2a_3(a_2-a_3)-(2a_3+a_4)(a_2^2-a_2a_3+a_3^2)}, & D_{11} &= -\frac{a_3}{a_2+a_3}, \\
 D_{12} &= \frac{2a_3+a_4}{a_2+a_3}, & D_{13} &= -\frac{a_2+2a_3+a_4}{a_2+a_3}, & D_{1C} &= a_2a_3-(2a_3+a_4)(a_2+a_3+a_4).
 \end{aligned}$$

A cubic element has four nodes, the centers of its four subelements (Figure 2). For the special case  $a_1 = a_2 = a_3 = a_4$ , the general shape functions given by (5) reduce to [Fatehi Marji et al. 2007]

$$\begin{aligned}
 N_1(\varepsilon) &= -\frac{3a_1^3 - a_1^2\varepsilon - 3a_1\varepsilon^2 + \varepsilon^3}{48a_1^3}, & N_2(\varepsilon) &= \frac{9a_1^3 - 9a_1^2\varepsilon - a_1\varepsilon^2 + \varepsilon^3}{16a_1^3}, \\
 N_3(\varepsilon) &= \frac{9a_1^3 + 9a_1^2\varepsilon - a_1\varepsilon^2 - \varepsilon^3}{16a_1^3}, & N_4(\varepsilon) &= -\frac{3a_1^3 + a_1^2\varepsilon - 3a_1\varepsilon^2 - \varepsilon^3}{48a_1^3}.
 \end{aligned} \tag{6}$$

Crouch [1976] expressed the displacements for a line crack in an infinite body along the  $x$ -axis in terms of single harmonic functions  $g(x, y)$  and  $f(x, y)$  as

$$u_x = 2(1-\nu)f_{,y} - yf_{,xx} - (1-2\nu)g_{,x} - yg_{,xy}, \quad u_y = (1-2\nu)f_{,x} - yf_{,xy} + 2(1-\nu)g_{,y} - yg_{,yy}, \tag{7}$$

while the corresponding stresses are

$$\begin{aligned}
 \sigma_{xx} &= 2\mu(2f_{,xy} + yf_{,xyy} + g_{,yy} + yg_{,yyy}), \\
 \sigma_{yy} &= 2\mu(-yf_{,xyy} + g_{,yy} - yg_{,yyy}), \\
 \sigma_{xy} &= 2\mu(2f_{,yy} + yf_{,yyy} - yg_{,xyy}).
 \end{aligned} \tag{8}$$

Here  $\mu$  is the shear modulus,  $\nu$  is Poisson's ratio, and the subscript comma denotes partial differential with respect to the following variable(s). These potential functions for the cubic element case can be found from

$$f(x, y) = \frac{-1}{4\pi(1-\nu)} \sum_{j=1}^4 D_x^j F_j(x, y), \quad g(x, y) = \frac{-1}{4\pi(1-\nu)} \sum_{j=1}^4 D_y^j F_j(x, y), \tag{9}$$

where

$$F_j(x, y) = \int_{-a}^a N_j(\varepsilon) \ln \sqrt{(x-\varepsilon)^2 + y^2} d\varepsilon. \quad j = 1, 2, 3, 4, \tag{10}$$

Using the coefficients in (6), one can write the  $F_j$  in terms of the integrals

$$I_k(x, y) = \int_{-a}^a \varepsilon^k \ln \sqrt{(x - \varepsilon)^2 + y^2} d\varepsilon, \quad (11)$$

whose explicit expressions are, in terms of the auxiliary quantities  $\theta_1 = \arctan \frac{y}{x-a}$ ,  $\theta_2 = \arctan \frac{y}{x+a}$ ,  $r_1 = \sqrt{(x-a)^2 + y^2}$ , and  $r_2 = \sqrt{(x+a)^2 + y^2}$ , given by

$$I_0(x, y) = y(\theta_1 - \theta_2) - x \ln \frac{r_1}{r_2} + a \ln(r_1 r_2) - 2a, \quad (12a)$$

$$I_1(x, y) = xy(\theta_1 - \theta_2) + \frac{y^2 - x^2 + a^2}{2} \ln \frac{r_1}{r_2} - ax, \quad (12b)$$

$$I_2(x, y) = \frac{y}{3}(3x^2 - y^2)(\theta_1 - \theta_2) + \frac{3xy^2 - x^3}{3} \ln \frac{r_1}{r_2} + \frac{a^3}{3} \ln(r_1 r_2) - \frac{6ax^2 - 6ay^3 + 2a^3}{9}, \quad (12c)$$

$$I_3(x, y) = -xy(x^2 - y^2)(\theta_1 - \theta_2) + \frac{3x^4 - 6x^2y^2 + 8a^2x^2 + a^4 - y^4}{4} \ln \frac{r_1}{r_2} - 2ax(x^2 + a^2) \ln(r_1 r_2) + \frac{9ax^3 - 18axy^2 + 7a^3x}{6}. \quad (12d)$$

As discussed, the boundary and crack of any specified problem are discretized by  $N$  elemental finite line segments. Let  $D_s^j$  and  $D_n^j$  be the shear and normal components of the nodal displacement discontinuities given in (4) for each boundary element.

The corresponding nodal stresses are

$$\begin{bmatrix} \sigma_s^i \\ \sigma_n^i \end{bmatrix} = \begin{bmatrix} A_{ss}^{ij} & A_{sn}^{ij} \\ A_{ns}^{ij} & A_{nn}^{ij} \end{bmatrix} \begin{bmatrix} D_s^j \\ D_n^j \end{bmatrix}, \quad (13)$$

where  $\sigma_n^i$  and  $\sigma_s^i$  are the normal and stress components at the  $i$ -th node, and the matrix entries ( $A_{ss}^{ij}$ , etc.) are the influence coefficients obtained by using (8)–(12). Similarly, the displacements are

$$\begin{bmatrix} u_s^i \\ u_n^i \end{bmatrix} = \begin{bmatrix} B_{ss}^{ij} & B_{sn}^{ij} \\ B_{ns}^{ij} & B_{nn}^{ij} \end{bmatrix} \begin{bmatrix} D_s^j \\ D_n^j \end{bmatrix}, \quad (14)$$

where  $u_n^i$  and  $u_s^i$  are the normal and shear displacement component, at the  $i$ -th node, and the matrix entries ( $B_{ss}^{ij}$ , etc.) are the influence coefficients obtained by using (7) and (9)–(12). By using the specified values of the stresses or displacements to the boundaries and crack of the problem, it is possible to find the required displacement discontinuities  $D_s^j$  and  $D_n^j$  at each elemental node.

### 3. Computation of mixed mode stress intensity factors

Consider a body of arbitrary shape with a crack subjected to mixed mode loading (that is, tensile and shear loadings). The displacements and stresses near the crack tip of a crack of arbitrary size (in a body of arbitrary shape) subjected to arbitrary tensile and shear loading are given in [Irwin 1957]. The

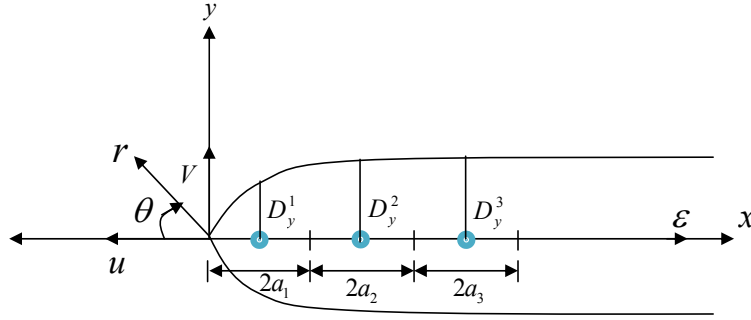


**Figure 3.** Special three-element crack tip for boundary collocation technique.

displacements are

$$\begin{aligned}
 u_x &= \frac{K_I}{4G} \sqrt{\frac{r}{2\pi}} \left[ (2\kappa - 1) \cos \frac{\theta}{2} - \cos \frac{3\theta}{2} \right] + \frac{K_{II}}{4G} \sqrt{\frac{r}{2\pi}} \left[ (2\kappa + 3) \sin \frac{\theta}{2} + \sin \frac{3\theta}{2} \right], \\
 u_y &= \frac{K_I}{4G} \sqrt{\frac{r}{2\pi}} \left[ (2\kappa - 1) \sin \frac{\theta}{2} - \sin \frac{3\theta}{2} \right] - \frac{K_{II}}{4G} \sqrt{\frac{r}{2\pi}} \left[ (2\kappa - 3) \cos \frac{\theta}{2} + \cos \frac{3\theta}{2} \right],
 \end{aligned} \tag{15a}$$

and the stresses are

$$\begin{aligned}
 \sigma_x &= \frac{K_I}{\sqrt{2\pi r}} \cos \frac{\theta}{2} \left[ 1 - \sin \frac{\theta}{2} \sin \frac{3\theta}{2} \right] - \frac{K_{II}}{\sqrt{2\pi r}} \sin \frac{\theta}{2} \left[ 2 + \cos \frac{\theta}{2} \cos \frac{3\theta}{2} \right] + \dots, \\
 \sigma_y &= \frac{K_I}{\sqrt{2\pi r}} \cos \frac{\theta}{2} \left[ 1 + \sin \frac{\theta}{2} \sin \frac{3\theta}{2} \right] + \frac{K_{II}}{\sqrt{2\pi r}} \sin \frac{\theta}{2} \cos \frac{\theta}{2} \cos \frac{3\theta}{2} + \dots, \\
 \sigma_{xy} &= \frac{K_I}{\sqrt{2\pi r}} \sin \frac{\theta}{2} \cos \frac{\theta}{2} \cos \frac{3\theta}{2} + \frac{K_{II}}{\sqrt{2\pi r}} \cos \frac{\theta}{2} \left[ 1 - \sin \frac{\theta}{2} \sin \frac{3\theta}{2} \right] + \dots,
 \end{aligned} \tag{15b}$$

where  $\kappa = (3 - 4\nu)$  for plane strain and  $\kappa = (3 - \nu)/(1 + \nu)$  for plane stress,  $K_I$  and  $K_{II}$  are the Mode I and Mode II stress intensity factors, and  $r$  and  $\theta$  are polar coordinates defined as in Figure 3.

The displacement discontinuity method allows crack surfaces to be discretized and computes the normal displacement discontinuity (crack opening displacement) and the shear displacement discontinuity (crack sliding displacement) directly as part of the solution for each element. Based on LEFM (linear elastic fracture mechanics) theory, the Mode I and Mode II stress intensity factors  $K_I$  and  $K_{II}$  can be written from (1) and (15a) in terms of the normal and shear displacement discontinuities as

$$K_I = \frac{\mu}{4(1 - \nu)} \sqrt{\frac{2\pi}{a}} D_y(a), \quad K_{II} = \frac{\mu}{4(1 - \nu)} \sqrt{\frac{2\pi}{a}} D_x(a). \tag{16}$$

In previous work, usually one or two special crack tip elements have been used [Shou and Crouch 1995; Fatehi Marji et al. 2006]. In the present paper, three special crack tip elements are used, to achieve better accuracy for the displacement discontinuities near the crack ends, and in particular to model the  $1/\sqrt{r}$  behavior of (15b), characteristic of the stress field in the near field region of the crack tip.

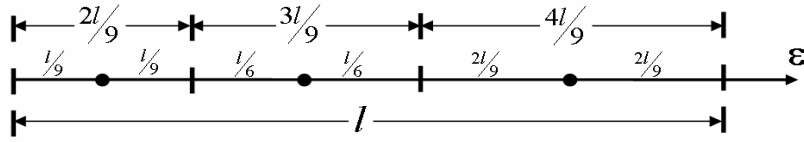


**Figure 4.** The three special crack tip element lengths  $l_1 = 2a_1 = \frac{2}{9}l$ ,  $l_2 = 2a_2 = \frac{3}{9}l$ , and  $l_3 = 2a_3 = \frac{4}{9}l$ .

Consider a crack tip of length  $l = 2a = 2(a_1 + a_2 + a_3)$  in an infinite isotropic elastic body, as shown in Figure 3. Omitting details, which can be found in [Fatehi Marji et al. 2006], the variation of displacement discontinuities along this crack tip element can be written as

$$D_i(\varepsilon) = N_{C1}(\varepsilon)D_i^1(a) + N_{C2}(\varepsilon)D_i^2(a) + N_{C3}(\varepsilon)D_i^3(a), \quad (17)$$

where the functions  $N_{Cj}$  are given below.

We first consider the subelement lengths  $l_1 = 2a_1 = \frac{2}{9}l$ ,  $l_2 = 2a_2 = \frac{3}{9}l$ , and  $l_3 = 2a_3 = \frac{4}{9}l$ , as shown in Figure 4. The general shape functions  $N_{C1}(\varepsilon)$ ,  $N_{C2}(\varepsilon)$ , and  $N_{C3}(\varepsilon)$  of (17) in this case are

$$N_{C1}(\varepsilon) = \frac{(a_{22} - a_{33})(a_{22}a_{33}\varepsilon^{1/2} - (a_{22} + a_{33})\varepsilon^{3/2} + \varepsilon^{5/2})}{a_{11}^{1/2}(a_{11} - a_{22})(a_{11}a_{22} - a_{11}a_{33} - a_{22}a_{33} + a_{33}^2)}, \quad (18a)$$

$$N_{C2}(\varepsilon) = \frac{(a_{33} - a_{11})(a_{11}a_{33}\varepsilon^{1/2} - (a_{11} + a_{33})\varepsilon^{3/2} + \varepsilon^{5/2})}{a_{22}^{1/2}(a_{11} - a_{22})(a_{11}a_{22} - a_{11}a_{33} - a_{22}a_{33} + a_{33}^2)}, \quad (18b)$$

$$N_{C3}(\varepsilon) = \frac{a_{11}a_{33}\varepsilon^{1/2} - (a_{11} + a_{33})\varepsilon^{3/2} + \varepsilon^{5/2}}{a_{33}^{1/2}(a_{11}a_{22} - a_{11}a_{33} - a_{22}a_{33} + a_{33}^2)}, \quad (18c)$$

where  $a_{11} = a_1 = \frac{1}{9}l$ ,  $a_{22} = 2a_1 + a_2 = \frac{7}{18}l$ , and  $a_{33} = 2(a_1 + a_2) + a_3 = \frac{7}{9}l$ .

If instead we take  $a_1 = a_2 = a_3$ , the shape functions  $N_{C1}(\varepsilon)$ ,  $N_{C2}(\varepsilon)$ , and  $N_{C3}(\varepsilon)$  become (see [Fatehi Marji et al. 2007])

$$N_{C1}(\varepsilon) = \sqrt{\frac{\varepsilon}{a_1}} \left( \frac{15}{8} - \frac{\varepsilon}{a_1} + \frac{\varepsilon^2}{8a_1^2} \right), \quad (19a)$$

$$N_{C2}(\varepsilon) = -\sqrt{\frac{\varepsilon}{3a_1}} \left( \frac{5}{4} - \frac{3\varepsilon}{2a_1} + \frac{\varepsilon^2}{4a_1^2} \right), \quad (19b)$$

$$N_{C3}(\varepsilon) = \sqrt{\frac{\varepsilon}{5a_1}} \left( \frac{3}{8} - \frac{\varepsilon}{2a_1} + \frac{\varepsilon^2}{8a_1^2} \right). \quad (19c)$$

Substituting (18) or (19) into (17), and then substituting these equations into (7) and (8), and working as in the derivation of the general potential functions  $F_j$  in (10), we can obtain the general potential function  $f_C(x, y)$  for the crack tip element as

$$f_C(x, y) = \frac{-1}{4\pi(1-\nu)} \sum_{j=1}^3 D_i^j \int_{-a}^a N_j(\varepsilon) \ln \sqrt{(x-\varepsilon)^2 + y^2} d\varepsilon, \quad (20)$$

which can conveniently be written in terms of the integrals

$$I_{Ck}(x, y) = \int_{-a}^a \varepsilon^{k-\frac{1}{2}} \ln \sqrt{(x-\varepsilon)^2 + y^2} d\varepsilon, \quad k = 1, 2, 3 \quad (21)$$

using the coefficients of powers of  $\varepsilon$  given in (18) or (19).

Two degrees of freedom are used for each node at the center of each subelement, as explained in [Shou and Crouch 1995].

#### 4. Crack initiation and propagation

Based on LEFM principles, a crack will start propagation in the direction of the crack initiation angle  $\theta = \theta_0$  [Ingraffea 1983]. (See Figure 3 for notation.) Several mixed mode fracture criteria have been proposed for the estimation of this angle [Ingraffea 1983; Broek 1989; Whittaker et al. 1992], the main three being the maximum tangential stress criterion or  $\sigma$ -criterion, the maximum strain energy release rate criterion or  $G$ -criterion, and the minimum strain energy density criterion or  $S$ -criterion. Modified forms of these criteria (for example, the  $F$ -criterion, which derives from the  $G$ -criterion) have also been used in the fracture mechanics literature [Ingraffea 1983; Broek 1989; Whittaker et al. 1992; Stephansson 2002].

All these criteria have demonstrated that a crack in a plate under a general in-plane load does not initiate and propagate in its original plane, that is,  $\theta_0 \neq 0$ . In brittle substances (like most rocks), although fracture of Mode II plays an important role under certain loading conditions and Mode I fracture toughness ( $K_{IC}$ ) is less than that of Mode II ( $K_{IIC}$ ), due to weakness (low strength) under tension the rock breaks due to tensile stress. In most such cases, the influence of  $K_{IC}$  prevails over that of  $K_{IIC}$  under pure tensile, pure shear, tension-shear, and compression-shear loading conditions [Rao et al. 2003].

To predict the crack initiation angle  $\theta_0$  and the path of crack propagation, the maximum tangential stress criterion or  $\sigma$ -criterion, is used here. This is one of the classical mixed mode fracture criteria which are widely used by several researchers [Ingraffea 1983; Guo et al. 1992]. Based on this criterion, the crack will start its propagation when the critical maximum tangential tensile stress  $\sigma_{\theta_0}$  (in the direction of the crack propagation angle  $\theta_0$ ) satisfies the following condition [Ingraffea 1983; Guo et al. 1992; Whittaker et al. 1992]:

$$\sigma_{\theta_0} = \frac{1}{\sqrt{2\pi r}} \cos \frac{\theta_0}{2} \left[ K_I \sin \frac{\theta_0}{2} \cos \frac{\theta_0}{2} + K_{II} \left( 1 - 3 \sin^2 \frac{\theta_0}{2} \right) \right] = 0. \quad (22)$$

From this equation, the crack propagation angle  $\theta_0$  can be estimated as

$$\theta_0 = 2 \tan^{-1} \left( \frac{K_I}{4K_{II}} \pm \frac{1}{4} \sqrt{\frac{K_I^2}{K_{II}^2} + 8} \right) \text{ for } K_{II} \neq 0 \quad \text{and} \quad \theta_0 = 0 \text{ for } K_{II} = 0. \quad (23)$$

Finally, the general form of the  $\sigma$ -criterion in term of the Mode I fracture toughness of the material, ( $K_{IC}$ ), and the crack propagation angle  $\theta_0$  can be expressed as

$$\cos \frac{\theta_0}{2} \left[ K_I \cos^2 \frac{\theta_0}{2} - \frac{3}{2} K_{II} \sin \frac{\theta_0}{2} \right] = K_{IC} \text{ (or } 0.866K_{II}). \quad (24)$$

In the present paper, Equations (22), (23), and (24) are used for a given crack length  $b$  (or a central crack length  $2b$ ). To predict the crack propagation path, the original crack of length  $b$  is extended by

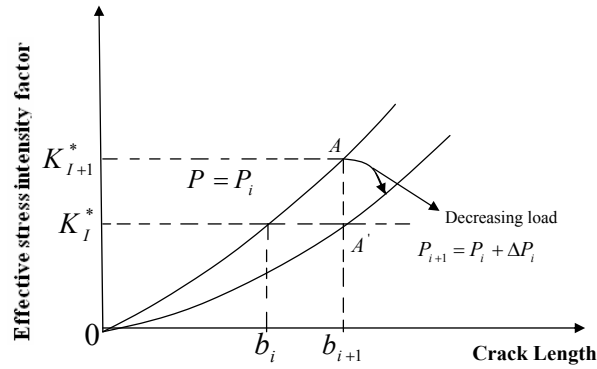


**Figure 5.** Variation of effective stress intensity with crack length [Ingraffea 1983].

an amount  $\Delta b$  so that a new crack length  $b + \Delta b$  is obtained, and again (22), (23), and (24) are used to predict the new conditions of crack propagation for this new crack. This procedure is repeated until the crack stops its propagation or the material breaks away. This procedure can give a propagation path for a given crack under a certain loading condition. Considering the effective (or normalized) stress intensity factor  $K_{IC}^* = K_I/K_{IC}$ , Figure 5 shows the stress intensity variation with crack length for any in-plane crack problem. The load level  $P_{i+1} = (K_{IC}/K_{I+1})P_i$  can be computed for each crack increment length,  $\Delta b$  [Ingraffea 1983]. Therefore, a new algorithm is added to the main displacement discontinuity program to evaluate the effective stress intensity factor  $K_{IC}^* = K_I/K_{IC}$  and a new crack propagation angle  $\theta_0$  in each iteration.

**5. A pressurized center crack in an infinite plane**

As an example, the pressurized crack problem shown in Figure 6 is solved numerically by the proposed method. The numerical results are compared with those results obtained analytically by [Sneddon 1951]. As shown in Figure 6, a center crack of length  $2b$  in an infinite plane is subjected to a uniform pressure  $p$ . The analytical solution for the normal displacement discontinuity  $D_y$  along the crack boundary and the normal stress  $\sigma_y$  near the crack tip ( $|x| > b$ ) can be written as

$$D_y = -\frac{2(1-\nu)P}{\mu} \sqrt{b^2 - x^2} \text{ if } |x| > b \text{ and } \sigma_y = \frac{Px}{\sqrt{x^2 - b^2}} - P \text{ if } |x| < b. \quad (25)$$

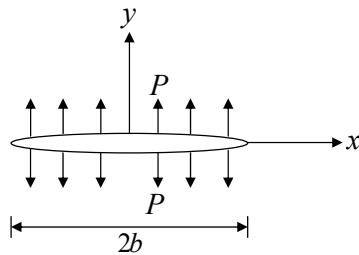


**Figure 6.** A pressurized crack in an infinite plane.



Number of elements	Distance from crack tip	$D_y(a)/b \times 10^3$			
		Analytical solution	Ordinary elements	One special crack tip element	Three special crack tip elements
4	0.25	-1.1906	-1.5463	-1.3275	-1.2092
10	0.1	-0.7846	-0.9964	-0.8569	-0.8168
20	0.05	-0.5621	-0.7089	-0.6104	-0.5874
40	0.025	-0.4000	-0.5029	-0.4332	-0.4183

**Table 1.** Displacement discontinuity  $D_y(a)/b \times 10^3$  at the center  $x = a$  of an element at the crack tip using ordinary elements, one special crack tip element and three special crack tip elements.

In the following analysis, a pressurized crack problem with half crack length  $b = 1$  m, normal pressure  $P = -10$  MPa, modulus of elasticity  $E = 2.2$  GPa, and Poisson’s ratio  $\nu = 0.1$  is considered.

Table 1 compares the different values of the normalized displacement discontinuity distribution  $D_y/b$  along the surface of the pressurized crack using the constant (ordinary) displacement discontinuity program TWODD with three crack tip elements [Crouch and Starfield 1983]. As shown in this table, by using only one special crack tip element, the percent error of displacement discontinuity  $D_y$  at a distance  $x = 0.05b$  from the crack tip is reduced from 26.12% to 8.59%, and by using three special crack tip elements it is reduced to 4.5%.

If the same problem is solved using 15 cubic elements (60 nodes) with the proposed method, the percentage error of displacement discontinuity  $D_y$  at a distance  $x = 0.05b$  from the crack tip will be 5.23% (without the special crack tip elements), and the results obtained by using the constant element displacement discontinuity method (the TWODD program) with the same number of nodes (60 constant elements) gives an error of 24.17% [Crouch and Starfield 1983]. Table 2 compares the variation of the normalized displacement discontinuity  $D_y/b$  along the surfaces of a pressurized crack using ordinary (constant element) and higher order (cubic element) displacement discontinuity methods. The results given in Tables 1 and 2 demonstrate that although all displacement discontinuity results are very close to their corresponding analytical values, those using three special crack tip elements are somewhat superior.

### 6. Edge cracks in a half plane

Edge crack problems in a half plane can also be solved using the cubic element formulation, but a proper mixed-mode fracture criterion such as that one explained in Section 3 should be implemented in the program to investigate the crack propagation direction and its propagation path. Figure 7 shows the oblique edge cracks with different inclination angles  $\beta$  on a traction-free half plane. For the problem shown in Figure 7, the inclination angle is  $\beta = 45^\circ$ , the crack length is  $b = 1$  m, and the ratio of the crack tip element length,  $l$ , to crack length,  $b$ , is 0.1 (that is,  $l/b = 0.1$ ). The normalized stress intensity factors  $K_I/(\sigma\sqrt{\pi b})$  and  $K_{II}/(\sigma\sqrt{\pi b})$  for this particular problem can be estimated from the results given by [Bowie 1973] as 0.729 and 0.371, respectively.

$x/b$	$D_y/b \times 10^3$				
	Analytical Results	Constant Elements (TWODD)	Error (%)	Cubic Elements	Error (%)
0.000	3.980	4.046	1.66	3.985	0.13
0.086	3.946	4.032	2.18	3.957	0.28
0.171	3.901	3.989	2.26	3.914	0.33
0.257	3.827	3.916	2.33	3.839	0.31
0.343	3.720	3.812	2.47	3.736	0.43
0.429	3.578	3.673	2.66	3.589	0.31
0.514	3.396	3.497	2.97	3.407	0.32
0.600	3.168	3.276	3.41	3.182	0.44
0.686	2.882	3.000	4.09	2.897	0.52
0.771	2.520	2.654	5.33	2.536	0.62
0.857	2.040	2.203	7.99	2.073	1.60
0.950	1.237	1.536	24.17	1.289	4.20

**Table 2.** Comparison of displacement discontinuity  $D_y/b \times 10^3$  along the surface of a pressurized crack using ordinary (constant) elements and higher order elements for displacement discontinuity methods without using a special crack tip element.

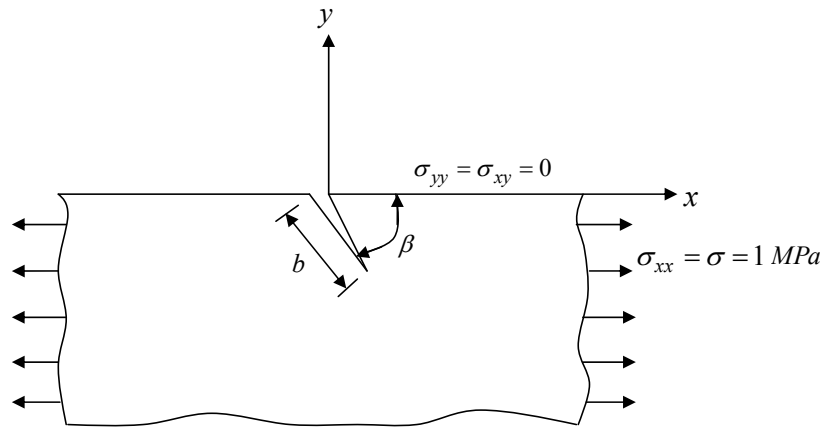


**Figure 7.** Oblique edge cracks in a semi-infinite plane.

The numerical results for the same problem are obtained by using the displacement discontinuity method for a traction-free half plane with different kind of elements, that is, ordinary elements (constant elements), quadratic elements, and the new cubic elements presented in this study. Table 3 shows the effect of the number of elements along the cracks using a constant  $l/b = 0.1$ , and taking sufficient elements (48 nodes) along the boundary of the problem (it should be noted that three special crack tip elements are used for obtaining these results).

Number of nodes	$K_I/(\sigma\sqrt{\pi b})$				$K_{II}/(\sigma\sqrt{\pi b})$			
	Constant elements	Error (%)	Cubic elements	Error (%)	Constant elements	Error (%)	Cubic elements	Error (%)
12	0.775	6.310	0.742	1.783	0.398	7.278	0.379	2.156
24	0.768	5.350	0.736	0.960	0.390	5.121	0.376	1.348
36	0.763	4.664	0.735	0.547	0.388	4.582	0.375	1.078
48	0.760	4.252	0.734	0.410	0.387	4.312	0.374	0.809
60	0.759	4.115	0.734	0.410	0.386	4.043	0.373	0.539

**Table 3.** Analytical and numerical values of the Mode I and Mode II stress intensity factors  $K_I/(\sigma\sqrt{\pi b})$  and  $K_{II}/(\sigma\sqrt{\pi b})$  for the  $45^\circ$  oblique edge crack using different number of elements along the crack ( $l/b = 0.1$ ).

$l/b$	$K_I/(\sigma\sqrt{\pi b})$				$K_{II}/(\sigma\sqrt{\pi b})$			
	Constant elements	Error (%)	Cubic elements	Error (%)	Constant elements	Error (%)	Cubic elements	Error (%)
0.05	0.764	4.801	0.732	0.137	0.390	5.121	0.370	-0.270
0.10	0.760	4.252	0.734	0.410	0.388	4.582	0.373	0.540
0.15	0.758	3.978	0.735	0.547	0.386	4.043	0.372	0.270
0.20	0.759	4.115	0.729	-0.274	0.387	4.312	0.374	0.809
0.25	0.760	4.252	0.727	-0.547	0.388	4.582	0.375	1.078

**Table 4.** Analytical and numerical values of the Mode I and Mode II stress intensity factors  $K_I/(\sigma\sqrt{\pi b})$  and  $K_{II}/(\sigma\sqrt{\pi b})$  for the  $45^\circ$  oblique edge crack using different  $l/b$  ratios.

Table 4 shows the effect of the crack tip element length,  $l$ , on the normalized stress intensity factors  $K_I/(\sigma\sqrt{\pi b})$  and  $K_{II}/(\sigma\sqrt{\pi b})$ . The results given in this table are obtained using a constant number of nodes (48, 12 cubic elements) along the crack. The results presented in Tables 3 and 4 demonstrate the accuracy and effectiveness of the proposed method.

### 7. Crack propagation mechanisms due to disc cutters in a semi-infinite rock mass

Disc cutters over the surface of a continuous rock mass are shown schematically in Figures 10 and 11. It is assumed that the disc cutters have diameter  $D$ , disc edge angle  $\varphi$ , penetration depth  $P_d$ , and spacing  $S$ . The thrust force  $F_t$  is required to maintain the disc at the desired depth of penetration, and the rolling force  $F_r$  is also necessary to keep the disc rolling at this penetration depth. Specific energy  $E_S$  (in MJ/m<sup>3</sup> in three dimensions or in MPa/m<sup>2</sup> in two dimensions) is a measure of the amount of energy that is required for breaking the rock under the disc cutter. Penetration depth  $P_d$ , disc edge angle  $\varphi$ , disc diameter  $D$ , spacing  $S$ , and speed are the primary variables related to disc cutters. Roxborough and Phillips [1975] showed that the specific energy  $E_S$  and rolling force  $F_r$  are nearly independent of the disc diameter, but the thrust force  $F_t$  increases with an increase of disc diameter.

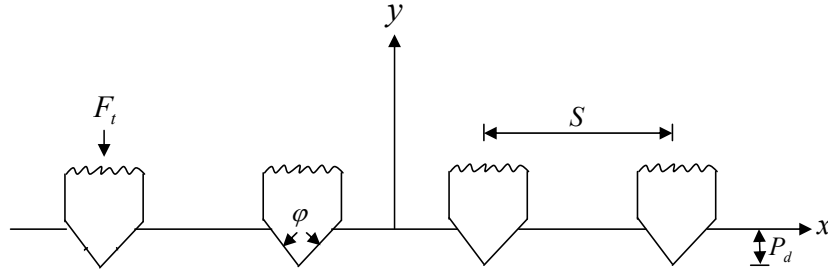


**Figure 8.** Side view of four equally spaced rows of disc cutters over the surface of a continuous rock mass.

In this section we use the semi-infinite displacement discontinuity method for crack analysis using cubic elements (SDDMCAC), with three special crack tip elements at each crack end, to find the approximate effects of the thrust force  $F_t$ , the rolling force  $F_r$ , and the specific energy  $E_S$ , for a constant disc diameter  $D$  (for example,  $D = 432$  mm) on the penetration depth  $P_d$  and the disc spacing  $S$ . We consider a typical TBM with a thrust of 250 kN per cutter, with disc cutters of 15 mm width and 432 mm diameter [Roxborough and Phillips 1975]. The typical rock is Aspö diorite, with  $K_{IC} = 3.83$  MPa m<sup>1/2</sup> and  $K_{IIC} = 5.09$  MPa m<sup>1/2</sup> [Backers 2004]. The other parameters of this rock, as reported in the same source, are  $\sigma_t = 15$  MPa,  $\sigma_c = 220$  MPa,  $E = 68$  GPa, and  $\nu = 0.24$ .

The symmetric problem of four rows of disc cutters is shown in Figure 8. Taking into account the symmetry of each wedge about a vertical plane, simple trigonometry shows that the normal and shear forces along each side of the groove equal, respectively,  $(F_t/2) \cos(\phi/2)$  and  $(F_t/2) \sin(\phi/2)$ , while the length  $b$  of the side of the cut is  $b = P_d / \cos(\phi/2)$ . Assuming strain conditions, we therefore obtain for the normal and shear components of stresses along the crack length  $b$

$$\sigma_n = F_t \frac{\cos(\phi/2)}{2bl}, \quad \sigma_s = F_t \frac{\sin(\phi/2)}{2bl}. \quad (26)$$

The values of the normal and shear stresses along these cracks are determined by fixing the normal stress at an assumed value and calculating the shear stress from the geometry of the wedge. By changing the value of normal stress and its corresponding shear stress and checking whether the crack starts its propagation or not, it is possible to predict the minimum value of the normal and shear stresses at which the crack propagation begins. Then, the minimum values of the thrust force  $F_t$  can be evaluated from (26) for different disc edge angles  $\phi$ .

The rolling force  $F_r$  can be estimated from the thrust force  $F_t$  through the formula

$$F_r = \frac{F_t}{\sqrt{(D - P_d)/P_d}}, \quad (27)$$

(see [Roxborough and Phillips 1975]), where  $D$  is the diameter of the disc cutter, taken here as 432 mm.

The primary crack propagation due to disc cutters, used here to investigate the effect of adjacent disc cutters on the penetration of cracks and the formation of major chips can be modeled as in Figure 9 [Guo et al. 1992; Whittaker et al. 1992]. The effect of the penetration depth  $P_d$  on the minimum value of the

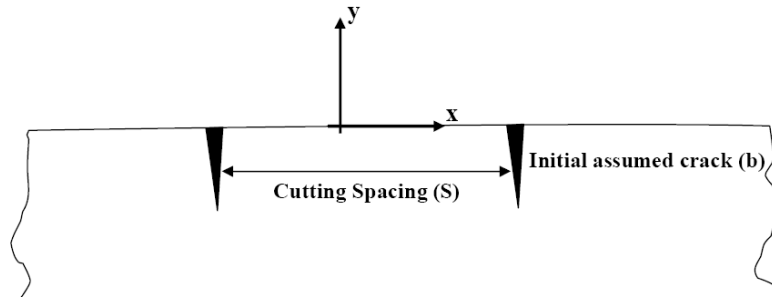


**Figure 9.** Geometry of adjacent disc cutters showing the cutting spacing  $S$  and initial assumed crack length  $b$  on a semi-infinite rock mass [Whittaker et al. 1992].

thrust force  $F_t$  and the corresponding rolling force  $F_r$  (which are needed to start the propagation of the crack) are obtained numerically for  $\varphi = 80, 90, \text{ and } 100^\circ$ , and disc spacing  $S = 30 \text{ mm}$ .

The numerical results for thrust force  $F_t$  and rolling force  $F_r$ , for different penetration depths  $P_d$ , and for three different disc edge angles,  $\varphi = 80, 90, \text{ and } 100^\circ$  are given in Table 5. The numerical results obtained here are normalized and verified by those given experimentally in [Bilgin et al. 2000] for  $\varphi = 90^\circ$  in Figure 10, which shows good agreement between numerical and experimental values.

The specific energy  $E_s$  for each disc cutter can be estimated numerically from the formula [Howarth and Roxborough 1982]

$$E_s = F_r / Q, \tag{28}$$

where  $Q$  is the extracted volume (area in two dimensions) of the rock measured in  $\text{m}^3$ . In all of the analysis here, a constant disc edge angle  $\varphi = 90^\circ$  and penetration depth  $P_d = 6 \text{ mm}$  are considered to estimate the value of the extracted area  $Q$  which is theoretically very difficult to evaluate. The geometry of the problem considered here is shown in Figure 11, in which each side of the cut (wedge) is considered to be a separate crack. The four cracks  $CR_1$ – $CR_4$ , from left to right in this figure, are solved numerically and the crack propagation angle  $\theta_0$  for each crack has been calculated in five different steps. In each step the crack length in the direction of  $\theta_0$  is extended between 1 mm and 4 mm (depending on the  $S/P_d$  ratio).

$P_d$ (mm)	$\varphi = 80^\circ$		$\varphi = 90^\circ$		$\varphi = 100^\circ$	
	$F_t$ (kN)	$F_r$ (kN)	$F_t$ (kN)	$F_r$ (kN)	$F_t$ (kN)	$F_r$ (kN)
2	74.045	5.005	79.804	6.412	82.540	5.589
4	112.406	10.911	117.123	11.489	130.173	12.853
6	142.878	17.623	152.453	18.231	172.172	20.873
8	171.916	24.025	183.230	25.785	197.281	29.569
10	193.114	30.436	207.987	31.897	224.549	34.754
12	213.986	35.719	231.012	39.125	245.167	41.895

**Table 5.** The minimum thrust force  $F_t$  and rolling force  $F_r$  corresponding to different penetration depths  $P_d$  for disc spacing  $S = 30 \text{ mm}$  and different disc edge angles  $\varphi$ .

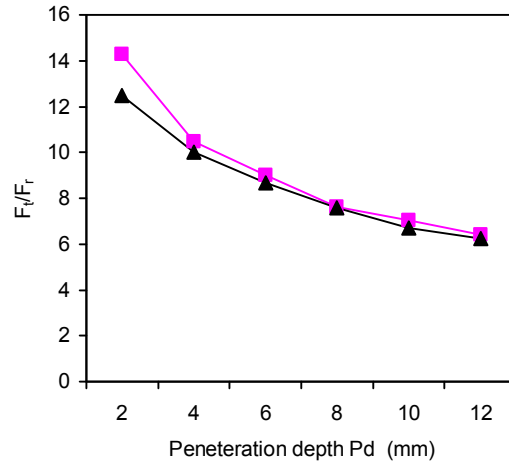


**Figure 10.** Comparison of the relation between  $F_t/F_r$  and  $P_d$  for a disc edge angle of  $90^\circ$ : pink squares, results from Table 5; black triangles, results from [Bilgin et al. 2000].

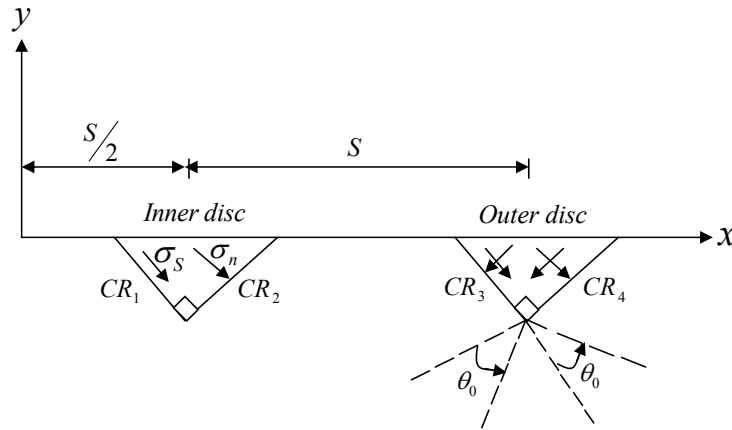


**Figure 11.** Symmetrical  $90^\circ$  disc cutters. Four cracks  $CR_1$ – $CR_4$  are shown from left to right.

Step	$CR_1$	$CR_2$	$CR_3$	$CR_4$
0	-68.95	51.18	-69.14	51.27
1	-27.89	8.51	-33.37	7.87
2	-23.85	10.13	-9.36	15.17
3	12.48	33.63	-2.15	18.14
4	-18.26	17.65	-8.98	11.79
5	-4.44	22.99	-8.65	13.42

**Table 6.** Numerical values of crack propagation angle  $\theta_0$  (in degrees) for  $S/P_d = 15$  for a  $90^\circ$  disc cutter.  $P_d = 6$  mm and crack increment  $\Delta b = 4$  mm (5 increments).

A ratio of crack tip element length  $l$  to crack length  $b$ , that is,  $l/b = 0.1$ , is used for the analysis of these cracks. We have taken 10 cubic elements along each original crack length and 2 cubic elements along each crack increment, and a crack tip element (with three subelements or three special crack tip elements) is added to the last crack increment. As the  $S/P_d$  ratio is one of the most important parameters in studying the mechanism of rock breaking due to disc cutters, different values of this parameter are considered here. As an example, the results obtained for  $S/P_d = 15$  showing the crack propagation angle  $\theta_0$  are given in Table 6. Approximate values of the extracted area  $Q$  are obtained by finding the area restricted by the crack propagation path. The numerical values of the extracted area  $Q$  ( $\text{mm}^2$ ) are estimated from the area under the crack propagation paths, for example, from those shown in Figures 12 and 13. The cracks labeled  $CR_1$  and  $CR_2$  are related to the inner disc, which represent its breaking

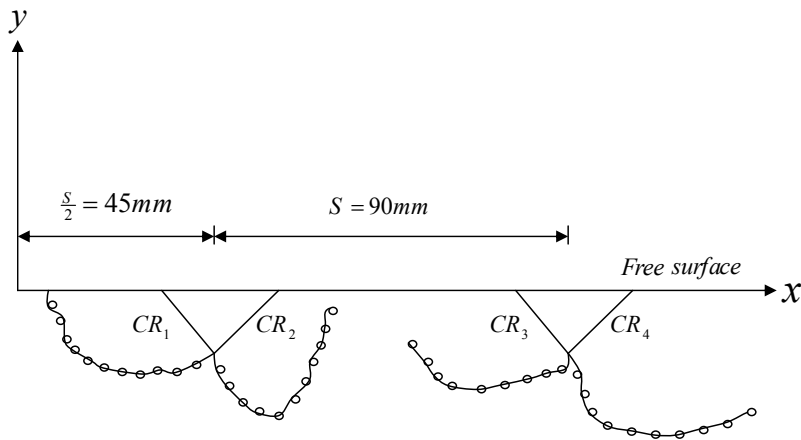


**Figure 12.** The crack propagation path for  $S/P_d = 15$ , for a  $90^\circ$  disc cutter,  $P_d = 6$  mm, and crack increment  $\Delta b = 4$  mm.

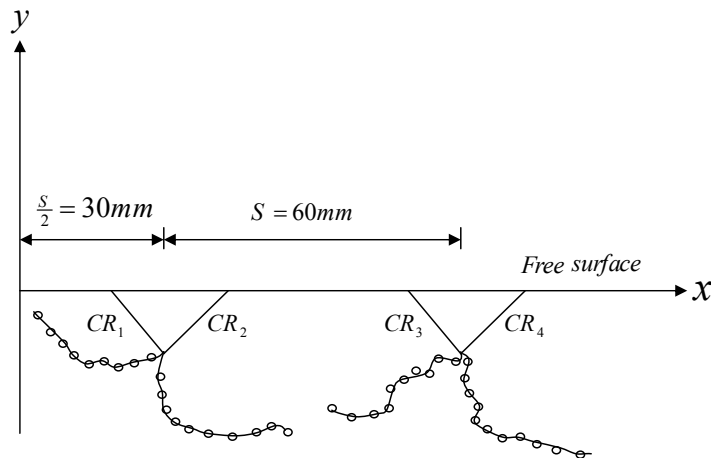


**Figure 13.** The crack propagation path for  $S/P_d = 10$ , for a  $90^\circ$  disc cutter,  $P_d = 6$  mm, and crack increment  $\Delta b = 4$  mm.

$S/P_d$	$\sigma_n$ (MPa)	$F_t$ (kN)	$F_r$ (kN)	$Q$ (mm <sup>2</sup> )	$E_s$ (MJ/m <sup>3</sup> )
3.33	-56	1344	159.53	176	906.42
5.00	-51	1224	145.29	352	412.76
6.67	-44	1056	125.35	451	277.94
8.33	-35	840	99.71	676	147.50
10.00	-39	936	111.10	903	123.03
11.67	-40	960	113.95	802	142.08
13.33	-41	984	116.80	751	155.53
15.00	-43	1032	122.49	676	181.20

**Table 7.** Estimated values of thrust force  $F_t$ , rolling force  $F_r$ , extracted area  $Q$ , and specific energy  $E_s$  for  $\Delta b = 1, 2$  and  $4$  mm, for different  $S/P_d$  ratios.

action. Here only the inner disc force and the area associated with this disc are used in estimating the final extracted area (Figure 14). Assuming a unit thickness for the rock, the specific energy  $E_s$  can be evaluated for different values of the ratio  $S/P_d$  (Figure 15).

In this analysis, the crack length  $b$  is increased incrementally by an amount  $\Delta b$ , and, correspondingly, the normal stress  $\sigma_n$  and shear stress  $\sigma_s$  are also increased to provide the sufficient energy for the crack to propagate in the direction of  $\theta_0$ . As a result of increasing the stresses at the crack boundaries, the crack starts its propagation, then a new crack length increment with 2 cubic elements and 3 crack tip elements is added in the propagation direction  $\theta_0$ , and the procedure is repeated for each crack increment  $\Delta b$ . Some estimated values for the forces  $F_t$  and  $F_r$  in kN, extracted area  $Q$  in mm<sup>2</sup>, and specific energy  $E_s$  in MJ/m<sup>3</sup> are tabulated in Tables 5 and 6 and also illustrated in Figures 14 and 15.

Table 7 shows that the thrust force is high for small disc spacing, and after reaching a minimum value it again increases to a larger value for very large disc spacing. Previous experimental work showed a steadily increasing thrust force with  $S/P_d$  ratio [Roxborough and Phillips 1975]. However, the model presented here is based on the propagation of existing cracks. These cracks require higher forces to propagate for smaller disc spacing due to the confinement effect of the adjacent cutters. As a result, higher forces are required to propagate the cracks for smaller disc spacings.

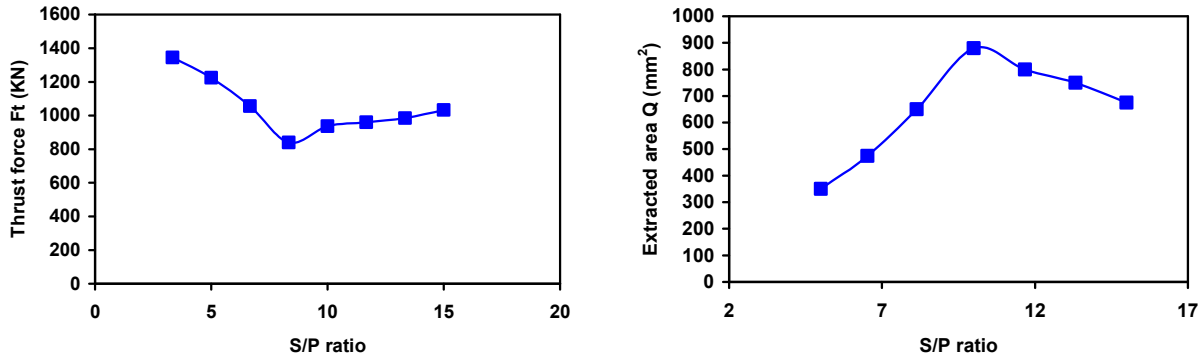
Figure 14, left, shows that the the thrust force  $F_t$  (kN) decreases as the  $S/P_d$  reaches about 10, but after this value it increases slowly. Figure 14, right, illustrates that the maximum extracted area that can be achieved occurs at  $S/P_d = 10$ . As shown in Figure 15, left, the optimum  $S/P_d$  ratio is between 8 and 15, which is in good agreement with the experimental results reported in [Roxborough and Phillips 1975; Howarth and Roxborough 1982].

Figure 15, right, illustrates the effect of the angle  $\phi$  on the specific energy  $E_s$ . These results show that  $E_s$  increases with the increase in the angle  $\phi$  (especially for the disc edge angles above  $90^\circ$ ).

## 8. Discussion

The tunnel boring machine (TBM) is a full-face excavator which cuts rock by means of disc cutters mounted on a circular revolving cutting head. The TBM breaks rock with disc cutters mounted on its rotating cutter-head in such a pattern that they roll against the rock of the tunnel face in a series of





**Figure 14.** Estimated values of the thrust force  $F_t$  (left) and extracted area  $Q$  (right) for different  $S/P_d$  ratios.

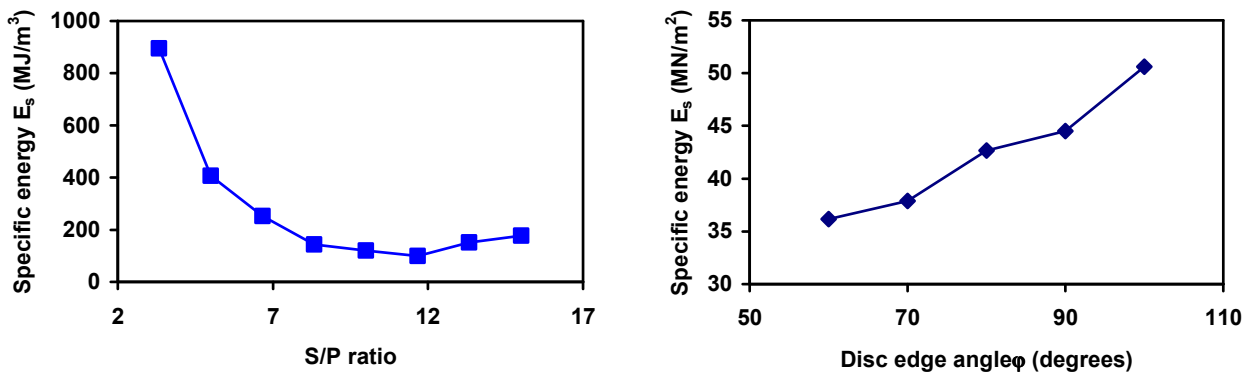


**Figure 15.** Specific energy  $E_s$  as a function of  $S/P_d$  at a constant  $F_r$  (left), and as a function of the disc edge angle  $\phi$  (right).

concentric circular grooves. The cutting force is produced by powerful hydraulic thrust rams. Each disc cutter is free to rotate within its mounting manifold. To maintain contact with the rock and to maintain the optimum spacing between cutting grooves, the machine is held stable by a combination of its great mass and by hydraulic jacks acting against the side of the tunnel.

It should be noted that there is no single universally accepted theory for the formation of rock chips by indenter tools. Most of the researches believe that the main cause of rock breakage is the propagation of tensile fractures, but the mechanism by which these fractures are first initiated is somewhat uncertain. Actually, rock breakage takes place because a tensile fracture is initiated and propagated. This fracture is induced as a result of combined loading (or mixed loadings), including the tensile extension of preexisting flaws along the fracture plane and tensile stresses induced by the crushed zone beneath the wedge. Hood and Roxborough [1992] describes a model for disc cutters developed by Lindqvist and Ranman [1980] which assumes that most of the force is directed normally into the rock, similar to the action of a flat-bottomed punch. Induced tensile stresses generate cracks that run nearly parallel to the rock surface, and if the spacing between the cutters is sufficiently small, tensile cracks propagating from each groove will join up to form a rock chip.

In the analysis proposed here, to simulate the cutting mechanism of the TBM disc cutters, each cutting groove is chosen as a single original crack and two successive grooves with varying spacing are simulated. The grooves are assumed to be vertical, although inclined grooves can also be easily modeled. In the displacement discontinuity method, each side of the crack can be discretized separately, and one of the crack surfaces can be considered as a fictitious boundary (this is one of the main advantages of the indirect boundary element methods). The higher order displacement discontinuity used here considers a cubic variation of the displacement discontinuities along each element on the boundary of the problem and also along the crack boundaries (except the crack tips) which results in very accurate general displacement discontinuities. The higher order crack tip elements are also used here to obtain more accurate results of the mixed mode stress intensity factors near the crack ends, where crack propagation begins. Although rock breakage theory predicts that tensile fractures are first initiated and then propagated, fractures are induced as a result of combined loading, where the action of the shear loading should also be taken into account.

If one only considers the tensile fracture and first mode of loading, propagated cracks may not theoretically meet each other or the rock surfaces, a prediction which deviates from experimental results and the reality of cheap formation processes. Therefore, in the analysis given in this study, one of the well-known mixed mode fracture criteria (the  $\sigma$ -criterion) has been used. All three fundamental mixed mode I-II fracture criteria can be used for the analysis. The  $\sigma$ -criterion is used based on the fracture toughness envelopes given by Whittaker et al. [1992], as shown schematically in Figure 16.

Here, the problem of a crack propagation mechanism under disc cutters is modeled in such a manner that the various effective parameters such as the thrust force,  $S/P_d$  ratio, the specific energy, etc. for various cases can be obtained. The numerical results are compared with those cited in the literature, and some good results are gained. For example, the results given in Table 6 show that the thrust force is high for small disc spacing, and after reaching minimum value, it again increases to a larger value for very large disc spacing. However, the model presented here is based on the propagation of existing cracks. These cracks require higher forces to propagate for smaller spacing due to the confinement effect of the adjacent cutters. As a result, for smaller disc spacing, higher forces are required to propagate the cracks. We see from Figure 14 that the thrust force  $F_t$  (kN) decreases as  $S/P_d$  approaches 10, but subsequently increases slowly.

Figure 14, right, indicates that the maximum achievable extracted area occurs at  $S/P_d = 10$ . As shown in Figure 15, left, the optimum  $S/P_d$  ratio ranges from 8 to 15. Figure 15, right, illustrates the effect of the angle  $\varphi$  on specific energy  $E_s$ . These results show that  $E_s$  increases with an increase in the angle  $\varphi$  (especially for the disc edge angles above  $90^\circ$ ).

## 9. Conclusion

In this work, crack propagation mechanisms under disc cutters are numerically modeled and studied using the higher order displacement discontinuity method. To increase the accuracy of displacement discontinuities near crack tips, three special crack tip elements are used for the treatment of each crack end. The maximum tangential stress fracture criterion is employed to investigate the crack propagation and its direction under disc cutters, and some of the computed results are compared with previously reported experimental results. This comparison shows that in most of the cases, the numerical results

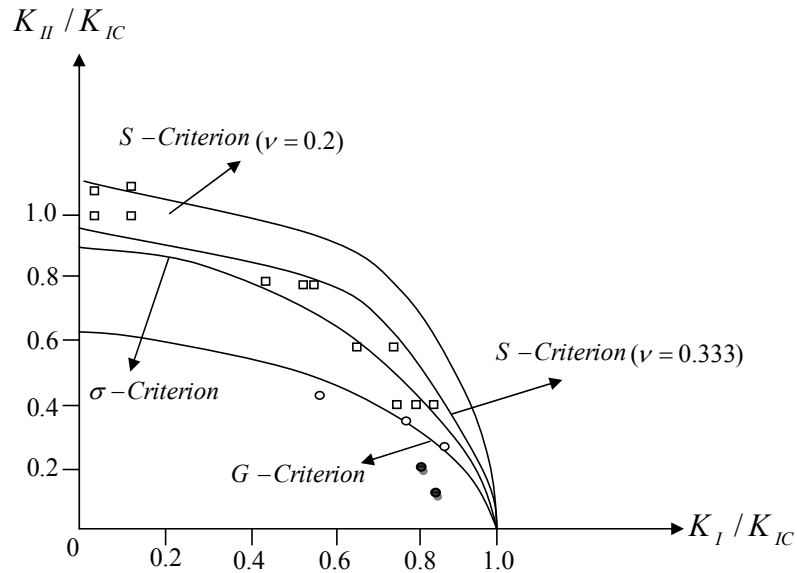


**Figure 16.** Fracture toughness envelopes based on various mixed mode fracture criteria [Whittaker et al. 1992]. Plotted experimental points taken [Ingraffea 1983] (open squares; Westerly granite), [Huang and Wang 1985] (black circles), and [Sun 1990] (open circles).

are in good agreement with their corresponding experimental values. As a result, for small disc spacing ( $S/P_d < 6$ ), higher forces (more energy) are required to propagate cracks for inner discs, and for large disc spacing ( $S/P_d > 15$ ), the specific energy  $E_s$  increases slowly because the extracted area  $Q$  tends to be constant as the spacing is increased. However, the optimum  $S/P_d$  ratio is between 8 and 15, as was expected from comparison to experimental results [Roxborough and Phillips 1975; Howarth and Roxborough 1982; Lislrud 1988; Nilsen and Ozdemir 1993; Rostami et al. 1994; Johanessen 1995; Bilgin et al. 2000]. It is also concluded that as the disc edge angle  $\phi$  increases, the specific energy  $E_s$  increases.

## References

- [Alehossein et al. 2000] H. Alehossein, E. Detournay, and H. Huang, "An analytical model for the indentation of rocks by blunt tools", *Rock Mech. Rock Eng.* **33**:4 (2000), 267–284.
- [Backers 2004] T. Backers, *Fracture toughness determination and micromechanics of rock under mode I and mode II loading*, Ph.D. Thesis, university of Potsdam, Potsdam, DE, 2004, Available at <http://opus.kobv.de/ubp/volltexte/2005/229/>.
- [Backers et al. 2002] T. Backers, O. Stephansson, and E. Rybacki, "Rock fracture toughness testing in mode II punch-through shear test", *Int. J. Rock Mech. Min.* **39**:6 (2002), 755–769.
- [Backers et al. 2003] T. Backers, N. Fardin, G. Dresen, and O. Stephansson, "Effect of loading rate on mode I fracture toughness, roughness and micromechanics of sandstone", *Int. J. Rock Mech. Min.* **40**:3 (2003), 425–433.
- [Backers et al. 2004] T. Backers, G. Dresen, E. Rybacki, and O. Stephansson, "New data on mode II fracture toughness of rock from the punch-through shear test", *Int. J. Rock Mech. Min.* **41**:3 (2004), 351–352. SINOROCK2004 Paper 1A 01.

- [Bilgin et al. 2000] N. Bilgin, C. Balcı, O. Acaroğlu, H. Tunçdemir, and c. Eskikaya, “Development of rapid excavation technologies for the Turkish mining and tunnelling industries”, NATO TU Excavation project report, Istanbul Technical University, Faculty of Mines, Mining Engineering Department, 2000. pp. 172.
- [Bobet 2001] A. Bobet, “A hybridized displacement discontinuity method for mixed mode I-II-III loading”, *Int. J. Rock Mech. Min.* **38**:8 (2001), 1121–1134.
- [Bowie 1973] O. L. Bowie, “Solutions of plane crack problems by mapping techniques”, in *Methods of analysis and solutions of crack problems. Recent developments in fracture mechanics. Theory and methods of solving crack problems*, edited by G. C. Sih, Mechanics of fracture **1**, Noordhoff International, Leyden, 1973.
- [Broek 1989] D. Broek, *The practical use of fracture mechanics*, 4th ed., Kluwer, Dordrecht, 1989.
- [Crawford and Curran 1982] A. M. Crawford and J. H. Curran, “Higher-order functional variation displacement discontinuity elements”, *Int. J. Rock Mech. Min.* **19**:3 (1982), 143–148.
- [Crouch 1976] S. L. Crouch, “Solution of plane elasticity problems by the displacement discontinuity method, I: infinite body solution”, *Int. J. Numer. Methods Eng.* **10**:2 (1976), 301–343.
- [Crouch and Starfield 1983] S. L. Crouch and A. M. Starfield, *Boundary element methods in solid mechanics: with applications in rock mechanics and geological engineering*, Allen and Unwin, London, 1983.
- [Erdogan and Sih 1963] F. Erdogan and G. C. Sih, “On the crack extension in plates under plane loading and transverse shear”, *J. Basic Eng. (ASME)* **85** (1963), 519–527.
- [Fatehi Marji et al. 2006] M. Fatehi Marji, H. Hosseini-Nasab, and A. H. Kohsary, “On the uses of special crack tip elements in numerical rock fracture mechanics”, *Int. J. Solids Struct.* **43**:6 (2006), 1669–1692.
- [Fatehi Marji et al. 2007] M. Fatehi Marji, H. Hosseini-Nasab, and A. H. Kohsary, “A new cubic element formulation of the displacement discontinuity method using three special crack tip elements for crack analysis”, *JP J. Solids Struct.* **1**:1 (2007), 61–91.
- [Guo et al. 1992] H. Guo, N. I. Aziz, and L. C. Schmidt, “Rock cutting study using linear elastic fracture mechanics”, *Eng. Fract. Mech.* **41**:5 (1992), 771–778.
- [Hood and Roxborough 1992] M. C. Hood and F. F. Roxborough, “Rock breakage: mechanical”, Chapter Chapt 9.1, pp. 680–721 in *SME mining engineering handbook*, vol. 1, edited by H. L. Hartman, Society for Mining, Metallurgy and Exploration, Littleton, CO, 1992.
- [Howarth and Roxborough 1982] D. F. Howarth and F. F. Roxborough, “Some fundamental aspects of the use of disc cutters in hard-rock excavation”, *J. South Afric. Inst. Min. Metall.* (1982), 309–315.
- [Huang and Wang 1985] J. Huang and S. Wang, “An experimental investigation concerning the comprehensive fracture toughness of some brittle rocks”, *Int. J. Rock Mech. Min.* **22**:2 (1985), 99–104.
- [Ingraffea 1983] A. R. Ingraffea, “Numerical modeling of fracture propagation”, pp. 151–208 in *Rock fracture mechanics*, edited by H. P. Rossmanith, Springer-Verlag, Wien, New York, 1983.
- [Irwin 1957] G. R. Irwin, “Analysis of stresses and strains near the end of a crack traversing a plate”, *J. Appl. Mech. (ASME)* **24**:3 (1957), 361–364.
- [Johanessen 1995] O. Johanessen, “Hard rock tunnel boring”, University of Trondheim, the Norwegian Institute of Technology, 1995. p.165.
- [Lindqvist and Ranman 1980] P. E. Lindqvist and K. E. Ranman, “Mechanical rock fragmentation: chipping under a disc cutter”, Technical report 59T, University of Lulea, Lulea, Sweden, 1980.
- [Lislerud 1988] A. Lislerud, “Hard rock tunnel boring: prognosis and costs”, *Tunn. Undergr. Space Technol.* **3**:1 (1988), 9–17.
- [Nilsen and Ozdemir 1993] B. Nilsen and L. Ozdemir, “Hard rock tunnel boring prediction and field performance”, in *Rapid excavation and tunneling conference (RETC) proceedings*, edited by L. D. Bowerman and J. E. Monsees, Boston, 1993. Chapter 52.
- [Ouchterlony 1988] F. Ouchterlony (coordinator), “Suggested methods for determining the fracture toughness of rock”, *Int. J. Rock Mech. Min.* **25**:2 (1988), 71–96.
- [Rao et al. 2003] Q. Rao, Z. Sun, O. Stephansson, C. Li, and B. Stillborg, “Shear fracture (mode II) of brittle rock”, *Int. J. Rock Mech. Min.* **40**:3 (2003), 355–375.

- [Rostami et al. 1994] J. Rostami, L. Ozdemir, and M. D. Neil, "Performance prediction: a key issue in mechanical hard rock mining", *Min. Eng.* **11** (1994), 1263–1267.
- [Roxborough and Phillips 1975] F. F. Roxborough and H. R. Phillips, "Rock excavation by disc cutter", *Int. J. Rock Mech. Min.* **12**:12 (1975), 361–366.
- [Shen and Stephansson 1994] B. Shen and O. Stephansson, "Modification of the  $G$ -criterion for crack propagation subjected to compression", *Eng. Fract. Mech.* **47**:2 (1994), 177–189.
- [Shen et al. 2004] B. Shen, O. Stephansson, M. Rinne, H.-S. Lee, L. Jing, and K. Roshoff, "A fracture propagation code and its applications to nuclear waste disposal", *Int. J. Rock Mech. Min.* **41**:3 (2004), 448–449. SINOROCK2004 Paper 2B 02.
- [Shou and Crouch 1995] K. J. Shou and S. L. Crouch, "A higher order displacement discontinuity method for analysis of crack problems", *Int. J. Rock Mech. Min.* **32**:1 (1995), 49–55.
- [Sneddon 1951] I. N. Sneddon, *Fourier transforms*, McGraw-Hill, New York, 1951.
- [Snowdon et al. 1982] R. A. Snowdon, M. D. Ryley, and J. Temporal, "A study of disc cutting in selected british rocks", *Int. J. Rock Mech. Min.* **19**:3 (1982), 107–121.
- [Stephansson 2002] O. Stephansson, "Recent rock fracture mechanics developments", pp. 675–698 in *1<sup>st</sup> Iranian Rock Mechanics Conference* (Tehran, 2002), 2002.
- [Stephansson et al. 2001] O. Stephansson, T. Backers, G. Dresen, and E. Rybacki, "Shear fracture mechanics of rocks and a new testing method for  $K_{IIC}$ ", pp. 163–168 in *Rock mechanics: a challenge for society: proceedings of the ISRM regional symposium, EUROCK 2001* (Espoo, Finland, 2001), edited by P. Sarkka and P. Eloranta, 2001.
- [Sun 1990] G. X. Sun, *Application of fracture mechanics to mine design*, Ph.D. thesis, Department of Mining Engineering, University of Nottingham, 1990.
- [Tan et al. 1996] X. C. Tan, S. Q. Kou, and P. A. Lindqvist, "Simulation of rock fragmentation by indenters using DDM and fracture mechanics", in *Rock mechanics: tools and techniques: proceedings of the 2nd North American Rock Mechanics Symposium, NARMS'96, a regional conference of ISRM* (Montreal, 1996), edited by M. Aubertin et al., A. A. Balkema, Rotterdam, 1996.
- [Whittaker et al. 1992] B. N. Whittaker, R. N. Singh, and G. Sun, *Rock fracture mechanics: principles, design and applications*, Elsevier, Amsterdam, 1992.

Received 31 Dec 2008. Revised 11 Mar 2009. Accepted 11 Mar 2009.

MOHAMMAD FATEHI MARJI: mfatehi@yazduni.ac.ir

Department of Mining Engineering, Yazd University, Safaiyeh, Yazd 89195741, Iran,

HASAN HOSSEINI NASAB: hhn@yazduni.ac.ir

Department of Industrial Engineering, Yazd University, Safaiyeh, Yazd 89195741, Iran,

AMIN HOSSEIN MORSHEDI: morshedy82@gmail.com

Department of Mining and Petroleum Engineering, Tehran University, Tehran, Iran



## SUBMISSION GUIDELINES

### ORIGINALITY

Authors may submit manuscripts in PDF format on-line. Submission of a manuscript acknowledges that the manuscript is *original and has neither previously, nor simultaneously, in whole or in part, been submitted elsewhere*. Information regarding the preparation of manuscripts is provided below. Correspondence by email is requested for convenience and speed. For further information, write to:

Marie-Louise Steele  
Division of Mechanics and Computation  
Durand Building, Room 262  
Stanford University  
Stanford CA 94305

### LANGUAGE

Manuscripts must be in English. A brief abstract of about 150 words or less must be included. The abstract should be self-contained and not make any reference to the bibliography. Also required are keywords and subject classification for the article, and, for each author, postal address, affiliation (if appropriate), and email address if available. A home-page URL is optional.

### FORMAT

Authors are encouraged to use L<sup>A</sup>T<sub>E</sub>X and the standard article class, but submissions in other varieties of T<sub>E</sub>X, and, exceptionally in other formats, are acceptable. Electronic submissions are strongly encouraged in PDF format only; after the refereeing process we will ask you to submit all source material.

### REFERENCES

Bibliographical references should be listed alphabetically at the end of the paper and include the title of the article. All references in the bibliography should be cited in the text. The use of B<sup>I</sup>B<sub>T</sub><sub>E</sub>X is preferred but not required. Tags will be converted to the house format (see a current issue for examples), however, in the manuscript, the citation should be by first author's last name and year of publication, e.g. "as shown by Kramer, et al. (1994)". Links will be provided to all literature with known web locations and authors are encouraged to provide their own links on top of the ones provided by the editorial process.

### FIGURES

Figures prepared electronically should be submitted in Encapsulated PostScript (EPS) or in a form that can be converted to EPS, such as GnuPlot, Maple, or Mathematica. Many drawing tools such as Adobe Illustrator and Aldus FreeHand can produce EPS output. Figures containing bitmaps should be generated at the highest possible resolution. If there is doubt whether a particular figure is in an acceptable format, the authors should check with production by sending an email to:

production@mathscipub.org

Each figure should be captioned and numbered so that it can float. Small figures occupying no more than three lines of vertical space can be kept in the text ("the curve looks like this:"). It is acceptable to submit a manuscript with all figures at the end, if their placement is specified in the text by means of comments such as "Place Figure 1 here". The same considerations apply to tables.

### WHITE SPACE

Forced line breaks or page breaks should not be inserted in the document. There is no point in your trying to optimize line and page breaks in the original manuscript. The manuscript will be reformatted to use the journal's preferred fonts and layout.

### PROOFS

Page proofs will be made available to authors (or to the designated corresponding author) at a web site in PDF format. Failure to acknowledge the receipt of proofs or to return corrections within the requested deadline may cause publication to be postponed.

# Journal of Mechanics of Materials and Structures

Volume 4, N<sup>o</sup> 3    March 2009

---

Design of crack-resistant two-dimensional periodic cellular materials FABIAN LIPPERMAN, MICHAEL RYVKIN AND MOSHE B. FUCHS	441
Influence of the nonlinear aerodynamic force components on a vibrating beam, simply supported or clamped at both ends, exposed to a high supersonic airflow along its axial direction SILVANO TIZZI	459
Finite element formulations via the theorem of expended power in the Lagrangian, Hamiltonian and total energy frameworks JASON HAR AND KUMAR K. TAMMA	475
Static bending analysis of laminated cylindrical panels with various boundary conditions using the differential cubature method S. MAHMOUD MOUSAVI AND MOHAMAD M. AGHDAM	509
Indentation analysis of fractional viscoelastic solids ROUZBEH SHAHSAVARI AND FRANZ-JOSEF ULM	523
Macroscale modelling of microstructure damage evolution by a rigid body and spring model SIRO CASOLO	551
Performance and parametric study of active multiple tuned mass dampers for asymmetric structures under ground acceleration CHUNXIANG LI, JINHUA LI, ZHIQIANG YU AND YAN QU	571
Effects of surface and initial stresses on the bending stiffness of trilayer plates and nanofilms HANXING ZHU, JIANXIANG WANG AND BHUSHAN KARIHALOO	589
Numerical modeling of crack propagation in rocks under TBM disc cutters M. FATEHI MARJI, H. HOSSEINI NASAB AND A. HOSSEIN MORSHEDI	605



1559-3959(200903)4:3;1-7